



Dipl.-Ing. Birgit Pichler, BSc.

Development of Stable Bifunctional Air Electrodes for Oxygen Electrocatalysis in Zinc-Air Flow Batteries

DOCTORAL THESIS

to achieve the university degree of
Doktorin der technischen Wissenschaften

submitted to

Graz University of Technology

Supervisor

Assoc.Prof. Dipl.-Ing. Dr.techn. Viktor Hacker

Institut für Chemische Verfahrenstechnik und Umwelttechnik

AFFIDAVIT

I declare that I have authored this thesis independently, that I have not used other than the declared sources/resources, and that I have explicitly indicated all material which has been quoted either literally or by content from the sources used. The text document uploaded to TUGRAZonline is identical to the present doctoral thesis.

Date

Signature

Abstract

Energy generation gradually shifts to renewable resources with growing capacities of installed wind and solar power systems, but the intermittent and fluctuating renewable power production requires electrical energy storage systems to stabilize the electricity grid. The rechargeable zinc-air flow battery is a promising stationary electrical energy storage system with low environmental impact and compact system design. It uses the abundant and inexpensive metal zinc as storing material. The main challenges of this system are the inhomogeneous zinc deposition during charging as well as the high overpotentials and low stability of the air electrode, resulting in limited lifetime, deteriorating cycle stability and low energy efficiency, which prevents the application of the zinc-air battery as stationary energy storage system.

This work focused on the development and optimization of bifunctional air electrodes for catalyzing oxygen reduction and oxygen evolution reaction in a single electrode. As catalysts, only precious metal-free oxide catalysts were employed. The electrodes were built via a straightforward and scalable manufacturing process using nickel foam as current collector and carbon nanofibers, nickel powder and PTFE as additives. The electrochemical performance regarding its catalytic activity toward oxygen reduction and oxygen evolution reaction and the long-term stability during repeated charge/discharge cycling was evaluated using custom-made test cells and flow cell set-ups.

In zinc-air unit cells with flowing alkaline electrolyte, operation times of over 1000 h and more than 500 charge/discharge cycles were achieved at practically applicable current density of 50 mA cm^{-2} . The voltage efficiency of the air electrode was over 50%, exhibiting charge potentials of below 2 V and discharge potentials of over 1.0 V vs. Zn/Zn^{2+} , respectively. End-of-life investigations revealed that mechanical degradation during charging as well as slowly deteriorating hydrophobicity due to PTFE degradation was the main cause of slowly decreasing performances of the air electrode after several hundred hours of operation.

Kurzfassung

Der umfassende Ausbau erneuerbarer, fluktuierender Energiequellen wie Wind- und Solarkraftwerke erhöht auch den Bedarf an stationären Energiespeichersystemen um die Stabilität des Elektrizitätsnetzes zu gewährleisten. Eine vielversprechende Technologie dafür ist die wiederaufladbare Zink-Luft Fließbatterie, die sich durch gute Umweltverträglichkeit, einen kompakten Systembau, sowie durch die Verwendung des häufig vorkommenden und daher kostengünstigen Speichermaterials Zink auszeichnet. Die Herausforderungen liegen dabei einerseits bei der inhomogenen Zinkabscheidung während des Ladens der Batterie, als auch bei den großen Überspannungen und der geringen Stabilität der Luftpole. Die daraus resultierende kurze Lebenszeit mit geringer Zyklenstabilität als auch die sehr niedrige Energieeffizienz des Systems verhindern bis jetzt die praktische Anwendung der Zink-Luft Fließbatterie als stationäres Energiespeichersystem.

Diese Arbeit beschäftigte sich mit der Entwicklung und Optimierung von bifunktionalen Luftpole für die elektrochemische Umsetzung von Sauerstoff in alkalischem Medium. Für die Katalyse der Sauerstoffreduktionsreaktion und der Sauerstoffentwicklungsreaktion wurden edelmetallfreie Oxidkatalysatoren verwendet. Mit diesen Katalysatoren wurden Elektroden über einen einfach skalierbaren Herstellungsprozess gefertigt, wobei Nickelschaum als Stromabnehmer und PTFE, Nickelpulver und Kohlenstoffnanofasern als Additive verwendet wurden. Die katalytische Aktivität sowie die Langzeitstabilität über wiederholte Lade-/Entladezyklen wurde in elektrochemischen Untersuchungen in selbst gebauten Testzellen und Fließtestständen überprüft und charakterisiert.

In Zink-Luft Einzelzellen mit fließendem Elektrolyt wurden Betriebszeiten von über 1000 h und über 500 Zyklen bei anwendungsnahen Stromdichten von 50 mA cm^{-2} erzielt. Dabei wurde für die Luftpole eine Spannungseffizienz von über 50% erreicht, was einer Ladespannung von unter 2.0 V und einer Entladespannung von über 1.0 V vs. Zn/Zn^{2+} entspricht. Die Charakterisierung der Luftpole nach mehreren hundert Stunden im Lade-/Entladebetrieb zeigte, dass sowohl mechanische Schädigung des Elektrodenaufbaus, als auch eine verringerte Hydrophobizität der Elektrode für die langsam sinkende Leistung der Luftpole verantwortlich waren.

Danksagung

An dieser Stelle möchte ich Univ.Prof. Viktor Hacker für die Möglichkeit diese Doktorarbeit zu verfassen und für seine Unterstützung während dieser Zeit danken. Es wurden mir ideale Bedingungen für die Forschungsarbeit und das Verfassen einer Dissertation ermöglicht und besonders die vielen Konferenzbesuche waren für mich eine besondere Erfahrung und Bereicherung. Weiters möchte ich der ganzen Brennstoffzellen-Arbeitsgruppe für die tolle Zusammenarbeit, die nette Atmosphäre und den vielen Spaß den wir über die ganzen Jahre gemeinsam hatten, danken. Die Diskussionen und Gespräche bei der Kaffeemaschine werden mir in toller Erinnerung bleiben! Mein Dank gilt außerdem meinen engagierten Projektpartnern, wobei ich besonders Univ.Prof. Bernhard Gollas für seine Unterstützung und die gesamte Koordination des Projektes danken möchte.

Meiner Familie – meinen Eltern, meiner Großmutter und meinem Bruder – möchte ich für die andauernde Unterstützung während meiner Dissertationszeit danken.

Nicht zuletzt gilt mein Dank meinem Christoph, der immer weiß wie er mir helfen und mich aufbauen kann, auch wenn es mal nicht so läuft. Zu zweit kann man einfach immer mehr schaffen. Die gemeinsame Zeit während dem Studium war einfach unbeschreiblich und ich bin unglaublich dankbar, dass du immer da bist.

Birgit Pichler

Graz, Oktober 2018

Contents

| | | |
|----------|----------------------------------------------------------------------------------------------------|-----------|
| 1 | Introduction | 1 |
| 1.1 | Electrical Energy Storage | 3 |
| 1.2 | Electrochemical Energy Storage with Batteries | 7 |
| 2 | Aims and Scope of this Thesis | 11 |
| 3 | Theory | 13 |
| 3.1 | Introduction to Rechargeable Zinc-Air (Flow) Batteries | 13 |
| 3.1.1 | Historical Development of Zinc-Air Systems | 15 |
| 3.2 | Design and Configuration of Zinc-Air Batteries | 17 |
| 3.2.1 | Primary Metal-Air Batteries | 17 |
| 3.2.2 | Rechargeable Battery Configurations | 18 |
| 3.2.3 | Electrolytes | 20 |
| 3.2.4 | Flow Batteries | 21 |
| 3.3 | Zinc Electrode | 29 |
| 3.4 | Air Electrode | 33 |
| 3.4.1 | Electrocatalysis of O ₂ | 33 |
| 3.4.2 | Bifunctional Electrocatalysts for O ₂ -Reduction and O ₂ -Evolution Reaction | 37 |
| 3.4.3 | Electrode Manufacture and Materials | 45 |
| 3.4.4 | Long-term Performance of Bifunctional Air Electrodes | 48 |
| 3.5 | Electrochemical Characterization | 53 |
| 4 | Experimental | 59 |
| 4.1 | Catalyst Synthesis | 59 |
| 4.2 | Electrode Manufacture | 61 |
| 4.3 | Test Cells and Electrochemical Characterization | 63 |

| | | |
|-----------|-------------------------------------------------------------------------------------------------------------------|------------|
| 5 | Results and Discussion | 69 |
| 5.1 | Project Outline | 69 |
| 5.2 | Preliminary Tests of Bifunctionally Catalyzed Air Electrodes | 71 |
| 5.2.1 | Dip-coated Electrodes Catalyzed with NiCo ₂ O ₄ | 72 |
| 5.2.2 | Air Electrodes Catalyzed with Batch-synthesized NiCo ₂ O ₄ | 77 |
| 5.2.3 | Perovskite-catalyzed Bifunctional Air Electrodes | 78 |
| 5.2.4 | Ag-MnO ₂ and Pt-catalyzed Bifunctional Air Electrodes | 84 |
| 5.3 | Bi-catalyzed Bifunctional Air Electrodes with NiCo ₂ O ₄ and Perovskites | 86 |
| 5.3.1 | Peer-Reviewed Publication in <i>Electrochimica Acta</i> | 90 |
| 5.4 | Optimizing the Operation Conditions of Bi-catalyzed Bifunctional Air Electrodes | 91 |
| 5.4.1 | Peer-Reviewed Publication in <i>Journal of Applied Electrochemistry</i> | 92 |
| 5.4.2 | Application of Carbon Paper as Backing Layer | 93 |
| 5.5 | RDE Cyclic Voltammetry of NiCo ₂ O ₄ and Nickel Powder | 96 |
| 5.6 | La _{0.6} Sr _{0.4} Co _{0.2} Fe _{0.8} O ₃ -only Electrodes | 99 |
| 5.6.1 | Additional Hydrophobic Backing Layer | 99 |
| 5.6.2 | Operation of Air Electrodes without Cycling | 104 |
| 5.6.3 | Scaled-up 60 cm ² -sized Air Electrodes with Flowing Electrolyte | 106 |
| 5.6.4 | Peer-Reviewed Publication in <i>Batteries & Supercaps</i> | 109 |
| 6 | Summary and Conclusion | 111 |
| 7 | Materials and Instruments | 115 |
| 7.1 | Chemicals | 115 |
| 7.2 | Materials | 116 |
| 7.3 | Instruments | 117 |
| 8 | References | 118 |
| 9 | List of Figures | 131 |
| 10 | List of Tables | 134 |
| 11 | Appendix A: Test Protocols for Electrochemical Characterization | 137 |

| | |
|------------------------------------------------------------------------------------------------------------------------------------------------------------|------------|
| 12 Appendix B: Dissemination | 143 |
| 12.1 List of Publications | 143 |
| 12.1.1 Peer-Reviewed Journal Articles | 143 |
| 12.1.2 Selected Reviewed Conference Proceedings | 144 |
| 12.1.3 Presentations at Conferences and Meetings | 144 |
| 12.1.4 Poster | 145 |
| 12.1.5 Book Chapters | 146 |
| 12.2 Publication 1: Bifunctional electrode performance for zinc-air flow cells with pulse charging | 147 |
| 12.3 Publication 2: The impact of operating conditions on component and electrode development for zinc-air flow batteries | 161 |
| 12.4 Publication 3: Long-term operation of perovskite-catalyzed bifunctional air electrodes in rechargeable zinc-air flow batteries | 177 |
| 12.5 Proceeding 1: Development of stable bifunctional air electrodes for zinc-air flow batteries | 197 |
| 12.6 Proceeding 2: Development of zinc-air flow batteries by investigating compact zinc deposition and improving air electrode cycling stability | 203 |

1 Introduction

The world energy demand rises steadily and is predicted to double by 2050 [1]. According to the Key World Statistics 2017 published by the International Energy Agency (IEA) [2], the world total primary energy supply in 2015 was 13 600 million tonnes of oil equivalent with over 80% provided from oil, gas and coal. The electricity production was 24 000 TWh with a share of fossil fuels of over 65%. In relation to this, electricity from renewable sources was about 22% with hydro power being the major part (16%) [2, 3]. The excessive burning of carbon-based fossil fuels resulted in an increase of CO₂ concentrations in the atmosphere by 40% since pre-industrial times as summarized in the last IPCC report [4]. Thus, our society has to employ alternatives in energy generation with a simultaneous reduction in green-house gas emissions released through burning of fossil-fuels. Instead of depleting the fossil fuel reserves, like crude oil, coal and natural gas, the energy production has to shift to renewables, namely solar, wind, tidal, wave, hydrokinetic from water currents, hydropotential, geothermal and various types of biomass [1]. All aforementioned energy forms are regarded as primary energy carriers as they are readily available in nature and need only extraction or capture [5]. Most of these sources directly produce electrical energy - a secondary energy carrier - via a generator. This poses together with their often intermittent and sometimes hard-to-predict availability a challenge in regard to imbalances in production and demand. As electricity is an energy carrier, which is in contrast to other secondary energy forms such as liquid gasoline or gaseous methane or hydrogen, very difficult to store, it needs to be converted into other forms of energy as depicted in Figure 1.1 [5]. The different forms can be classified as chemical, electrochemical, mechanical and thermal energy storage [1, 6].

Up to now, electricity is primarily generated by reliable and storable fossil fuels, thus storage of electricity is of less importance [5]. The existing energy storage systems were primarily installed for economical reasons instead of solving the issue of integrating fluctuating renewable energy sources into the electrical grid. For example in the US, 88% of storage capacity is used for profit maximization by exploiting arbitrage, *i.e.* by charging during low demand and low price periods

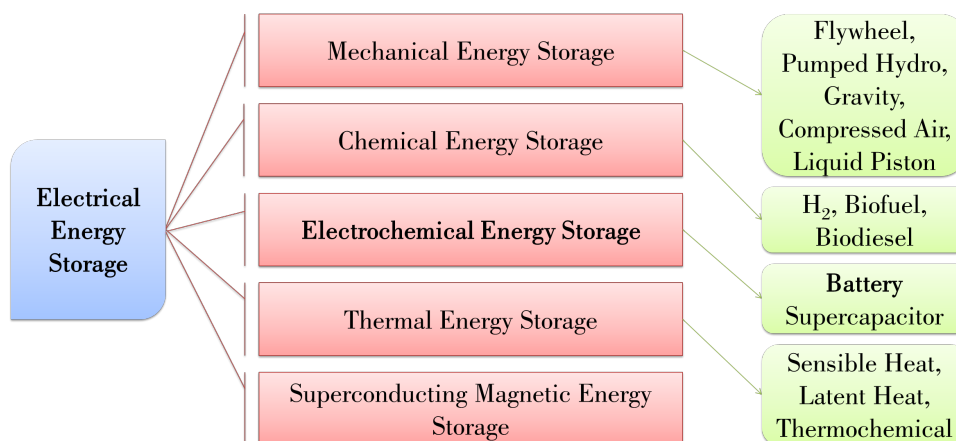


Figure 1.1: Classification of different types of electrical energy storage according to Aneke *et al.* [5]. This thesis focuses on electrochemical energy storage with batteries.

and discharging during high demand times with higher prices [7]. However, the share of electricity generation by renewable sources is rising. Looking at the European Union, by 2014, already over 100 GW of wind turbines and nearly 100 GW of – often decentralized – photovoltaic systems have been integrated into the European electricity network. These decentralized systems together with the growing number of offshore wind parks in the northern countries pose a challenge for maintaining stable transmission grids throughout Europe [8]. In Austria, hydro power is still by far the main renewable source for electricity generation, whereas the main renewable source for the total energy production is biomass (forest coverage in Austria is 47%). The biomass is primarily converted in combined heat and power plants as well as in small household heating systems [9]. This overall expansion of renewables is in accordance with the goals of the European Union as stated 2012 in the *European Roadmap 2050* [10]. Therein, a transition to a competitive low-carbon economy by 2050 is presented with the goal of reducing greenhouse gas emissions to 80–95% below 1990 levels. For achieving this goal, in nearly all scenarios, the share of renewable energy sources has to rise to a minimum of 55% of the gross final energy consumption (today about 10%), and in electricity consumption the share of renewable energy sources has to reach in some scenarios even 97%. This highlights the demand for a significant capacity for electricity storage. However, this is very challenging to achieve. It is estimated that for every 10% of electricity generation by intermittent sources such as wind power, 2-4% of this installed capacity has to be balanced by a reliable source in order to maintain power system stability [11]. In 2015, 96% of the world-wide large-scale energy storage capacity was attributed to pumped hydro storage (with an estimated amount of 150 GW in hydro power) [12], whereby many favorable

geographical sites were already exploited. Nevertheless, there are no installed facilities in practical operation, which can store a capacity in the TWh range for duration times of several months (seasonal storage) [6]. Moreover, the cost targets set, for example, by the US Department of Energy are very strict. For batteries, in the near-term the targeted cost are as low as 250 \$ kWh⁻¹ capital cost (system efficiency of > 75%) and in the long-term even below 150 \$ kWh⁻¹ with required efficiencies of 80% [6, 9]. These goals have to be achieved by putting a higher emphasis on pilot and demonstration programs (RD&D) for new technologies as was summarized by the European Association for Storage of Energy (EASE) [12]. They demanded in their 2017 report a higher number of research projects and a better coordinated collaboration policy for RD&D within the EU, highlighting that in 2014, 70% of the newly installed storage capacity world-wide were still pumped hydro storage [12]. In addition, the EU-wide goals need to include a better management across borders and increased investments for power transmission infrastructure in order to compensate favorable and unfavorable sites for renewable energy generation and storage. A shared energy market across more countries can thus result in economical and technological benefits for all participating countries [9].

In the following chapter the different types of electrical energy storage as listed in the schematic in Figure 1.1 and the associated conversion technologies are shortly discussed.

1.1 Electrical Energy Storage

When integrating electrical energy storage systems into electricity grids, three aims are of high importance: first, they have to contribute to the reliability of renewable energy sources, second, the resilience of the grid has to be increased and third, the generation has to suit the demand, thereby improving the overall efficiency (implementation of smart grids) [13]. As shown in Figure 1.2(a), depending on how much power and how long the required power has to be supplied, different services can be distinguished. Among others, these applications can be categorized as power quality for voltage and frequency synchronization, load leveling for ensuring stable electricity generation, transmission and distribution services for efficiency maximization and black start as needed in auxiliary power systems [5, 6].

The energy storage itself suffers thereby from conversion losses at each step: first during charging, then during storage (time-dependent) and again during discharge [13]. This is summarized in equation 1.1, whereby the term ($\Delta E_{charge} + \Delta E_{storage} + \Delta E_{discharge}$) refers to the energy losses

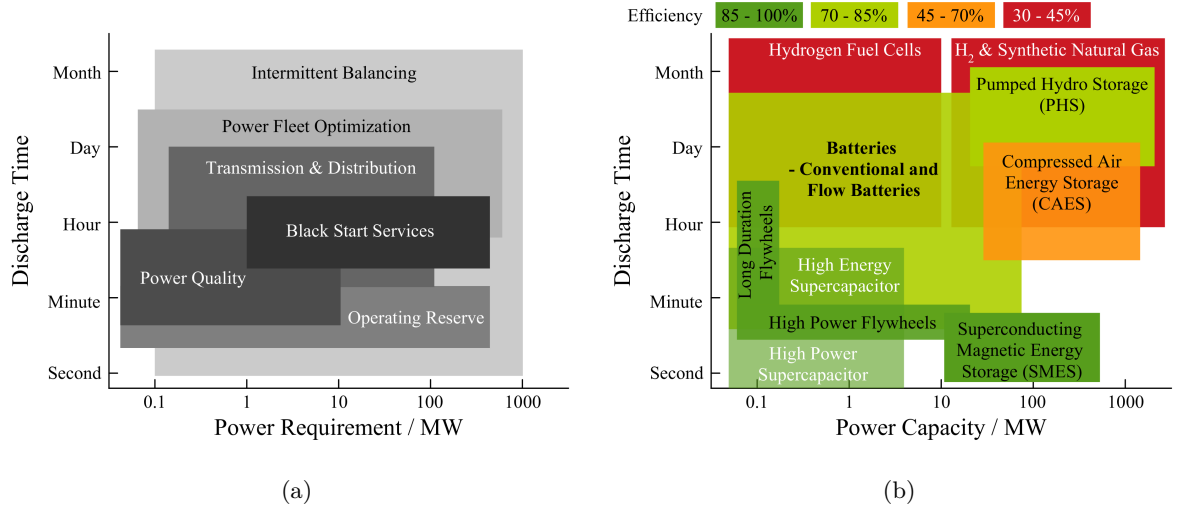


Figure 1.2: Power requirement of different services (a) in comparison to the power delivered by different electrical storage systems (b) in regard to the discharge time. Schematics adapted from [5] and [14].

during each step resulting in the overall energy loss ΔE_{loss} . $E_{generated}$ is the energy generated by the sources and E_{out} describes the energy delivered by the system.

$$E_{generated} - (\Delta E_{charge} + \Delta E_{storage} + \Delta E_{discharge}) = E_{out} \quad (1.1)$$

The efficiency during each step can be calculated by the ratio of the energy in and out of each step as listed in equations 1.2, 1.3 and 1.4.

$$\eta_{charge} = \frac{E_{storage}^{in}}{E_{charge}} \quad (1.2) \quad \eta_{storage}(t) = \frac{E_{storage}^{out}}{E_{storage}^{in}} \quad (1.3) \quad \eta_{discharge} = \frac{E_{storage}^{out}}{E_{discharge}} \quad (1.4)$$

Thus, the overall efficiency of the energy storage process (*i.e.* charging, storing, discharging) can be calculated as shown in equation 1.5 [13].

$$\eta_{overall} = \frac{E_{out}}{E_{generated}} = \eta_{charge} \cdot \eta_{storage}(t) \cdot \eta_{discharge} \quad (1.5)$$

There are several important parameters for characterizing the feasibility of different energy storage systems [5]. Rather easy comparison is possible by determining the *energy density* (either in Wh kg^{-1} or Wh L^{-1}) and the *power density* (W kg^{-1} or W L^{-1}) of the system. Another important parameter is the *lifetime* of different technologies. For example, mechanical systems

are generally characterized by long lifetimes, especially compared to electrochemical systems such as batteries, which suffer from chemical deterioration over time. Looking at the economical feasibility of the various technologies, low *capital and operational costs* are essential. The capital cost also include auxiliary power systems for providing extra power and the operating cost comprise not only maintenance and operation but also the disposal costs. Costs are compared either by cost per kW, cost per kWh or by cost per kWh per cycle [5].

Other important parameters are *storage capacity and duration*, which are influenced by the self-discharge rate, the *round-trip efficiency*, which describes the ratio between energy output and input (compare to equation 1.5), the *response time*, ranging between milliseconds (frequency control) to minutes (bulk storage), and the *technological maturity* of the various technologies [5].

In the following some important energy storage technologies as depicted on the right in Figure 1.1 are briefly discussed (batteries are described in the following sub-chapter) [5, 6, 9, 15–17]:

- *Pumped Hydro Energy Storage*: PHES is the most mature and most widely applied energy storage technology and is especially suitable for large-scale long-term storage with high power up to GW levels (100-2000 MW). These systems can provide power within 1 min and have an efficiency of 65-86%. The hydro power installed worldwide for energy storage totaled 127 GW, which represents 99% of the worldwide electrical energy storage capacity. PHES is economically attractive due to long lifetimes, long discharge times and low operational cost. But as the capital costs are high, the size of the plant is very important. For example, for a 14.4 GWh plant they are about 69 \$ kWh⁻¹, but already 103 \$ kWh⁻¹ for a 11.7 GWh plant. In less mountainous regions underground-PHES is considered as an alternative. Nevertheless, ecological issues such as the high environmental impact in the respective region and the geographical and topological restrictions must be considered.
- *Compressed Air Energy Storage*: This technology is already in second place regarding the global storage capacity with only two commercial large-scale facilities in operation. A 320 MW diabatic system (42% efficiency) is installed in Huntorf (Germany) as support of a nuclear plant (discharge duration 3 h). The second has been installed since 1991 in McIntosh (Alabama, USA) with a power of 110 MW (discharge duration 26 h). Similar to PHES, this technology is restricted by the availability of suitable locations. It uses conventional gas turbines for energy generation, whereby the efficiency can be increased by an adiabatic system (no additional fuel needed when expanding the gas due to the use of an additional thermal energy storage system). An adiabatic demonstration plant was

built in Germany with a storage capacity of 260 MWh and electric power of 90 MW. The advantages of CAES are the long possible storage periods, comparably low capital cost of 50-100 \$ kWh⁻¹ depending on the site and the good efficiency of 70-89% (when adiabatic).

- *Flywheels*: They are a very fast responding storage system with response times in the scale of milliseconds but with short duration discharge periods in the range of a few minutes. This technology is mainly suitable for frequency regulation and power applications. Two types are distinguished: low-speed with < 6000 rpm and high-speed, which has a higher efficiency and is mainly used for longer storage periods but lower power capacities. The advantages include low maintenance cost, long cycle life and low environmental impact. As example, a 200 kW flywheel with a capacity 5 kWh was installed in a Norwegian wind-hydrogen plant. Another interesting application might be as kinetic energy recovery system implemented in cars, where the breaking energy is stored in a flywheel.
- *Supercapacitors*: These systems have a high efficiency of 95% as no chemical reactions are involved, however the self-discharge rate lies in the range of 5% per day. This technology is primarily suitable for short storage duration. Especially compared to batteries, supercapacitors are characterized by low degradation rates. Their energy density is very low with < 10 Wh kg⁻¹.
- *Superconducting Magnetic Energy Storage*: SMES store energy in a magnetic field with a very high efficiency of about 97%. This system responds in a few milliseconds and is characterized by a cycle life of > 100 000 cycles. SMES is suitable for grid-stabilization applications (uninterruptible power supply, pulse power source), but has high capital as well as operational cost because of the use of a superconducting wire and due to high amount of energy needed for cryogenic cooling. In addition, the influence of the strong magnetic fields on the environment has to be considered.
- *Thermal Energy Storage*: There are three TES principles : 1.) Sensible heat storage uses a solid or liquid material like water, bricks, sand, rock, oil or soil; 2.) Latent heat storage utilizes the heat adsorption/release of a material which undergoes phase transition and; 3.) Thermochemical energy storage exploits the energy, which is released/required during breaking/building of chemical bonds within a reversible (photo-)chemical reaction (including water release/adsorption from zeolites and hydrates). The advantage of thermochemical energy storage are low losses during storage as the two chemicals can be stored separately. It is especially attractive for long-term seasonal storage.

- *Chemical Energy Storage:* The main carbon-free chemical storing compound is hydrogen. H_2 can be directly produced with renewable electricity through electrolysis of H_2O without any carbon emission. The overall round-trip efficiency including electrolysis (up to 70% [18]), storage of H_2 (about 10% losses), and electricity generation using fuel cells (about 50-60%) lies in the range of 30%-40%.

As can be seen in Figure 1.2(b), batteries find their application in a broad power range and differ in their storage times due to the many different chemistries employed in the cells and the ease of configuration. Also in regard to energy density, electrochemical systems range from below $< 100 \text{ Wh kg}^{-1}$ in the case of redox flow batteries and lead-acid batteries and might reach over 1000 Wh kg^{-1} in the case of metal-air batteries (practically attainable in the range of 500 Wh kg^{-1}) [6, 19]. In addition, due to the broad variety of cell chemistries, also the material cost play an important role when comparing different battery systems. Cl, Cr, Fe, Mn, Na, S and Zn are regarded as elements with high energy storage potential and comparably low extraction cost [20]. Thus, no single battery technology meets all requirements at the same time, as there is a large dependency on the scale of the application [6]. In the following sub-chapter a short overview of current battery technologies is given with the focus on their applicability in large-scale energy storage.

1.2 Electrochemical Energy Storage with Batteries

Secondary batteries are electrochemical systems, which not only provide electrical energy during discharge, but which can also be recharged again by reversing the electrochemical processes within the cell by applying an external current. The most prominent rechargeable battery is the Li-Ion battery, which is due to its high energy density and thus good applicability in portable devices, an important part of our every day life. Other systems of high relevance are the Lead-Acid batteries, mainly employed in vehicles as starter battery, Nickel-Cadmium (Ni-Cd) and Nickel-Metal Hydride (Ni-MH) batteries, which were the dominant consumer cells in the 1990's before the breakthrough of Li-ion batteries and high-temperature molten-salt batteries such as the Sodium-Sulfur (NaS) or the Sodium-Nickelchloride (ZEBRA) cells. In addition, redox flow batteries (RFB) are considered for large-scale electrical energy storage in the power range from 10kW to 10MW. They are especially attractive for large-scale energy storage due to reduced cost at larger sizes, easy customization of power and energy rating for the required application

and because of long discharge times of several hours. The most important flow battery systems are the all-vanadium redox system, the older Fe-Cr RFB and the Zn-Br RFB [1, 5, 21].

The following short list describes the most prominent secondary battery systems for large-scale electricity storage [1, 5, 6, 9, 15–17, 21].

- *Lead-Acid Battery*: This is the most mature secondary battery technology with the advantage of high reliability, fast response and low cost (conventional battery about $200 \text{ \$ kWh}^{-1}$, but "ultra-battery" about $500 \text{ \$ kWh}^{-1}$). Its round-trip efficiency lies in the range of 80%, the cycle life ranges between 500 - 1500 cycles and the upper power limit is in the multiple tens of MW. The energy density is limited to 50 Wh kg^{-1} . The lead-acid battery is mainly suitable for short discharge durations. As example, a storage facility of 10 MW power and 4 h discharge time is installed in California (USA).
- *Li-Ion Battery*: This battery has a very high efficiency of 95% with up to 10 000 cycles lifetime but is limited in power to the kW range. Its high cost of $>1000 \text{ \$ kWh}^{-1}$ and the very limited resources are the main drawback for stationary systems. A significant cost reduction can probably be achieved by using LiFePO_4 as cathode material (lower energy density but higher safety).
- *Ni-Cd*: The Ni-Cd battery has an efficiency of about 70%, a limited power in the tens of MW and an energy density of $55 - 75 \text{ Wh kg}^{-1}$. The cycle life is in the range of 2500 cycles however, when only depleted by 10% depth of discharge up to 50 000 cycles are possible. The cost are about 10 times higher than for lead-acid batteries and due to the toxicity of cadmium this type is hardly in use anymore. The largest Ni-Cd battery is installed in Alaska (USA) (since 2003) and has a power of 27 MW with 15 min discharge time and a boost power to 40 MW with 7 min discharge time.
- *Sodium-Sulfur Battery*: This system has a high efficiency of about 75 - 85%, life time of 2500-4500 cycles (lifetime 15 years), discharge time of a few hours and is applicable up to the MW scale (specific energy density is about 760 Wh kg^{-1}). It was developed during the 1970's and commercialized in Japan since the 1980's. Due to the high abundance of sodium, the cost are in the range of $350 \text{ \$ kWh}^{-1}$. Cell and system engineering as well as safety concerns are still a challenge. It is one of the most developed MW-scale electrochemical storage technologies. In 2012, about 60 MW were installed.

As this thesis focuses on the zinc-air flow battery, details on flow battery systems as well as metal-air batteries in general with focus on the zinc-air cell are discussed. Metal-air batteries, especially using zinc as storing metal, are regarded as the most compact (energy densities of $> 500 \text{ Wh kg}^{-1}$ [19]) and potentially least costly battery system with projected cost of about $160 \text{ \$ kWh}^{-1}$ [22] and estimated operational cost of $< 10 \text{ \$ kWh}^{-1}$ [23]. This is due to the abundance of zinc resources, as well as the low environmental impact of zinc. The main drawbacks are the low efficiency of 50% due to the chemical reactions on the air electrode, the limited cycle-life and the low rate capability limiting its practical applicability to low power services [19].

2 Aims and Scope of this Thesis

This thesis was carried out as part of the project *Luziflow*, which aimed to improve the cycle stability as well as power and energy density of the alkaline rechargeable zinc-air flow battery. The zinc-air flow battery holds – in comparison to the few available other redox flow systems – very high potential as low-cost, flexible and environmentally friendly electrochemical energy storage technology. The system is comparably compact because oxygen – as one of the two reaction partners – does not have to be stored, but is taken from the surrounding air. This project aimed at overcoming the technical hurdles that prevent the zinc-air storage system from practical application and commercialization. The challenges lie in the formation of zinc dendrites in alkaline electrolytes and in the insufficient stability of the reversible oxygen electrode, leading to a lack of cycle stability, specific power and specific energy.

The project *Luziflow* was funded by the Austrian Forschungsförderungsgesellschaft (FFG) and the Climate and Energy Fund in the call "Energieforschungsprogramm" and was successfully carried out between April 2015 and September 2018 in close cooperation between the Fuel Cell Group at the *Institute of Chemical Engineering and Environmental Technology*, the *Institute for Chemistry and Technology of Materials*, both at Graz University of Technology, and the German company *RECAT GmbH*. The goal of this project was on one side the improvement of the zinc electrode by investigating zinc morphologies during charging/discharging and on the other the development of stable bifunctional air electrodes for catalyzing oxygen reduction reaction during discharge and oxygen evolution reaction during charge. Finally, the optimized electrodes were tested in unit-cell operation with flowing electrolyte at practical current densities of 50 mA cm^{-2} . With this, the *Luziflow* project supported the development of zinc-air flow batteries for achieving the objectives of the climate change policy of Austria.

This doctoral thesis focused on the development of bifunctional air electrodes in regard to achieving charge/discharge efficiencies of over 50% (which corresponds to a voltage difference between oxygen reduction reaction and oxygen evolution reaction of below 1 V) at a practical

current density of 50 mA cm^{-2} . This is especially challenging due to the slow kinetics of oxygen electrocatalysis resulting in very high overpotentials already at very low applied current densities. At the same time, their long-term stability during cycling operation was improved and the degradation mechanisms investigated. A broad variety of precious metal-free oxide catalysts were tested, amongst other several types of perovskite, but also many different materials for the build-up of a mechanically and chemically stable air electrode were employed. For assessing the performance and cycle life of these in-house custom-made air electrodes, electrochemical characterization was carried out in half-cell set-ups and unit flow cells. This allowed good selection of suitable materials and components for long-term operation. Moreover, the applicability of the pulse interrupt charging method, which is a beneficial mode for achieving dendrite-free zinc morphologies but which can be harmful to the air electrode due to high charging currents, was investigated in regard to the bifunctional air electrode. Three peer-reviewed publications were written during this thesis, summarizing the results in regard to the development of stable bifunctional air electrodes and the optimization of the operating parameters of a zinc-air flow system.

3 Theory

3.1 Introduction to Rechargeable Zinc-Air (Flow) Batteries

The rechargeable zinc-air flow battery is an electrochemical hybrid system, which includes many design principles and engineering solutions from battery as well as fuel cell technology [24]. A schematic of the various technologies influencing the zinc-air flow battery system is shown in Figure 3.1. The detailed aspects of each branch shown in the schematic will be discussed in the following chapters.

In principle, a rechargeable zinc-air (flow) battery consists of a zinc electrode, a gas diffusion electrode, where oxygen is electrochemically converted (*i.e.* bifunctional air electrode), and an highly alkaline electrolyte, which can be pumped through the cell. The theoretical cell potential of this electrochemical system is 1.67 V. The chemical reactions in alkaline environment taking place in the flow cell are shown in Table 3.1 and depicted in the schematic of the flow cell in Figure 3.2 [25].

Table 3.1: Chemical reactions in an alkaline rechargeable zinc-air flow battery (discharge left to right, charge right to left)

| | | |
|-------------------------|------------------------------------------------------------------------------------------------------------------|---------------------------------------|
| Negative Zinc Electrode | $\text{Zn} + 4 \text{OH}^- \rightleftharpoons \text{Zn}(\text{OH})_4^{2-} + 2 \text{e}^-$ | $E_0 = -1.266 \text{ V}_{\text{SHE}}$ |
| Positive Air Electrode | $\text{O}_2 + 2 \text{H}_2\text{O} + 4 \text{e}^- \rightleftharpoons 4 \text{OH}^-$ | $E_0 = +0.401 \text{ V}_{\text{SHE}}$ |
| Overall Reaction | $\text{Zn} + 4 \text{OH}^- + \text{O}_2 + 2 \text{H}_2\text{O} \rightleftharpoons 2 \text{Zn}(\text{OH})_4^{2-}$ | $E_{\text{cell}} = 1.67 \text{ V}$ |

When discharging the battery, metallic zinc from the negative electrode is dissolved into the electrolyte as zincate ($\text{Zn}(\text{OH})_4^{2-}$) and the resulting two electrons from the zinc oxidation are transferred via the external electrical circuit to the positive air electrode. There, they reduce oxygen from the ambient atmosphere to hydroxide ions via the oxygen reduction reaction (ORR). The hydroxide ions migrate into the electrolyte, which closes the electrochemical circle. As

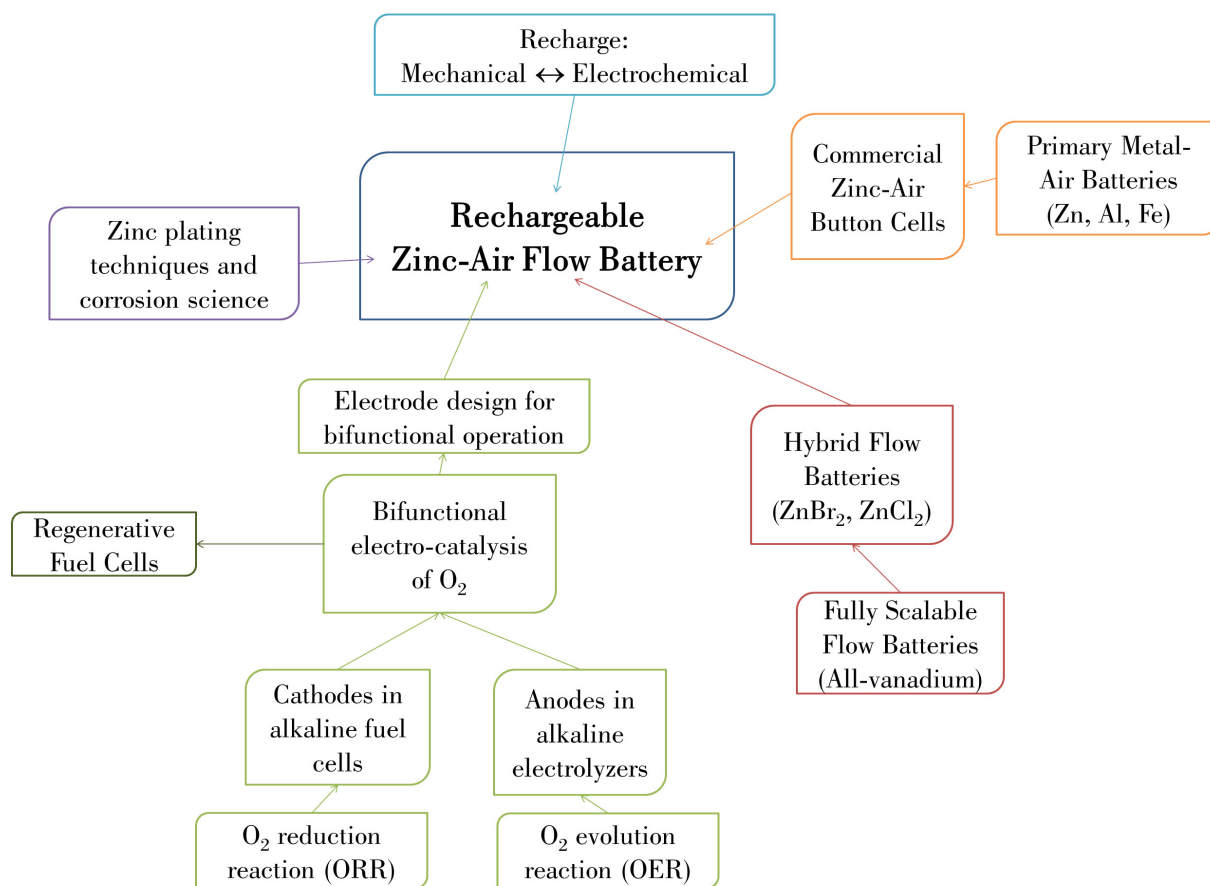


Figure 3.1: The zinc-air system combines knowledge from the field of electrochemical engineering, electroplating, fuel cell and (flow) battery technology.

oxygen is not stored within the cell, this battery type is an open system and its capacity is only determined by the zinc electrode [26]. Moreover, this system does not necessarily need an ion-exchange membrane or separator between the two electrodes and the single electrolyte can be fully mixed [27].

During charging the electrochemical process is reversed: zincate is reduced to elemental zinc on the negative electrode via an electroplating process and on the positive electrode the hydroxide ions are oxidized generating oxygen gas, which is the oxygen evolution reaction (OER). The electrical recharging process is hindered by several technical problems, which consequently reduce the cycle life and result in low round-trip energy efficiencies of the system of $< 55\text{-}65\%$ at 1 to 50 mA cm^{-2} [22]. The different electrode components and the respective technological challenges are discussed in the following chapters. The renewed relevance of this topic is apparent when considering the increasing number of publications from ~ 20 to ~ 70 per year between 2010-2016

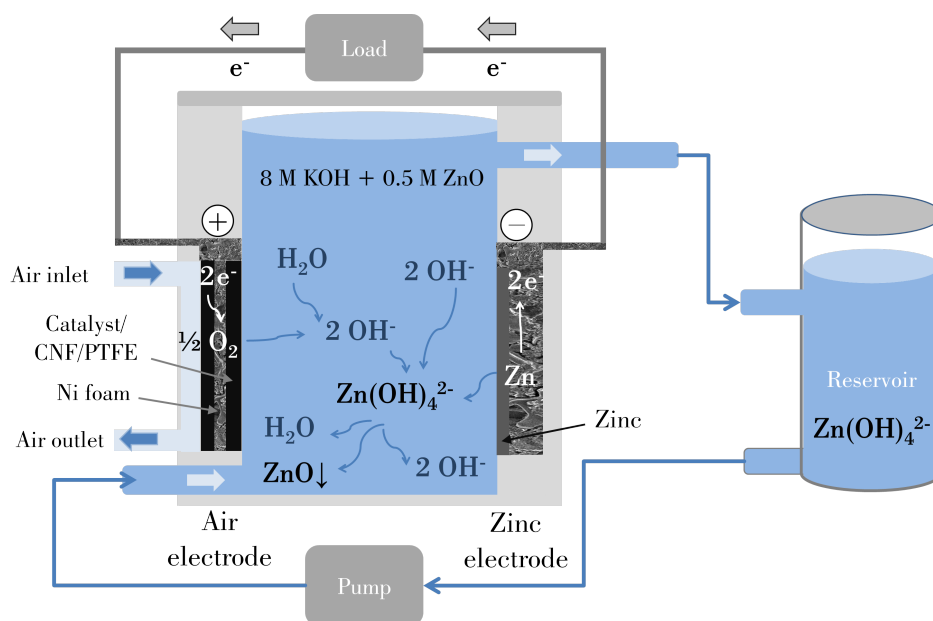


Figure 3.2: Schematic of the zinc-air cell including the chemical reactions occurring during discharge. When zincate (Zn(OH)_4^{2-}) reaches supersaturation it precipitates in form of ZnO according to the reaction $\text{Zn(OH)}_4^{2-} \longrightarrow \text{ZnO} + \text{H}_2\text{O} + 2 \text{OH}^-$.

according to Scopus and Google Scholar [22] including the high number of reviews published within the last five years [19, 22, 23, 26–34].

3.1.1 Historical Development of Zinc-Air Systems

The first zinc-based battery was the Leclanché galvanic element, which was patented in the 1860s and consisted of a negative zinc electrode and a positive manganese oxide electrode. The basic principle of the zinc-air battery was first demonstrated in the late 19th century and then patented as Walker-Wilking battery, which employed a zinc electrode and a carbon-based air electrode on a nickel current collector [26]. However, the first commercialization of primary zinc-air batteries started only in the 1930s, followed by military application in the 1960s. These were mainly mechanically rechargeable systems, which means that for repeated use the spent zinc electrode was exchanged with a new one [23, 26, 35, 36]. Since the 1970s the primary zinc-air battery is employed in the form of button cells for powering hearing aid devices [28] with an specific energy of $1300\text{--}1400 \text{ Wh L}^{-1}$. Nevertheless, these primary batteries, also in multi-cell form, found only (historic) niche applications, for example railroad signaling, underwater navigation and electric fencing, due to their limited power density [22, 28]. Much research and

development was conducted between 1975 - 2000 for finding solutions in making the system electrically rechargeable, but also in regard to zinc-air fuel cells/flow batteries as demonstrated by Compagnie Générale d'Electricité [37]. Nevertheless, research was mainly stopped because of the advance of Li-ion battery technology [26, 36]. In the last years, the need for alternatives to Li-ion battery technology has renewed the interest in metal-air batteries. Especially the zinc-air system is regarded as the most widely developed with several companies developing commercial products, *e.g.* EOS Energy Storage (USA), Fluidic Energy (USA) and ZincNyx Energy Solutions (Canada). All three companies developed grid-scale flow-type batteries for stationary energy storage applications. Other commercial attempts include Revolt (USA), with a stationary alkaline zinc slurry-system with mechanical recharge (bifunctional catalysts, 200 cycles at 100 mA cm^{-2}), ZOXY Energy systems from Germany (10 times rechargeable), the Israeli company Electric Fuel Ltd. (described in section 3.2.2), who manufactured mechanically rechargeable zinc air batteries for buses and passenger cars, and EDF (France), who use two oxygen catalysts (MnO_2/NiCo) and a $\text{Zn}/\text{TiN}/\text{polymer}$ binder negative electrode in their zinc-air battery (200 cycles at 15 mA cm^{-2}). The EDF derived start-up ZnR Batteries (France, founded 2016) develops medium sized zinc-air batteries under the product name Zinium. In addition, the Israeli company Phinergy produces Al-air primary batteries for electric vehicles with highly durable air cathodes (thousand of hours). The following list summarizes recent commercial activities on the grid-scale, whereby there is a significant lack of information on the air electrode design and catalyst [22, 28, 30–33, 36].

- *EOS Energy storage (USA, founded 2008)*: Stationary energy-storage flow system with 1 MW/4 MWh system for estimated $160 \text{ \$ kWh}^{-1}$; predicted lifetime of 10 000 cycles (30 years); horizontal cell configuration with no separator; near-neutral pH chloride-based electrolyte (10-20 wt% NH_4Cl / 10-20 wt% ZnCl_2 / 5 wt% LiCl + 1-20 wt% ammonium citrate, ammonium acetate and ammonium hydroxide); Zn/ZnCl_2 electrode; Non-corroding air electrode with Ti current collector coated with a type of Ti suboxide; Perhaps tri-electrode configuration; Up to 75% efficiency; Charge potential at 2.1 V and discharge at 0.9 V and 2700 stable cycles.
- *Fluidic Energy (USA, founded 2006)*: Overall 250 MWh installed in 500 remote Indonesian communities (in connection with photovoltaic); small stationary energy storage back-up systems at $200\text{-}300 \text{ \$ kWh}^{-1}$; use of sulfonate-containing ionic liquid (R-SO_3^- with $\text{R} = \text{C}_2\text{-C}_{20}$ alkyl group) with additives and mixed with water as electrolyte and a nanostructured zinc electrode with porous 3D network; 5000 cycles demonstrated.

- *ZincNyx Energy Solutions Inc. (Canada)*: 5 kW/40 kWh; use of zinc particle suspension with separate compartments and two separate air electrodes for charging and discharging.

3.2 Design and Configuration of Zinc-Air Batteries

3.2.1 Primary Metal-Air Batteries

Due to their high theoretical energy density metal-air batteries are regarded as one of the most promising alternative technologies to Li-ion batteries, although they still have a very limited power output in the range of 0.1 - 10 mA cm⁻² [38]. The energy density of Li-ion batteries lies in the range of 160-250 Wh kg⁻¹ [26, 28, 39], whereas Li-air batteries have a theoretical energy density of 11 000 Wh kg⁻¹ and will probably reach 1700 Wh kg⁻¹ in practical applications [26, 39, 40]. Although the zinc-air couple has a much lower theoretical energy density of 1084 Wh kg⁻¹ (including oxygen) [26], its achievable practical energy density of 300-500 Wh kg⁻¹ surpasses Li-ion batteries [26, 39, 40].

Looking at the periodic table, Li, Ca, Mg and Al are considered mainly for application in primary metal-air systems, whereas Zn, Fe and Cd can be recharged. Although Li-air batteries, first introduced in the middle of the 1990's [41], have the highest theoretical cell voltage of 3.3 V (practical ~2.4 V), the technical development is hindered by safety concerns due to the reactivity of Li metal with air (also in organic electrolytes) and the economical issue regarding the Li resources [26], which is already today one of the major concerns for Li-based batteries. Li, but also other alkali metals, like Na and K, have to be operated with non-aqueous organic electrolytes, which severely changes and slows the ORR mechanism resulting in lower power rating and superoxide anion as intermediate product [42]. The endproducts are oxidative electrolyte-corrosive superoxides and peroxides, *i.e.* Li₂O₂, Na₂O₂/Na₂O and KO₂, respectively, which have low solubility in the organic electrolytes. In consequence, they precipitate within the air cathode, which gradually blocks the pores, reduces catalytic surface area and finally leads to battery failure. This mechanism is the reason why the discharge capacity of M(Li,Na,K)-air batteries is often limited by the capability of the air electrode to store the discharge product [19]. These discharge products are very stable, thus the recharging is kinetically irreversible/quasi reversible resulting in large OER overpotentials and charging potentials of about 4 V. Moreover, it was recently found that generated singlet O₂ is able to trigger parasitic reactions [42]. Much research is done in regard to the applied electrolytes (*i.e.* either aprotic, aqueous with protective LISICON

glass ceramic, hybrid or all solid-state) due to the much different reaction mechanisms, whereby the type of solvent (including polarity, viscosity and oxygen solubility) has a big influence on the kinetics [41].

Mg and Al-based air batteries show high cell voltages with 3.1 and 2.7 V_{theo} (practical 1.4 and 1.6 V), respectively, but undergo rapid corrosion and self-discharge, which allows only mechanical recharge [22] and results in 6-9 times lower energy efficiency compared to the zinc system [30, 40]. Although Fe-air (V_{theo} = 1.3 V; practical = 1.0 V) can also be recharged the practical energy density is very low with only 60-80 Wh kg⁻¹, which makes this system mainly suitable for stationary low cost energy storage and not for application in electric vehicles [19, 40].

Primary, commercially available zinc-air batteries employ non-noble metal catalysts for ORR, mainly MnO_x varieties. For example, the hearing-aid battery by Duracell uses γ -MnO₂ and achieves an energy density of 400 Wh kg⁻¹. When sealed these batteries have a long storage life with only 2% decay per year [22]. Primary zinc-air batteries are built in conventional planar configuration, which was originally designed for high energy density. In these cells, zinc powder is mixed with gelled KOH electrolyte [28]. For limiting Zn²⁺ diffusion, the separator Celgard®5550 (PP/PE/PP) is the standard material employed [22].

3.2.2 Rechargeable Battery Configurations

There are two main strategies for achieving recharge capability in the zinc-air system: 1.) mechanical recharge by replacing the spent zinc electrode with a new one and 2.) electric recharge as in a conventional secondary battery using either two or three electrodes per cell. The challenges for both strategies are discussed in the following.

Mechanically rechargeable systems are advantageous because the cell lifetime is only dependent on the air electrode, as the zinc electrode and electrolyte can be easily replaced [41]. Also, the air electrode is operated in a less stressful way, as it is only used as cathode and not for charging. This type was furthest developed by the Israeli company Electric Fuel Ltd. [43], who demonstrated buses and passenger cars, powered by primary zinc air batteries. These vehicles could be fast "refueled" by replacing the spent zinc electrode with a fresh one. The energy density was 200 Wh kg⁻¹. 47 cells were assembled into a module and six modules were mounted in a bus with overall 312 kWh and 99 kW. Because of the low power output of the zinc-air battery, an additional auxiliary NiCd battery with 22 kWh was added to increase the peak power to 125 kW.

With this configuration, the bus was able to drive a range of 280 km with 50 km h^{-1} (max. speed 80 km h^{-1}) [30]. Field tests were done in the US (2000) and with postal cars in Germany between 1996 and 1998. Nevertheless, the production was stopped due to the limited driving speed and acceleration and the cost for setting-up the regeneration infrastructure with Zn electrowinning plants. For regeneration, the spent zinc oxide had to be dissolved in KOH to form zincate and electroplated again as zinc using electricity from off-peak times. Regeneration can also be done by thermal dissociation/carbothermic reduction at $1100\text{-}1200 \text{ }^\circ\text{C}$ in a high-temperature chemical reactor, which can be heated from a renewable source by using concentrated solar energy [24, 30]. A second company still developing mechanically rechargeable zinc-air batteries/fuel cells for electric vehicles is Powerzinc Electric Inc. (USA) [36].

Electrical recharge means, that the discharge product zincate has to be redeposited as metallic zinc via an electroplating process within the cell. In a two electrode cell one zinc electrode is employed together with one bifunctional air electrode, catalyzing ORR and OER in a single electrode. The system is hence very compact, but utilizing only one air electrode often results in reduced lifetimes due to the high charging potentials and the oxygen bubble formation during OER as discussed in section 3.4.3. In the tri-electrode set-up, ORR and OER occur on two separated electrodes, thus reducing the mechanical stress through the product O_2 bubble generation on the more complex ORR electrode [31, 40]. The tri-electrode mode prolongs lifetime of the zinc-air battery system and yields much more stable performances [44], however, in return, the system is structurally more complex [31] and the power density is reduced because of increase of volume and weight [26]. As charging electrode nickel oder nickel-alloys (often form of meshes or foils) are commonly incorporated [31].

Electrically rechargeable zinc-air batteries can be designed in three principal configurations: 1.) conventional planar cells in vertical or horizontal set-up, 2.) flow batteries (horizontal or vertical) designed for long-cycle life in stationary application and 3.) flexible batteries [28]. Thin and bendable batteries are a rather new development are aimed for applications in advanced (flexible) electronics where energy dense power sources are needed. They often employ a bendable air electrode, where the catalyst is directly deposited on a flexible current collector such as stainless steel mesh or lightweight carbon based sheets made up of graphene and carbon nanotubes [26]. Flexible batteries only work with gelled or solid-state electrolyte. Their main advantages are the good safety (no protective casing needed), low cost, high energy density, and broad design varieties (films, cable-type, plasters, etc.)[28].

3.2.3 Electrolytes

Testing and developing new alternative electrolytes is also considered to be a promising approach for improving electrical recharge capability. In classical zinc-air batteries, including the primary button-cells, highly alkaline electrolytes are used due to their high ionic conductivity. Potassium hydroxide (KOH) is commonly preferred over sodium hydroxide (NaOH) due to its better zinc salt solubility, higher O₂ diffusion coefficients, higher ionic conductivity (K⁺ with $73.50 \Omega^{-1} \text{cm}^2_{equiv}$ compared to Na⁺ with $50.11 \Omega^{-1} \text{cm}^2_{equiv}$) and lower viscosity. In addition, unwanted K₂CO₃ has higher solubility at high pH than Na₂CO₃, which delays carbonate precipitation within the cell. 30 wt% KOH (~7 M) is considered the best compromise due to the high ionic conductivity at 25 °C with 640 mS cm^{-1} and still 220 mS cm^{-1} at -15 °C [22, 26, 30, 41]. In 35 % KOH solution (8.2 M, density 1.34 g cm^{-3}) ZnO solubility is 1 M, but supersaturation of zincate can increase the solubility by a factor 2-4. At higher molarities, Zn corrosion is enhanced and the O₂ diffusion slowed due to increased viscosity, thereby limiting ORR [22, 26, 39]. A few alternatives to the common liquid alkaline electrolyte are listed in the following:

- *Gelled electrolyte/Solid state electrolyte*: In order to prevent leakages and pore flooding as well as minimize water evaporation, KOH electrolyte is entrapped in polymer matrices. This gelled KOH is mainly utilized in primary zinc air batteries for immobilizing the ionic conductive electrolyte. Common polymer gels are poly-methylmethacrylate (PMMA), polyvinylidene fluoride (PVdF), amorphous poly-ethylene oxide (PEO), polyacrylonitrile (PAN), polyvinyl alcohol (PVA), polyvinyl acetate or cellulose nanofibers, which can also be used in flexible configurations (*e.g.* plaster sheets) [22, 30]. They exhibit good conductivity of 300 mS cm^{-1} , however, the challenge lies in the formation of the electrode/immobile electrolyte interface [45]. A very high conductivity of 460 mS cm^{-1} was achieved with gelled 6 wt% poly(acrylic acid) (PAA) doped with 6 wt% KOH [30].
- *Chlorine-based electrolyte*: Acidic electrolytes are not suited for zinc-based systems due to high corrosion rates resulting in hydrogen evolution and capacity loss [26]. However near-neutral chloride-based electrolytes are a viable low-cost alternative [22] and have been employed in Leclanché elements (ZnCl₂/NH₄Cl) and in the flow battery by EOS. Their main advantage are the minimized carbonate formation and the reduced dendrite growth. During charging, however, chlorine evolution can be favored over OER and other chlorine intermediates in water, such as dissolved Cl₂ or HCl and HClO, further reduce the pH [33].

- *Ionic liquids*: Room-temperature ionic liquids (RTIL), are salts with low melting points so that they are liquid at room temperature. They are composed of ions which are commonly an organic cation and an organic or inorganic anion [33], which can be protic or aprotic. They are a viable alternative as they have some advantages over classical alkaline electrolytes. First, as they are nearly non-volatile, the cell is protected from the "drying out" effect, which is a frequent problem in small prismatic button cell-types. Also, RTILs have a positive effect on zinc dissolution and deposition, depending on the RTIL's chemistry. Their main drawback is their labor- and cost-intensive production and their usually high viscosity. In addition, the different wetting behavior compared to aqueous solutions, can severely alter the ORR/OER reaction pathways. In completely aprotic RTILs, oxygen electrocatalysis does not take place due to the need of protons for oxygen conversion [26, 28]. Thus, either protic RTILs have to be applied or additives like water, ethylene glycol or alcohols are required. However, a multi-component electrolyte can alter the cell's electrochemistry and further increase its complexity [28, 30].
- *Deep eutectic solvents*: They are ionic solvents, which consist of a solid salt and a complexing agent, so that the mixture forms an eutectic system with a melting point much lower than each of the components. They are easy to synthesize, non-toxic and less expensive and often biodegradable, but also highly viscous [33]. Salts like methyltriphenylphosphonium bromide, N,N-diethylene-ethanol ammonium chloride and choline-based materials such as choline chloride are mixed together with a hydrogen bond donor like ethylene glycol or glycerol forming the deep eutectic solvent [46]. An example is the choline chloride/ethylene glycol mixture [47].

Table 3.2 summarizes some advantages/disadvantages of common KOH aqueous electrolyte and pure RTILs (not mixed) [30, 33, 46].

3.2.4 Flow Batteries

With the increasing number of nuclear plants built during the oil crisis in the 1970s, large scale electrical energy storage became an important issue for the first time. During this decade, the first redox flow battery pilot plants were tested, as they are much safer than conventional large-scale batteries with their active materials stored outside the cell. Moreover, RFBs allow better thermal management, easier cell to cell balancing and, because there are - in most types - no phase changes at the electrodes themselves, deep discharge is possible without damaging the

Table 3.2: Comparison of the advantages and disadvantages of alkaline aqueous electrolyte to ionic liquids.

| Aqueous (alkaline) | Ionic Liquid |
|----------------------------------------------------------------------------------------------------------------------------------------------------------------------------------------------------------------------------|--------------------------------------------------------------------------------------------------------------------------------------------------------------------------------------------------------------------------------------------------------------------------------|
| <ul style="list-style-type: none"> • not flammable | <ul style="list-style-type: none"> • low vapor pressure |
| + <ul style="list-style-type: none"> • not toxic • inexpensive • high ionic conductivity | <ul style="list-style-type: none"> • thermal stability ($> 300\text{ }^{\circ}\text{C}$) • electrochemical window of 4.5 - 5.5 V • preferred Zn morphologies |
| - <ul style="list-style-type: none"> • evaporation • moisture uptake • small electrochemical window • low thermodynamical stability • carbonate formation/precipitation | <ul style="list-style-type: none"> • lower ionic conductivity of $\sim 0.130\text{ mS cm}^{-1}$ • impurities altering the properties • high viscosity • cost • complicated synthesis • wetting of pores |

cells (State-of-Charge (SOC) varies between 80-85% at charge and 15-20% discharge to avoid local depletion). Already these early systems, such as the polysulfide-bromine RFB (mainly developed in the 1990s by Regenesys (UK) with capacity up to 120 MWh), the zinc-bromine RFB, and the iron-chromium RFB, were considered as a technical success, but they did not achieve widespread commercialization as they did not meet the cost targets of about $100\text{ } \$ \text{ kWh}^{-1}$ [48]. Nevertheless, these systems exhibit high economical efficiency with increasing power and are well suited for long discharge durations of 10 h or more for thousands of cycles, especially when compared to conventional batteries, which are mainly suited as frequency response reserve. However, RFBs work only at current densities in the range of 50 - 100 mA cm^{-2} , which is very low especially in comparison to state-of-the-art fuel cells with a range of 100 - 1000 mA cm^{-2} [36, 38, 48].

Most redox flow batteries (RFB) use protic or aqueous (often acidic) electrolytes due to the much better solubility of the metal ion redox couples and the good flow properties (low viscosity results in low pumping losses). Acidic systems are often preferred, as in alkaline electrolyte less soluble hydroxide salts can be formed. However, the main drawback of aqueous solutions is the small electrochemical operation potential window of $< 2\text{ V}$ limited by water electrolysis reaction

[49]. This property in combination with the solubility limits of the active redox species results in low energy densities for RFBs [48].

When designing a RFB system many parameters and engineering aspects have to be considered and optimized. These are - amongst many others - the operating conditions (temperature, flow rate, cell current/voltage, operation times and SOC boundaries), the electrolyte management (SOC, concentrations, viscosity, conductivity, recirculation/single pass), the redox reaction itself (electrocatalysis on suitable materials, current/potential distribution, mass transport, flow dispersion, pressure drop, electrode kinetics, parasitic reactions) as well as the principal cell design (flow fields, manifolds, shunt current management, and ease of manufacturing) [50]. Concerning the cell design, shunt currents (also named bypass, leakage or stray currents) lead to efficiency loss and occur due to low resistivity pathways through the highly conductive electrolyte. In result, the cell stack is not operated uniformly. For achieving $< 1\%$ shunt currents of the total current, the electrical resistance within the electrolyte has to be increased, for example by increasing the length of the external tubes or by using tortuous/spiral-type inlet/outlet manifolds (as has been employed by Regenesys (UK)). The manifolds themselves are often made from low cost polymers (HDPE, PVDF) and fabricated by CNC machining, injection molding or 3D printing (for prototypes) [50].

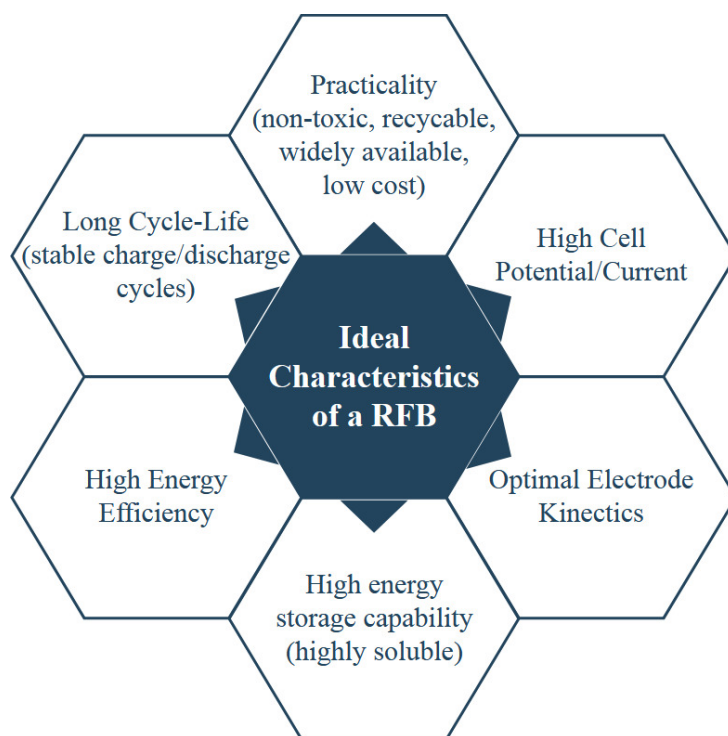


Figure 3.3: Schematic list of the ideal characteristics of a redox flow battery according to [50].

To achieve the goals listed in Figure 3.3, the complex system has to include many components such as the piping, pumps, heat exchanger, valves and tanks for electrolyte management, the electrical components (circuits, power electronics, AC/DC rectifier, transformer and cooling system), and of course a high number of control sensor systems for monitoring flow rates, SOC, temperature, pH, gas release, potential and current [50]. The SOC (state-of-charge) can be monitored by UV-Vis (optical absorption and transmission spectra), IR spectroscopy, volumetric titration or by measuring the electrolyte conductivity or viscosity, all depending on the flow battery system. The energy required for pumping has to be considered as well, when calculating the energy efficiency of the system and is a function of flow rate and pressure drop. Heat management is important as the temperature increase by the resistivity of the components can be 10-30 °C (above room temperature). Pump and flow friction can add another 2-10 °C and in some systems exothermic heat from the redox reaction itself has also to be taken into account [50].

Concerning the flow design, the RFB cells and the array of stacks can be operated in different modes, whereby turbulent flow is often preferred. This is achieved by implementing flow dispersers. In industrial scale flow cell, a conversion rate of 1-10% is achieved for a single pass through the cell, which can be increased to 50% with low flow rates and large stack sizes. The following list describes the different flow modes, which can be applied for the operation of zinc-air flow batteries with only one storage tank. Nevertheless, the described operation modes are also applicable for other (two tank) systems [50].

- *Electrolyte Circulation:* 1.) Batch recirculation, where the electrolyte continuously flows through the stacks and the constantly mixed reservoir. During cycling operation, the concentration of zincate changes gradually in a uniform way in the whole system. 2.) Batch mode, where electrolyte flows single pass from one reservoir to a second separate reservoir. This mode is not practically applied due to low conversion efficiency.
- *Arrangement of Stacks:* 1.) In parallel, where electrolyte flows equally through several stacks from bottom to top. This mode maintains even volumetric flow rates and the same zincate concentrations at every inlet. 2.) Cascade flow, where several modules are supplied with electrolyte in series, resulting in different inlet concentrations in each stack. Only used in large systems in order to reduce size and cost of piping system.
- *Flow within Stacks:* Only parallel flow is practically applied, as cascade serial flow can lead to local under-supply and non-uniform flow, *i.e.* in the last cells, thus damaging the

system. However, shunt currents pose a problem, when cells within a stack are operated in parallel (labyrinth manifolds needed).

Two different principle types of flow battery can be distinguished: 1.) the all fluid or full-flow systems employing two fully soluble active redox species, which allow independent scaling of power and energy capacity and 2.) hybrid flow systems, where phase changes (for example zinc deposition/dissolution) on the electrodes occur [48, 50]. Both types are discussed in the following sections.

Full-flow Redox Flow Batteries

The furthest developed RFB system is the all-vanadium system, which employs the V_2^+/V_3^+ (anolyte) and VO^{2+}/VO_2^+ (catholyte) redox couples fully dissolved in two separated sulfuric acid electrolytes. They are stored in two separate external tanks. The widespread commercialization is mainly hindered by the high cost of the system of about $400 \text{ \$ kWh}^{-1}$ due to the scarcity of vanadium (about 48% of system cost) and the costly ion-exchange membrane (22% of system cost) [48, 49]. Low cost alternatives to Nafion®, such as PBI membranes are investigated, but they have to withstand the highly oxidizing VO_2^+ ion. Moreover, thermal management is important in order to prevent the precipitation of VO_2^+ as V_2O_5 at temperatures higher than 40 °C (additives often needed) and to minimize solubility decrease at low temperatures [48, 49].

As there is no phase-change in the system, carbon and carbon-felt electrodes can be utilized, but sometimes a catalyst such as Mn_3O_4 , Bi or Nb_2O_5 , is employed in addition [49]. The Japanese company Sumitomo Electric Industries develops RFB pilot plants since two decades and operates a 1 MW/5 MWh vanadium RFB in connection with a 1 MW solar plant in Yokohama [48].

Hybrid Flow Batteries

The zinc-air flow battery is a hybrid flow battery (also called flow-assisted battery), because power and energy can not be completely decoupled from each other as in the fully soluble flow batteries. That means, that the energy that can be stored is not only dependent on the size of the tank and the solubility/concentration of the active redox species, but on the quantity of electro-deposited zinc, which is in turn also limited by the active electrode area and by the gap between the zinc and air electrode [51]. As one reaction is a solid-phase electrode reaction these

systems can be operated without any costly membrane. The storage capacity of zinc electrodes in common zinc-based flow batteries is about 500 mAh cm^{-2} [27].

It is believed that the flowing electrolyte can prolong the operation and cycling lifetime of the zinc-air system. Common problems, like zinc dendrite formation, shape change and passivation are reduced, because of lower concentration gradients and a more even current distribution on the electrode. The same is true for the air electrode, where the electrolyte flow can take away carbonates as well as product oxygen bubbles [28, 34]. Nevertheless, the peripheral system with tanks, tubes and pumps and excess electrolyte volume increases the complexity of the system and reduces the energy efficiency as well as the volumetric energy density [28].

The work by Amunátegui *et al.* [51] is a very recent and detailed description of a large-scale zinc-air flow battery system and gives important insight on the challenges occurring during up-scaling. At the facility *Técnicas Reunidas* in Spain one of the first real alkaline zinc-air flow battery pilot plants was built, which consisted of 3 stacks connected in parallel, each with its own tank. Each stack in turn consisted of 20 cells connected in series.

Each cell had three electrodes: 1.) zinc was dissolved and redeposited on a Ni sheet electrode, 2.) for charging an OER electrode was used, which was a Ni mesh with NiO and CoO catalyst (sandwiched between two separators) and 3.) for discharge a commercial ORR electrode (PTFE and carbon on Ni wire mesh with expanded PTFE backing (0.5 mm thickness)) was used with MnO_2 as catalyst. The air electrodes used oxygen from the ambient air, which was supplied to the cells in parallel. For removal of CO_2 the air was passed through an adsorption dryer. Further system details are listed in Table 3.3.

Table 3.3: Technical design specification of the Spanish zinc-air flow battery pilot plant.

| | | | |
|-------------------------|--------------------|-------------------------|---------------------------------------|
| • Power(nominal): | 1 kW | • Voltage: | 20 V |
| • Energy(nominal): | 4 kWh | • Current: | 20 A |
| • Stack length: | 164 cm | • Capacity: | 200 Ah |
| • Electrode size: | 20 cm x 30 cm | • Tank size: | 3 x 250 L |
| • Active area per cell: | 500 cm^2 | • Electrolyte: | 7 M KOH |
| • Depth of Discharge: | 20% | • $c(\text{Zn}^{2+})$: | $0.6 \text{ M} = 50 \text{ g L}^{-1}$ |
| • Cells per stack: | 20 | • Gas supply: | Air |
| • No. of stacks: | 3 | • Max. efficiency: | 40% |
| • ORR Catalyst: | MnO_2 | • Max. No. of cycles: | 2000 |

The results show that the flowing electrolyte influences the zinc deposit morphology and can remove the produced oxygen gas as well as the generated heat from the cell. Nevertheless, this system had severe problems with shunt currents, reducing the current/coulombic efficiency of the system and resulting in agglomeration of zinc in the first and final cells of the stack (and depletion in the middle), so that short circuits occurred. Furthermore, energy losses caused by the numerous electrical relays (for switching between ORR and OER electrodes) highlighted the need of true bifunctional air electrodes. Also, the cathode was damaged by GDE flooding and electrolyte leakage could only be prevented by use of PTFE gaskets.

At medium power of 0.5 kW, the 3-stack system delivered 1.8 kWh (11 V, 37.5 A (charge), 45 A (discharge), 173 Ah), showing that the system is mainly suited for long duration energy storage with energy delivered with medium to low power density. 30 g L⁻¹ of carbonates were found after testing in the otherwise colorless and clear electrolyte. Cycle testing of one stack with 20 mA cm⁻² charge current density (5 min) and 10 min discharge at 10 mA cm⁻² delivered cell voltages of 2.3 V (46 V stack) during charge and 1.1 V (22 V stack) during discharge. The operation time was 760 h and 2000 cycles.

Other electrically rechargeable zinc-air (flow) battery systems - in lab-scale - were reported in these publications: [52–56]. Bockelmann *et al.* [52] assembled a three-electrode system using commercially available electrodes, which were a Cu foam for Zn deposition (2 cm²), a silver-based ORR electrode and a Ni foam for OER (both 5 cm²). They also applied the pulse charging method for achieving better zinc deposition and achieved (with pure O₂ flow) 600 cycles at 20 mA cm⁻², although the measurement was interrupted a few times by shorts from zinc dendrites. The system reported by Pan *et al.* [53] consisted of a multi-layered bifunctional air electrode with MnO₂ and NaBiO₃ as ORR and Ni(OH)₂ as OER catalysts, respectively. Cycling efficiency at 20 mA cm⁻² (60°C) was 70% for 150 cycles with 1.78 V charge and 1.32 V discharge voltage. A non-flow system was developed by Ma *et al.* [54], who built a small three-cell stack using α -MnO₂ and LaNiO₃ as ORR and OER catalysts. Cycling for 17 h was done at 15 mA cm⁻² (charge) and 25 mA cm⁻² discharge, resulting a voltage gap of about 0.94 V per cell.

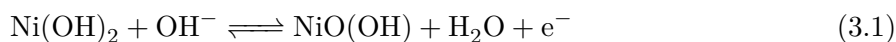
Already in 1998, Müller *et al.* [55] reported a rechargeable bipolar Zn-O₂ battery, using copper as substrate for zinc deposit and La_{0.6}Sr_{0.4}CoO₃ perovskite as bifunctional catalyst. Seven cells á 100 cm² exhibited a cell voltage of about 10 V and achieved 90 W peak power. In a recent publication by Wang *et al.* [56] some new ideas for obtaining stable charge and discharge performances at high current densities of 50 mA cm⁻² were presented. In a 9 cm² tri-electrode

zinc-air flow battery, stable potentials were achieved by using a magnetic field for improved oxygen bubble outtake and by utilizing a trapezoidal cell framework for reducing dendrite growth. With this, dendrite growth and short circuits could be suppressed also at small electrolyte flow rates, which is important for minimizing the system efficiency losses by the pump.

Other Zn-based flow batteries: There are four other zinc-based battery technologies, which have been investigated and employed to a varying degree as possible large-scale energy storage systems, namely zinc-bromine (Zn-Br₂), zinc-chlorine (Zn-Cl₂) zinc-cerium (Zn-Ce) and zinc-nickel (Zn-Ni), with theoretical cell potentials of 1.82 V, 2.12 V, 2.48 V and 1.71 V, respectively [36]. All four types have higher theoretical cell voltages than the all-vanadium redox flow battery with 1.25 V, however, their operational current density lies only in the range of 10- 50 mA cm⁻².

Of these systems, the Zn-Br₂ is the most mature technology, and was mainly developed in the 1970s due to its low cost, abundant materials (especially compared to vanadium) and better safety (compared to the chlorine system). In this system, highly corrosive Br₂ is generated during charging, so that often costly complexing-agents such as N-methyl-N-ethylmorpholinium bromide are needed, whereby the precipitation of bromine salts has to be avoided as well [27, 36]. The operating pH is in the range of 1 to 3.5 [27]. The exemplary design specifications of a modern 10 kWh Zn-Br₂ redox flow system (developed by the company Redflow Ltd. (Australia)) are: 48 V nominal voltage, nominal 3 kW, 100 L reservoir, system size 82 cm x 83 cm x 40 cm, efficiency 80%, 10 years guaranteed lifetime with 36 500 kWh of energy delivered over that time [36].

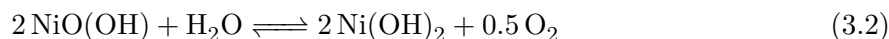
Although zinc-nickel batteries have been on the market for decades, the zinc-nickel flow battery was first introduced only in 2007. The capacity is determined by the available Ni on the Ni electrode's surface according to the reaction 3.1 in alkaline electrolyte (KOH or NaOH) [36, 57]:



Knowledge on the mass manufacturing of Ni electrodes used for Ni-Cd batteries can be applied, whereby sinter-type nickel electrode are preferred due to their higher stability [36]. Although this system can sustain high current densities of up to 300 mA cm⁻², the discharge capacities are severely limited by the nickel electrode with often less than 4 h discharge time and 50 mAh cm⁻² [27]. Demonstration systems with 28 Wh and a bigger one with 25 kWh, developed by Turney *et al.* [57] achieved 2000 cycles, which is much higher compared to commercial Zn-Ni batteries with 700 cycles. This was attributed to the improved zinc deposition with the flowing electrolyte. The pumping with flow velocity of 0.5 - 1 cm s⁻¹ reduced the energy of the cell by 4%. In conclusion,

zinc deposition proved to be the main factor for limited lifetimes. In addition, because of the high prices for nickel, the system cost of 400 \$ kWh⁻¹ does not reach the DOE target price for energy storage systems of 150 \$ kWh⁻¹.

Nevertheless, an interesting concept is the combined Zn-Ni/Zn-air flow battery, which uses the surface oxidation of Ni for boosted discharging and ORR on the air electrode for constant discharge but at lower power rates [58]. Also regarding the OER, Ni can facilitate oxygen conversion. Always when Ni is incorporated in the air electrode, its surface gets oxidized during charging and can thus function as a redox mediator [34, 53]. Following reaction 3.1, the OER can therefore be enhanced through this synergistic effect according to the reaction 3.2, whereby surface Ni(OH)₂ is regenerated [34]:



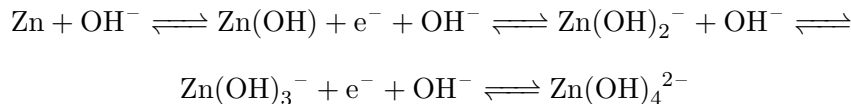
3.3 Zinc Electrode

Zinc is the 24th most abundant element in the earth crust with world resources estimated to be 1.8 Gt. 2008, about 200 Mt were available and the market price is low with about 2 \$ kg⁻¹. Furthermore, zinc can be fully recycled and its abundance would allow the production of 1 billion 10 kWh zinc-air batteries using the zinc, which is produced in only 21 months time, with China, Australia, Canada and USA being the largest producers worldwide. Important for electrochemical applications is also its low electrical resistivity of 5.95 μΩ cm⁻² [22, 33, 39, 59]. It has a density of 7.14 g cm⁻³ and it melts at the rather low temperature of 419.5 °C [27].

For electrode manufacturing, different zinc varieties in the form of gelled granulated powders (often applied in primary batteries), foils, fibers, spheres, flakes, ribbons or foams can be used, whereby at a porosity of 60-80% the capacity lies at about 1.2-2.2 Ah cm⁻³ [22, 24, 31, 39]. According to the Pourbaix diagram, zinc is thermodynamically unstable in aqueous solutions over the whole pH range and corrodes under formation of hydrogen [19, 33]. But although the redox potential of Zn/ZnO is -1.26 V vs. SHE at pH 14, which is 0.44 V more negative than the hydrogen evolution reaction (HER) with -0.83 V vs. SHE (pH 14), its low catalytical activity toward HER and its less compact passivation layer makes it possible to recharge zinc electrodes. This is in contrast to Mg and Al, which form a compact oxide layer (= corrosion) in contact

with aqueous electrolytes in short time. Nevertheless, zinc corrosion can occur over time during shut-off times [28].

During discharge, metallic zinc gets oxidized to zincate ($\text{Zn}(\text{OH})_4^{2-}$), which is the preferred discharge product in the zinc-air flow battery. The elementary steps for each of the four hydroxide ion transfers for zinc oxidation and zincate formation can be written as in the following, whereby the oxidation of $\text{Zn}(\text{OH})_2^-$ is considered the rate determining step [60]:



When supersaturation within the electrolyte is reached, zincate can precipitate as ZnO. This porous ZnO passivation film (type I ZnO) then limits the OH^- diffusion, but further discharge is still possible. In consequence, there is a depletion of OH^- on the electrode/electrolyte interface, thus a local reduction in pH. Under these conditions, the overpotential increases and a more compact irreversible ZnO layer of the type II is formed, which leads to complete insulation/passivation of the zinc electrode. Therefore, the cell cut-off voltage as well as the depth of discharge must be selected carefully (*i.e.* a discharge voltage of > 1.1 V limits the formation of Type II ZnO) [33, 60].

The charging of the zinc electrode is an electroplating process, where zinc is redeposited from the zincate-containing electrolyte onto the zinc electrode's surface. During charge, five principal zinc morphologies are possible depending on the applied current density, on the convection/flow of electrolyte and on the concentrations of zincate and OH^- : *mossy* and *heavy spongy* morphologies are dominant at low current densities under activation control, and at medium current densities *layered* (epitaxial growth) or *boulder-like* (isoprobability growth) types are present, respectively. At high current densities under diffusion control the growth of *dendrites* is dominant, whereby the substrate surface conditions only affect the early stages of dendritic growth [31–33]. In flow-type batteries the morphology of the zinc deposit is influenced by the flow rate and flow type (*i.e.* Reynolds number). In the laminar regime, dendrite formation is mainly suppressed with increasing flow rate, however compact morphologies, like boulder- and layer-like, are primarily obtained at turbulent flow regimes. At high current densities, flow rates of $> 15 \text{ cm s}^{-1}$ can prevent short-circuits due to the dendrite growth in flow direction. The boulder-like morphology is the most desired morphology in flow batteries as it exhibits the highest mechanical strength against the shear forces of the flowing electrolyte [36, 61–65]. The parameters influencing zinc morphology were closely studied by Wang *et al.* [65], who not only developed a phase-field model

for simulating dendrite growth but also experimentally demonstrated that a Reynolds number of 500 resulted in longer lifetimes compared to a Reynolds number of only 100. Another factor, which can positively influence the deposited zinc morphology are pulsating charging currents [63, 65]. When applying the current in short pulses with no current in between, there is more time for zinc ions to diffuse to the electrode's surface and the activation overpotential is reduced. Thus, the deposition process is not diffusion limited anymore and dendrite growth is suppressed. Further discussion on the pulse current interrupt method for charging of the zinc-air battery is found in section 3.5.

There are four main challenges concerning the rechargeable zinc electrode as shown in Figure 3.4: 1.) dendrite growth during charging, leading to capacity loss and short circuits, 2.) shape change during discharge, resulting in densification and caused by uneven current distribution, high pH and convective flows 3.) passivation and internal resistance increase, resulting in formation of insulating ZnO (type II) and zinc electrode expansion by about 37% and 4.) parasitic reactions like hydrogen evolution, reducing the coulombic efficiency.

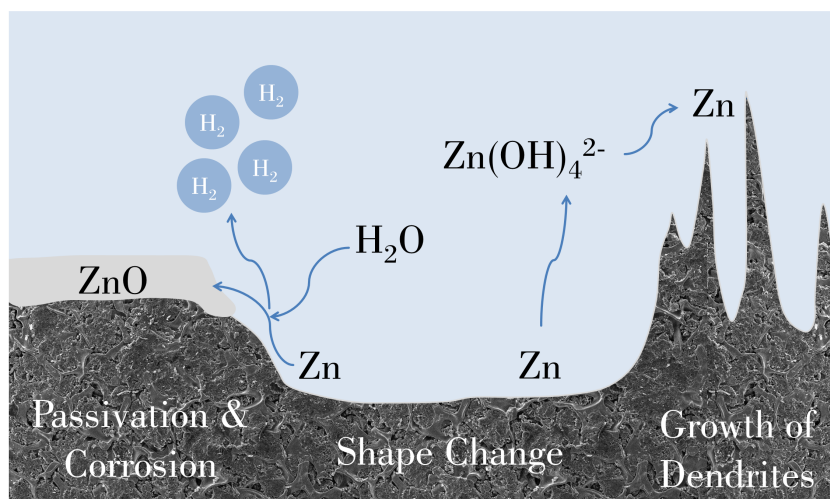


Figure 3.4: Side reactions and unwanted effects on the zinc electrode: corrosion, passivation, shape change and dendrite growth (adapted from [28]).

All of these effects are influencing each other and their respective impact on the zinc electrode's performance is mainly determined by the shape and build of the zinc electrode and the design of the cell itself. For example, shape change is a more pronounced effect in highly alkaline electrolytes as zincate formation is dependent on pH. With rising pH zinc solubility decreases, however at $\text{pH} > 9$ solubility increases again as the formation of zincate (Zn(OH)_4^{2-}) is enhanced (*i.e.* high Zn/Zn^{2+} exchange current density). Also, smaller particle sizes lead to a higher

degree of active material utilization, which is important for reaching high capacities. However, reduction of particle size also leads to pronounced corrosion [31]. The same effect is apparent when employing high surface areas or 3D-type structures, like open Cu-foams as substrate. They can minimize shape change, dendrite formation and passivation due to the low overpotentials for zinc deposition, however, large surface areas promote H_2 evolution and thus corrosion and self-discharge [28]. Nevertheless, high surface area zinc structures are needed for high current discharge [23].

For counteracting these unwanted effects on the zinc electrode, various additives were investigated and tested in literature. For improving mechanical strength, polymeric binder materials, such as PTFE, CMC and PVDF, are used although they are insulators. For better conductivity and thus less passivation, highly conductive carbon, like carbon black or carbon nanofibers, can be added. For avoiding HER, heavy metal additives have been employed since several decades also in primary batteries. However, toxic materials such as Hg are not allowed anymore. Oxides, hydroxides and nitrides of Bi, In, Pb, Ti and Sn have been investigated as well. Because they stay in their metallic form, they provide good electrical conductivity, act as substrates for compact zinc morphologies and have a higher overpotential for HER, therefore preventing zinc corrosion [24, 28].

Non metal-containing additives to prevent H_2 -evolution are often also applied in zinc electroplating industry and include polyvinyl alcohols, polyamines and quaternary ammonium ions [36]. For obtaining finer zinc particles by promoting grain growth, cationic or anionic surfactants can be added to the electrolyte as is also often used in electroplating industry [27].

The above mentioned challenges are less pronounced in flowing electrolyte, but in small, thin batteries with static or gelled electrolyte shape change and dendrite formation pose a severe problem. Therefore, coatings and trapping additives are employed in order to reduce zincate migration but at the same time maintain sufficient hydroxide diffusion [28]. In flowing electrolyte zinc is more uniformly distributed resulting in later onset of dendritic growth. For example in static electrolyte, dendritic growth can already occur at current densities as low as 8 mA cm^{-2} , whereas in flowing electrolyte (*i.e.* 2 cm s^{-1}) current densities in the range of $20 - 40 \text{ mA cm}^{-2}$ are possible [27]. Another strategy is to build the cell in an horizontal set-up, where the zinc electrode is on the bottom and the air-electrode on top. Gravity helps to settle the zinc more uniformly in an even layer on the surface, which prevents effectively dendrite growth so that no separator is needed [22, 31].

3.4 Air Electrode

The air electrode is considered as the most complicated part in a zinc-air battery [22, 26] with oxygen electrocatalysis limiting the power density of the cell [28]. Highly efficient catalysts are needed to reduce the overpotentials for the oxygen reduction and oxygen evolution reactions, although even with the best catalysts it is not assumed to be able to obtain voltage efficiencies of $> 65\%$ at practical current densities (Li-ion exhibits $> 90\%$) [19]. Air electrodes are also often called gas diffusion electrodes (GDE) and consist of a porous and electrically conductive structure, usually formed by varying types of high surface area carbon. The carbon network is then rendered water/electrolyte repellent by a hydrophobic binder material like PTFE (polytetrafluoroethylene) [26].

Reduction of oxygen and the reverse reaction, the oxygen evolution, are multi-step reactions with overall $4e^-$ transfer steps, which results in large overpotentials (*i.e.* polarization) for both reactions. Because of the high kinetic hindrance of both reactions, the obtained voltages are deviating from the theoretical thermodynamic potential of 1.23 V vs. RHE (at norm conditions) by several hundred mV already at very low currents. In addition, ORR and OER do not follow the exact same catalytic mechanism, therefore it is challenging to find catalysts, which exhibit true bifunctional activity toward both reactions [26].

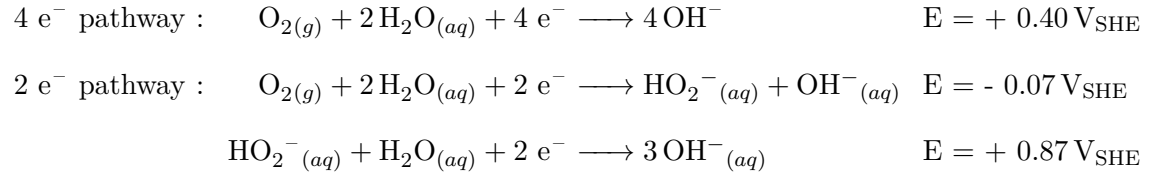
3.4.1 Electrocatalysis of O_2

Electrocatalysis of O_2 plays an important role in many renewable energy technologies such as rechargeable metal-air batteries, (regenerative) fuel cells and electrochemical water splitting in electrolyzers [66]. The reason for the slow reaction kinetics of electrochemical O_2 conversion is the complicated multi-step reaction mechanisms for ORR and OER in aqueous alkaline solutions and the strong O-O bond strength of 498 kJ mol^{-1} [24]. For ORR, oxygen has first to diffuse through the porous electrode to the catalyst's active sites, whereby oxygen diffusion in gas is much faster compared to diffusion in liquids. Then, the oxygen molecule is adsorbed on the catalyst surface [23]. Thereby, it can bind in bi-dendate form (side-on) or end-on with just one oxygen atom depending on the catalyst surface [29]. In the Griffiths-model the oxygen molecule binds side-on via its π -orbitals to the empty d-orbitals of the surface metal atom, resulting in increased O-O bond length and thus splitting and direct reduction of the molecule. In the quite similar Yeager model, O_2 binds side-on to two metal surface atoms with partially filled d-orbitals.

The Pauling model describes end-on adsorption of only one oxygen atom of the O₂-molecule to one metal atom on the surface. Thereby only partial charge transfer occurs and formation of peroxide and superoxides is pronounced [22]. Regardless which binding mode is preferred, electrons released from zinc oxidation at the anode need to be conducted to the adsorbed oxygen, which weakens and consequently breaks the O–O bond reducing the O₂ to OH[−]. The resulting hydroxide ions then move through the electrolyte to the metallic anode [23].

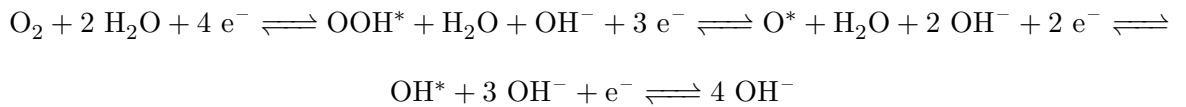
The step-wise reduction of adsorbed oxygen can occur either via the four-electron or the two-electron mechanism (shown in Table 3.4), depending on the type of catalyst and its surface structure including surface geometry, electronic structure and oxygen adsorption sites. Generally, the four-electron pathway is preferred on (noble)-metal atoms, whereas the two-electron pathway is mostly dominant on carbonaceous materials [22].

Table 3.4: Four and two electron mechanism in alkaline electrolyte: O₂ is either directly reduced to OH[−] or via formation of peroxide intermediates.



It is noteworthy, that the highly oxidative peroxide intermediate HO₂[−] can also either desorb and diffuse from the active site (which is often harmful to the surrounding material) or decompose/disproportionate again to HO[−] and 0.5 O₂ [38, 66].

The elementary steps for each of the four electron transfers for ORR/OER can be written as



with * denoting intermediates adsorbed on the catalyst surface. It is important to note, that ORR and OER are dependent on the same three reaction intermediates, namely OOH*, O* and OH*. For OER, the adsorption energies (ΔE) of OH* and OOH* co-linearly scale to each other with a difference of 3.3 ± 0.2 eV. Thus, the difference of adsorption energies ΔE or the Gibbs free energy of adsorption (ΔG), respectively, between O* and OH* can be used as activity descriptor in relation to the theoretical overpotential. For ORR, the Gibbs free energy of adsorbed HO* (ΔG_{OH*}⁰) can be used as descriptor. The resulting volcano-shaped plots allow then assessment of

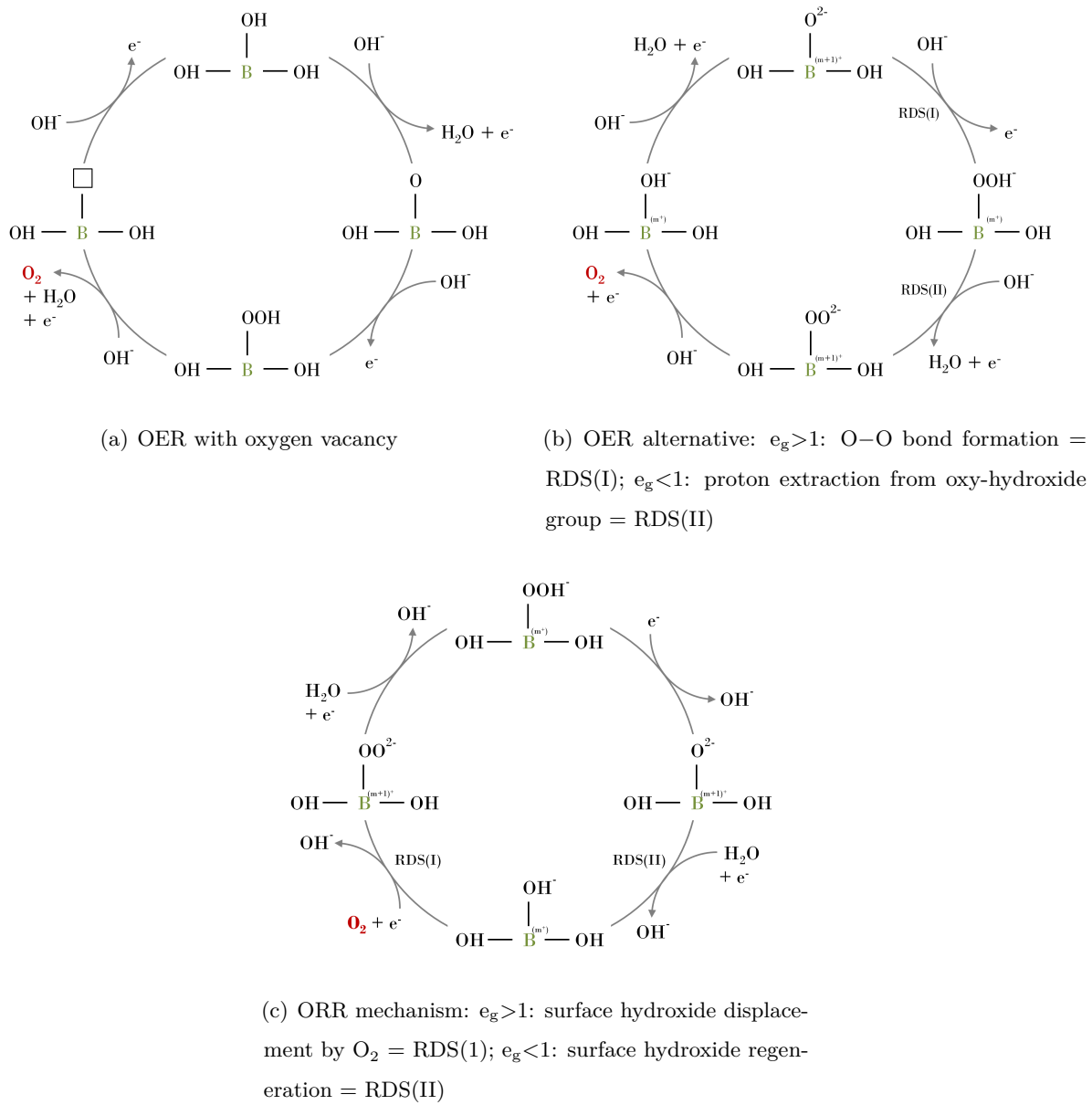


Figure 3.5: Proposed mechanism for OER and ORR on perovskite oxide surfaces with rate determining steps (RDS) indicated. Images of the reaction mechanisms adapted from [67–69].

the optimal intermediate binding energies. That means, that the adsorbates bind to the catalyst surface neither too strongly nor too weakly, which is called the Sabatier principle [38, 68, 70, 71].

Nevertheless, adsorbate binding energies are hard to determine experimentally (for example with spectroscopic methods), therefore alternative activity descriptors are needed, which are mainly derived from molecular orbital theory and band theory [38, 66, 67]. DFT (density functional theory) calculations help to correlate the adsorption energies to the physical properties, like band structure and electronic configurations of the catalyst. There is, for example, a linear trend between adsorption energies of reaction intermediates and the outer electron number of transition metals [38]. On metal oxide surfaces, *e.g.* perovskites with the formula ABO_3 , the catalytic activity is dependent on the B-site transition metal element and the occupation/filling of its σ -orbital conduction band [66], as is further described in section 3.4.2. Nevertheless, these correlations usually neglect the reaction environment (*i.e.* pH, temperature, surface area, crystallite sizes etc.), which explains the much broader variety of catalytic activities obtained by experiments [38].

The ORR mechanism on perovskite catalyst surface with four catalytic steps, shown in Figure 3.5(c), was proposed by Suntivich *et al.* [69] and comprises 1.) surface OH^- displacement, 2.) surface OOH^- formation, 3.) surface oxide formation and 4.) surface OH^- regeneration. Two slightly different OER mechanisms proposed by Man *et al.* and Suntivich *et al.* [71, 72] are shown in Figure 3.5(a) and 3.5(b). The OER mechanism is an acid-base mechanism, where the oxygen nucleophile (Lewis acid) in OH^- attacks the metal-bound electrophilic oxygen surface species (Lewis base) [68]. Most oxides including perovskites have an pH value at zero charge (pH_{pzc}) of 7-11, which is lower than the pH of highly alkaline solution used as electrolytes (pH 13-14). Therefore, it is plausible that the oxide catalyst surface is negatively charged with accumulated OH^- ions, which is more preferable for OER than ORR [67, 68].

Research on ORR/OER pathways including DFT modeling has been done mostly for alkaline and acidic electrolytes. The reaction mechanism in ionic liquids can differ significantly and proceeds via single electron reduction steps with superoxide intermediate $\text{O}_2^{\bullet-}$ [22]. A schematic of the reaction pathway in protic ionic liquids is given in Figure 3.6.

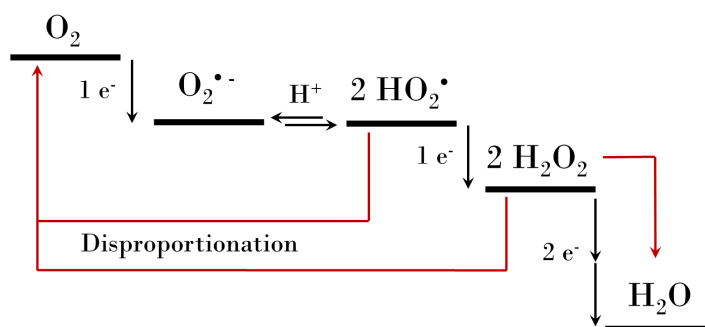


Figure 3.6: Schematic of the ORR in protic ionic liquids via formation of superoxide and perhydroxyl radicals (adapted from [30]).

3.4.2 Bifunctional Electrocatalysts for O_2 -Reduction and O_2 -Evolution Reaction

A suitable ORR/OER catalyst has to fulfill three important requirements. First, bifunctional catalytic activity is needed, which is connected to a good understanding of the ORR and OER mechanism involved. The second required property is versatility, which includes the catalysts applicability in a broad temperature range and wide potential window as well as its stability in various electrolytes. The third requirement is the scalability, which describes the capability of synthesizing and of incorporating the catalysts in large-scale. This is needed for widespread application/commercialization of air electrodes [28]. So far, many synthesis routes for bifunctional (hybrid)-catalysts are costly and often time-consuming [22]. In addition, for achieving high catalytic activity these parameters have to be controlled [28]:

- Crystallographic structure (exposed crystal planes ([100],[111], etc.) or present crystal type (e.g. α -, β -, γ - or δ - MnO_2))
- Composition (tuning of oxide catalysts (spinel, perovskites) by doping them with different metals)
- Size (different properties of bulk materials compared to nano-sized particles)
- Morphology (various carbon-types, 3D frameworks, core-corona structures, etc.)

Four types of bifunctional catalysts have been investigated by many research groups because they can be applied, not exclusively, but mainly in alkaline systems [22]: 1.) precious metals, also often in form of alloys, 2.) transition metals, 3.) carbon-based materials, also often functionalized

with heteroatoms such as N, B, P and S [66] and 4.) transition metal oxides, which were mainly investigated in this work. Combinations of these four catalysts are also possible and especially the synergistic effect of carbon materials together with metal/metal oxides for improving their bifunctional activity was widely investigated [66]. Concerning the electrochemical stability, all catalysts must withstand the alternating reductive/oxidative environment while cycling the air electrode [19].

The most commonly employed transition metal oxides can be categorized in single/mixed metal oxides such as MnO_x , spinel-type with the general formula AB_2O_4 , and the perovskite-type with the general formula ABO_3 . The different types are described in the following sections, whereby the focus lies on the perovskites and spinels, who were investigated in the course of this thesis due to their intrinsic bifunctional activity and high stability in alkaline solution [38].

Perovskites

The general formula of the perovskite structure is $\text{A}_{1-x}\text{A}'_x\text{B}_{1-y}\text{B}'_y\text{O}_{3-\delta}$, whereby δ denotes non-stoichiometry by vacant oxygen places in the lattice structure. A is the larger, more electropositive cation, usually a rare-earth or alkaline metal such as Ca, Sr, Ba and La, and B is a smaller, more electronegative transition metal cation like Cr, Mn, Fe, Co and Ni. A is 12-fold coordinated with an oxygen atom and B has a 6-fold coordination [66, 67] as shown in Figure 3.7. This structure allows high compositional and structural flexibility as A and B sites can be substituted with a broad range of elements thereby altering the chemical and physical properties of the material [66].

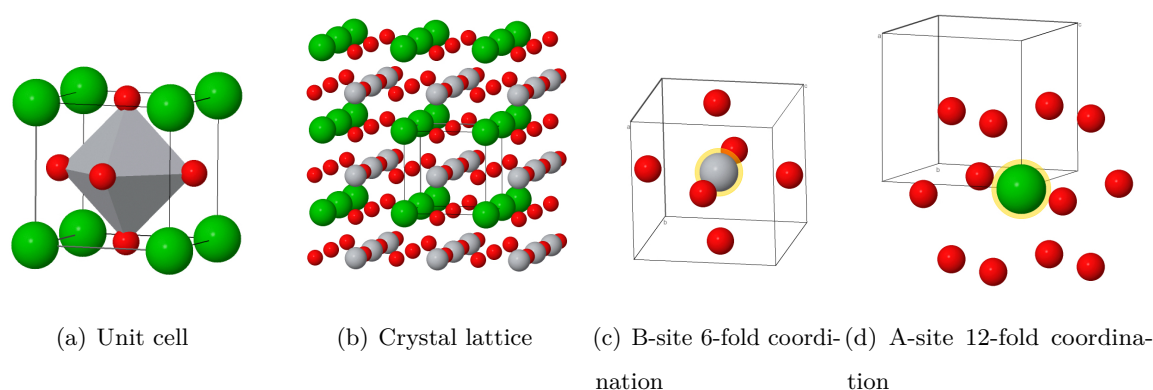


Figure 3.7: Perovskite structure shown as BaTiO_3 with Ba in green, Ti in grey and oxygen in red. Images obtained from the ICSD database http://www2.fiz-karlsruhe.de/icsd_home.html.

Due to their broad variety of compositions and due to good oxygen anion mobility/oxygen exchange kinetics, perovskite-type materials can be employed in many applications like solid oxide fuel cells, as oxygen permeation membranes, sensor materials, supercapacitors and heterogeneous catalysts. The mineral perovskite (CaTiO_3) was already discovered in 1839 by Gustav Rose and was named after Lew A. Perowski, but the catalytic activity toward electrochemical oxygen conversion was only first investigated in the 1980s. Incredibly, 90% of all metallic natural elements are stable in the perovskite structure [38, 66, 67].

Its catalytic activity is determined by four key properties, which are discussed in the following paragraphs: 1.) the electronic structure of the B-site transition metal including its flexibility in oxidation states ($\text{B}^{m+}/\text{B}^{m+1}$), 2.) the available oxygen vacancies and defects, 3.) the crystal structure/non-stoichiometry and 4.) the, often very low, electrical conductivity, which is one main drawback of this material for electrochemical applications. Thus, perovskites are frequently combined with carbon as electrically conductive support material. In this regard, the smaller the perovskite particles and the tighter the interface, the shorter the internal electron conduction pathways and the better the overall electron transfer, respectively [38, 66].

As already shown in section 3.4.1 and in Figure 3.5 the ORR/OER mechanism occurs through the bonding of the oxygen atom with the B-site element as active site. The five d-orbitals of the B-site transition metal are split into 3 t_{2g} orbitals (d_{xy}, d_{xz} and d_{yz} , respectively) and two e_g orbitals with higher energy [38]. The two e_g orbitals form with the oxygen 2p orbitals a σ - and σ^* -antibonding orbital and with the other three orbitals π - and π^* -antibonding orbitals, depending on the direction of the B-O interaction. The σ -bonds are stronger than the π -bonds, therefore, the number of 3d electrons influences the B to O bond. Depending on the element the e_g filling is influenced by oxidation state as well as spin state [38, 67]. An e_g filling of < 1 is better for ORR, whereas > 1 gives better OER catalysts [22]. For OER the higher the d electron number, the better the catalyst in the order $\text{Ni} > \text{Co} > \text{Fe} > \text{Mn} > \text{Cr} > \text{V}$. Investigating common elements for the B-site, LaCoO_3 and LaMnO_3 are considered very good bifunctional catalysts with LaMnO_3 being less stable [38, 69, 73, 74]. On the other hand, the A site cations indirectly influence the activity by altering the electrical conductivity and as well as the B-O bonding length and the O-B-O bond angles. For ORR the smaller the ionic radius of the A-site element, the higher the activity. For example, La is the best element from the rare-earth elements [38].

Non-stoichiometry means that the charge of all cations is higher or lower than the nominal charge of +6. That means that the crystal structure is disordered by defects such as vacancies (Schottky defect), interstitial atoms, vacancy-interstitial atoms (Frenkel defect) or substitutional defects of differently sized atoms [38]. Surface oxygen vacancies can enhance ORR and OER reaction rates as they behave as donors and acceptors (see equation 3.3), although too many empty places in the lattice disrupt the crystal structure and result in low conductivity and change of electronic properties. The vacancies can be incorporated by high temperatures and vacuum during annealing [66, 67].



The partial substitution of A with lower valency metal ions creates more vacancies and induces less stable oxidation states in the B-sites, which enhances oxygen mobility and the reaction kinetics. An example is shown in equation 3.4. Doping of La A-site cation with Sr leads to typical defects according to the Kröger-Vink notation (V means vacancy, subscript element denotes the original element on the lattice place, X means no change in charge, ' means one more negative charge, • and •• means one and two times more positive charge). The equation shows that the oxygen vacancy concentration increases, which results in better oxygen adsorption. Ca and Sr are the most often applied A' doping materials as they have a nearly similar ionic radius as La [38].



In general, for oxide catalysts, the ORR seems to be more challenging than the OER [67]. For increasing catalytic activity of oxide catalysts, the addition of carbon not only enhances the electrical conductivity of the perovskite but many research groups found that there is a catalytic "synergistic effect" between carbon support and the oxide material. This synergy makes the final catalyst more active toward ORR and OER than both materials separately (the high inherent catalytic activity of carbonaceous materials toward ORR is well known as described in section 3.4.2). Beside the enhanced conductivity, there is a ligand effect, which facilitates electron transfer. In addition, when the oxide catalyst is directly synthesized on carbon support, the resulting strong interface between C-O-Metal becomes more like a covalent-type bond. It was found, that in the catalytic process, carbon functions as main electrochemical catalyst for the $2 e^-$ reduction of O_2 to HO_2^- . The perovskite works as co-catalyst and reduces in the second

$2e^-$ transfer the formed peroxide HO_2^- to OH^- . This combined catalytic pathway with carbon initially catalyzing O_2 reduction to peroxide and subsequent further reduction/decomposition of peroxide to OH^- can explain the often experimentally measured $4e^-$ reduction pathway for perovskite/carbon co-catalytic materials [66]. This synergistic effect is also beneficial for bifunctional ORR and OER activity. Whereas carbon is a good catalyst for ORR but less active for OER, perovskites are generally better OER catalysts [29, 66].

For the synthesis of perovskites, metal nitrates, acetates or carbonates can be used as precursor salts, which are mixed in the desired molar ratios and then thermally decomposed at temperatures of 600-900 °C. However, direct conversion, also called solid-state route, at high temperatures and with long annealing times often results in a phase-impure product with big particles sizes of a few μm ($> 100\text{ nm}$) and thus small surface areas of $< 10\text{ m}^2\text{ g}^{-1}$ and low mass activity. As it is a type of ceramic preparation route, the rate of diffusion determines the final product and this in turn is determined by the type of salt (carbonates and nitrates decompose very easily), by the grinding/mixing and by the annealing temperature, time and atmosphere [22, 38, 67].

Better reproducible and more favorable wet-synthesis routes leading to higher activities and more porous structures are listed in the following, whereby the sol-gel process is the most common one [67]:

- *Sol-Gel Process*: An aqueous solution of the precursor salts together with citric acid or EDTA functioning as complexing agent is prepared and, under stirring, the solvent slowly evaporated until a gel is obtained. The gel is decomposed at 200 °C, the product ground to powder and then annealed at high temperatures of about 650 °C. By additionally using Vulcan carbon as pore former exceptionally high surface areas of up to $210\text{ m}^2\text{ g}^{-1}$ could be obtained via this method [75].
- *Co-Precipitation*: To the solution of precursor salts a base is added, which results in precipitation of these salts in form of hydroxides. The precipitate is filtered, dried and then heat-treated. Although it is possible with this method to obtain small catalyst particles the phase-purity is rather low because of the different hydroxilation rates of the various metals.
- *Reverse Micelle Method*: This method is in principle a more controlled co-precipitation synthesis route using surfactants to create water-in-oil or oil-in-water micelles. Two different micelle solutions are prepared, one with the precursor salts and one with the base, which are then mixed in order to trigger controlled hydroxilation and precipitation with small

particles sizes and a more defined composition. The product is centrifuged, washed and annealed.

- *Hydrothermal Route:* Nitrates or acetates of the respective salts are hydroxylated with NH_4OH and then hydrothermally processed in a PTFE-lined autoclave. After centrifugation the product is annealed at 500 - 600 °C.

Moreover, electrospinning is a good method for obtaining nanostructured perovskites or it can be used to manufacture nanotubes or templates as conductive support [38, 66]. As example, this method was applied by Park *et al.* [76] who manufactured porous nanorod $\text{La}_{0.5}\text{Sr}_{0.5}\text{Co}_{0.8}\text{Fe}_{0.2}\text{O}_3$ perovskite using an electrospinning machine and mixed the catalyst with nitrogen-doped reduced graphene oxide carbon. By means of cyclic voltammetry they attributed the hybrid-catalysts high ORR activity to the carbon material and the good OER activity to the perovskite.

The following short list presents some examples in literature, where other research groups investigated perovskites with compositions similar to those used in this thesis. The most studied catalyst in this thesis was a commercially acquired $\text{La}_{0.6}\text{Sr}_{0.4}\text{Co}_{0.2}\text{Fe}_{0.8}\text{O}_3$ with a particles size of $d_{50} = 0.4 - 0.8 \mu\text{m}$ and $10 - 14 \text{ m}^2 \text{ g}^{-1}$ surface area, but also $(\text{La}_{0.8}\text{Sr}_{0.2})_{0.95}\text{MnO}_{3-x}$ (commercial), LaNiO_3 and $\text{La}_{0.6}\text{Ca}_{0.4}\text{CoO}_3$ (both synthesized) were investigated.

Using rotating ring-disk (RDE) cyclic voltammetry, Rincon *et al.* [77] showed in their comparative study of various perovskites that $\text{La}_{0.58}\text{Sr}_{0.4}\text{Co}_{0.2}\text{Fe}_{0.8}\text{O}_3$ exhibited the highest catalytic activity toward OER. However, slight variations in composition already resulted in high performance loss and no trend or rational design principle could be found. They concluded that La on the A-site and Co on the B-site, respectively, are the best choices for achieving high OER activity. In an other early comparative cyclic voltammetry study by Tiwari *et al.* [78] $\text{La}_{0.8}\text{Sr}_{0.2}\text{Co}_{1-y}\text{B}_y\text{O}_3$ was investigated by varying the B-site between Ni, Fe, Cu, and Cr ($y = 0.1 - 0.4$). Ni and Fe proved to be beneficial for OER activity, whereas doping with Cu and Cr had a negative effect. Ahn *et al.* [79] studied a similar perovskite - $\text{La}_{0.7}\text{Sr}_{0.3}\text{Co}_{1-x}\text{Fe}_x\text{O}_3$ - but varied the ratio of B-site elements, obtaining the best results with a ratio Co : Fe of 7 : 3. In half-cell measurements this catalyst exhibited a very low ORR/OER potential difference ΔV of only 0.82 V at 100 mA cm^{-2} (sweep polarization curves with 5 mV s^{-1} , not repeated cycling). In addition, they manufactured the air electrode in a similar process as applied in this thesis by using PTFE binder and Ni mesh as current collector.

Jung *et al.* presented in a series of publications ([80–82]) methods for optimizing perovskite catalysts using $\text{Ba}_{0.5}\text{Sr}_{0.5}\text{Co}_{0.8}\text{Fe}_{0.2}\text{O}_{3-\delta}$, an often applied material in solid-oxide fuel cells. Using

RDE cyclic voltammetry they measured an increase in electron transfer number to 3.60–3.72 (close to reaching full O₂-conversion of via the 4e⁻-pathway) by doping the material with La on the A-site (La_{0.3}(Ba_{0.5}Sr_{0.5})_{0.7}Co_{0.8}Fe_{0.2}O_{3-δ}) [80]. Also heat-treatment at 950 °C in oxygen atmosphere increased the electrocatalytic performance of Ba_{0.5}Sr_{0.5}Co_{0.8}Fe_{0.2}O_{3-δ} by modifying the surface structure and crystallinity [81]. In full-cell tests at 10.5 mA cm⁻², 50 nm-sized La_x(Ba_{0.5}Sr_{0.5})_{1-x}Co_{0.8}Fe_{0.2}O_{3-δ} perovskite reached good performances with ΔV < 1 V for 100 cycles (10 min per cycle) [82]. Wang *et al.* [83] physically mixed Ba_{0.5}Sr_{0.5}Co_{0.8}Fe_{0.2}O_{3-δ} perovskite with high surface area carbon thus achieving a high electron transfer number of 3.9 and good stability in RDE cyclic voltammetry experiments. Further good bifunctional catalytic performance presented in literature was achieved with La_{0.6}Sr_{0.4}Co_{0.8}Fe_{0.2}O₃ perovskite by Alegre *et al.* [84], who obtained very stable ORR potentials of about 1.1 V vs. Zn/Zn²⁺ at 80 mA cm⁻² but deteriorating OER potentials within 1 h operation time, and by Elumeeva *et al.* [85], who reached with that catalyst good ex-situ performances during RDE measurements by growing N-doped carbon nanotubes onto the perovskite particles using chemical vapor deposition (CVD).

Spinel

The general spinel formula is ABO₃, with the A-site in oxidation state +2 and the B-site having oxidation state +3 [40]. The crystallographic structure is shown in Figure 3.8. The spinel Co₃O₄ is one of the most often investigated bifunctional catalysts due to the high OER activity of the Co redox couple. As with perovskites, spinel oxides exhibit low intrinsic electrical conductivity [22, 26], which is why they are often directly synthesized on carbon support. The activity is attributed to the different oxidation states of Co in the potential range between ORR and OER. The active sites for ORR are the Co²⁺ atoms in tetrahedral positions (A-site). For OER the octahedral Co³⁺ atoms are the active sites, thus forming cubane-like structures with the oxygen atoms. At OER potentials these Co³⁺ atoms get then oxidized to Co⁴⁺ [29].

Another often studied spinel catalyst is NiCo₂O₄, where Ni replaces the tetrahedral place of Co²⁺ within the structure as shown in 3.8. This catalyst was also extensively tested and investigated during this project due to its facile synthesis by a dip-coating impregnation approach presented by Li *et al.* [86]. In a comparative study by Pletcher *et al.* [87] it was shown that the NiCo₂O₄ exhibited slightly better OER but significantly higher ORR activity compared to the Co₃O₄ catalyst. The high OER activity of the spinel catalysts was also studied by Abidat *et al.* [88]

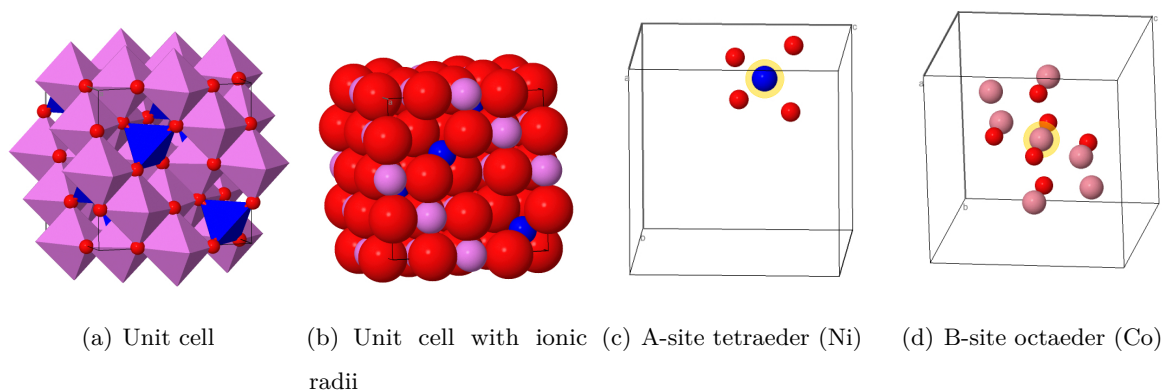


Figure 3.8: Spinel structure shown as NiCo_2O_4 with Ni in blue, Co in pink and oxygen in red.

Images obtained from the ICSD database http://www2.fiz-karlsruhe.de/icsd_home.html

by means of RDE cyclic voltammetry, whereby again NiCo_2O_4 exhibited superior OER activity compared to Co_3O_4 and MnCo_2O_4 . In addition, NiCo_2O_4 spinel proved to be the most stable of these three catalysts during repeated OER cycling. Very good charge/discharge potentials of about 2.1 V and 1.0 V at 50 mA cm^{-2} , respectively, were obtained by Ma *et al.* [89], who synthesized a NiCo_2O_4 -carbon nanotube hybrid catalysts via a hydrothermal synthesis route. The catalyst exhibited stable potentials for about 50 h.

An interesting approach is the substitution of oxygen with sulfur, thus further modifying the Co d-orbitals. Because of surface sulfur vacancies, the Co^{3+} d-orbitals are electronically altered and the NiCo_2S_4 spinel is able to reduce oxygen via the four electron pathway [29].

Other Catalysts

Noble-metals such as Pt, Ir and Ru are considered to exhibit the highest catalytic activity toward ORR or OER with Pt being the best catalyst for ORR and IrO_2 and RuO_2 showing the highest activity toward OER. Nevertheless, these catalyst have only low bifunctional activity. At high anodic potentials Pt forms an oxide layer in form of Pt-OH and Pt=O, which decreases the activity toward OER. In contrast, IrO_2 and RuO_2 do not show catalytic activity toward ORR [26, 67]. For widespread application these materials are too costly and scarce, nevertheless, they are often used for benchmarking other catalysts such as the oxide types [22].

MnO_2 is the most often utilized catalyst in primary zinc-air batteries because of the very high ORR activity and the low cost [90]. Manganese oxides in general (*e.g.* MnO_2 , Mn_2O_3 , Mn_3O_4)

are affordable and environmentally benign with low toxicity [23, 58], but are also characterized by a low inherent electrical conductivity, which limits their activity toward ORR [91]. Generally the number of $\text{Mn}^{4+}/\text{Mn}^{3+}$ redox couples was found to determine the ORR activity, as they function as oxygen mediator species [91]. In addition, manganese can exist in many different oxidation states as well as crystal structures [23]. For example, the catalytic activity of different oxide compounds is reported to follow the sequence of $\text{MnOOH} > \text{Mn}_2\text{O}_3 > \text{Mn}_3\text{O}_4 > \text{Mn}_5\text{O}_8$ [91]. Regarding the crystal structure of MnO_2 , the highest ORR activity is reached with $\alpha\text{-MnO}_2$ and $\delta\text{-MnO}_2$ [90]. Manganese oxides exhibit good catalytic activity toward OER as well, but keeping the high bifunctional activity during cycling is challenging. Because of the alternating reduction and oxidation of the catalyst during repeated cycling, the catalyst's activity gradually deteriorates. Especially the oxidation of manganese oxide to MnO_4^- during OER poses a challenge [24].

Because of low cost materials, carbon-based metal-free compounds are of high interest as bifunctional catalysts. Many carbon-based catalysts are highly ordered and comprise graphene, (reduced) graphene oxide ((r)GO), and carbon nanotubes (CNT). These materials are then doped - for example with nitrogen. The incorporated heteroatoms provide electrons to the conjugated π -system of the carbon, which in turn makes the carbons in the neighboring rings more nucleophilic. Therefore, oxygen atoms are adsorbed with higher probability during ORR and during OER the N-atom can more easily accept the electrons from the adsorption intermediates [22]. Also, quaternary N-atoms are electron donors (ORR), whereas pyridinic N-atoms withdraw electrons (OER) [28]. Nevertheless, many pure carbon based materials exhibit low catalytic activity toward OER, which again highlights the benefits of incorporating carbon/metal oxide composites in the air electrode build [23]. Electrospinning is an interesting manufacturing method for heteroatom-doped carbon fibers. They can be obtained by spinning polyacrylonitrile as carbon precursor with a nitrogen source, followed by pyrolysis. With this nanotubular structures with an outer diameter of 100 - 150 nm are obtained [22].

3.4.3 Electrode Manufacture and Materials

Although the catalysts described in the previous section 3.4.2 have been successfully tested ex-situ using cyclic voltammetry, it is still challenging to transfer their full catalytic activity into a practical rechargeable zinc-air battery. Due to their poor integration into the air electrode, these often nano-sized catalysts are completely covered within the air electrodes resulting in severe accessibility limitations [28]. Thus, especially the porosity of the air electrode plays a

crucial role and a fine balance of macro- and micropores has to be achieved [92]. The most important parameter, which have to be considered for air electrode manufacture are summerized in the schematic in Figure 3.9.

Since the invention of the first zinc-air batteries and fuel cells, the development of suitable gas diffusion electrodes (GDE) has been of high importance. Already in 1932, carbon based electrodes were impregnated with hydrophobic waxes in order to prevent electrolyte leakage [24]. A GDE must provide porosity through a high surface area, electrical conductivity and stability with high resistance toward oxidation and corrosion. This includes stability in a wide potential range of minimum 0.6–2.0 V vs. RHE. Common materials utilized, which meet more or less these requirements, are carbon (in many different morphologies) as main electrical support material and PTFE used as hydrophobic binder material [26]. Other wet-proofing materials are PVDF and fluorinated ethylene propylene. Commercial GDEs are impregnated woven or non-woven carbon papers or cloths sold under the names Toray, Freudenberg, Sigracet and Zoltek. These were developed for polymer electrolyte fuel cells and often do not meet the requirement in zinc-air batteries (which is the liquid alkaline electrolyte and high OER potentials leading to corrosion) [28].

For ORR to take place a three-phase boundary is necessary. For this, the solid electrically-connected high surface area catalyst has to be in contact with the liquid electrolyte for OH^- transfer and gaseous O_2 must have access to the catalyst as well. Thereby the diffusion path in the liquid phase must be as short as possible in order to minimize mass transport limitations [22, 26]. For ORR the formation of as many triple-phase boundaries as possible is crucial. In contrast to this, the OER only requires a two-phase boundary between catalyst and electrolyte, nevertheless, the generated oxygen must be effectively taken away from the active sites. Taking advantage of these different requirements, the electrode can be built in a multi-layered form. This approach was also applied within this thesis and led to beneficial results by exploiting the preferred catalytic activity of two bifunctional catalysts (*i.e.* one with high activity toward ORR and one for OER). Because the porous structure of the OER catalytic sites can be flooded with electrolyte (two-phase boundary), the OER catalyst is applied on the electrolyte facing side. On the opposite, the ORR catalyst needs good gas supply and is therefore implemented on the air facing side of the electrode. In addition, the hydrophobicity/hydrophilicity of the electrode can be optimized layer-wise. Nevertheless, as both catalyst are incorporated into one single air electrode and undergo repeated reduction/oxidation, both catalysts have to be stable both at ORR and OER conditions, respectively [31, 40].

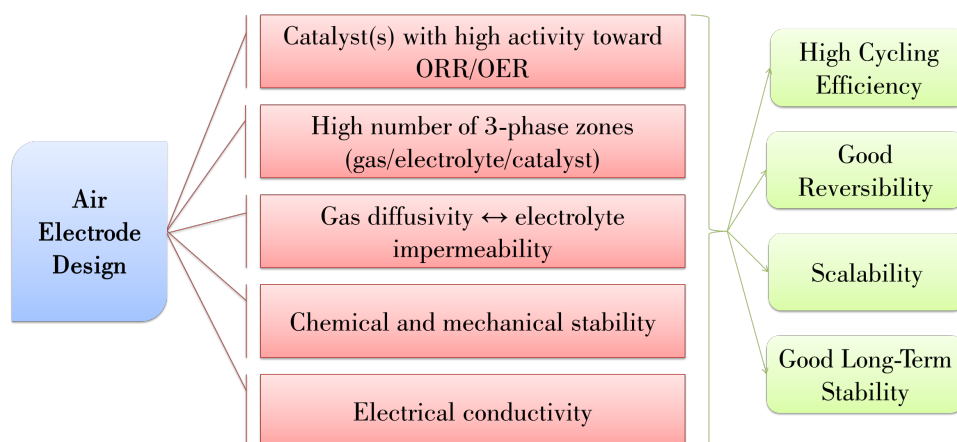


Figure 3.9: Summary of various design parameters needed for achieving high-performing air electrodes.

As current collector material Ni mesh or Ni foam is often utilized, although Ni foam increases the weight and is much more costly than Ni mesh [26, 93]. However, its higher surface area can result in a better performance of the air electrode [39, 94]. Other substrates are Ti mesh, Cu foam or stainless steel mesh, on which the catalyst (for example Co_3O_4) can be directly grown [28].

Due to the many similarities between alkaline fuel cell technology and metal-air batteries regarding the air electrode architecture as well as the utilized catalysts [24], the most commonly applied manufacturing method is the rolling process [95, 96]. It was primarily developed for aqueous alkaline fuel cell systems [92, 93, 97] and was also tested and applied in the scope of this thesis. Thereby a gas diffusion layer and an active layer are separately mixed, kneaded and cross-rolled together onto a mesh current collector using for example a heavy cylinder drum.

A variety of the rolling process is the spray-coating method [98, 99]. Instead of rolling the active layer containing the catalyst onto the GDE, it is homogeneously dispersed in a solvent and sprayed onto the (commercially acquired) GDE. By this, a much thinner and more defined active layer is obtained. Besides the classical mixing or spray-coating manufacturing procedure, also chemical vapor deposition is a viable method. Thereby the catalyst is directly grown on the current collector support [28]. A modified synthesis route is the dip-coating method, which was successfully applied by Price et al. [100] and which was also investigated at the start of this project.

3.4.4 Long-term Performance of Bifunctional Air Electrodes

So far, there has been not much applied research on the practical use of bifunctional catalysts in flow cell systems, especially at high current densities and long-term cycling operation [29, 36]. Commonly employed cathodes developed for alkaline fuel cell technology can not be applied without alterations as they were not designed to withstand OER conditions [36]. The maintenance of stable three-phase boundaries, needed for ORR, is one of the biggest challenges. Due to material degradation the electrolyte can slowly flood the pore system within the GDE, which slows down oxygen diffusion until the reaction becomes mass transport limited. Consequently, also an ohmic resistance increase can be observed as well as efficiency and power loss [22]. Besides air electrode flooding and thus limited oxygen diffusion, also drying-out effects are often a prominent cause for degrading performances, especially in small batteries [30].

The main degradation mechanisms are discussed in the following and comprise 1.) catalyst degradation (discussed in section 3.4.2), 2.) carbon corrosion, 3.) hydrophobic binder (PTFE) degradation, 4.) carbonate precipitation and 5.) mechanical degradation by oxygen bubble formation or electrolyte/gas pressure. Moreover, all the above mentioned mechanisms influence each other. For example, carbon corrosion or PTFE degradation can promote deteriorating catalyst performance by increased catalyst particle agglomeration or by complete particle detachment [28]. In addition, the applied current density has a severe impact on the performance and the stability of the battery. For example, modeling has shown that too high charging current densities can lead to local OH^- depletion limiting OER [22]. Moreover, the operating temperature is of high importance. In this thesis, most experiments were carried out at room-temperature, as a temperature increase can lead to pronounced flooding. With rising temperature the viscosity as well as the surface tension of the electrolyte is reduced resulting in pronounced infiltration of liquid into the GDE. The maximum operating temperature for a zinc-air battery is at around 80°C , thus cooling and heat management can be required in a battery pack [22].

- *Carbon Corrosion:* Carbon black, often used in primary batteries, exhibits a high corrosion rate at potentials $> 0.7\text{ V}$ vs. SHE [22]. Degradation is further enhanced by the large surface area of the carbon support [23]. The slow degradation of carbon support follows the reaction $\text{C}_{\text{solid}} + 6\text{OH}_{\text{aq}}^- \longrightarrow \text{CO}_3^{2-}_{\text{aq}} + 3\text{H}_2\text{O} + 4\text{e}^-$, and pronounced oxidation can be observed by the brown coloring of the electrolyte, which is caused by the formation of carboxylic acids such as mellitic acid and humic acid [22]. Employing carbons with more

graphitized morphologies such as carbon nanofibers, carbon nanotubes, and graphene can slow down the corrosion rate [66].

- *PTFE Degradation:* Keeping the hydrophobicity within the air electrode is especially important for achieving sufficient O₂ diffusion without electrolyte leakage [23]. Therefore, the slow reduction of hydrophobicity by PTFE degradation poses a severe challenge in highly alkaline solution and if the cell is operated at elevated temperatures up to 80 °C this effect is especially pronounced. [22]. Although carbon-free electrodes have been developed for example by Li *et al.* [86] in order to minimize degradation by carbon corrosion, plastic binders are unavoidable in the electrode built, therefore their degradation in the caustic/corrosive and oxidizing environment poses a severe problem [28]. On perovskite as well as carbon-based catalysts the ORR proceeds to some degree via the two electron pathway, whereby H₂O₂ is formed as the intermediate product [22, 38, 66]. A reason for PTFE degradation can hence be attributed to H₂O₂ or HO• radical attack of the F-C chain, an effect known from polymer electrolyte fuel cells [101, 102].
- *Carbonate Precipitation:* When supplying the air electrode with ambient air, fractions of CO₂ can react with the alkaline electrolyte to CO₃²⁻/HCO₃⁻. Especially in small static zinc-air batteries these carbonates can precipitate within the cell, which in consequence blocks the gas diffusion channels within the air electrode [22, 24, 31, 103]. In addition, the formation of carbonates reduces the ionic conductivity, as the mobility of the carbonate is lower than of hydroxide, and increases the electrolyte viscosity, which is especially challenging in small zinc-air cells [33]. The resulting cause for end-of-life of an air electrode thus includes decreased electrolyte conductivity and blocked catalytic sites by carbonate precipitation [30]. In a study by Drillet *et al.* [103], the stability of bifunctional air electrodes was assessed by adding an increasing amount of CO₂ into the gas feed. At CO₂ concentrations up 1000 ppm end-of-life was reached by limited ORR performances caused by pore clogging within the air electrode. Thus, the utilization of either a CO₂ filter or a chemical scrubber like piperazine or amines is recommended [36]. LiOH and LiOH-Ca(OH)₂ or soda-lime can function as adsorbent materials [24, 33]. But, although carbonates are formed in the electrolyte [51], the CO₂ issue is less severe in circulated electrolyte as the respective saturation points are rarely reached [59].
- *Mechanical Degradation:* Mechanical stress is harming the air electrode on one hand by the oxygen bubble formation during OER especially at high current densities resulting in

internal gas pressure built-up [31, 104] and on the other by the high shearing forces of the electrolyte in the zinc-air flow cell [31]. Nevertheless, the flowing electrolyte has the benefits to take away discharge products, remove heat and reduce concentration gradients [31]. In addition, the air electrode must withstand the hydrostatic pressure from the electrolyte, which can be counteracted by a slight gas pressure from the air supplied side. This approach was successfully tested within this thesis.

In Table 3.4.4 a few zinc-air batteries reported in literature with documented long-term tests are summarized. The table was put together from lists reported in several reviews [22–24, 26, 28] and consists of long-term tests with either $\geq 20 \text{ mA cm}^{-2}$ cycling current density and/or operation times of minimum 100 h. The list comprises a broad variety of test cells (flow, flexible, etc.) and electrode sizes, which makes the comparison of the different catalysts very challenging. As can be seen in Table 3.4.4 most catalysts employ the transition metals Co and Ni in oxide form. Also noteworthy is the high number of different carbon morphologies used as support or as pure catalyst. Most literature references in this table are from recent years providing thereby a state-of-the-art overview on zinc-air (flow) battery development.

Table 3.5: Comparative list of zinc-air batteries found in literature.

| Catalyst ^a | Mode | CD ^b [mA cm ⁻²] | Time [h] | No. of cycles | Charge ^c [V] | Discharge ^c [V] | Supply | Ref. |
|------------------------------------------------------------------------------|------|-------------------------------------------|-------------|------------------|----------------------------|-------------------------------|----------------|-------|
| •Ni foam + Ag | tri | 20 | ~ 85 | 600 | ~ 2.5 ^d | ~ 1.25 | O ₂ | [52] |
| •Ni foam-Fe + stain- less steel | tri | 50 | 25 | 100 | ~ 2.2 | ~ 1 | air | [56] |
| •Pd ₃ Pb/C- NiCo ₂ O ₄ | tri | 10 | 560 | 135 | ~ 2.1 | ~ 1.2 | air (?) | [105] |
| •NH ₃ -activated N-C + Co ₃ O ₄ /Ni foam | tri | 10 | 830 | 200 | ~ 2 | ~ 1.2 | air | [106] |

^a Abbreviations: rGO = reduced graphene oxide; LDH = layered double hydroxide; CNT = carbon nanotubes; NC = nanocrystal or nanocarbon; NP = nanoparticle; CNF = carbon nanofiber; PFC = porous fibrous carbon; CNS = carbon nitride sponge ; GRW = graphene nanoribbons network, CF = carbon fiber

^b CD = Current density; when possible related to air electrode surface area, first number is related to charge, the second to discharge

^c Cell voltage, when possible, taken at the end of testing

^d Pulse charging

^e In bi-mode not stable

^f Half-cell measurement

^g Chloride-based electrolyte

^h Three cells in stack

| Catalyst ^a | Mode | CD ^b [mA cm ⁻²] | Time [h] | No. of cycles | Charge ^c [V] | Discharge ^c [V] | Supply | Ref. |
|-----------------------------------------------------------|------------------|-------------------------------------------|-------------|------------------|----------------------------|-------------------------------|----------------|-------|
| • CoO/N-CNT + Ni-Fe-LDH/CNT | tri ^e | 20 | 200 | 20 | 1.05 | 1.25 | O ₂ | [44] |
| | | 50 | 40 | 10 | ~ 2.05 | ~ 1.18 | | |
| • Fe-histidine | tri ^e | 50 | 30 | 30 | 2.60 | 1.20 | O ₂ | [107] |
| • P,S co-doped CNS | tri (?) | 25 | 100 | 500 | 2.02 | 1.22 | air | [108] |
| • N,P co-doped mesoporous NC | tri ^e | 2 | 100 | 600 | ~ 2.5 | 1.25 | air | [109] |
| • MnO ₂ + stainless steel | tri ^g | 100 | 1000 | 500 | ~ 1.9 | ~ 1.1 | air | [104] |
| • NiCo ₂ O ₄ | bi ^e | 50 | 50 | 50 | ~ 1.95 | ~ 1.15 | O ₂ | [100] |
| • Ag/LaMnO ₃ nanorods/rGO | bi | 25 | 80 | 80 | ~ 2.05 | ~ 1.17 | air (?) | [110] |
| • Co ₂ MnO ₄ /N-rGO | bi | 20 | 17 | 100 | 2.06 | 1.13 | air | [111] |
| • Co ₂ MnO ₄ /N-rGO | bi | 20 | 17 | 100 | ~ 1.9 | ~ 1.05 | O ₂ | [112] |
| • 1D NiCo ₂ O ₄ | bi | 20 | 33 | 50 | 1.84 | 1.00 | O ₂ | [113] |
| • α-MnO ₃ -LaNiO ₃ /CNT | bi | 20 | 13 | 75 | 2.05 | 1.19 | air | [114] |
| • α-MnO | bi ^h | 15/25 | 16 | 100 | ~ 2.0 | ~ 0.8 | air | [54] |
| • P-doped graphitic C,N/C-fiber paper | bi | 20 | 8 | 50 | 2.46 | 1.05 | air | [115] |
| • NiCo ₂ O ₄ -CNT | bi | 50 | 55 | 330 | ~ 2.3 | ~ 1 | air | [89] |
| • Co ₃ O ₄ nanowire | bi | 18 | 600 | 100 | ~ 2.1 | ~ 0.8 | air | [99] |
| • LaMnO ₃ | bi | 25 | 1 | 4 | ~ 2.8 | 1.10 | air | [116] |
| • Co ₃ O ₄ NC/N-CNT | bi | 20 | 40 | 240 | ~ 2.16 | ~ 1.14 | air (?) | [117] |
| | | | 100 | 25 | ~ 2.3 | ~ 1.1 | | |
| • LaNiO ₃ -CNT | bi | 20 | 30 | 15 | ~ 2.1 | 1.00 | air | [118] |
| • Co ₃ O ₄ N-CNT on stainless steel | on bi | 25 | 516 | 1550 | ~ 1.95 | ~ 1.2 | air | [45] |
| • NiCo/PFC aerogel | bi | 10 | 600 | 150 | ~ 2 | ~ 1.1 | air | [119] |
| • Ni ₃ FeN | bi | 10 | 170 | 310 | ~ 2.0 | ~ 1.2 | air | [120] |
| • Co ₃ O ₄ NP/CNF | bi | 20 | 55 | 55 | 2.04 | 1.10 | air | [121] |

| Catalyst ^a | Mode | CD ^b [mA cm ⁻²] | Time [h] | No. of cycles | Charge ^c [V] | Discharge ^c [V] | Supply | Ref. |
|----------------------------------------------------------------------------------------------------------|-----------------|-------------------------------------------|-------------|------------------|----------------------------|-------------------------------|----------------|-------|
| • microporous carbon sheets | bi | 2 | 160 | 160 | ~ 2.2 | ~ 1.2 | air (?) | [122] |
| • Co-polydopamine-Carbon | bi | 5 | 580 | 580 | 2.18 | 1.01 | air | [123] |
| • NCNT/CoO-NiO-NiCo | bi | 20 | 16 | 100 | ~ 1.9 | ~ 1.05 | air | [124] |
| • Nanoporous CNF films | bi | 10 | 84 | 500 | 1.93 | 1.07 | air | [125] |
| • Co ₃ O ₄ /MnO ₂ -CNT | bi | 10 | 198 | 1200 | ~ 2.6 | ~ 0.9 | air | [126] |
| • La ₂ O ₃ /Co ₃ O ₄ /MnO ₂ -CNT | bi | 10 | 90 | 543 | ~ 1.95 | ~ 1.1 | air | [127] |
| • Ni ₃ FeN/Co ₃ N-CNF | bi | 50 | 140 | - | ~ 2.2 | ~ 0.8 | air | [128] |
| • Co(II) _{1-x} Co(0) _{x/3} Mn(III) _{2x/3} S NPs on B/N-Co-doped Mesoporous NC | bi | 20 | 21 | 5 | ~ 2.0 | 1.25 | O ₂ | [129] |
| • N-doped C@graph.C | bi | 5 | 220 | ~ 220 | ~ 2.1 | ~ 1.15 | air | [130] |
| • Ag-Cu nanoalloy on Ni foam | bi | 20 | 125 | 250 | ~ 2.05 | 1.05 | air | [131] |
| • AgCu-metal glass | bi | 20 | 420 | 420 | ~ 2.0 | ~ 1.0 | air | [132] |
| • Mn oxide grown on carbon paper | bi | 15/7.5 | 125 | 500 | 2.23 | 1.11 | air | [133] |
| • MnO _x | bi ^g | 1 | 2200 | 500 | 2.15 | 0.94 | air | [134] |
| • La _{0.6} Ca _{0.4} Co _{0.2} Fe _{0.8} O ₃ | bi ^f | 100 | 80 | 240 | ~ 1.85 | ~ 0.8 | air | [135] |
| • MnO ₂ + β-Ni(OH) ₂ | bi | 20 | 375 | 150 | ~ 1.8 | ~ 1.3 | air | [53] |
| • La _{0.6} Ca _{0.4} CoO ₃ | bi ^f | 50 | 300 | 100 | ~ 2.0 | ~ 1.1 | air | [75] |
| • La _{0.7} Sr _{0.3} NiO ₄ | bi | 25 | 2 | 20 | ~ 2.1 | ~ 1.0 | air (?) | [136] |

| Catalyst ^a | Mode | CD ^b [mA cm ⁻²] | Time [h] | No. of cycles | Charge ^c [V] | Discharge ^c [V] | Supply | Ref. |
|--------------------------------------------------------|-----------------|-------------------------------------------|-------------|------------------|----------------------------|-------------------------------|--------|-------|
| • MnO _x | bi ^g | 0.5 | 1400 | 117 | ~ 2.1 | ~ 0.8 | air | [137] |
| | | 5 | 300 | 25 | ~ 2.3 | ~ 0.5 | | |
| • RuO ₂ /CNF | bi | 4 | 160 | 80 | ~ 1.9 | ~ 1.1 | air | [138] |
| • 3D N-GRW | bi | 20 | 30 | 15 | ~ 2.3 | ~ 0.8 | air | [139] |
| • Co ₄ N/CF on carbon cloth | bi | 10 | 136 | 408 | 2.00 | 1.16 | air | [140] |
| • 3D ordered mesoporous Co ₃ O ₄ | bi | 10 | 400 | 200 | 2.00 | 1.20 | air | [141] |
| • 5 % Co-doped TiO ₂ NP | bi | 5 | 1050 | 3150 | ~ 1.85 | ~ 1.2 | air | [142] |
| | | 20 | 750 | 38 | ~ 2.15 | ~ 1.1 | | |
| • NiO/CoN porous nanowires | bi | 50/2 | 8 | 50 | ~ 2.25 | ~ 1.3 | air | [143] |
| • B,N-doped Carbon | bi | 2 | 100 | 600 | 2.19 | 1.16 | air | [144] |
| • FeCo NPs/ N-doped graphitic CNT | bi | 120 | 40 | 120 | ~ 2.2 | ~ 0.6 | air | [145] |

3.5 Electrochemical Characterization

The performance of flow batteries is characterized by the coulombic efficiency η_c (which is the ratio between charge and discharge capacities), the voltage efficiency η_v (ratio charge/discharge voltages) and the energy efficiency η_e , which is the multiplied product of the two ($\eta_e = \eta_c \cdot \eta_v$) [49]. The coulombic efficiency loss is calculated according to equation 3.5 and describes the energy which is not used for zinc deposition during charge and which leads to more zinc dissolution during discharge as is available at clamps [51].

$$\eta_c = I_{nominal} - \frac{I_{cell}}{I_{nominal}} \quad (3.5)$$

The important performance characteristics of a zinc electrode include the cycle life, which is a function of its capacity retention in relation to cycle number, the capacity itself, which is determined by the zinc utilization, and the coulombic efficiency, which is affected by the current losses caused by parasitic side reactions such as the HER [28].

The cell potential E_{cell} is lower than the equilibrium cell potential E_{cell}^e because of several losses within the cell (see equation 3.6): the overpotential losses $\sum \eta$ of both electrodes and the ohmic losses $\sum(I \cdot R)$ in the electrolyte, the electrode materials and - if present - the membrane or separator. Due to the flowing electrolyte the ohmic losses can be bigger than in static batteries resulting from the less compact electrode arrangement [50]. $\sum \eta$ is the sum of activation overpotential (electrode kinetics including charge transfer) and the mass transport overpotentials, each for positive and negative electrode. Figure 3.10 shows the polarization curves, *i.e.* current-potential curves, for ORR and OER of the air electrode with the three respective regions marked with A, B and C. In addition, the power density of the air electrode during discharge, calculated by multiplying potential and current density as well as the voltage efficiency of the air electrode (discharge potential divided by charge potential) is shown.

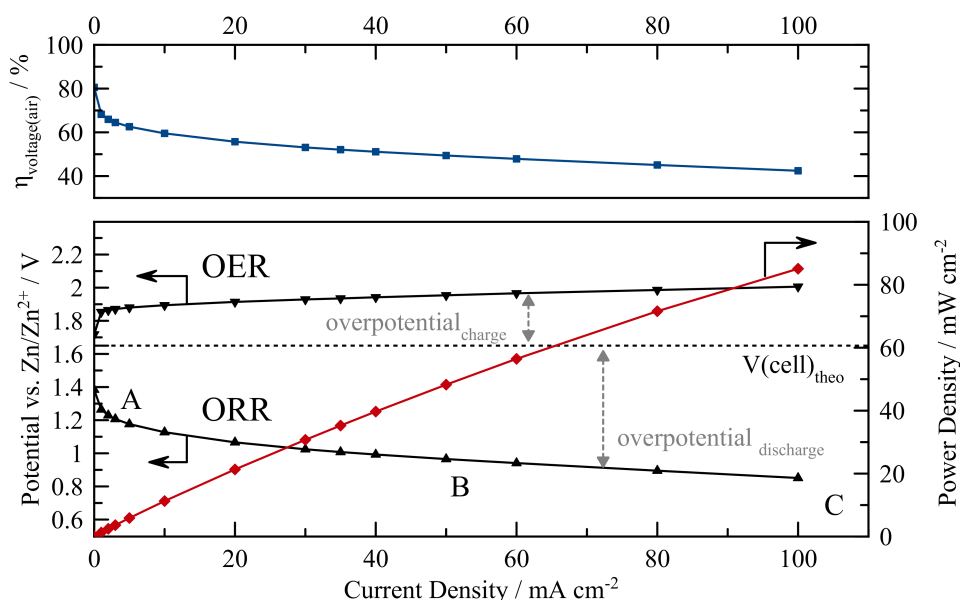


Figure 3.10: ORR and OER polarization curves with power density and voltage efficiency of the air electrode at various current densities. **A** marks the activation loss region, **B** the ohmic loss region and **C** the mass-transport limited region, which is beyond the recorded current densities (own data, adapted from [28]).

In case of the zinc-air flow battery, the activation overpotentials for oxygen electrocatalysis are significantly larger than of the zinc electrode. Nevertheless, it can be important to obtain polarization curves for both electrodes separately, in order to determine in which control regime (charge transfer, mixed or mass transport) each reaction is. Both half-cells should be charge transfer controlled, because mass transport limitations can result in local depletion of active materials. Also, under mass transport control the performance of the cell is highly dependent on the electrolyte flow rate [50].

$$E_{cell} = E_{cell}^e - \sum \eta - \sum (I \cdot R) \quad (3.6)$$

Whereby the equilibrium cell potential E_{cell}^e is determined by the choice of redox reactions and the thermodynamics and can be calculated with the standard cell potentials of each half cell (anode and cathode) as in equation 3.7. $E_{cathode}^e$ and E_{anode}^e can each be separately calculated by the Nernst equation (only the cathode equation shown in equation 3.8) with the standard potential $E_{cathode}^0$ (at standard conditions) [50].

$$E_{cell}^e = E_{cathode}^e - E_{anode}^e \quad (3.7)$$

$$E_{cathode}^e = E_{cathode}^0 - \frac{2.303RT}{zF} \cdot \log \left(\frac{c_{ox}}{c_{red}} \right) \quad (3.8)$$

For comparison of different flow cells and systems the volumetric energy density [Wh dm⁻³] at constant current and considering the total volume V_{tot} of the system can be calculated according to equation 3.9 [50].

$$E_v = \frac{E_{cell} \cdot I \cdot t}{V_{tot}} \quad (3.9)$$

The electrochemically converted material over time can be calculated using Faraday's law (equation 3.10) with ϕ , the current efficiency. This equation can be used for calculation of the dissolved/deposited amount of zinc and thus the capacity of the cell [50].

$$\frac{dn}{dt} = \frac{\phi \cdot I}{z \cdot F} \quad (3.10)$$

A zinc-air flow battery is operated in a limited concentration span due to the low solubility of the zincate ($\text{Zn}(\text{OH})_4^{2-}$) in alkaline electrolyte. For example, if the electrolyte concentration varies between 0.2 M zincate in charged state and 0.5 M zincate in discharge state, 0.3 mol L^{-1} are available for cycling. That means, that a zinc-air flow battery providing an energy of 1 kWh ($1000 \text{ A} \cdot 1 \text{ h}$ if the discharge cell voltage is 1 V) requires an electrolyte volume of 56 L according to the calculations in equation 3.11 using Faraday's law (current efficiency ϕ is estimated to be 0.9 due to parasitic side reactions).

$$m_{\text{Zn}} = \frac{\phi \cdot I \cdot t \cdot M_{\text{Zn}}}{z \cdot F} = \frac{0.9 \cdot 1000 \text{ A} \cdot 3600 \text{ s} \cdot 65.38 \text{ g mol}^{-1}}{2 \cdot 96485 \text{ A s mol}^{-1}} = 1098 \text{ g}_{\text{Zn}} \quad (3.11)$$

1098 g_{Zn} correspond to 16.9 mol zinc, which is cycled between charge and discharge. As the concentration varies by 0.3 M this corresponds to 56 L. Overall the zinc-air system has an energy density (only considering the tank volume and not the volume of the stack) of 18 Wh L^{-1} . Assuming a zinc electrode area A of 200 cm^2 the thickness of the (uniformly) deposited zinc layer in the charged state can be calculated using the density of zinc (7.14 g cm^{-3}) according to equation 3.12.

$$d_{\text{Zn}} = \frac{m_{\text{Zn}}}{\delta \cdot A} = \frac{1098 \text{ g}_{\text{Zn}}}{7.14 \text{ g cm}^{-3} \cdot 200 \text{ cm}^2} = 0.77 \text{ cm}_{\text{Zn}} \quad (3.12)$$

As the rechargeable zinc-air flow battery can be only discharged with 0.05 A cm^{-2} at 1 V, this cell theoretically delivers 10 A, which corresponds to 10 W. Thus, for an energy output of 1 kWh it has to be discharged for 100 h. This calculations are in good accordance with the specification values reported by Amunátegui et al. [51] as listed in table 3.3 in section 3.2.4.

Electrochemical testing of zinc-air batteries can be done with various methods, whereof galvanodynamic polarization (current-potential curves) and galvanostatic cycling (repeated alternating charging and discharging) are the most common ones. There are no standardized charge/discharge cycling conditions, which makes the comparison of the various results found in literature rather difficult. Testing parameters include the choice of discharge/charge current density (with or without charging pulses), the number of cycles and the duration of each cycle, and if there is a cut-off voltage or not [28]. Short cycles (duration approximately 200 s per cycle) give information on the responsiveness of the system and are usually limited by the air electrode as only a small fraction of the capacity of the zinc electrode is discharged. Due to the fast changes, stable voltages are often not reached. In contrast to this, long cycles allow evaluation of the real charge capacity

retention of the zinc electrode as a much higher zinc fraction gets dissolved and redeposited. Also, more stable voltages are reached and information for application in long-term storage is gained. When a cut-off voltage is set, assessment of the zinc electrode's capacity in each cycle is possible (coulombic or current efficiency) [28].

For example, the zinc-air cell tested in this work employed electrodes with a size of 4 cm² and had an electrolyte volume of 0.5 L with a concentration of 0.5 M ZnO. If cycled between 0.5 M and 0.2 M, 0.125 mol of Zn are available for cycling, which corresponds to 8.2 g zinc (M = 65.38 g mol⁻¹). Using Faraday's law in equation 3.10 (assuming 100% conversion efficiency), this cell has a nominal capacity of 6.7 Ah. In addition, also using Faraday's equation, the conversion time with a current density of 50 mA cm⁻² (= 0.2 A) can be calculated:

$$t = \frac{n \cdot z \cdot F \cdot}{I} = \frac{0.125 \text{ mol} \cdot 2 \cdot 96485 \text{ A s mol}^{-1}}{0.2 \text{ A}} = 120\,606 \text{ s} = 33.5 \text{ h} \quad (3.13)$$

That means that in 1 h only 0.004 mol Zn are converted (= 0.24 g), which corresponds to a fraction of only 3%. That means that it would have been very easy to test larger sized electrodes (*i.e.* apply higher currents) with this set-up without completely depleting the available zinc.

In addition, it is very beneficial to separately monitor the respective half-cell potentials of air and zinc electrode, respectively, beside the cell voltage. With this further insight on the (failure) mechanisms within the cell can be allocated and problems more easily detected [146]. For this, a third reference electrode is needed. In literature the Hg/HgO reference electrode is the most widely applied due to its good stability also in highly alkaline solutions. Another is the reference hydrogen electrode (RHE), which was also applied in this work and is especially convenient in aqueous systems as it directly references to the hydrogen evolution/oxidation potential. Also utilized in this work, was pure zinc as reference electrode. It has a low polarizability and is generally stable in alkaline electrolyte, rendering it a suitable substitute for Hg/HgO reference electrode [28, 146].

Concerning the zinc electrode, charging the cell with pulsed currents has been proven to be beneficial for achieving more compact and less dendritic zinc morphologies, because the pauses with no current give time for the zinc ions to diffuse to the electrode [62, 63, 65, 147]. The time of the pulse, the pause as well as the ratio between them can be optimized. Thus, especially in a flow system, a fine balance between electrolyte flow velocity and duty cycle γ , which is defined as t_{puls} divided by $(t_{puls} + t_{pause})$, has to be found [62, 147]. Although investigations were carried

out regarding the behavior of zinc during these conditions, for example by the project partners Zelger *et al.* [63] or by Wang *et al.* [65, 147], the impact of the pulse interrupt charging method on the performance of the air electrode has never been tested. For example, when the pause with no current is very long in comparison to the pulse length, the pulse current density has to be increased accordingly in order to reach the targeted mean current density. If the pause is 100 ms and the pulse 50 ms (duty cycle $\gamma = 0.33$) the applied current densities have to be tripled. When these high current densities are applied on the air electrode during charging, more severe corrosion effects or increased mechanical degradation due to a more pronounced oxygen formation is possible. To investigate these effects and to evaluate, if this pulse interrupt charging method is applicable for operation of a full zinc-air flow battery, was one of the scopes of this thesis as described in section 5.

4 Experimental

4.1 Catalyst Synthesis

Synthesis of $\text{La}_{0.6}\text{Ca}_{0.4}\text{CoO}_3$ via sol-gel process (according to Müller *et al.* [148])

In a 1 L round-bottom flask 9.3 g of water-free citric acid are dissolved in 48.4 mL ultrapure water (1 M solution). 6.17 g (14.25 mmol) $\text{La}(\text{NO}_3)_2 \cdot 6 \text{H}_2\text{O}$, 2.29 g (9.68 mmol) $\text{Ca}(\text{NO}_3)_2 \cdot 4 \text{H}_2\text{O}$ and 7.04 g (24.2 mmol) $\text{Co}(\text{NO}_3)_2 \cdot 6 \text{H}_2\text{O}$ are added. The solvent is slowly evaporated under stirring at 80 °C until the pink solution turns to a gelled consistency. The gel is slowly heated in the muffle furnace to 200 °C within two 2 h (major volume increase) and then kept at 200 °C for 18 h (air, no active gas supply). The resulting fluffy, black-violet, dry powder is ground in a mortar and the calcined in a tube furnace for 2 h at 700 °C (heating rate 10 °C min⁻¹) with synthetic air supply. The yield was 4.6 g (92%).

Synthesis of LaNiO_3 via sol-gel process (according to Ma *et al.* [114] and Müller *et al.* [148])

In a 500 mL round-bottom flask 7.82 g of water-free citric acid are dissolved in 41 mL ultrapure water (1 M solution). 8.82 g (20.4 mmol) $\text{La}(\text{NO}_3)_2 \cdot 6 \text{H}_2\text{O}$ and 5.92 g (20.4 mmol) $\text{Ni}(\text{NO}_3)_2 \cdot 6 \text{H}_2\text{O}$ are added to the solution, which is slowly evaporated at 80 °C using an oil bath under vigorous stirring. The resulting green gel is heated to 200 °C in a muffle furnace within 3 h and then kept at 200 °C for another 3 h. The fluffy dry powder is ground in a mortar and calcined at 900 °C in air atmosphere in the muffle furnace (heating rate 10 °C min⁻¹) for 10 h. The yield was 4.8 g (96%).

Synthesis of 20 wt% Ag + 10 wt% MnO_2 supported on carbon nanofibers (CNF)

In a 250 mL round-bottom flask, 1.75 g of CNF are dispersed in 100 mL ultra-pure water with 5 mL 2-propanol using an ultrasonic probe. 0.785 g (4.64 mmol) AgNO_3 and 0.455 mg (2.88 mmol) KMnO_4 are added to dispersion, which is ultrasonicated for another 10 min. Then the solvent is slowly evaporated under vigorous stirring at 70 °C on the heating plate. The product is ground

to powder and heat-treated in the tubular furnace at 400 °C in N₂ atmosphere for 2 h (heating rate 5 °C min⁻¹). The yield was 2.6 g (105%, impurities probably caused by K⁺ residues).

Synthesis of NiCo₂O₄ via dip-coating process (according to Price *et al.* [100])

The precursor solution is prepared by dissolving 14.5 g (25.0 mmol) Ni(NO₃)₂ · 6 H₂O and 29.1 g (50.0 mmol) Co(NO₃)₂ · 6 H₂O in ultrapure water/2-propanol 1:1 (v:v) in a 50 mL volumetric flask obtaining concentrations of 1 M for Ni and 2 M for Co, respectively. The nickel cloth support is dipped into the solution for 1-2 min, dripped off, and calcined in the preheated muffle furnace at 375 °C in air atmosphere for 10 min. The electrode is thereby placed horizontally at the edges on a rack, so that the calcination can take place on both sides of the electrode. After cooling, the electrode is dipped into the impregnation solution again, and the whole process repeated another two times (overall three rounds of dip-coating). During this process, the electrode becomes black and coarse. Final calcination is done at 375 °C in air for 3 h.

Batch-synthesis of NiCo₂O₄ without support

In a 250 mL beaker 7.27 g Ni(NO₃)₂ · 6 H₂O and 14.55 g Co(NO₃)₂ · 6 H₂O are dissolved in 50 mL ethanol. The solution is stirred and the solvent is slowly evaporated. The dark red, dry salt is ground to powder and calcined in the tubular furnace for 20 h at 375 °C with synthetic air supply for removing nitrous gases (heating rate 5 °C min⁻¹). Yield was 6.05 g (100%, probably inhomogeneous Ni and Co oxidation products).

Synthesis of NiCo₂O₄ on nickel powder

In order to increase the catalytic surface area as well as the electrical connectivity of the NiCo₂O₄ spinel, it is directly synthesized on the nickel powder support (30 wt% catalyst on support). 3.5 g nickel powder is ultrasonically dispersed in 50 mL ethanol and 50 mL ultra-pure water in a 250 mL round bottom flask. 1.81 g Ni(NO₃)₂ · 6 H₂O and 3.63 g Co(NO₃)₂ · 6 H₂O are added to the dispersion and the solvent slowly evaporated at 80 °C using a mechanical stirrer for vigorously stirring the dispersion without any magnetic parts. The dry powder is ground in a mortar and calcined in the muffle furnace at 375 °C for 2 h in air atmosphere (heating rate 5 °C min⁻¹). Yield was 4.9 g (99%).

Synthesis of NiCo₂O₄ on carbon nanofiber support

3.5 g of carbon nanofibers are dispersed with an ultrasonic probe in 200 mL ultrapure water/ethanol 1:1 (v:v) for 30 min. Then 1.81 g Ni(NO₃)₂ · 6 H₂O and 3.63 g Co(NO₃)₂ · 6 H₂O are added to the dispersion. The solvent is slowly evaporated at 80 °C under vigorous stirring. The black powder is ground to powder and calcined in the muffle furnace at 375 °C for 2 h in air

atmosphere (heating rate $5\text{ }^{\circ}\text{C min}^{-1}$) Yield was about 70-80% due to carbon decomposition to CO_2 . The decomposition is probably catalyzed by the high temperatures and the metal particles. The catalyst on the support needs to be therefore calculated again and is in the range of 40-50 wt% NiCo_2O_4 on CNF.

Homogeneous dispersion of commercial $\text{La}_{0.6}\text{Sr}_{0.4}\text{Co}_{0.2}\text{Fe}_{0.8}\text{O}_3$ on CNF support

$\text{La}_{0.6}\text{Sr}_{0.4}\text{Co}_{0.2}\text{Fe}_{0.8}\text{O}_3$ was commercially acquired from Sigma-Aldrich. For a better distribution of the fine powder on the electrically conductive support and for breaking up the coarse CNF particles, the catalyst is premixed with the CNF using ultrasonication. 3.75 g $\text{La}_{0.6}\text{Sr}_{0.4}\text{Co}_{0.2}\text{Fe}_{0.8}\text{O}_3$ were added to 1.25 g CNF in 100 mL ultrapure water and 100 mL 2-propanol. The suspension is ultrasonicated for 1 h using the ultrasonic probe without any cooling. Then the solvent is then slowly evaporated over about 10 h at $80\text{ }^{\circ}\text{C}$ on the heating plate with vigorous stirring. When it is dry enough that the stirrer stops mixing, the product is mixed by hand and completely dried in the $80\text{ }^{\circ}\text{C}$ drying compartment. The fine product is finally ground in a mortar.

4.2 Electrode Manufacture

In principle, for all manufactured electrodes presented in this work the respective catalysts are mixed together with additives such as carbon nanofibers and nickel powder and PTFE (suspension) as hydrophobic binder material (in the range of 10-30 wt%). But also gas diffusion layers (GDE) without catalyst consisting of carbon/PTFE and/or nickel powder/PTFE can be prepared this way. As solvent a 1:1 (v:v) mixture of ultrapure water/2-propanol is added with about 10 ml per g paste. The paste is stirred until a dough-like consistency is obtained and all the material is clumped together but still soft enough for forming about 1.5 mm thick sheets. The mixing process is accelerated by frequently heating the mixture in a $80\text{ }^{\circ}\text{C}$ drying chamber with repeated stirring in between. If clear supernatant solvent remains it can be decanted. The resulting paste is then further processed depending on the utilized current collector material (see the three sections below). For this, the current collector is cut into appropriate sizes. For the standard 4 cm^2 electrode holder used in the project, it is a 3 cm broad piece with a length of about 8-12 cm (so that a large enough current collector piece remains protruding out of the cell for clamping of the cables). On cutouts with this size, the lower 4 cm are then coated with catalyst paste. Another option is to increase the amount of paste as well as the current collector size and then cut the finished electrode into appropriate pieces. This method allows direct comparison of the same electrode at different operating conditions.

After drying overnight between two pieces of filter paper weighed down with half kilogram weights, the electrode is pressed at 150 kg cm^{-2} for 20 - 30 min. In addition, improved performances are achieved by performing the pressing step at high temperatures of $300 \text{ }^\circ\text{C}$ due to softening of the PTFE material and decomposition of the emulsifier contained in the suspension. For this, the electrode is put between two steel plates and several layers of non-sticking aluminum foil (for preventing detachment of the electrode paste from the current collector).

Electrodes on Nickel Cloth

For the utilization of fine-meshed nickel cloth as current collector, a catalyst or GDE suspension instead of a paste has to be used, as a too dense paste does not stick on the material. The paste is applied portion-wise onto the cloth, dried in between and then finally pressed. These electrodes are very dense and thin with a thickness of about 0.3 mm. Additional coating of this electrode with the dip-coating process as described in section 4.1 can be done. Electrodes E4, E6 and E9 were manufactured with nickel cloth as current collector.

Electrodes on Nickel Mesh

The catalyst paste is cross-rolled using a 20 kg cylinder drum. For this the paste is repeatedly rolled to a thickness of 1.5 mm, rolled together, turned by 90° and then rolled again to 1.5 mm. This is performed several times until the sheet has no apparent holes or inhomogeneities. A piece of nickel mesh is placed onto one half of the electrode paste sheet, folded in half so that the mesh is in the middle and then again rolled down to 1.5 mm or 1.0 mm. The electrode is dried overnight and press-sintered. Electrodes E7, E10, E13, E15, E16, E17, E18, E20, E22, E_{Pt} were manufactured with nickel mesh as current collector.

Electrodes on Nickel Foam

This manufacturing process is the most widely applied method in this thesis as it is straightforward, results in homogeneous electrodes without holes and can be easily up-scaled up to minimum 100 cm^2 (see Figure 4.1). In addition, two different electrode pastes can be used, optimized for each side of the nickel foam. The soft pastes are applied onto the foam using a spatula and evenly spread and slight pressed into the foam. For larger electrodes, the pastes are cross-rolled prior to spreading to about the size of the nickel foam in order to obtain more uniform amount of paste over the whole electrode area. About 1 - 1.5 g of the dry catalyst/support/PTFE mixture per 25 cm^2 for larger sized electrodes or about 30–40 mg per 1 cm^2 for the small electrodes is applied onto the nickel foam. After drying overnight, the electrodes are press-sintered. Electrodes E1,

E3, E28, E25, E26, E32, E34, E36 and all numbers \geq E37 were manufactured with nickel foam as current collector.



Figure 4.1: Image of five 100 cm² sized air electrodes after manufacture.

Attachment of additional hydrophobic backing layers onto the air electrodes is either done directly at the press-sintering step by just placing a fitting sheet onto the electrode or during a post-sintering step after the first press-sintering at 300 °C. This needs to be done for materials, which are degraded by 300 °C temperature. For this, the backing material, for example 0.2 mm PTFE filter foil, is press-sintered onto the already once press-sintered air electrode at 200 °C at 150 kg cm⁻² for 20 min.

More details on electrode manufacture as well as images of the electrodes can be found in the three publications in Appendix B.

4.3 Test Cells and Electrochemical Characterization

In-situ electrode testing

The air electrode are mounted in custom-made PMMA electrode holders using an alkali-resistant polymeric sealing material (wedi) leaving open a 2x2 cm area in the small cells (see Figure 4.2 (left)) and a 4x4 cm in the larger sized in-house made cells (16 cm²). The same area is open on the backside for gas supply (either a closed chamber or open set-up) The electrode holders are screwed together with fittingly cut EPDM sealings (1 mm thickness) as can be seen in Figure 4.2 (middle). The blue test cell with 100 cm² electrode sizes shown in Figure 4.2 (right) was designed and provided by the *Luziflow* cooperation partner Hans-Jürgen Pauling from the German company RECAT GmbH. The set-up was adapted for operation of 50-60 cm²-sized

electrodes and for measurements with active gas supply (additional closed compartment attached to the blue cell) as is further described in section 5.6.3.

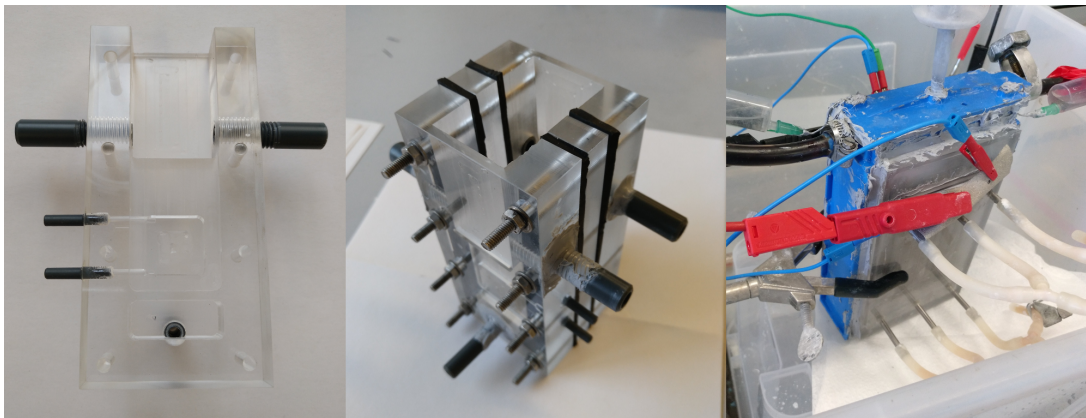


Figure 4.2: Images of the two flow test cells: left image - electrode holder with 2 x 2 cm left out space for attachment of the electrode; middle - assembled small flow cell; right - assembled 100 cm² blue test cell.

All long-term electrochemical tests are performed on a BaSyTec Test Cell System (CTS Lab) with 32 separate channels and corresponding software from the company BaSyTec (Germany) as shown in Figure 4.3. Air electrodes are always measured in a three-electrode set-up with a working electrode (*i.e.* air electrode), a counter electrode (either a stainless steel plate, a second air electrode or a zinc electrode) and a reference electrode. Up to electrode E37, the air electrodes are referenced against a Gaskatel reference hydrogen electrode (RHE) in the three-electrode set-up. Later on, this is changed to zinc as reference with the addition of zinc oxide to the electrolyte. Because of the constant zinc concentration within the test cell, a zinc plate can be used as first order electrode (vs. Zn/Zn^{2+}). As zinc reference about 1 x 8 cm pieces of zinc foil are utilized. The referencing is done via Luggin capillaries. Metal cannulas are implemented as Luggin capillaries, which are bend so that the opening is a few millimeters in front of the electrode surface. The reference electrodes are then put into the connected open syringe cases as can be seen in the images in Figure 4.4.

As electrolyte either 8 M KOH or 8 M KOH with 0.5 M ZnO is utilized. The air electrodes are either actively supplied with oxygen/air via an inlet and outlet through a closed compartment (no flow fields) or are open on the backside to the ambient air with no active gas supply. To counter the hydrostatic pressure from the electrolyte inside the cell, the air outlet from the closed compartment is put into 10-15 cm of water to apply a slight pressure onto the air electrode. The

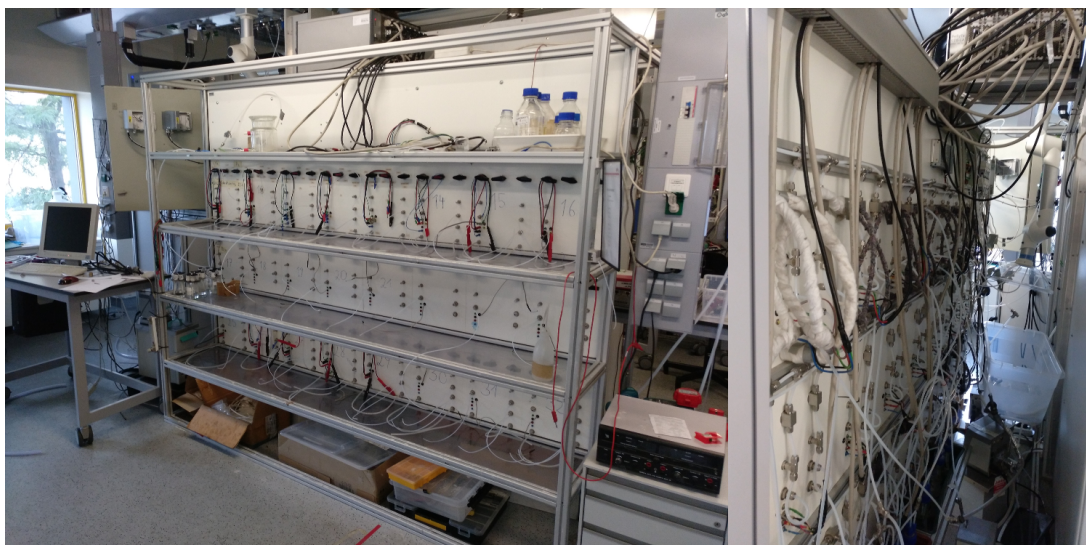


Figure 4.3: Images of the BaSyTec test rig: left image - side front view with computer, 24 fixed test places with valves and electric plugs and 8 mobile test places (free cables), potentiostat at the top, power supply for DC pump on the right; right image - view of the backside with gas supply, and heated water supply from the Julabo thermostats (bottom).

air electrode is either supplied with pure oxygen (5 mL min^{-1}), synthetic air (SA; 80% N_2 / 20% O_2 , 25 mL min^{-1}) or pressurized air from a compressor (CA; 25 mL min^{-1}).

Measurements are performed at lab temperature (20 – $27 \text{ }^\circ\text{C}$) or at 35 – $40 \text{ }^\circ\text{C}$ by indirect heating using warmed water from the Julabo thermostat, which is pumped through steel tubes immersed in the electrolyte. Electrolyte flow is generated by a centrifugal DC pump (completely made from plastic materials), which is controlled via a power supply (see Figure 4.3 (left image)). In the small flow test set-up in the configuration as seen in Figure 4.4 (left) the achieved flow is 5.5 cm s^{-1} or 1.4 L min^{-1} at 7 V , 6.0 cm s^{-1} or 1.6 L min^{-1} at 9 V and 8.0 cm s^{-1} or 2.1 L min^{-1} at 12 V , respectively. In the blue test cell the small in- and outlets allow only flow rates of 1.5 – 2 cm s^{-1} , which were obtained at voltages of 4 – 5 V .

Images of the small flow test cell and bigger flow set up are depicted in Figure 4.4. A schematic of the test set-up and further description can be found in the three publications in Appendix B. Images of the test cell, which was open at the backside can be seen in section 5.4.2 in Figure 5.14 and more images of the blue test cell are depicted in section 5.6.3 in Figure 5.23.

Electrochemical characterization is done in galvanostatic mode by recording the potentials. Measurements consist commonly of "activation" cycling at the beginning with increasing current density over time, the recording of galvanostatic polarization curves each for OER and ORR and

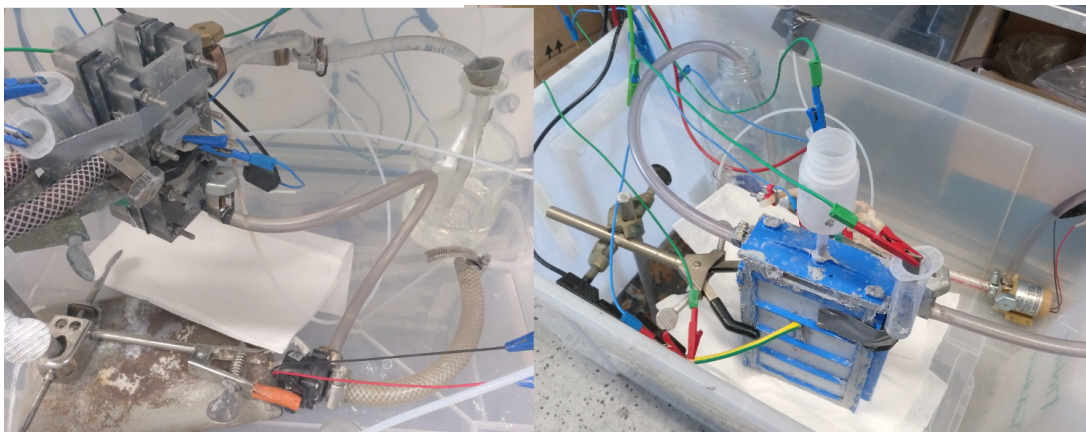


Figure 4.4: Images of the two flow test set-ups: left - small scale with 0.5 L reservoir and open cell; right - closed blue 100 cm²-sized test cell with 1 L reservoir.

the long-term cycling at fixed charge/discharge current densities. In addition, charging using pulse interrupt currents (*i.e.* pulse charging) is carried out according to Zelger *et al.* [63]. Two different modes are tested: (i) tripled pulse currents *e.g.* 150 mA cm⁻² pulse for 50 ms followed by 100 ms pause with no current (duty cycle $\gamma = 0.3$, 24.000 pulses per 1 h) or (ii) doubled pulse currents *e.g.* 100 mA cm⁻² pulse for 50 ms followed by 50 ms pause (duty cycle $\gamma = 0.5$, 36.000 pulses per 1 h). A few, often applied BaSyTec Test Protocols for recording of polarization curves and long-term charge/discharge cycling can be found in Appendix A.

Cyclic voltammetry using rotating disk electrodes (RDE)

RDE measurements are performed on a Gamry potentiostat with a rotator and corresponding software. Always 10 μL catalyst ink are deposited onto the disk of the 0.196 cm² electrode. The catalyst ink is prepared according to Abidat *et al.* [88]. For getting 0.072 mg cm⁻² loading of NiCo₂O₄ spinel catalyst on the RDE, the catalyst ink contains 9.2 mg of 49 wt% NiCo₂O₄/CNF homogeneously dispersed in 2.1 mL ultrapure water, 0.9 mL 2-propanol and 180 μL 5 wt% Nafion solution as binder. In the Ni powder ink, 4.5 mg Ni powder and 4.7 mg CNF are dispersed in the same amount of ultrapure water/2-propanol/Nafion. The inks are dispersed for 45 min in an ultrasonic bath. 10 μL of the ink are deposited in two 5 μL portions onto the electrode tip and dried while rotating the tip. Measurements are performed in 1 M KOH (Titrisol) at 30 °C. As reference, a reference hydrogen electrode (RHE by Gaskatel), and as counter electrode, a platinized titanium rod is utilized. The scan rate is 10 mV s⁻¹. The inner resistance of the electrolyte and the set-up was 5-9 Ω . The electrolyte is either flushed with N₂ or O₂ for 20 min before starting the measurement. The minimum and maximum potentials are 0.1 V (min.) and

1.1 V or 1.55 V vs. RHE (max.), respectively. ORR curves are always baseline corrected by the base CV curves in N₂.

The measurement protocol is:

- O₂-flushed: ORR curves recorded at 600, 900, 1200, 1600 and 2000 rpm (2 cycles each)
- N₂-flushed: Base CV (3 cycles)
- O₂-flushed: ORR curves recorded at 1600 rpm (3 cycles)
- N₂-flushed: Base CV (7 cycles)
- O₂-flushed: ORR curves recorded at 1600 rpm (3 cycles)
- N₂-flushed: Base CV (10 cycles)
- O₂-flushed: ORR curves recorded at 1600 rpm (3 cycles)

5 Results and Discussion

5.1 Project Outline

In the course of this thesis several different oxide-type catalysts – perovskites as well as spinels – were investigated with special focus on their implementation in an optimized air electrode design. 4 cm^2 ($2\text{ cm} \cdot 2\text{ cm}$) was chosen as standard electrode size in nearly all electrochemical tests. In the first stage of the project *Luziflow*, a broad variety of different catalysts, support materials as well as manufacturing methods were tested, including dip-coating and cross-rolling on nickel foam, nickel mesh and nickel cloth as current collector materials. In addition, PTFE binder in form of solid powder as well as in suspension was tested, whereby the suspension soon proved to be better suitable to achieve a more homogeneous distribution and was utilized for nearly all electrodes. The target current density was $\pm 50\text{ mA cm}^{-2}$, and nearly all electrodes were cycled during long-term operation at this current density. However, at the beginning of the project, the achieved current density was much lower so that 20 mA cm^{-2} or 30 mA cm^{-2} is used for comparison of the first tested electrodes. Also, nearly from the start of the project pulse charging tests were performed for investigation of the charging behavior of the electrodes at high and fluctuating currents.

A selection of a few promising and interesting results of the first electrodes (up to electrode number E34) summarized as "preliminary tests" is described in section 5.2. At the beginning of the project many different parameters for manufacturing bifunctional air electrodes were investigated but it was generally hard to distinguish all the effects resulting in good or bad performance. The causal relationship between manufacturing method, used materials, amount of utilized materials, as well as inherent catalytic activity of the catalyst, was not always straightforward. However, in conclusion to the first experiments the results showed that with perovskite-type catalysts good ORR performances during discharge and with NiCo_2O_4 spinel high catalytic OER activities during charge were achievable. Also, from the three different nickel current collector materials

(nickel mesh, nickel foam and nickel cloth), nickel foam - although comparably costly - proved to be mechanically the most stable material, providing high stability for the catalyst paste and good electrical conductivity throughout the electrode. Thus, electrodes catalyzed with the two oxide catalysts were investigated as described in section 5.3. These results were summarized in a first publication in *Electrochimica Acta*. Within this publication, physical characterization by XRD, SEM and EDX of the synthesized NiCo_2O_4 catalyst is presented.

As the results of the electrodes with nickel foam as current collector were promising regarding their stability, the main focus during the project lay on this type of current collector material. Nevertheless, it has to be mentioned that nickel mesh was still investigated as the less costly alternative to nickel foam. The results of many of those electrodes is summarized in the diploma thesis by Lucas Rešćec titled *Bifunctional air electrodes catalyzed with nickel-cobalt-oxide for application in zinc-air redox flow batteries*.

In continuation to the successful manufacture of stable bi-catalyzed bifunctional air electrodes (achieving on average about 700 h of operation) the operating conditions were investigated. Foremost, the stability of these electrodes during flow operation with electrolyte flow rates of up to 8 cm s^{-1} were studied. For this, a new test cell and set-up were built, which is described in more detail in the bachelor thesis of Nikolaus Rauch titled *Analyse von bifunktionalen Elektroden in Zink-Luft Batterien*. Further tests, including variation of gas supply (active, passive), electrolyte molarity as well as size (up-scaling to 16 cm^2 and then to 100 cm^2) were conducted. In collaboration with the *Institute for Chemistry and Technology of Materials* (TU Graz), who investigated zinc deposition, these results were summarized in a publication in the *Journal of Applied Electrochemistry* (see section 5.4).

Because leakage of electrolyte during long operation times proved to be challenging, several different hydrophobic materials were investigated as backing layer (carbon paper, PTFE-coated glass fiber cloth and PTFE filter foils). Of these, the thin 0.2 mm PTFE filter managed to effectively block electrolyte permeation even in the closed set-up. In parallel to this, ex-situ tests of the NiCo_2O_4 spinel catalyst by means of rotating disk electrode (RDE) cyclic voltammetry (see section 5.5) revealed the insufficient stability of this catalyst towards repeated potential cycling. Moreover, comparable OER performances could be achieved by utilizing only fine nickel powder within the electrode paste. Thus, several electrodes (numbers $\geq \text{E60}$) were manufactured with $\text{La}_{0.6}\text{Sr}_{0.4}\text{Co}_{0.2}\text{Fe}_{0.8}\text{O}_3$ perovskite as the only bifunctional catalyst employed (section 5.6).

The final stage of the project and this thesis was the up-scaling to 60 cm²-sized air electrodes and unit cell operation with one air electrode and one zinc electrode. The results of these experiments are described in section 5.6.3 and summarized in a accepted peer-reviewed manuscript in a special issue in the journal *Batteries & Supercaps*.

Only the most relevant results from the project *Luziflow*, showing the most important optimization steps, are presented in this thesis. For better comparability and ease of relocating the raw data, the numbering of the electrodes was kept the same as allocated in the *Luziflow* data files and the protocol books used during the project.

5.2 Preliminary Tests of Bifunctionally Catalyzed Air Electrodes

The following section summarizes the most relevant experiments performed during the first stage of the project, where a broad variety of catalysts, current collector materials, additives, as well as manufacturing methods were investigated as summarized in Table 5.1. Through the many different variations considered and investigated for the design of a bifunctional air electrode, a principle understanding of the processes and requirements for well-performing air electrodes was gained.

Table 5.1: All utilized materials and methods (and combinations thereof), which were investigated in the first stage of the project.

| Catalysts | Current Collector | Additives | Method |
|---------------------------------------------------------------------------|-------------------|-------------------|-------------------------------|
| NiCo ₂ O ₄ (dip-coating) | Ni foam (580 μm) | Carbon (Vulcan) | Dip-coating |
| NiCo ₂ O ₄ (batch) | Ni cloth | Carbon nanofibers | Cross-rolling/pressing |
| La _{0.6} Ca _{0.4} CoO ₃ | Ni mesh | PTFE suspension | Cross-rolling/press-sintering |
| (La _{0.8} Sr _{0.2}) _{0.95} MnO _{3-x} | Ni foam (450 μm) | PTFE powder | Impregnating/pasting |
| LaNiO ₃ | | Nickel powder | |
| Ag–MnO ₂ | | | |

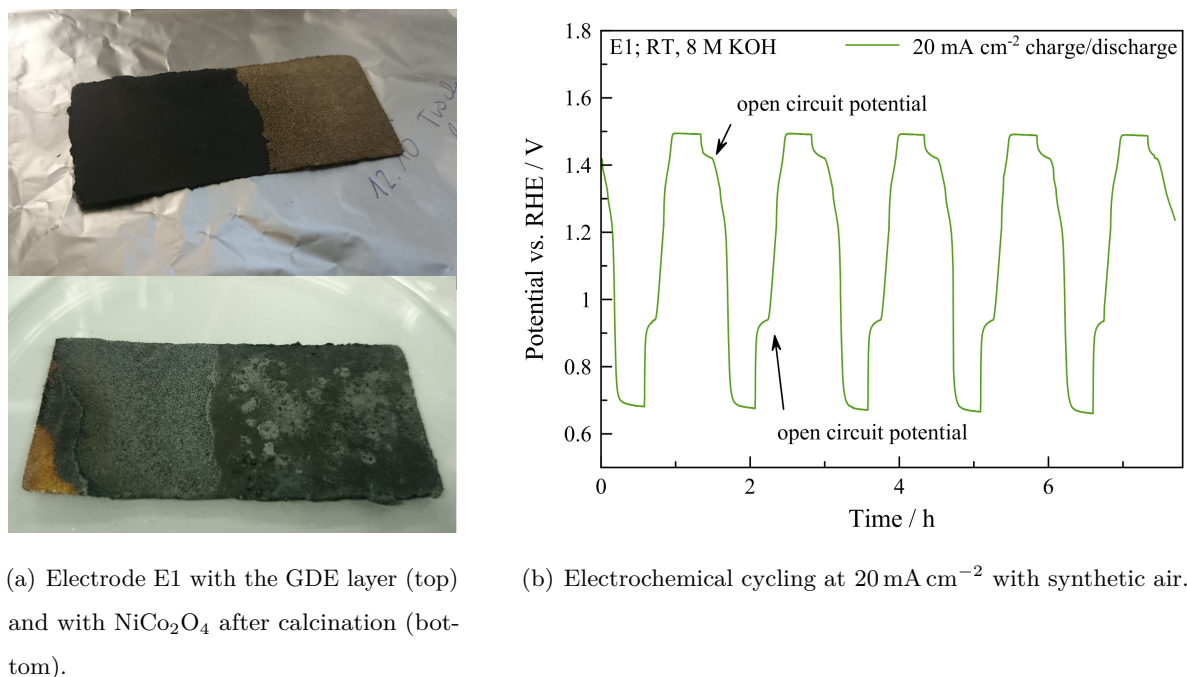
5.2.1 Dip-coated Electrodes Catalyzed with NiCo₂O₄

Direct synthesis of NiCo₂O₄ spinel was done via a dip-coating process first described by Price *et al.* [100], whereby the whole electrode, or only the current collector, was dipped into a concentrated Ni and Co salt solution and then heat-treated at 375 °C in the oven. By repeating this impregnation for 3-5 times a spinel oxide layer was grown on the electrode. Often, the product looked very inhomogeneous and coarse (see Figure 5.1(a) (bottom)), which can be attributed to the uneven distribution of the impregnation solution due to its low viscosity. Price *et al.* [100] achieved with this method about 50 h of long-term operation at 50 mA cm⁻² with a potential difference ΔV of < 1 V (however supplied with pure O₂). These electrodes were completely free of carbon material, which is a promising approach, because degradation of the electrode by carbon corrosion can be avoided.

E1 was manufactured using nickel foam (pore 580 μm) as current collector. A carbon-free gas diffusion layer (GDE) consisting of PTFE and nickel powder (1:3 weight ratio) was pasted onto the foam and then pressed at 150 kg cm⁻² (Ni loading about 80 mg cm⁻²). The pressure of 150 kg cm⁻² for pressing was deducted from the publication by Price *et al.* [100] and was kept constant throughout the whole thesis for ease of comparison. Then, NiCo₂O₄ was impregnated onto the electrode by the dip-coating method resulting in a spinel catalyst loading of 7 mg cm⁻².

The results of the electrochemical characterization of E1 are shown in Figure 5.1(b). It is apparent that at 20 mA cm⁻² stable OER potentials of 1.5 V vs. RHE were achieved, whereas the discharge ORR potential was only around 0.75 V vs. RHE (ΔV of 0.75 V). Increase of current density resulted in very low ORR potentials with a negative trend within one cycle, indicating insufficient O₂ supply. After charging, the open circuit potential (OCP) always stayed at > 1.4 V vs. RHE, which shows the oxidation of Ni in the electrode to NiOOH [34]. During discharge, NiOOH gets reduced again, so that the OCP after discharge is around 0.95 V vs. RHE.

A similar electrode to E1 was manufactured using fine nickel cloth instead of nickel foam as current collector material (E6). However, because of the finer mesh it was very challenging to properly attach the PTFE/Ni GDE layer onto it. This could only be achieved by drying the thin PTFE/Ni suspension portion-wise on the nickel cloth and then pressing the final electrode at 150 kg cm⁻². After this, the cloth was dip-coated and calcined three consecutive times to obtain the NiCo₂O₄ layer on the electrode. The electrode was operated for about 50 h but exhibited poor



(a) Electrode E1 with the GDE layer (top) and with NiCo_2O_4 after calcination (bottom). (b) Electrochemical cycling at 20 mA cm^{-2} with synthetic air.

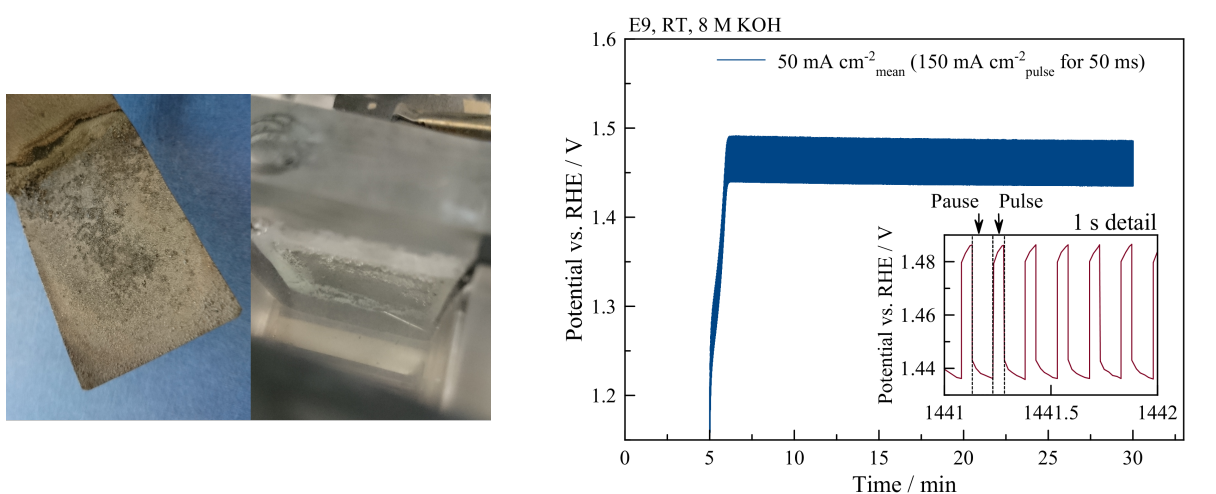
Figure 5.1: Electrode manufacture and electrochemical performance of E1.

discharge potentials. Also, because the electrode had a thickness of only 0.3 mm, it immediately leaked electrolyte after stopping the gas flow at the end of operation.

Due to low mechanical stability of the Ni/PTFE GDE layer, another electrode was fabricated (E9), which consisted of only NiCo_2O_4 dip-coated nickel cloth current collector (impregnated four times) as shown in Figure 5.2(a)(left). This electrode had a metallic appearance, but the coarse spinel catalyst attached well to the nickel cloth current collector.

E6 and E9 achieved very stable (and initially also improving) and low OER potentials even at high current densities up to 250 mA cm^{-2} with 1.62 V vs. RHE (E6) and even 1.52 V vs RHE for E9. This can be attributed to the high catalytic OER activity of all used materials, which were the nickel current collector, NiCo_2O_4 spinel catalyst as well as probably other Ni and Co oxides in the oxidation states Co^{3+} , Co^{4+} and Ni^{3+} [88]. During charging at these high current densities, vigorous oxygen bubble formation was observed as shown in Figure 5.2(a)(right) resulting in a turbid electrolyte. Nevertheless, both electrodes did not exhibit any activity toward ORR. Even at the beginning of operation (no KOH leakage observed) no stable ORR potentials could be achieved even at current densities as low as 5 mA cm^{-2} .

Figure 5.2(b) shows the results of one of the first pulse charging experiments, which were performed with electrode E9, applying 150 mA cm^{-2} pulses for 50 ms with 100 ms pause in between (duty cycle $\gamma = 0.33$). Thereby the potential remained constant over a period of 25 min at 1.49 V vs. RHE during pulse and 1.44 V vs. RHE during pause (pulse-pause gap of 0.05 V), as can be seen in the inlay in Figure 5.2(b), where a one second detail of the pulse charging is shown. Although high current densities are applied, the results suggest that the pulse charging method does not harm the electrode and that stable non-deteriorating OER potentials can be achieved.



(a) E9 electrode with NiCo_2O_4 after calcination (left) and the electrode during OER charging (right).

(b) Electrochemical pulse charging at $50 \text{ mA cm}^{-2}_{\text{mean}}$. The inlay shows a one second detail of the pulsating potentials.

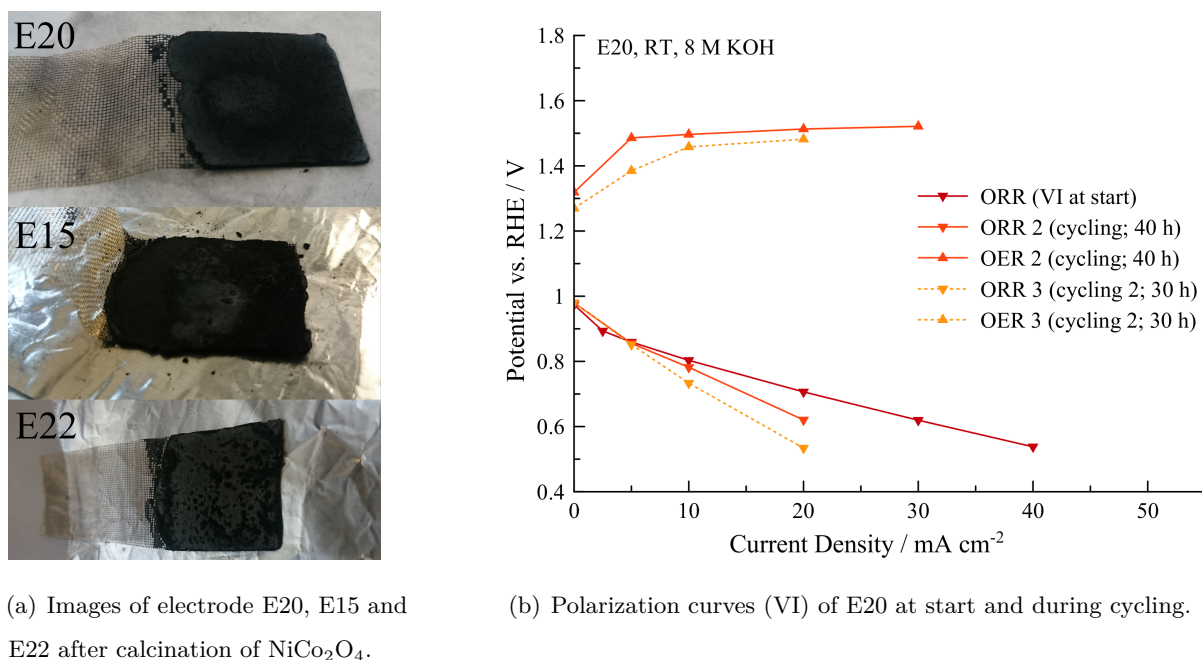
Figure 5.2: Electrode manufacture, testing and electrochemical performance of E9.

Electrode E20 was manufactured using Ni mesh as current collector, which is the least expensive of the three investigated nickel current collector materials (*i.e.* compared to Ni cloth and especially Ni foam). First, a GDE was prepared by mixing 25 wt% nickel powder, 25 wt% carbon nanofibers (CNF) and 50 wt% PTFE (overall 1.0 g). The paste was cross-rolled onto nickel mesh to a thickness of 1.0 mm, dried over night and pressed at 150 kg cm^{-2} at room temperature for 30 min. The electrode was then dip-coated and calcined with Ni/Co salts three times (with about 5 min soaking, 10 min calcination at $375 \text{ }^\circ\text{C}$). Final calcination was done for another 2 h at the same temperature in air atmosphere in the muffle furnace (see Figure 5.3(a)(top)). The thickness was 1.1 mm and NiCo_2O_4 catalyst loading was about 28 mg cm^{-2} indicating good attachment of the precursor salts in the GDE network.

CNF were added because the previously manufactured GDEs consisting only of nickel powder and PTFE were very dense and increasingly difficult to cross-roll onto Ni mesh. CNF provide a fine porous network for good gas accessibility and they exhibit at the same time a much higher corrosion stability compared to other carbon types (for example Vulcan XC72 or Black Pearls 2000 (Cabot Corporation)). The results of the electrochemical characterization of E20 as shown in Figure 5.3(b) were promising. An initially good ORR performance was obtained achieving 0.76 V vs. RHE at 20 mA cm^{-2} . This can perhaps be attributed to the added CNF fibers. The OER performance was very stable at $\sim 1.5 \text{ V}$ vs. RHE with slight improvement over time throughout the operation time of more than 50 h (including cycling at various current densities as well as a three pulse charging tests). However, in contrast to the very stable charge potentials, the ORR performance slowly decreased over the operation time as shown in the three polarization curves in Figure 5.3(b). In the activation controlled region up to 5 mA cm^{-2} no change was apparent, however in the ohmic region a significant potential decrease was observed indicating altered wetting of the electrode.

As the OER performance of the dip-coated NiCo_2O_4 was very promising with stable potentials of 1.5-1.6 V vs. RHE, two more electrodes were manufactured, both with the aim of improving the ORR performance of the electrode. E15 and E22 were manufactured both on nickel mesh as current collector (as E20) but with additionally implementing a second catalyst next to NiCo_2O_4 . E15 used a cross-rolled carbon-free PTFE (5 wt%)/Ni powder(35 wt%) paste as GDE containing 60 wt% $(\text{La}_{0.8}\text{Sr}_{0.2})_{0.95}\text{MnO}_{3-x}$ perovskite resulting in a catalyst loading about 100 mg cm^{-2} (for comparison for other electrode using this perovskite see section 5.2.3). The electrode was pressed at 150 kg cm^{-2} at room temperature. Afterwards, the whole electrode was one time dip-coated with the Ni/Co impregnation solution for 1 h, dried over night and calcined at $375 \text{ }^\circ\text{C}$ for 3 h in air atmosphere in the muffle furnace. The resulting electrode was very brittle and crumbly (see Figure 5.3(a) (middle)) and hard to attach to the electrode holder in the test cell. E22 was manufactured by cross-rolling a paste consisting of 25 wt% (30 wt% Ag-MnO₂)/CNF, 25 wt% nickel powder and a high amount of PTFE (50 wt%) in order to provide sufficient hydrophobicity (one GDE layer on nickel mesh). The electrode was dip-coated and calcined three-times exhibiting finally a silvery metallic surface (see Figure 5.3(a) (bottom)).

Although both electrodes contained a ORR catalysts with, in principal, high catalytic activity [52, 95, 149–151], no stable ORR potentials were measured indicating either complete blocking of the respective ORR catalyst by the dip-coated NiCo_2O_4 or insufficient O_2 accessibility to the active sites with no formation of three phase boundaries. Nevertheless, similarly to the results of



(a) Images of electrode E20, E15 and E22 after calcination of NiCo₂O₄.

(b) Polarization curves (VI) of E20 at start and during cycling.

Figure 5.3: NiCo₂O₄-catalyzed electrodes E20, E15 (additional (La_{0.8}Sr_{0.2})_{0.95}MnO_{3-x} perovskite) and E22 (additional Ag–MnO₂/CNF catalyst) and the electrochemical performance of E20.

E9, E15 and E22 showed good and stable OER potentials (for example E15 achieved 1.63 V vs. RHE at 250 mA cm⁻²). The results of all investigated electrodes presented in this sub-chapter are summarized in Table 5.2.

Conclusion to the Dip-coating Method for Synthesizing NiCo₂O₄

The dip-coating proved to be a practical method as it allows direct manufacture of an electrode without the need of first synthesizing the catalyst. However, this method can be only applied because of the low calcination temperature of NiCo₂O₄ catalyst of around 400 °C and it is hardly applicable for other catalysts. Perovskites, for example, have to be calcined at much higher temperatures of 600-900 °C, which is a much too high temperature for the utilized PTFE binder materials resulting in complete decomposition. Moreover, all manufactured electrodes looked very inhomogeneous as can be seen in the images of the various electrodes and the layer often proved to be very brittle. These issues can be especially problematic when manufacturing larger electrode sizes. The whole process appeared to lack reproducibility and severe damage of the electrode during the calcination process, for example small holes, could not always be avoided. Low or even no significant catalytic activity toward ORR was obtained, indicating that the

Table 5.2: Summary of NiCo₂O₄ catalyzed electrodes using the dip-coating method. Charge (OER) and discharge (ORR) potentials vs. RHE for the best performance at 20 mA cm⁻² are listed.

| Electrode | Support | OER [V] | ORR [V] | Comments |
|-----------|----------|---------|---------|----------------------------------------------------------------------------------------------|
| E1 | Ni foam | 1.492 | 0.683 | GDE (Ni powder and PTFE) |
| E6 | Ni cloth | 1.486 | - | GDE (Ni powder and PTFE) |
| E9 | Ni cloth | 1.478 | - | no GDE, only current collector |
| E20 | Ni mesh | 1.482 | 0.706 | GDE (Ni powder, CNF and PTFE) |
| E15 | Ni mesh | 1.523 | - | cross-rolled; with (La _{0.8} Sr _{0.2}) _{0.95} MnO _{3-x} |
| E22 | Ni mesh | 1.705 | - | cross-rolled; with Ag-MnO ₂ |

electrode build was still not sufficiently developed and needed much improvement. Concluding, the results show, that because of the very good catalytic activity of these electrodes toward OER during charging even at very high current densities up to 250 mA cm⁻², the dip-coating process is a viable method for manufacturing charging electrodes for example used in three-electrode zinc-air battery set-ups.

5.2.2 Air Electrodes Catalyzed with Batch-synthesized NiCo₂O₄

Another approach was to synthesize the NiCo₂O₄ spinel not directly on the electrode but first in a separate batch and incorporating it later into the electrode paste (together with PTFE binder and additives such as nickel powder and CNF). The main drawback of this method is that during batch-synthesis of NiCo₂O₄ there is less control of the product's particle size and surface area (no gelating agent such as citric acid was used in the synthesis). The results and the manufacturing of electrode E7 and E13 catalyzed with batch-synthesized NiCo₂O₄ and both cross-rolled on nickel mesh, are summarized in Table 5.3. With these two electrodes good OER potentials up to 150 mA cm⁻² were achieved, which is comparable to most of the NiCo₂O₄-catalyzed electrodes described in section 5.2.1. However, none of these electrodes exhibited any significant ORR activity. The OER potentials of <1.8 V vs. RHE were quite comparable between these two electrodes, although for the less-homogeneous appearing electrode E13, PTFE powder instead of the suspension was used. However, as this approach did not lead to satisfactory results, especially regarding ORR, it was not further pursued.

Table 5.3: Summary of NiCo₂O₄ catalyzed electrodes (both 50 wt%) synthesized by the batch method. Charge potentials (OER) vs. RHE at 20 mA cm⁻² are listed.

| Electrode | Support | OER [V] | ORR [V] | Comments |
|-----------|---------|---------|---------|---------------------------------------|
| E7 | Ni mesh | 1.539 | - | 38% Ni powder + 12% PTFE (suspension) |
| E13 | Ni mesh | 1.561 | - | 30% Ni powder + 20% PTFE (powder) |

5.2.3 Perovskite-catalyzed Bifunctional Air Electrodes

Parallel to the NiCo₂O₄-catalyzed electrodes, electrodes catalyzed with different types of perovskites were manufactured and tested. In a previous zinc-air project as well as in several publications [75, 148, 152], La_{0.6}Ca_{0.4}CoO₃ was applied as highly active bifunctional catalyst and thus was tested in two different electrodes (E3 and E4). Also, LaNiO₃ was successfully investigated and tested for bifunctional operation in several publications [114, 152–154] (E34). Both catalysts were synthesized in-house using the sol-gel method with citric acid as gelating agent. A third perovskite containing manganese on the B-site was also studied [95]. The utilized (La_{0.8}Sr_{0.2})_{0.95}MnO_{3-x} perovskite was not synthesized but acquired from the company fuelcellmaterials (USA). This commercial catalyst had a high surface area of 18.1 m² g⁻¹ and small particle sizes of d₅₀ = 0.48 μm (electrodes E10, E16, E17, E18 and E28). The results of all electrochemically characterized electrodes presented in this section is summarized in Table 5.4. The detailed manufacture of each electrode is described and discussed in each subsection.

Table 5.4: Summary of perovskite-catalyzed electrodes listing charge (OER) and discharge (ORR) potentials vs. RHE for the best performance at 20 mA cm⁻².

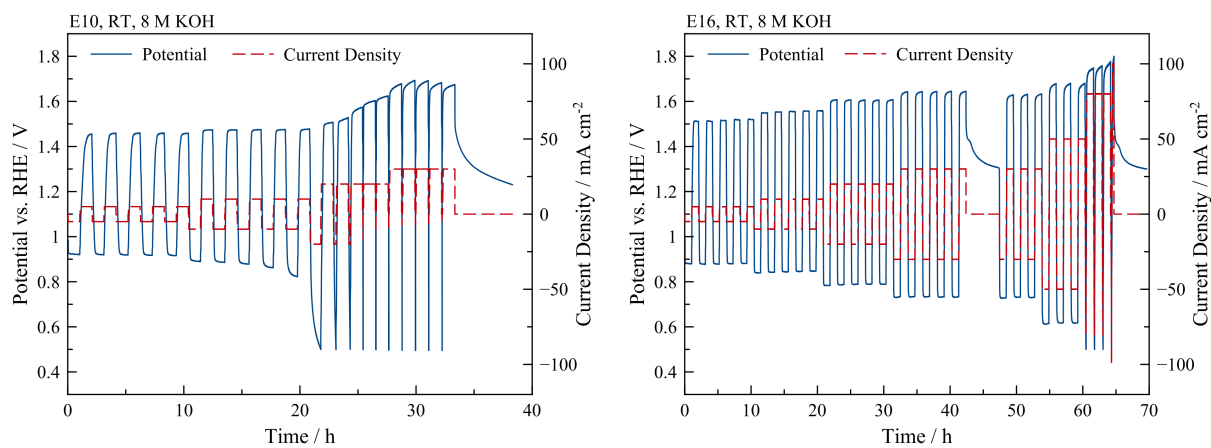
| Electrode | Support | OER [V] | ORR [V] | Comments |
|-----------|----------|---------|---------|-----------------------------------------------------------------------------|
| E3 | Ni foam | 1.486 | - | GDE (Ni powder/PTFE/La _{0.6} Ca _{0.4} CoO ₃) |
| E4 | Ni cloth | 1.518 | - | GDE (Ni powder/PTFE) + La _{0.6} Ca _{0.4} CoO ₃ |
| E10 | Ni mesh | 1.506 | - | Vulcan XC72/Ni powder/PTFE |
| E16 | Ni mesh | 1.605 | 0.790 | CNF/PTFE; sintered at 300 °C |
| E17 | Ni mesh | 1.689 | - | Ni powder/PTFE; sintered |
| E18 | Ni mesh | 1.528 | 0.782 | Ni powder/CNF/PTFE; sintered |
| E28 | Ni foam | 1.715 | 0.641 | CNF/PTFE; sintered |
| E34 | Ni foam | 1.445 | 0.597 | LaNiO ₃ , CNF/PTFE;sintered |

La_{0.6}Ca_{0.4}CoO₃

Electrode E3, utilizing the in-house synthesized La_{0.6}Ca_{0.4}CoO₃ perovskite, was similarly manufactured to E1 on nickel foam with a carbon-free PTFE/nickel powder GDE layer. The difference was the addition of 35 wt% perovskite to the suspension. The wet electrode was pressed at RT at 150 kg cm⁻² and then dried overnight. The resulting electrode had a perovskite catalyst loading of about 50 mg cm⁻². The second electrode, electrode E4 used nickel cloth as current collector material and was manufactured comparably to E6, consisting of a GDE (nickel powder/PTFE) and an active layer (AL) on top of it with nickel powder/PTFE and perovskite catalyst (45 wt%, loading 21 mg cm⁻²). Both electrodes had a smooth surface, which is in contrast to the dip-coated NiCo₂O₄ electrodes. Especially E3 exhibited in electrochemical measurements very good OER performance with 1.50 V vs. RHE at 100 mA cm⁻² and 1.53 V vs. RHE at 250 mA cm⁻² (but already fluctuating potentials due to vigorous bubble formation). Both electrodes showed very comparable performance to the similarly manufactured NiCoO₄-catalyzed electrodes E1 and E6, with good OER but very low ORR activity. This indicates that this electrode build was not suitable for obtaining good ORR performances, which is most likely because of the very dense nickel powder/PTFE (weight ratio 10:3) GDE layer preventing sufficient gas supply to the active sites.

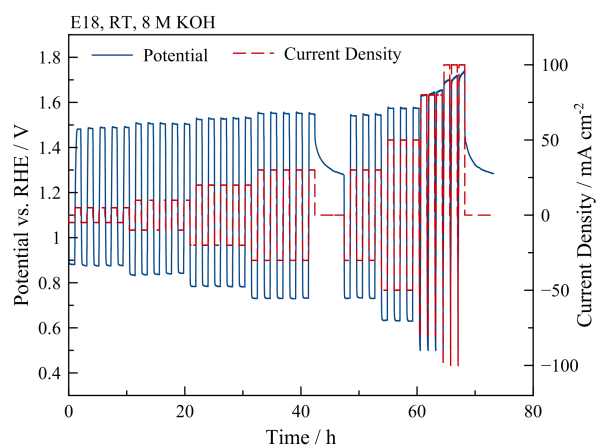
(La_{0.8}Sr_{0.2})_{0.95}MnO_{3-x}

Some of the first electrodes were manufactured with Vulcan XC72 as carbon additive. One of these was E10, utilizing 50 wt% commercial (La_{0.8}Sr_{0.2})_{0.95}MnO_{3-x} perovskite mixed together with 30 wt% nickel powder, 10 wt% PTFE (low content, thus less hydrophobic) and 10 wt% Vulcan XC72 for improving gas permeability and electrical conductivity and thus ORR activity. The paste was cross-rolled onto nickel mesh (1.0 mm) and then pressed at RT (150 kg cm⁻²). The results are shown in Figure 5.4(a). Within the first 20 h and at low current densities of 10 mA cm⁻², the electrode exhibited good ORR and OER potentials of 0.90 V vs. RHE and 1.47 V vs. RHE, respectively (first cycle). However, after that the ORR potentials as well as the OER potential deteriorated. The increasing OER potentials over time are in sharp contrast to the NiCo₂O₄ containing electrodes, who generally exhibited very stable and low OER potentials up to high current densities. The results of E10 show, that although the addition of Vulcan XC72 carbon proved to be beneficial to obtain good ORR performances, its cycling stability especially at high anodic potentials was not sufficient.



(a) Charge/discharge cycling of E10 with Vulcan XC72 carbon and nickel powder.

(b) Charge/discharge cycling of E16 with CNF.



(c) Charge/discharge cycling of E18 with CNF and nickel powder.

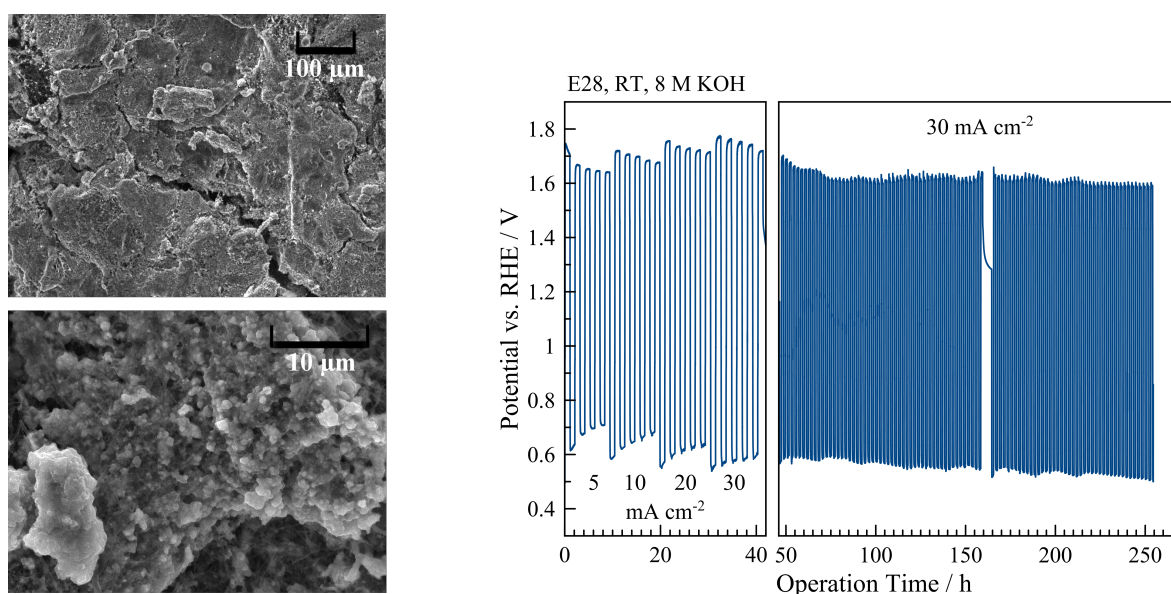
Figure 5.4: Electrochemical measurement of E10, E16 and E18 using $(\text{La}_{0.8}\text{Sr}_{0.2})_{0.95}\text{MnO}_{3-x}$ perovskite catalyst at increasing current densities (supplied with synthetic air).

In comparison to E10, electrode E16 was one of the first electrodes, which exhibited stable ORR and OER potentials over a longer operation time period (60 h) as depicted in Figure 5.4(b). E16 consisted of a cross-rolled paste (60 wt% $(\text{La}_{0.8}\text{Sr}_{0.2})_{0.95}\text{MnO}_{3-x}$ perovskite, 20 wt% CNF and 20 wt% PTFE) on a nickel mesh current collector. Importantly, it was the first electrode, which was press-sintered at high temperatures of 300 °C, which, in combination with the use of more oxidative stable CNF, significantly improved the electrode's stability as well as charge/discharge performance compared to all previous electrodes. Thus, the press-sintering step was performed with all subsequent electrodes manufactured during this project. Electrochemical measurements show, that even at the target operating current density of 50 mA cm⁻² stable discharge potentials (0.617 V vs. RHE) as well as charge potentials (1.675 V vs. RHE) could be achieved, reaching a potential difference ΔV of 1.06 V (voltage efficiency of about 49%). This good performance is attributed to the beneficial effect resulting from heating to 300 °C. Because at this temperature PTFE is close to its glass transition temperature, it becomes soft, which leads to a more homogeneous distribution of the hydrophobic binder additive within the electrode. It has to be noted, that the OER potential of E16 at 50 mA cm⁻² was about 0.15 V higher compared to the nickel based electrodes described in section 5.2.1. The results indicate, that nickel in form of NiCoO₄ spinel or also just by adding nickel powder has a positive influence on the charging performance.

This conclusion can also be drawn, when comparing the performance of E16 to electrode E17, which was manufactured in the same way as E16 but was completely carbon-free and only employed nickel powder/PTFE as additives. As expected, the OER potentials were more stable, but interestingly also slightly higher than obtained from the measurements of E16. Its ORR performance was negligible, indicating again, that the PTFE/nickel powder mixture is too dense for sufficient O₂ supply to the perovskite catalyst. However, as it is hard to obtain information on the processes within the electrode, already small alterations of the electrode paste's composition can result in very different results in the electrochemical measurements. For example, although the same nominal wt% of PTFE were used in both electrodes, PTFE/nickel powder GDEs were more hydrophobic because of the significantly less voluminous nickel powder compared to CNF (*i.e.* different volumetric ratios). From these preliminary results, it was still very difficult to assign the resulting performances to the individual components within the electrode build-up. For example, as the effects were still not conclusive, it was not clear if the different measurement results indicated altered catalytic activity (*i.e.* catalyst degradation), incomplete formation of a fine porous structure with limited electrolyte/gas accessibility, or if the catalyst was covered by

too much PTFE. These considerations show that a very fine balance between all components was necessary for obtaining high and reproducible ORR and OER performances.

Following the promising results of E16, electrode E18 was manufactured similarly but contained CNF and, in addition, nickel powder as additives. The results are depicted in Figure 5.4(c), clearly showing much more stable OER potentials compared to E16 even up to current densities of 50 mA cm^{-2} . At this current density, the ORR potentials between E16 and E18 were only 0.012 V apart (E16 - 0.619 V and E18 - 0.630 V) and, as hoped, the OER potential of E18 with the nickel powder (1.575 V) was 0.105 V lower than of E16 (1.680 V).



(a) SEM images of E28 after operation.

(b) Long-term cycling of E28 at 30 mA cm^{-2} .

Figure 5.5: Results of $(\text{La}_{0.8}\text{Sr}_{0.2})_{0.95}\text{MnO}_{3-x}$ -catalyzed electrode E28.

Electrode E28 employed the new nickel foam by Alantum Corporation with a pore size of $450 \mu\text{m}$, area density of 420 g m^{-2} and thickness 1.6 mm . This type of nickel foam was used for the rest of the project and many subsequent electrodes were in principle quite similarly manufactured to E28. The paste had the same composition as E16 and consisted of $60 \text{ wt}\%$ perovskite, $20 \text{ wt}\%$ PTFE and $20 \text{ wt}\%$ CNF. The paste was spread on both sides of the nickel foam. After press-sintering of the dried electrode at $300 \text{ }^\circ\text{C}$, E28 had a catalyst loading of 38 mg cm^{-2} and a thickness of $0.7\text{-}0.8 \text{ mm}$. The results of the electrochemical long-term cycling measurement are depicted in Figure 5.5(b). Within the first 40 h of operation with increasing current densities up to 30 mA cm^{-2} , a significant gradual improvement of ORR and OER potentials was apparent. This effect was attributed to the thicker build of the nickel foam based electrode compared to the

thinner cross-rolled electrode on nickel mesh. Seemingly, an "activation" time is necessary for the electrolyte to reach all catalytic sites throughout the thicker electrode, where the fine perovskite particles are distributed. Within the following 200 h charge/discharge cycling at 30 mA cm^{-2} the ORR potential slowly degraded to 0.5 V vs. RHE, whereas the final OER potential was much improved compared to the beginning of operation with 1.509 V vs. RHE after overall 250 h. The SEM images depicted in Figure 5.5(a) show the electrode after operation. The electrode's surface appears cracked, whereby it was unclear if this resulted from the drying process or the electrochemical measurements itself. In the lower image some μm sized particles - most likely the perovskite catalyst - are visible.

These first results of the $(\text{La}_{0.8}\text{Sr}_{0.2})_{0.95}\text{MnO}_{3-x}$ perovskite-catalyzed bifunctional air electrodes, either supported on nickel mesh or nickel foam current collector, were presented in a poster on *The 67th Annual Meeting of the International Society of Electrochemistry (ISE)* in Den Haag (Netherlands).

LaNiO₃

Another in-house synthesized perovskite was LaNiO_3 , which was used in electrode E34 (catalyst loading of 40 mg cm^{-2}). This electrode utilized nickel foam as current collector and was similarly manufactured to the $(\text{La}_{0.8}\text{Sr}_{0.2})_{0.95}\text{MnO}_{3-x}$ -catalyzed electrode E28. The results of the electrochemical characterization of E34 over a time of 450 h are shown in Figure 5.6 and were presented in a poster at the *13th Minisymposium Chemical and Process Engineering* in Innsbruck (Austria).

Within the first 250 h of operation an increasing ORR performance could be observed, which is similar to the "activation" effect measured with E28. The increased soaking time of the electrode with electrolyte can be assigned to the comparably high thickness of the electrode with 0.85-0.9 mm. During repeated cycling operation at 30 mA cm^{-2} , the resulting ORR potentials were about 0.08 V lower than of E28, but more stable. More importantly, the charging potentials of E34 were as low as 1.47 V throughout the long-term operation, which can be attributed to the nickel within the LaNiO_3 perovskite structure.

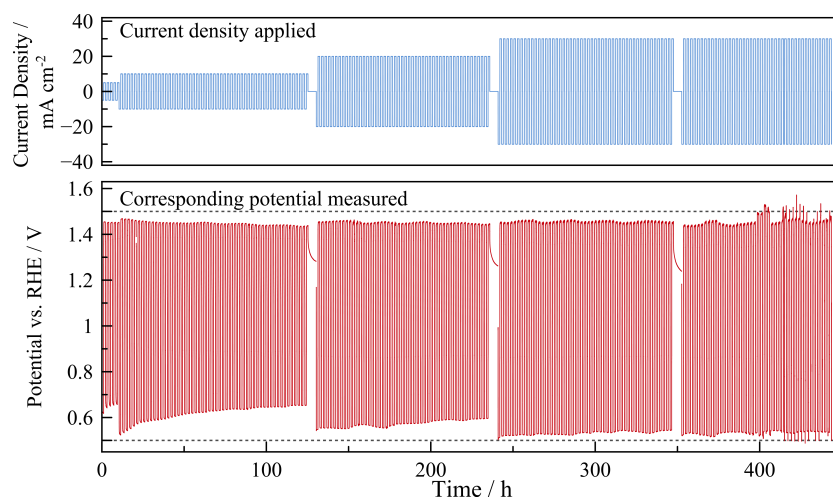


Figure 5.6: Long-term operation of E34 catalyzed with LaNiO_3 .

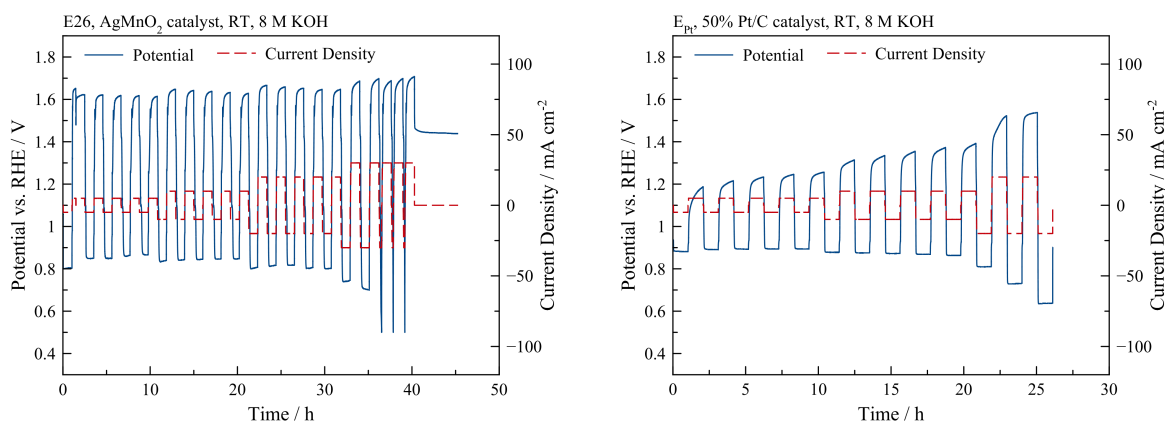
Conclusion to the Perovskite-catalyzed Air Electrodes

The different perovskite-type catalysts exhibited good bifunctional ORR/OER activity, whereby the longest operation time was reached with E34 using LaNiO_3 but the best catalytic activity was achieved with the commercial $(\text{La}_{0.8}\text{Sr}_{0.2})_{0.95}\text{MnO}_{3-x}$ catalyst (E18). This can be attributed to the smaller particles size, higher surface area and more defined composition compared to the in-house manufactured $\text{La}_{0.6}\text{Ca}_{0.4}\text{CoO}_3$ and LaNiO_3 . As the focus lay mainly on optimizing the electrode build than on finding the optimal perovskite composition (whereby it is still unclear which perovskites exhibit the highest catalytic activity, with significant differences between ORR and OER [38, 66, 68]), it was decided to work with the more defined commercial catalysts. Furthermore, this choice was also made, because achieving the same reproducible properties of the catalyst with each synthesized batch could not be guaranteed, thus comparison of the electrode's composition and subsequent optimization would have been very difficult.

5.2.4 Ag-MnO₂ and Pt-catalyzed Bifunctional Air Electrodes

Only a few experiments were performed using in-house synthesized Ag-MnO₂ catalyst directly supported on CNF (30 wt% Ag-MnO₂/CNF). This catalyst was tested because of its high ORR activity, however the experiments showed too low stability of the silver as well as the manganese oxide species during potential cycling, especially at high current densities. The results of the cycling test of E26 at different current densities is shown in Figure 5.7(a). As expected, the ORR performance was very high, but could not be sustained for more than 35 h. Similar results were

obtained for a cross-rolled Pt-catalyzed electrode E_{Pt} using commercial 50 wt% Pt/C catalyst (by Alfa Aesar) as shown in Figure 5.7(b). This Pt electrode is a benchmark cathode optimized during other projects and was tested in this project as benchmark for bifunctional operation. However, due to the low stability of the support carbon (high amount of Vulcan XC72 and Black Pearls 2000), increasing OER charge potentials were measured, which in consequence accelerated the decrease of the otherwise very excellent ORR performance. As listed in Table 5.5, the high ORR activity of both electrodes was achieved with very low catalyst loadings of 7 mg cm^{-2} (E_{26}) and 0.8 mg cm^{-2} (E_{Pt}), respectively.



(a) Charge/discharge cycling of E_{26} with $\text{Ag-MnO}_2/\text{CNF}$.

(b) Charge/discharge cycling of E_{Pt} using 50 wt% Pt/C

Figure 5.7: Results of $\text{Ag-MnO}_2/\text{CNF}$ -catalyzed and Pt-catalyzed air electrodes.

As discussed in the theory part (section 3.4.2), Pt, Ag and Mn_xO_y are very good ORR catalysts, however are not suitable as bifunctional catalysts for ORR and OER. This is on the one side because of the low catalytic activity toward OER and on the other because of their insufficient stability at high potentials, undergoing oxidation and reduction cycles at every charge and discharge. In addition, commercial platinum nanoparticle catalysts are often supported on high surface area carbon-types with lower stability towards oxidative potentials. As both "classical" ORR catalysts did not exhibit better bifunctional activity than the perovskite and spinel catalysts, this approach was not further pursued.

Table 5.5: Summary of Ag–MnO₂/CNF-catalyzed and Pt-catalyzed electrodes listing charge (OER) and discharge (ORR) potentials vs. RHE for the best performance at 20 mA cm⁻².

| Electrode | Support | OER [V] | ORR [V] | Comments |
|-----------------|---------|---------|---------|-----------------------------------------------------|
| E26 | Ni foam | 1.652 | 0.818 | loading 7 mg cm ⁻² , 20% PTFE |
| E _{Pt} | Ni mesh | 1.522 | 0.810 | loading 0.8 mg cm ⁻² , with carbon paper |

5.3 Bi-catalyzed Bifunctional Air Electrodes with NiCo₂O₄ and Perovskites

In the preliminary tests discussed in section 5.2, the NiCo₂O₄ spinel catalysts showed promising OER performances (i.e. low discharge potentials) of ~ 1.5 V vs. RHE, however, both synthesis methods - the dip-coating as well as the batch-synthesis - proved to be impractical with too low reproducibility. Thus, the process of NiCo₂O₄ synthesis was adapted by directly depositing the Ni and Co salts on support material followed by calcination. As support material CNFs and nickel powder (< 50 μm) were chosen. The two supported catalysts, NiCo₂O₄/CNF and NiCo₂O₄/Ni powder, were mixed with PTFE and the resulting paste spread on nickel foam. It has to be mentioned that all electrodes from this point on incorporated the Alantum nickel foam (pore size 450 μm , area density 420 g m⁻², thickness 1.6 mm) as current collector. Also the press-sintering step at 300 °C and 150 kg cm⁻² was kept the same for the remaining time of the project.

The results of electrode E25, as shown in Figure 5.8, were presented on a poster during the 9th *International Summer School on Advanced Studies of Polymer Electrolyte Fuel Cells* (Graz, Austria). In the electrochemical cycling test up to 30 mA cm⁻² (Figure 5.8(a)) electrode E25 exhibited stable OER potentials at 1.5 V vs. RHE, but deteriorating ORR performance within the first 50 h. This effect was seen also with the following electrodes as discussed below. In addition, pulse charging was performed at three conditions as depicted in Figure 5.8(b). At tripled current density of 150 mA cm⁻² during the 50 ms pulse (100 ms pause), which corresponds to 50 mA cm⁻² mean current density, the maximum OER potentials were only 1.6 V vs. RHE and the pulse profile was close to rectangular as shown in the inset of Figure 5.8(b).

After operation, SEM images were taken of the backside of the electrode, which was the synthetic air supplied side. Because only the electrolyte-facing side of the nickel foam was coated with

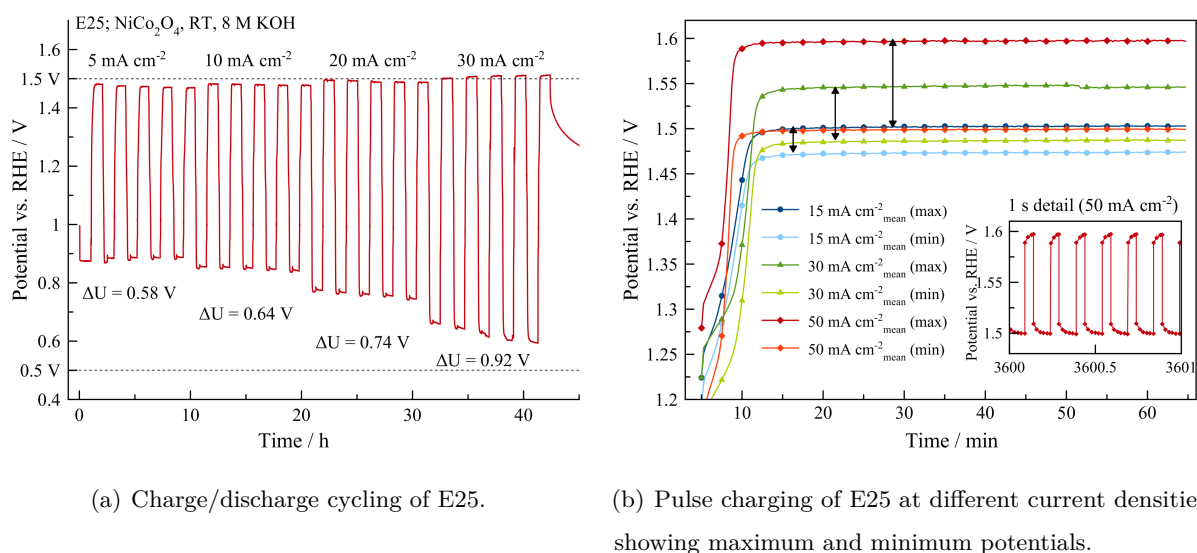


Figure 5.8: Results of the electrochemical characterization of E25 catalyzed with $\text{NiCo}_2\text{O}_4/\text{CNF}$ and $\text{NiCo}_2\text{O}_4/\text{Ni}$ powder.

the catalyst paste, the nickel foam current collector is clearly recognizable in the images by the smooth surface. In between, the electrode paste containing the NiCo_2O_4 catalyst, CNF, Ni powder and PTFE binder can be seen. At the highest magnification the fiber network of the CNFs becomes clearly visible.

Due to the high OER activity of the supported NiCo_2O_4 spinel catalyst but not sufficiently stable ORR performance, the NiCo_2O_4 spinel was combined with different perovskite catalysts. These were $(\text{La}_{0.8}\text{Sr}_{0.2})_{0.95}\text{MnO}_{3-x}$ (E32), in-house synthesized LaNiO_3 (E36), and a new type of commercial perovskite - $\text{La}_{0.6}\text{Sr}_{0.4}\text{Co}_{0.2}\text{Fe}_{0.8}\text{O}_3$ (E37), which had a small particle size (surface

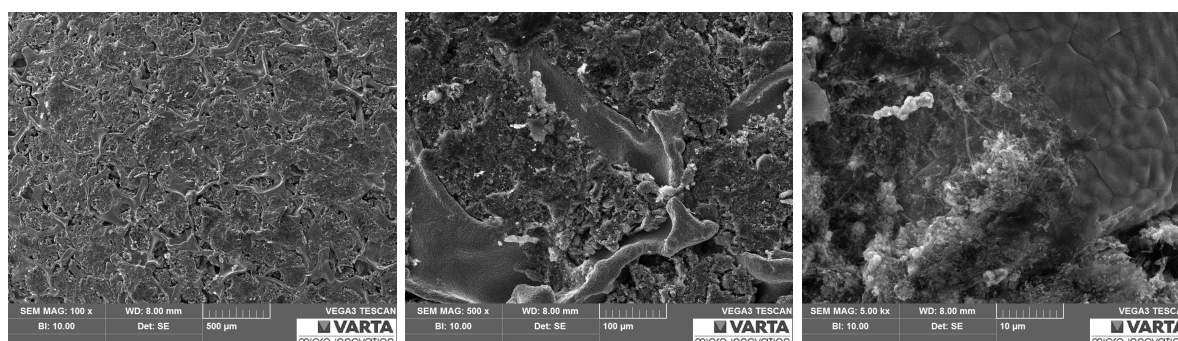


Figure 5.9: SEM images of E25 after operation (backside). Clearly visible is the incorporated nickel foam and the fine carbon nanofibers within the paste.

area $10-14\text{ m}^2\text{ g}^{-1}$, size $d_{50} = 0.4-0.8\text{ }\mu\text{m}$). Using commercial perovskites in contrast to in-house synthesized ones had the advantage of higher reproducibility as well as more defined catalyst composition. Thus, effects during optimization of the electrode build could be more easily attributed to the electrode paste composition and the manufacturing process and was less influenced by inhomogeneity of the perovskite catalyst itself.

Table 5.6: Summary of $\text{NiCo}_2\text{O}_4/\text{CNF} + \text{NiCo}_2\text{O}_4/\text{Ni}$ powder + perovskite electrodes listing start charge (OER) and discharge (ORR) potentials vs. RHE at 30 mA cm^{-2} (first cycling).

| Electrode | Support | OER [V] | ORR [V] | Comments |
|-----------|---------|---------|---------|--------------------------------------------------------------------------------------|
| E25 | Ni foam | 1.501 | 0.659 | only $\text{NiCo}_2\text{O}_4/\text{CNF} + \text{NiCo}_2\text{O}_4/\text{Ni}$ powder |
| E32 | Ni foam | 1.495 | 0.664 | + $(\text{La}_{0.8}\text{Sr}_{0.2})_{0.95}\text{MnO}_{3-x}$ |
| E36 | Ni foam | 1.480 | 0.544 | + LaNiO_3 |
| E37 | Ni foam | 1.486 | 0.529 | + $\text{La}_{0.6}\text{Sr}_{0.4}\text{Co}_{0.2}\text{Fe}_{0.8}\text{O}_3$ |

The electrode manufacturing of these bi-catalyzed air electrodes (E32, E36, E37) was slightly different to previous electrodes, namely that two separate electrode pastes were prepared and each spread on opposite sides of the nickel foam. The first paste, facing the electrolyte in the cell, contained the two NiCo_2O_4 catalysts in ratio 55 wt% $\text{NiCo}_2\text{O}_4/\text{CNF}$ and 20 wt% $\text{NiCo}_2\text{O}_4/\text{Ni}$ powder with addition of 25 wt% of PTFE. The second paste, which was on the gas supplied side, contained the respective perovskite (60 wt%) mixed with 20 wt% CNFs and 20 wt% PTFE. This separation had the effect, that the spinel with high OER activity was more soaked with electrolyte (two-phase boundary as well as fast O_2 removal from surface) and the better ORR catalyst (perovskite) was facing the gas side for short gas diffusion paths to the three-phase zones. This approach was also applied in several other electrodes as is discussed in the *Electrochimica Acta* publication (see section 5.3.1 and Appendix B).

The results of E32, E36 and E37 using the three respective perovskites is shown in Figure 5.10 and compared in Table 5.6. All three electrodes exhibited a significant decrease in ORR performance within the first 50 h of cycling as observed with E25, however from the beginning highly stable and very similar charging potentials were obtained for all three electrodes, which is attributed to the high catalytic activity of the NiCo_2O_4 towards OER. As can be seen in Figure 5.10, the $(\text{La}_{0.8}\text{Sr}_{0.2})_{0.95}\text{MnO}_{3-x}$ -catalyzed (E32), exhibited the fastest degradation (stopped after 100 h of cycling), whereas the other two electrodes operated at stable potentials for several hundred hours (oscillating potential profile caused by lab temperature fluctuations). Up to

this point these two were the longest achieved operating times. Importantly, in case of the $\text{La}_{0.6}\text{Sr}_{0.4}\text{Co}_{0.2}\text{Fe}_{0.8}\text{O}_3$ -catalyzed electrode (E37) the current density could be increased up to the target current density of 50 mA cm^{-2} due to the slowly improving performance (marked with \times in Figure 5.10). Even after 900 h of measurement the potential difference between charge and discharge (ΔV) was below 1 V, which corresponds to a voltage efficiency of $> 50\%$.

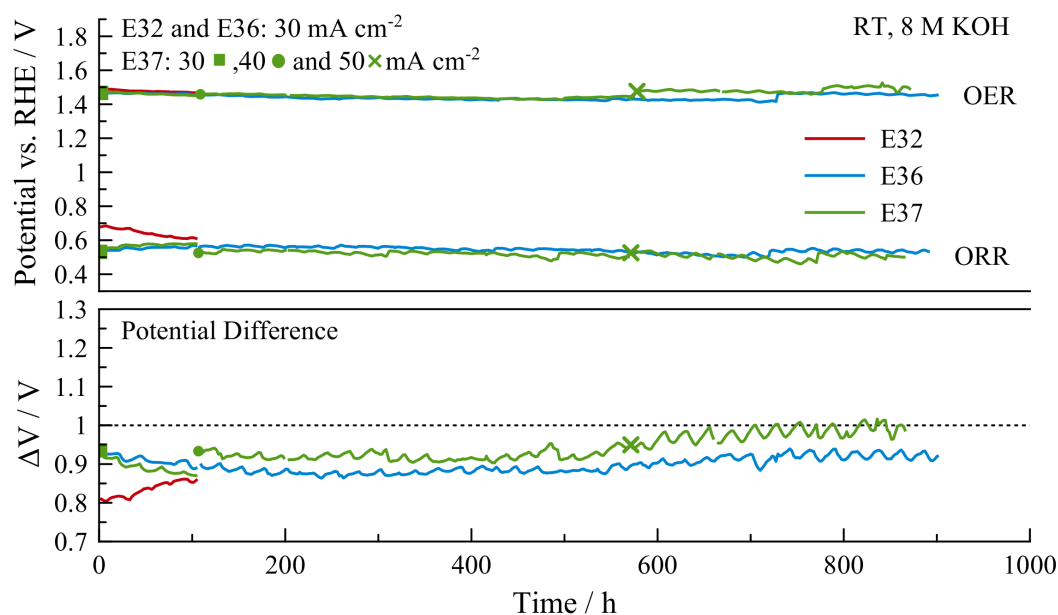


Figure 5.10: Long-term cycling operation with 2 h cycles (alternating 1 h charge, 1 h discharge) of three different bi-catalyzed bifunctional air electrodes (NiCo_2O_4 +perovskite).

As the combination of the spinel and the perovskite yielded on one hand very good ORR and OER potentials and on the other high stability over several hundred hours of operation, a test series was performed on studying the influences of each catalyst as summarized in the following sub-chapter. From the three different perovskites, $\text{La}_{0.6}\text{Sr}_{0.4}\text{Co}_{0.2}\text{Fe}_{0.8}\text{O}_3$ was chosen due to its significantly higher stability compared to the Mn-containing perovskite and because of its better defined composition and narrow particle size distribution compared to the synthesized LaNiO_3 perovskite. In addition, pretests with zinc as counter electrode as well as with zinc as reference electrode were performed. Thus, all following tests were referenced against Zn/Zn^{2+} instead of vs. RHE. For this, 0.5 M ZnO were added to the 8 M KOH electrolyte.

5.3.1 Peer-Reviewed Publication in *Electrochimica Acta*

Title: "*Bifunctional electrode performance for zinc-air flow cells with pulse charging*"

Abstract

"Bifunctional air electrodes with tuned composition consisting of two precious metal-free oxide catalysts are manufactured for application in rechargeable zinc-air flow batteries and electrochemically tested via long-term pulse charge and discharge cycling experiments at 50 mA cm^{-2} (mean). NiCo_2O_4 spinel, synthesized via direct impregnation on carbon nanofibers or nickel powder and characterized by energy dispersive X-ray spectroscopy and X-ray diffraction experiments, shows high activity toward oxygen evolution reaction with low charge potentials of $< 2.0 \text{ V}$ vs. Zn/Zn^{2+} . $\text{La}_{0.6}\text{Sr}_{0.4}\text{Co}_{0.2}\text{Fe}_{0.8}\text{O}_3$ perovskite exhibits bifunctional activity and outperforms tenfold the NiCo_2O_4 spinel in long-term stability. By combining the catalysts in one bi-catalyzed bifunctional air electrode, stable performances of more than 1000 h and 450 cycles are achieved when supplied with oxygen and over 650 h and 300 cycles when supplied with synthetic air. In addition, the pulse charging method, which is beneficial for compact zinc deposition, is successfully tested on air electrodes during long-term operation. The oxygen evolution potentials during pulse, i.e. at tripled charge current density of 150 mA cm^{-2} , are only 0.06–0.08 V higher compared to constant charging current densities. Scanning electron microscopy confirms that mechanical degradation caused by bubble formation during oxygen evolution results in slowly decreasing discharge potentials."

Highlights

- "Manufacture of bi-catalyzed bifunctional air electrodes via scalable process.
- Direct synthesis of NiCo_2O_4 on carbon nanofibers or nickel powder support.
- 450 charge and discharge cycles over 1000 h at 50 mA cm^{-2} demonstrated.
- Pulse charging with 150 mA cm^{-2} is successfully applied on air electrodes.
- Charge and discharge ΔV of $< 0.8 \text{ V}$ at 50 mA cm^{-2} when supplied with O_2 ."

The publication as well as the supplementary information can be found in the Appendix B.

The publication comprises the results of four different electrodes (E41 to E44), catalyzed with both $\text{NiCo}_2\text{O}_4/\text{CNF}$ + $\text{NiCo}_2\text{O}_4/\text{Ni}$ powder together with $\text{La}_{0.6}\text{Sr}_{0.4}\text{Co}_{0.2}\text{Fe}_{0.8}\text{O}_3$, or - for comparison -

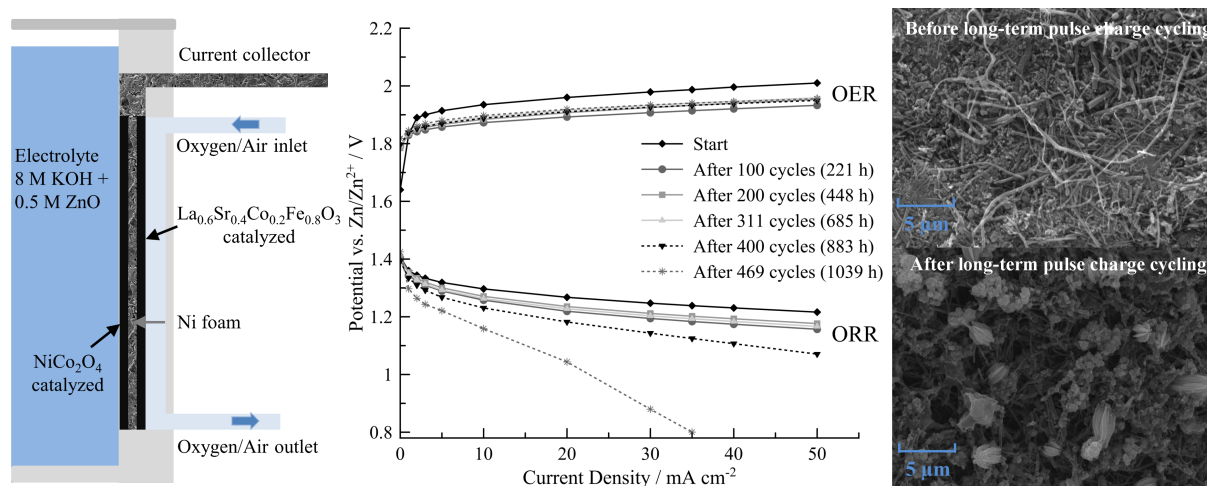


Figure 5.11: Graphical abstract to the publication in *Electrochimica Acta*.

only with the spinel or the perovskite. Testing was carried out at 50 mA cm^{-2} with pulse charging at 150 mA cm^{-2} (duty cycle $\gamma = 0.33$). With pure oxygen over 1000 h and with synthetic air 650 h of testing were achieved. In addition, the spinel catalyst and the electrode were characterized with X-ray spectroscopy (EDX) showing high dispersion of all materials on the support and within the electrode, respectively. As discussed in the publication, X-ray diffraction experiments (XRD) including Rietveld analysis yielded that not only NiCo₂O₄ was obtained during calcination but also to some degree Ni_{1-x}Co_xO or other oxide forms such as NiO and CoO.

All authors contributed to the publication. Stephan Weinberger helped with the test cell design and the experimental set-up for long-term operation (two air electrodes measured in one cell with zinc as reference), Lucas Rešćec did the NiCo₂O₄ spinel catalyst synthesis, Ilena Grimmer and Florian Gebetsroither contributed to the design of air electrodes, the test cells as well as with the set-up of the test rig, Brigitte Bitschnau did the XRD measurement including Rietveld analysis, and Viktor Hacker supervised the work.

5.4 Optimizing the Operation Conditions of Bi-catalyzed Bifunctional Air Electrodes

Following the first publication, the investigations focused on further increasing the long-term stability of the bi-catalyzed bifunctional air electrodes. This was done on one hand by continued optimization of the electrode composition and on the other hand by investigating the operating parameters.

Electrode E50 was similarly manufactured to the bi-catalyzed bifunctional air electrodes but had a reduced PTFE content in the perovskite paste (15 wt% instead of 20%). The results of this 500 h long cycling test with pulse charging including discussion of the obtained potentials as well as evaluation of the resulting efficiencies of this air electrode were summarized in the reviewed conference proceeding *ECS Transactions* submitted in context of the 232nd Meeting of the *Electrochemical Society* (National Harbor, USA). Also, additional discussion about this electrode was presented together with information on pulse charging of zinc electrodes in the reviewed conference proceedings of the 7th *Transport Research Arena* (Vienna, Austria). Both contributions can be found in the Appendix B.

5.4.1 Peer-Reviewed Publication in *Journal of Applied Electrochemistry*

Title: "*The impact of operating conditions on component and electrode development for zinc-air flow batteries*"

Abstract

"Rechargeable zinc-air flow batteries are investigated as possible technology for fast responding large-scale electrical energy storage due to the use of inexpensive, non-toxic and abundant materials, and compact system design. The operating ranges for several parameters such as flow rate (2–8 cm s⁻¹), concentration of electrolyte (6 or 8 M KOH), charge/discharge current densities (up to 100 mA cm⁻² mean), and active or passive air supply as well as their influence on the performance and stability of the electrodes are investigated and compared. Bi-catalyzed bifunctional air electrodes are tested by means of half-cell measurements achieving minimum 200 charge/discharge cycles at 50 mA cm⁻² with the longest operation time being 800 h. At this current density, charge/discharge efficiencies are in the range of 50% for all tested air electrodes. End-of-life characterization by means of scanning electron microscopy reveals mechanical degradation of the electrode material. On the negative zinc electrode, zinc deposition morphology on different current collector materials (nickel, brass, and steel) is investigated using Rota-Hull cylinders showing nickel to be the most suitable material. The pulse interrupt current method is thereby successfully applied for compact zinc deposition in a broad current density range without any electrolyte additive. Subsequent scale-up of the rechargeable zinc-air flow battery and unit cell operation is finally performed for proof-of-concept."

The publication as well as the supplementary information can be found in Appendix B.

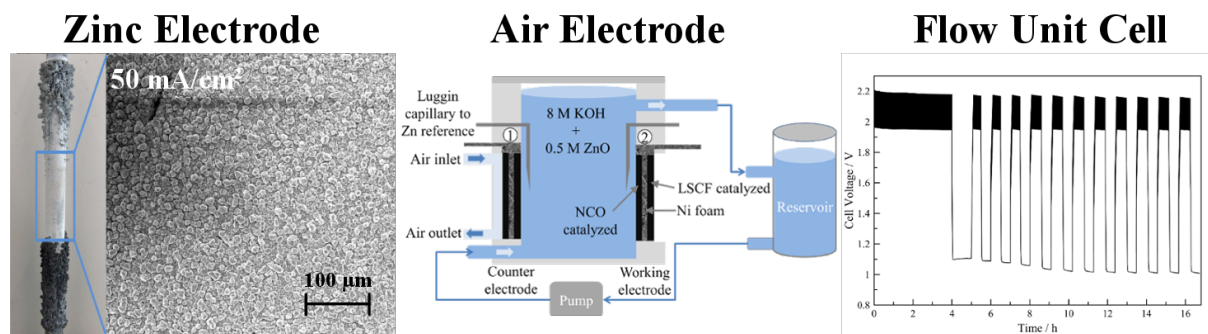


Figure 5.12: Graphical abstract to the publication in the Journal of Applied Electrochemistry.

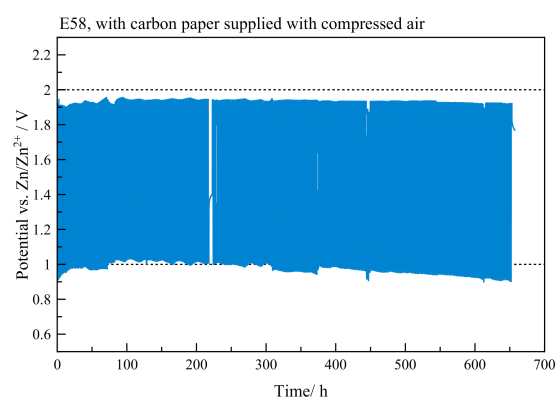
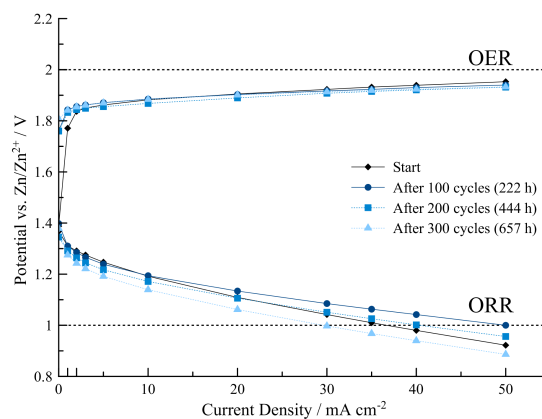
The publication comprises the practical testing of air electrodes as well as investigations on zinc morphology during pulse interrupt current deposition at different current densities and on three different current collector materials. The air electrodes presented in this publication were E51_1, E51_3, E53, E54, E56 with 16 cm^2 and E57 with 100 cm^2 . They were manufactured in the same way using $\text{NiCo}_2\text{O}_4/\text{CNF} + \text{NiCo}_2\text{O}_4/\text{Ni}$ powder together with $\text{La}_{0.6}\text{Sr}_{0.4}\text{Co}_{0.2}\text{Fe}_{0.8}\text{O}_3$ perovskite as catalysts. Besides the successful up-scaling of the electrode manufacturing process, the good stability of the electrodes at high electrolyte flow rates in regard to the shearing forces has to be mentioned. Moreover, the charging potentials were more stable because of the fast oxygen bubble outtake promoted by the electrolyte flow. Nevertheless, gradual wetting of the electrode with electrolyte caused by PTFE and CNF degradation, thus leading to reduced hydrophobicity and bigger pores in the electrode's structure, respectively, resulted in too low ORR potentials and end of testing at about 400-800 h depending on the operation conditions.

All authors contributed to the joint publication in the framework of the project *Luziflow*. Nikolaus Rauch set-up the test stand for measurements with flowing electrolyte and helped with electrode manufacture. Bernhard S. Berner, Christian Zelger and Bernhard Gollas did the investigations on zinc deposition morphology on the zinc electrode by means of Rota-Hull cylinder experiments on different current collector materials and at various current densities. Hans-Jürgen Pauling did the testing of the unit cell and Viktor Hacker supervised the work.

5.4.2 Application of Carbon Paper as Backing Layer

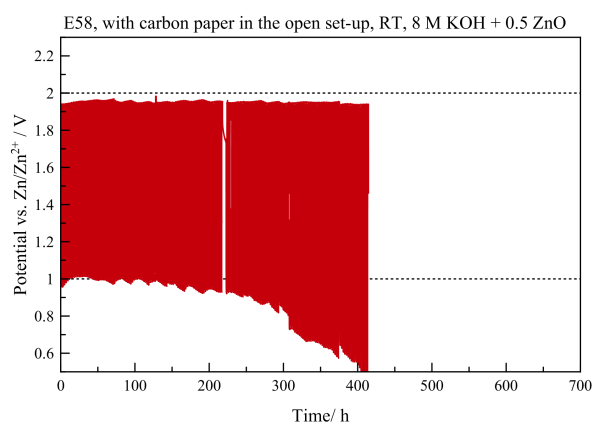
As leakage posed a significant challenge especially during long-term operation and in the open set-up, it was attempted to prevent electrolyte loss by attaching additional hydrophobic layers on the gas-side of the electrode as so called "backing layer". The first material tested was hydrophobic

carbon paper, which was attached onto the electrode during the final press-sintering step at 300 °C and 150 kg cm⁻². The electrochemical results of two electrodes (E58_1 and E58_2), which were manufactured similarly to the electrodes presented in the *Journal of Applied Electrochemistry* publication employing both the NiCo₂O₄ spinel and the La_{0.6}Sr_{0.4}Co_{0.2}Fe_{0.8}O₃ perovskite, are shown in Figures 5.13 and 5.14, respectively. E58_2 was tested in an open set-up and E58_1 was operated in a closed set-up, using this time air from a compressor (CA) instead of synthetic air. Utilizing CA is much closer to practical application as ambient air comprises also CO₂, which can dissolve into the alkaline electrolyte forming carbonates. E58_1 operated with CA exhibited stable and comparable performances to the previously tested electrodes, again achieving about 650 h of operation (Figure 5.13(a)) with a voltage efficiency of > 50%. Also, stable OER potentials at about 1.95 V vs. Zn/Zn²⁺ and slowly decreasing ORR potentials over the duration of the measurement were observed (Figure 5.13(b)). Throughout the measurement the closed gas-side was much drier compared to the previous electrodes, however the performance could not be significantly improved. In regard to the open set-up, shown in Figure 5.14, the additional hydrophobic carbon paper could not improve the long-term stability of the electrode. Already after five days, electrolyte leaked through the electrode as is visible in Figure 5.14(b)(bottom). After 100 h of stable testing with nearly the same performance as E58_1 in the closed set-up, the ORR potentials gradually decreased until the measurement was stopped after 400 h (Figure 5.14(a)). Interestingly, as can be seen in Figure 5.14(b), the droplets always formed at the same place along small tears, which were probably inflicted during the harsh sintering process rendering the carbon paper very brittle. Consequently, if the carbon paper would have been attached by a milder process, damage and thus leakage of electrolyte could probably have been prevented (comparable to section 5.6.1, where the backing layer was attached in an additional 200 °C sintering step). However, in regard to longevity and activity of the air electrode, the addition of hydrophobic carbon paper led to no beneficial effect.

(a) Long-term operation of E58_1 at 50 mA cm^{-2} .

(b) Polarization curves of E58 supplied with CA over the course of the long-term measurement.

Figure 5.13: Electrochemical characterization of E58_1 with additional carbon paper backing operated in the closed set-up supplied with compressed air (CA).

(a) Long-term operation of E58_2 at 50 mA cm^{-2} .

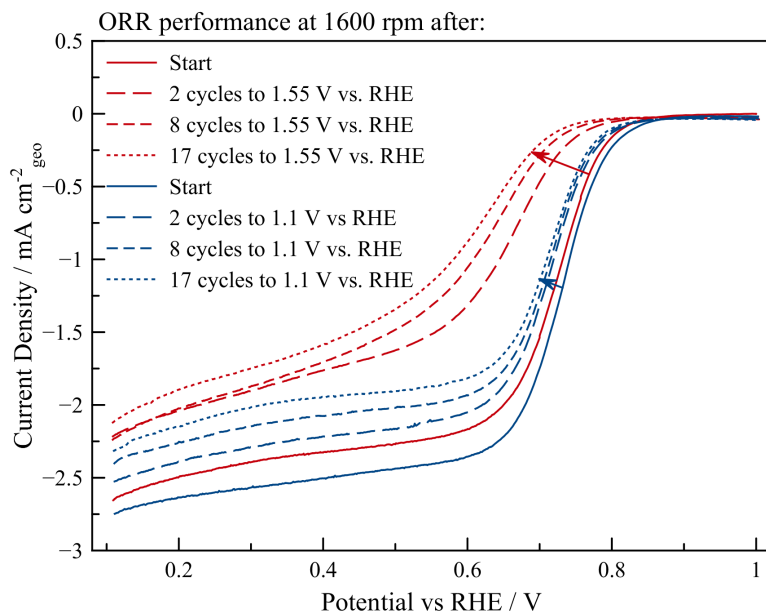
(b) Image of the backside of the electrode after start (top) and after 5 days (bottom).

Figure 5.14: Electrochemical characterization of E58_2 with additional carbon paper backing operated in the open set-up with no active air supply.

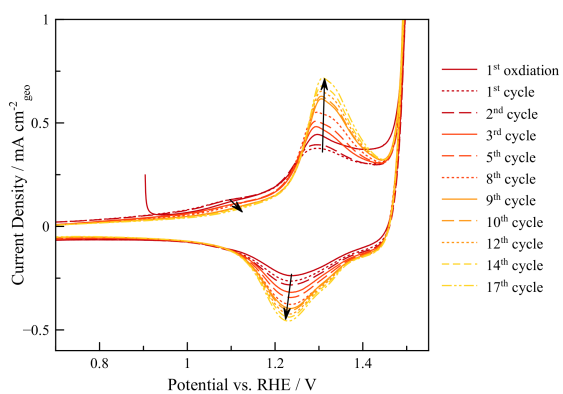
5.5 RDE Cyclic Voltammetry of NiCo₂O₄ and Nickel Powder

Most electrodes manufactured in this project so far utilized NiCo₂O₄ as bifunctional catalyst, however its stability during repeated cycling, which means a reoccurring potential change over a span of about 1 V between about 0.7 to 1.7 V vs. RHE, was always limited to about 40-50 h of long-term operation. This was shown in the *Electrochimica Acta* publication in Fig.2 and also Pletcher *et al.* [87] reached only about 40 h of operation time with NiCo₂O₄-catalyzed electrodes. In this range, nickel as well as cobalt have redox peaks as shown in Figure 5.15 and also in the supplementary Fig.S4 of the *Electrochimica Acta* publication (see Appendix B). The redox peaks in these ex-situ cyclic voltammetry diagrams can be interpreted according to Abidat *et al.* [88]. It can be seen that the nickel oxidation peak (Ni²⁺ to Ni³⁺) at about 1.35 V vs. RHE grows during cycling and the cobalt peak (Co²⁺ to Co³⁺) at about 1.1 V vs. RHE decreases, clearly indicating significant changes within the spinel structure probably resulting in various Ni(OH)₂/NiOOH species. These changes have a direct influence on the ORR activity as can be seen in Figure 5.15(a). When cycled to 1.1 V the CV in N₂ in Figure 5.15(c) only shows a small decline of the Co oxidation peak and the corresponding ORR curves in Figure 5.15(a)(blue) exhibit nearly the same ORR on-set at about 0.82 V vs. RHE as well as half-wave potential at about 0.70 V vs. RHE even after repeated cycling. The decline in limited current density can be attributed to the stability of the catalyst film on the RDE, slowly degrading by the many CV cycles. In contrast to this, the catalyst, which was repeatedly cycled to 1.55 V vs. RHE shows dramatically decreasing ORR performances with deteriorating ORR on-set and half-wave potentials. Moreover, during repeated cycling, the OER on-set potential, visible in Figure 5.15(b) at about 1.50 V vs. RHE, stays constant throughout the measurement, although the nickel redox peak dramatically changes. These ex-situ results fit very well with charge/discharge potentials obtained from the in-situ electrode measurements. That means that the NiCo₂O₄-catalyzed electrodes always exhibited very stable and good OER potentials, but that the high ORR performance obtained at the beginning of operation could only be maintained for a few hours.

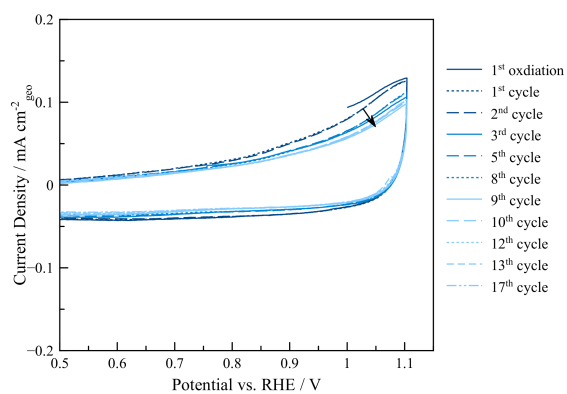
Electrode E59, shown in Figure 5.16(a) was manufactured in order to be tested as blank "benchmark" electrode, using only the support materials (CNF, nickel powder and PTFE) spread on Ni foam current collector. As can be seen in Figure 5.16(a), even without catalyst, reasonable ORR and OER potentials could be obtained up to a current density of 30 mA cm⁻², proving on one hand the importance of optimizing the electrode build (especially when compared to the poor performance of the first electrodes manufactured during this project) and on the other hand



(a) ORR CV curves recorded after repeated cycling either to 1.1 V (blue) or 1.55 V vs. RHE (red).



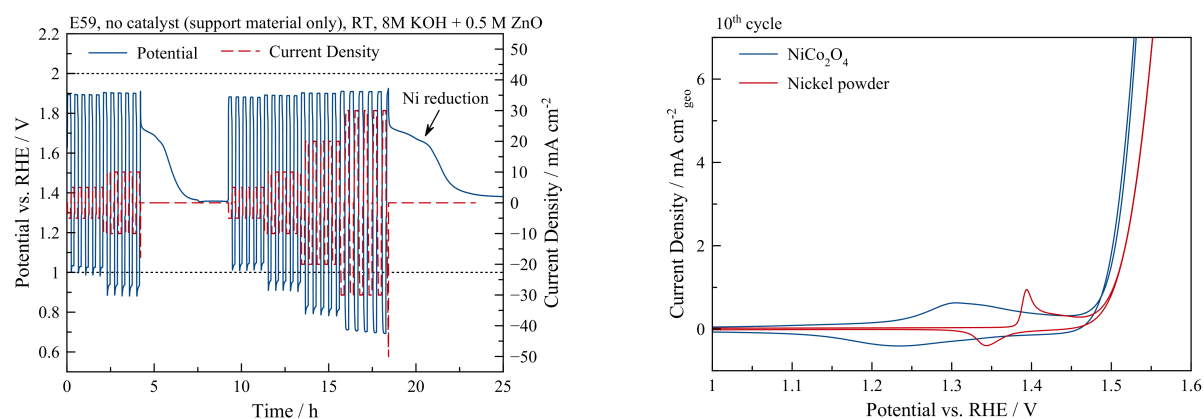
(b) CV curves in N_2 up to 1.55 V showing change of redox peaks.



(c) CV curves in N_2 up to 1.1 V showing nearly no change.

Figure 5.15: Rotating disk electrode measurement of NiCo_2O_4 spinel catalyst.

that carbon and nickel have an inherent catalytic activity toward ORR and OER, respectively. However, whereas the low ORR performance slowly deteriorated during repeated cycling, the OER potentials were very stable and low at 1.92 V vs. Zn/Zn^{2+} .



(a) Charge/discharge cycling of E59 with no catalyst but only made of CNF and Ni powder bound with PTFE on Ni foam.

(b) Cyclic voltammetry in N₂ of NiCo₂O₄ and Ni powder showing nearly the same OER on-set potential

Figure 5.16: Results of the electrochemical characterization of E59 (no catalyst) and comparison between CVs of NiCo₂O₄ and Ni powder.

Figure 5.16(b) shows comparative CV diagrams (10th cycle) obtained of NiCo₂O₄ and pure nickel powder with particle sizes < 50 μm . Usually, when stored in air, nickel forms an oxide layer (NiO), but when put into an aqueous electrolyte already at OCP a Ni(OH)₂ surface is formed, whereby first a poorly crystalline α -Ni(OH)₂ phase is obtained. After repeated cycling a more crystalline β -Ni(OH)₂ phase is formed, which usually exhibits higher OER activity [155]. Although the redox peaks in Figure 5.16(b) are very different with the spinel showing a broad nickel peak at lower potentials and the pure nickel powder a more defined oxidation peak at 1.4 V vs. RHE and a reduction peak at 1.35 V vs. RHE, the NiCo₂O₄ catalyst only exhibited a slightly better OER potential at 1 mA cm⁻² with 1.49 V vs. RHE compared to 1.50 V vs. RHE of the Ni powder, respectively.

In conclusion to the RDE measurements of NiCo₂O₄ spinel and the electrochemical testing of the blank support-only electrode E59, it was argued, that the spinel is well suitable as either ORR or OER catalyst, but that its bifunctional stability is insufficient and its laborious synthesis procedure does not pay off, especially, when comparable OER potentials can also be achieved with fine commercial nickel powder only. These considerations are important in regard to the scalability of the electrode manufacturing process, where simple process steps and low-cost

materials are of high importance for scale-up of electrode sizes. Consequently, the following electrodes were only manufactured with the commercial $\text{La}_{0.6}\text{Sr}_{0.4}\text{Co}_{0.2}\text{Fe}_{0.8}\text{O}_3$ perovskite.

5.6 $\text{La}_{0.6}\text{Sr}_{0.4}\text{Co}_{0.2}\text{Fe}_{0.8}\text{O}_3$ -only Electrodes

Omitting $\text{NiCo}_2\text{O}_4/\text{CNF}$ and $\text{NiCo}_2\text{O}_4/\text{Ni}$ powder catalysts, which were the main compounds of the electrolyte-facing catalyst paste, significantly altered the overall air electrode structure. Thus many electrodes, some of them with a simplified build using only one paste, were manufactured and tested, but these electrodes mainly showed poor ORR performances. However, using nickel powder on the electrolyte-facing side resulted in overall good OER performances of $< 2.0\text{ V}$ vs. Zn/Zn^{2+} . The OER activity could further be increased by utilizing finer nickel powder with a particle size of 2.2-2.8 μm (type 2; by the US company Novamet). It was determined, that too thin electrodes of $< 0.5\text{ mm}$ thickness were prone to electrolyte leakage, even with a carbon paper backing layer. In addition, because of the use of a new Dyneon 3M PTFE suspension (type 2; TF5135 GZ; 58 wt%) the PTFE content in both catalyst pastes had to be optimized again.

After some testing, first good results were obtained with electrode E66 as shown in Figure 5.17. Electrode E66 comprised of 40% perovskite on CNF, 40% Novamet Ni powder and 20% of the new PTFE in the electrolyte paste. On the gas-supplied side, the paste consisted of 85% perovskite/CNF and 15% PTFE. One half of the electrode was backed with carbon paper (E66_1), whereas the second half had no additional backing (E66_2). With these two electrodes comparable performances to the previous bi-catalyzed air electrodes were achieved without the addition of NiCo_2O_4 spinel catalyst. The operation times were 850 h and 600 h, respectively, as shown in Figure 5.17. OER potentials were stable and low at about 1.90 V vs. Zn/Zn^{2+} and the respective ORR potentials were close to 1 V vs. Zn/Zn^{2+} for 200 cycles, thus achieving a voltage efficiency of over 50% ($\Delta V < 1\text{ V}$).

5.6.1 Additional Hydrophobic Backing Layer

As carbon paper proved to be very brittle and no significant improvement regarding stability and activity was observed, other hydrophobic backing materials were tested. From the company HighTechflon (Germany) two different types of PTFE-coated glass fiber cloth (one white wide-meshed and one brown close-meshed) were obtained and press-sintered as additional backing layer onto $\text{La}_{0.6}\text{Sr}_{0.4}\text{Co}_{0.2}\text{Fe}_{0.8}\text{O}_3$ -catalyzed air electrodes, which were manufactured similarly to

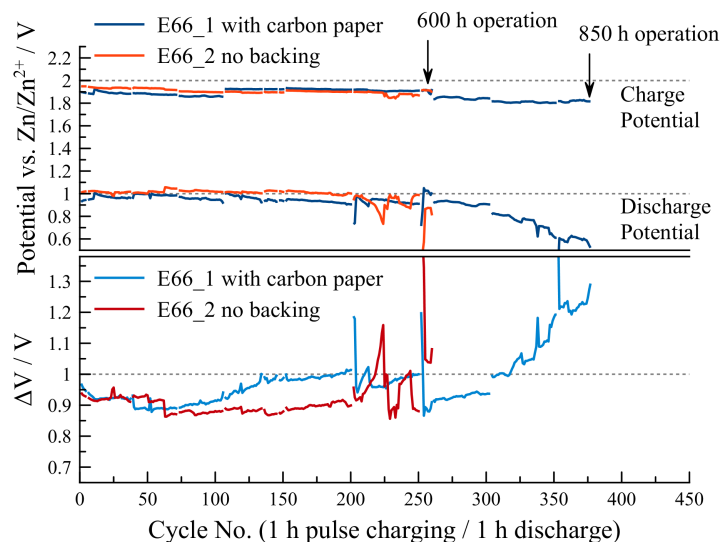
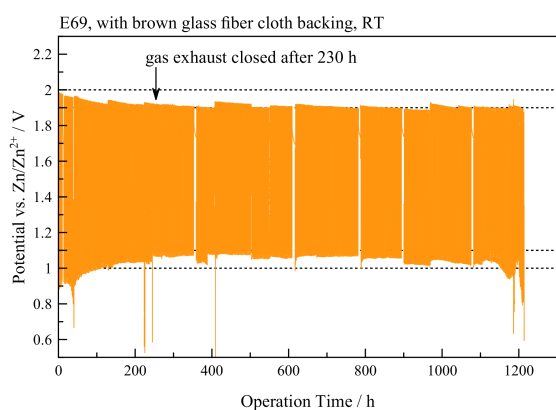


Figure 5.17: Long-term cycling measurement of E66_1 with carbon paper backing and E66_2 without additional hydrophobic layer.

E66. The glass fiber cloths attached very well during the press-sintering and exhibited a better heat-stability compared to the carbon paper (see Figure 5.18(b) (1) and (2)).

The results of the best of these electrodes E69 is shown in Figure 5.18(a), which achieved the longest operation time so far with 1200 h of testing and over 500 cycles at a potential difference $\Delta V < 1$ V (voltage efficiency $> 50\%$). Within the first 200 h of operation this electrode showed a significant improvement in charge as well as discharge potentials. However, the good ORR performance could only be maintained by closing the gas exhaust and allowing the CA to bubble through the electrode itself. This was probably caused by leakage of the electrode up to the glass fiber cloth and subsequent drying of the KOH within or close to the glass fiber cloth as well as formation of carbonates, which blocked the access to the electrode. Nevertheless, when enough oxygen supply was ensured (*i.e.* closing of the gas outlet after 230 h), stable ORR potentials as high as 1.05-1.09 V vs. Zn/Zn^{2+} were achieved. At the same time, the OER potentials were about 1.9 V vs. Zn/Zn^{2+} , which is the same performance as obtained with E66, showing the good OER activity of the $\text{La}_{0.6}\text{Sr}_{0.4}\text{Co}_{0.2}\text{Fe}_{0.8}\text{O}_3$ perovskite in combination with the nickel powder. As described by Han et al. [34], the OER activity in zinc-air batteries can benefit from the assistance of $\text{Ni}(\text{OH})_2/\text{NiOOH}$ redox couple functioning as a redox promoter. At the end of operation, the electrode was severely bulged inwards due to the high gas pressure and was completely detached from the glass-fiber cloth.

Nevertheless, E69 was the first electrode with which a long-term operation of over 1000 h only with the supply of compressed air (and not pure O_2 as shown in Fig.4 of the *Electrochimica Acta* publication in Appendix B) could be achieved. However, the glass fiber cloth was not suitable for application in the open set-up as shown in Figure 5.18(b) (3). After a few days of operation electrolyte droplets were visible on the backside, which easily leaked through the rather wide-meshed glass fiber cloth. As the good electrochemical performance was only achieved at high gas pressure and because the glass fiber cloth had no beneficial effect in the open set-up, this material was not further utilized as hydrophobic backing layer.



(a) Long-term operation of E69 at 50 mA cm^{-2} operated for 1200 h exhibiting low charge ($< 2 \text{ V}$ vs. Zn/Zn^{2+}) and exceptionally high discharge potentials ($> 1 \text{ V}$ vs. Zn/Zn^{2+}).



(b) Image of the backside (1) and side view (2) of the electrode after manufacture with the brown glass fiber cloth and image of electrode (E72) in the open set-up with the white glass fiber cloth (3).

Figure 5.18: Electrochemical characterization of E69 with additional PTFE-coated glass fiber cloth backing operated with CA supply and images of electrodes with this backing layer.

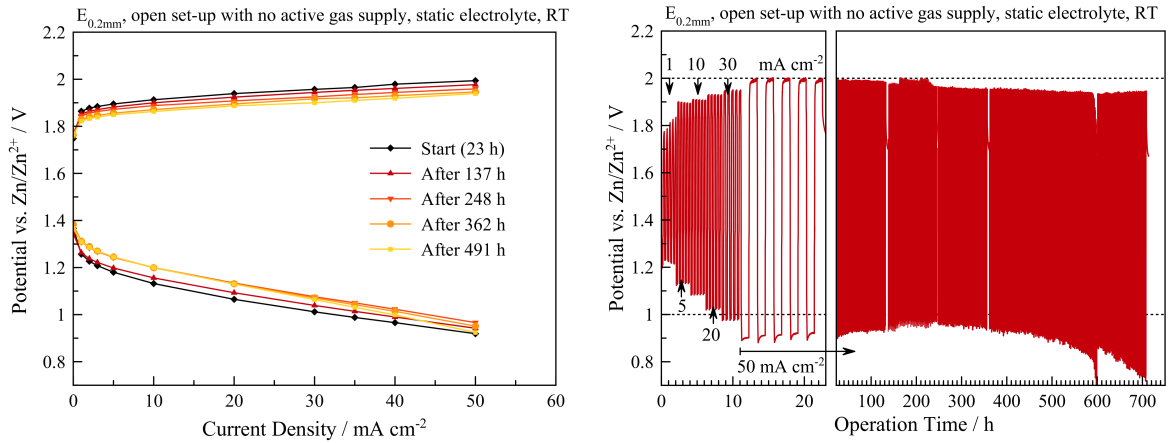
In the next test series, different PTFE filter foils (A4 sized sheets) were obtained by the company BOLA (Germany) and investigated. In the master thesis of Douglas Allan (exchange student University of Strathclyde) titled *Development of Stable and Efficient Bifunctional Air Electrodes for Zinc-air Flow Battery Systems*, several electrodes with these PTFE filter foils as backing material were presented and also first full-cell tests in the small flow set-up (4 cm^2 sized air electrodes) were carried out within the framework of this master thesis.

The first employed PTFE filter foil had a thickness of 1.0 mm and a pore size of $10 \mu\text{m}$. As the maximum temperature of this material was specified as $250 \text{ }^\circ\text{C}$ the manufacturing process had to be adapted. While $300 \text{ }^\circ\text{C}$ sinter temperature are required for obtaining a good distribution of the PTFE suspension utilized in the electrode pastes (softening of the material) as well as for

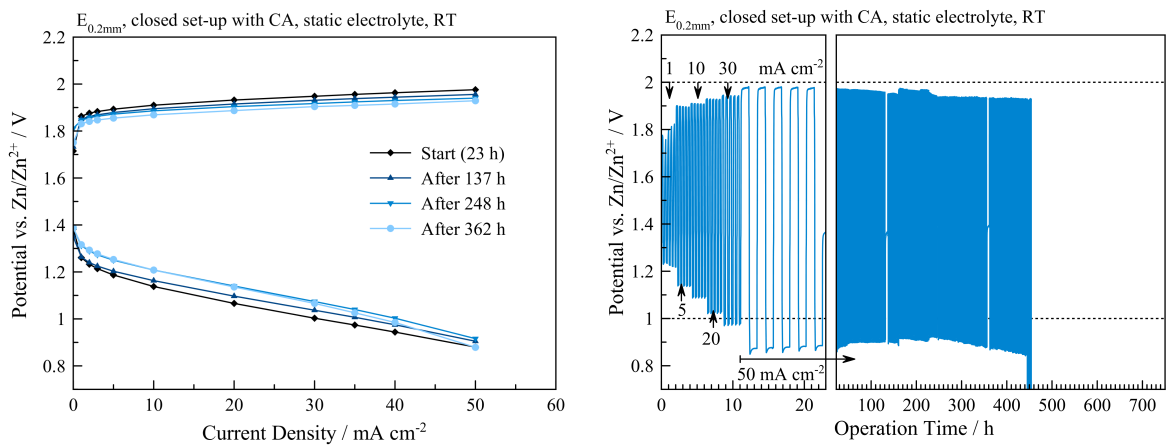
decomposing the added emulsifier contained in the suspension, the fine porous structure of the filter foil is in return destroyed at too high temperatures. After a few tests, the best results were achieved by first sintering the electrode at 300 °C and 150 kg cm⁻² and then attaching the filter foil in a second press-sintering step at 200 °C. However, the electrodes fabricated with this rather thick filter foil exhibited always severe diffusion limitations at > 30 mA cm⁻² discharge current density. This was attributed to the long gas diffusion paths through the 1.0 mm thick foil. Thus, a thinner membrane with 0.2 mm thickness (again pore size 10 μm) was obtained, attached as described above (slightly unevenly pressed as shown in Figure 5.20 (a)) and tested in long-term cycling at 50 mA cm⁻². The results of electrodes E_{0.2mm} (one half tested in the open set-up (red) and the other in the closed set-up with CA supply (blue)) is shown in Figure 5.19. Remarkably, for the first time the open set-up exhibited better charge/discharge potentials as well as a higher long-term stability than the electrode operated in the closed set-up with active gas supply.

E_{0.2mm} (open), shown in Figures 5.19(a) and 5.19(b), exhibited continuously improving OER performance, probably because of enhanced wetting of the electrode with electrolyte. Within the first 300 h also the ORR potentials gradually improved, indicating better catalyst utilization within the electrode. This conclusion can be drawn, because of the higher potentials obtained in the kinetic activation region up to 5 mA cm⁻² in the recorded ORR polarization curves. However, diffusion limitations at > 20 mA cm⁻² became apparent after 350 h of operation, indicating that the electrode became gradually flooded with electrolyte. The same trend was apparent for electrode E_{0.2mm} (closed) depicted in Figures 5.19(c) and 5.19(d). Again, very low OER potentials of about 1.93 V vs. Zn/Zn²⁺ at 50 mA cm⁻² were achieved. However after 250 h of operation, ORR became diffusion limited at current densities higher than 20 mA cm⁻² as can be seen in the ORR polarization curves. After 450 h the gas inlet dropped off, resulting in oxygen starvation conditions (thus water splitting and hydrogen evolution), which in consequence irreversibly damaged the electrode so that the measurements were stopped.

Although, the ORR performance of both electrodes stayed below 1.0 V vs. Zn/Zn²⁺, E_{0.2mm} (open) was the first electrode which could be operated in the open set-up without any electrolyte droplet visible on the backside of the electrode (shown in Figure 5.20 (b)) even after 700 h of operation (about 1 month). The thinner PTFE foil did not limit gas diffusion as was observed with the 1.0 mm foils, however, as expected, it functions as barrier for electrolyte permeability. This is of course on one hand desired as severe leakage of the highly alkaline electrolyte poses a safety issue and so far prevented the frequent utilization of the open set-up, but on the other



(a) Polarization curves of $E_{0.2\text{mm}}$ in the open set-up. (b) Long-term operation of $E_{0.2\text{mm}}$ in the open set-up.



(c) Polarization curves of $E_{0.2\text{mm}}$ in the closed set-up. (d) Long-term operation of $E_{0.2\text{mm}}$ in the closed set-up.

Figure 5.19: Results of the electrochemical characterization of $E_{0.2\text{mm}}$ with additional PTFE filter backing layer (0.2 mm thickness, 10 μm pore size) measured in the open set-up with no active gas supply (red) and in the closed set-up with CA (blue).

hand, the PTFE barrier does not solve the soaking problem of the air electrode, which was so far the main cause for termination of the long-term operation.

Nevertheless, of all tested materials applied as backing layer, which were hydrophobic carbon paper, two types of PTFE-coated glass fiber cloth and well as two types of PTFE filter foils with 10 μm pores size, the PTFE filter foil with a thickness of 0.2 mm was by far the most suitable material. Thus, its applicability for preventing electrolyte leakage was also tested in up-scaled 60 cm^2 sized electrodes (E86 and E87) as described in section 5.6.3.

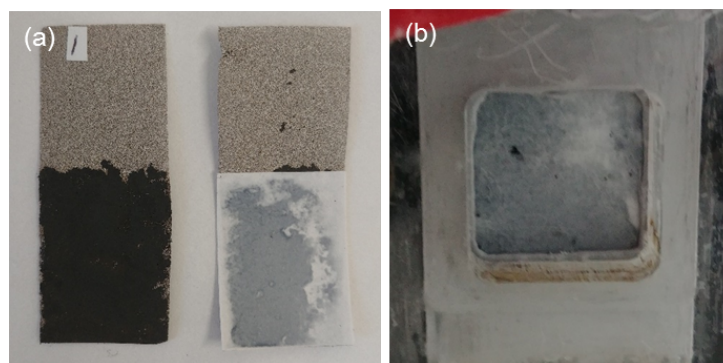
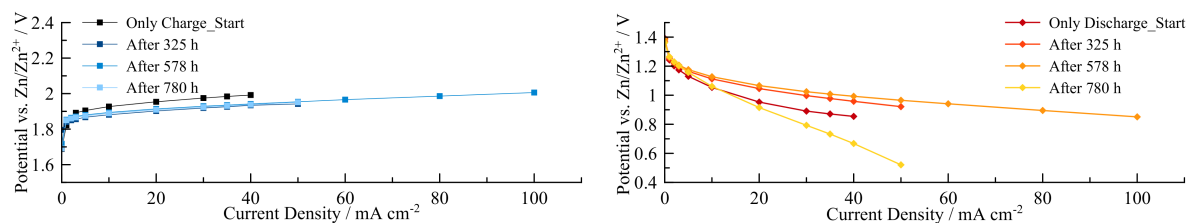
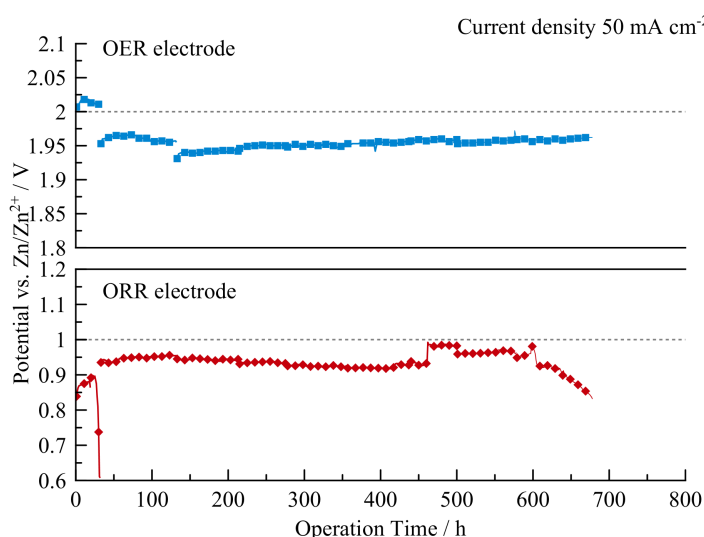


Figure 5.20: Image of $E_{0.2\text{mm}}$ after manufacture (a) with the PTFE filter foil on the gas-facing side, and (b) the built-in electrode after several days of measurement in the open set-up with no electrolyte droplets visible on the backside.

5.6.2 Operation of Air Electrodes without Cycling

As all of the electrodes described so far were tested as bifunctional air electrodes with improvement of their stability during continuous charge/discharge cycling as the main goal, their stability has never been assessed as purely charge (OER, anode mode) or discharge (ORR, cathode mode) electrode. This "benchmark" experiment was performed with electrode E77, again only catalyzed with $\text{La}_{0.6}\text{Sr}_{0.4}\text{Co}_{0.2}\text{Fe}_{0.8}\text{O}_3$ perovskite but without any backing layer (paste 1 with 40% perovskite/CNF, 40% Novamet Ni powder and 20% PTFE, paste 2 with 80% perovskite/CNF and 20% PTFE). Electrode E77 was cut in half and one part was always operated as anode for OER and the other half as cathode for ORR. The results of $E77_{\text{OER}}$ and $E77_{\text{ORR}}$ are depicted in Figure 5.21. Interestingly, the electrodes exhibited nearly the same performance (including the "activation" period) as well as long-term stability of 700 h as obtained with previous electrodes. Again, stable OER potentials were achieved, although this electrode looked greatly damaged after operation due to the constant bubble formation and high potentials of about 1.95 V vs. Zn/Zn^{2+}

during charging. The ORR electrode exhibited again good ORR potentials at about 0.95 V vs. Zn/Zn^{2+} until severe electrolyte leakage and precipitation on the backside - although repeatedly washed out - resulted in irreversible damage of the electrode after about 600 h of testing. The very good performance of both electrodes at current densities as high as 100 mA cm^{-2} can be seen in the polarization curves in Figures 5.21(a) and 5.21(b).

(a) Polarization curves of E77_{OER} (only anodic).(b) Polarization curves of E77_{ORR} (only cathodic).

(c) Separate long-term measurement of an OER and an ORR electrode.

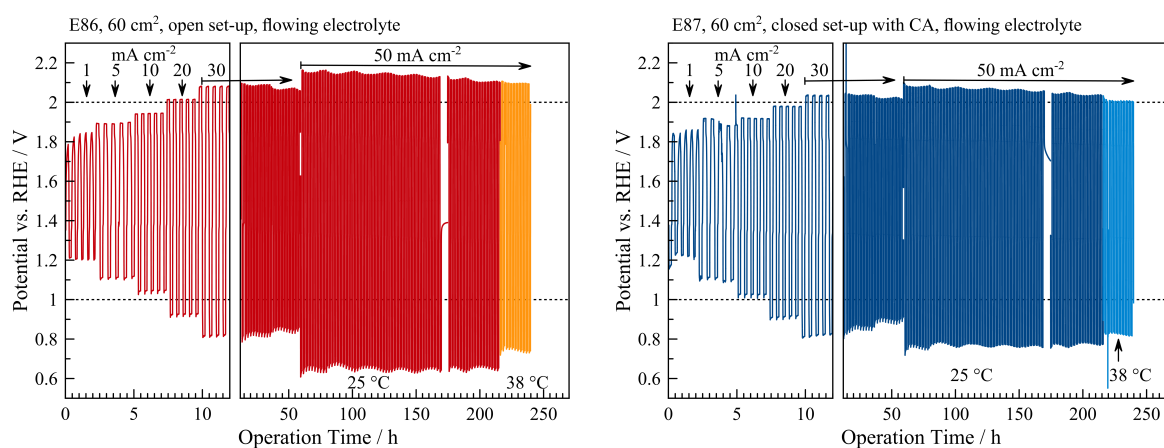
Figure 5.21: Electrochemical characterization of E77, where one half was only used as cathode (ORR) and the other as anode (OER).

In conclusion, this experiment shows, that the repeated potential cycling is not necessarily the reason for the slowly decreasing ORR potentials observed with so many electrodes. This indicated good stability of the CNF carbon towards high anodic potentials. Moreover, as nearly the same ORR and OER potentials were obtained with the cycled air electrodes as with the two E77 electrodes, it can be concluded that the $\text{La}_{0.6}\text{Sr}_{0.4}\text{Co}_{0.2}\text{Fe}_{0.8}\text{O}_3$ perovskite is not harmed by the repeated cycling procedure. This is in clear contrast to the NiCo_2O_4 spinel. The results show that optimization of the air electrodes stability as cathode is the most important issue for

obtaining highly stable bifunctional air electrodes. This can mainly be achieved by maintaining the electrode's hydrophobicity in the highly alkaline environment, which means that other more stable binder materials should be tested.

5.6.3 Scaled-up 60 cm²-sized Air Electrodes with Flowing Electrolyte

In parallel to the tests with the various backing layers, also the zinc-air flow cell set-up was further improved with the aim of demonstrating zinc-air unit cell operation with flowing electrolyte. In the small set-up with 4 cm² sized air electrodes, first full cells with zinc foil as second air electrodes operated with flowing electrolyte and with pulse charging were performed and very long operation times (1800 h) could be achieved (E84). The results and the set-up are described in the accepted peer-reviewed manuscript in the Appendix B (see also section 5.6.4).



(a) Long-term operation of E86 in the open set-up. (b) Long-term operation of E87 in the closed set-up.

Figure 5.22: Results of the electrochemical characterization of the 60 cm²-sized electrodes E86 and E87 with additional PTFE filter backing layer (0.2 mm thickness, 10 μm pore size) measured in the up-scaled blue test cell with flowing electrolyte with one side open set-up (red) and the second closed with active CA supply (blue).

In addition, a second flow test set-up was built, including a 1 L electrolyte reservoir for utilization of the 100 cm²-sized test cell designed by the *Luziflow* cooperation partner Hans-Jürgen Pauling from the German company RECAT GmbH (shown in the supporting information of the *Batteries & Supercaps* manuscript in Appendix B). Using PTFE templates, the 100 cm² openings of the cell were reduced to 50-60 cm² because of the limited maximal current of 3 A per channel of the BaSyTec potentiostat. The set-up was utilized for operation of unit-cells with a zinc and

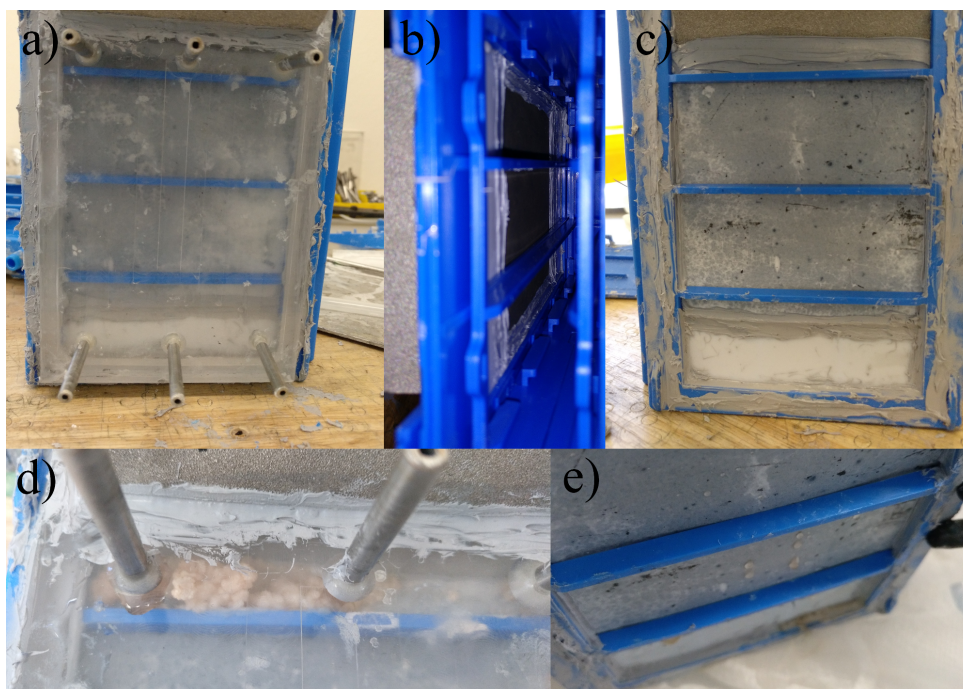


Figure 5.23: Image of 100 cm²-sized test cell with closed (a) and (d) and with open set-up (c) and (e). Top-view into the cell shown in (b).

an air electrode as described in the accepted peer-reviewed manuscript (see Appendix B) and shown in Figure 5.24, but also experiments with two air electrodes cycled against each other were performed with the larger-sized test cell (see Figure 5.22). Electrodes E86 and 87 had a size of 60 cm² and had both an additional PTFE filter foil membrane (0.2 mm) as investigated in section 5.6.1. The filter foil was press-sintered at 200 °C in an additional manufacturing step onto the gas side of the already press-sintered (300 °C) electrodes. E86 was measured in the open set-up (Figure 5.23(c)) and E87 had an additional sealed compartment for air supply on the backside (see image (a) in Figure 5.23) with three gas inlets on the top and three outlets at the bottom. In Figure 5.23 (b) the inside of the cell with the attached air electrode can be seen. The results of electrochemical cycling is depicted in Figures 5.22(a) and 5.22(b), respectively. Although both electrodes showed the "activation" behavior, both exhibited also about 100 mV lower ORR potentials compared to previous electrodes but also very high OER potentials of up to 2.1 V vs. Zn/Zn^{2+} , indicating severe ohmic or diffusion limited losses within the electrode. Also the increase of temperature (done by indirectly heating the electrolyte in the reservoir with heated water within steel tubes) did not improve the performance significantly. In the closed set-up, electrolyte precipitates (carbonates, KOH) were visible right at the gas inlet as can be seen in Figure 5.23 (d), which can probably be prevented by not directly blowing the air onto the

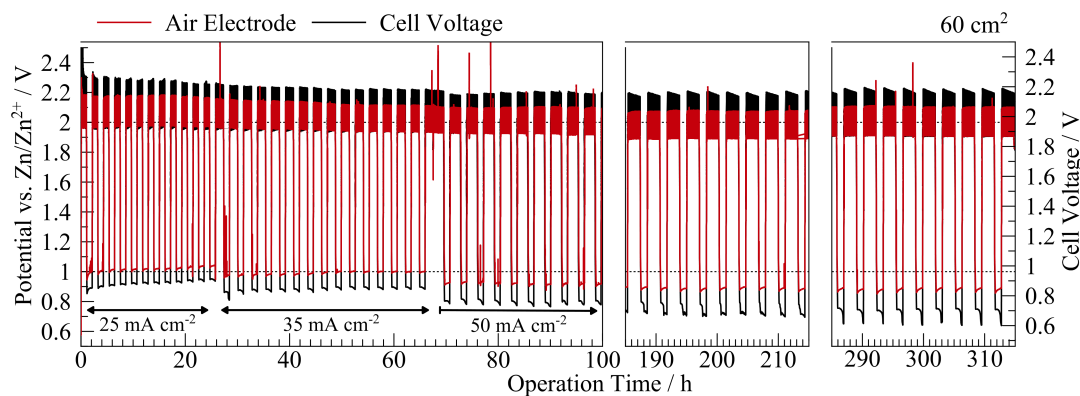


Figure 5.24: Results of the electrochemical characterization of the 60 cm²-sized electrodes E88 measured with a zinc electrode (unit zinc-air cell) in the up-scaled test cell with flowing electrolyte (1.5- 2 cm s⁻¹).

electrode itself at the inlets. The open set-up was more or less electrolyte tight, only a few small droplets were observable after 100 h of testing (Figure 5.23 (e)), again proving the applicability of the thin PTFE filter foil for usage in open set-up without any gas counter pressure to compensate the hydrostatic pressure from the electrolyte within the cell.

Electrode E88 was manufactured without any backing and tested in the closed set-up together with a zinc-foil as second electrode. The cell was operated via the air electrode using a zinc reference in order to obtain comparable results, but in addition the cell voltage as well as the zinc electrode potential (via a second Luggin capillary and zinc reference) were recorded as well. The air electrode potentials and the cell voltage measured during the 300 h long-term cycling are shown in Figure 5.24. These results of the 60 cm² electrode E88 in unit-cell operation were presented in a poster at the 4th *International Workshop on Hydrogen and Fuel Cells* in Graz, Austria. Although the performance of the air electrode was not as good as with the small set-up, the main issue was the uneven precipitation of zinc during the prolonged cycling even with pulse charging (50 ms pulse, 50 ms pause, duty cycle $\gamma = 0.5$). This can be attributed to the vertical set-up, the too slow flow velocities of only 1.5- 2 cm s⁻¹ (compared to the 8 cm s⁻¹ in the small flow set-up) or the reduced pulse currents. In the bigger cell the pulse currents had to be lowered to the limited maximum currents of the potentiostat, e.g. instead of 100 mA cm⁻² in the 50 ms pulse only 50 mA cm⁻² were applied. In consequence, the charging time had to be prolonged to 2 h to match the capacity of the 1 h discharge cycle.

The results in the up-scaled flow set-up show that minor problems like zinc corrosion and shape change in the small set-up proved to be severe problems in the bigger cells. The uneven gas

supply of the air electrode, the limited flow velocities and the more complicated sealing of the cell posed a significant challenge during operation of this larger-sized cell. Nevertheless, several hundred hours of operation could be achieved, which is much longer than many experiments carried out in other comparable publications (compare to Table 3.4.4 in the Theory section). Especially the recording of both half-cell potentials and the cell voltage proved to be very helpful in identifying the problems occurring within the closed cell. Nevertheless, a new, more easily assembled/disassembled test cell could further help to optimize the whole unit-cell allowing faster exchange of the two electrodes. In addition, tests with horizontal flow could prove beneficial for zinc deposition.

Further measurements with flowing electrolyte in unit cell operation (one air electrode and one zinc electrode) were summarized in a recently accepted manuscript as described in the following sub-chapter.

5.6.4 Peer-Reviewed Publication in *Batteries & Supercaps*

Title: "*Long-term Operation of Perovskite-catalyzed Bifunctional Air Electrodes in Rechargeable Zinc-Air Flow Batteries*"

Abstract

"Rechargeable zinc-air flow batteries are investigated as promising stationary energy storage system due to compact system design and low cost materials. Bifunctional air electrodes employing $\text{La}_{0.6}\text{Sr}_{0.4}\text{Co}_{0.2}\text{Fe}_{0.8}\text{O}_3$ perovskite catalyst for O_2 -reduction and O_2 - evolution are manufactured in small scale (4 cm^2) and in up-scaled sizes ($50-55\text{ cm}^2$) and tested in unit cell configuration with flowing electrolyte. Stable operation of 1000 h is achieved in the small set-up with an overall 1800 h of operation over 700 cycles at high voltage efficiencies of $> 50\%$ (air electrode) at 50 mA cm^{-2} . The up-scaled flow cell reaches nearly the same performance for 320 h and 130 h, respectively, proving the successful scale-up. Slowly decreasing hydrophobicity is found to be the main reason of initially increasing but then decreasing performance. This is confirmed by electrochemical impedance spectroscopy. Although many problems are suppressed with flowing electrolyte, zinc morphology proves to be the major challenge especially in larger cells in long-term operation of a few hundred hours."

The printed form as well as the supplementary information can be found in Appendix B.

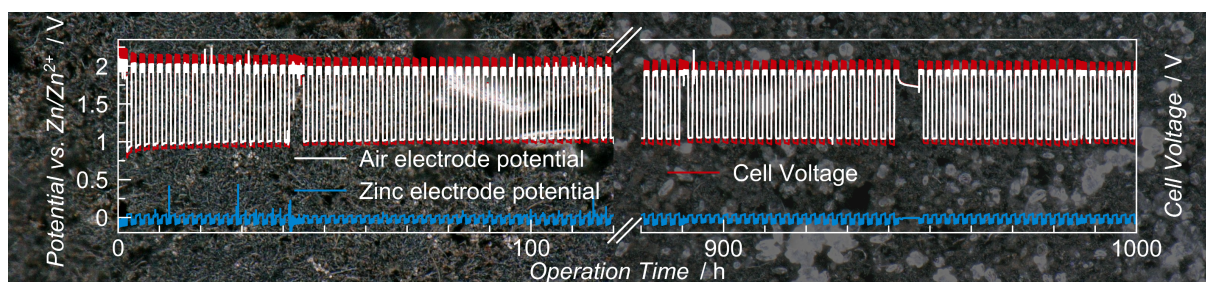


Figure 5.25: Graphical abstract to the publication in *Batteries & Supercaps* with the text "**One more cycle:** $\text{La}_{0.6}\text{Sr}_{0.4}\text{Co}_{0.2}\text{Fe}_{0.8}\text{O}_3$ perovskite is implemented as highly active bifunctional catalyst in optimized air electrode architecture and reaches 1000 h (500 cycles) of stable performance at 50 mA cm^{-2} (see picture). Up-scaled 50 cm^2 -sized zinc-air cells are investigated by means of electrochemical impedance spectroscopy and operated for 300 h. Loss of hydrophobicity is found to be the main reason for slowly decreasing performance of the air electrode."

The manuscript found in Appendix B was accepted in the journal *Batteries & Supercaps* in its special issue on "Bifunctional Catalysts for Metal–Air Batteries" (invited). It comprises results of a small-scale flow battery and two larger-sized full-cells tested in the bigger flow set-up. The air electrodes presented in this publication were E84, E85 and E90. Special focus lay on investigating the degradation behavior of the air electrode by recording polarization curves and electrochemical impedance spectra as well as by performing end-of-life characterization by light microscopy. It was found that decreasing hydrophobicity over time results in initially improving but then degrading performance, which mainly affects the ORR potentials. Nevertheless, the small test cell employing E84 reached 1800 h of operation and stable charge and discharge potentials for 1000 h, which is the longest measurement time achieved within this project.

All authors contributed to the publication. Kurt Mayer recorded, evaluated and interpreted the electrochemical impedance spectra and Viktor Hacker supervised the work.

This is the peer-reviewed version of the following article: *Long-term Operation of Perovskite-catalyzed Bifunctional Air Electrodes in Rechargeable Zinc-Air Flow Batteries*, which has been published in final form at DOI:10.1002/batt.201800094. This article may be used for non-commercial purposes in accordance with Wiley-VCH Terms and Conditions for Self-Archiving.

6 Summary and Conclusion

In this work bifunctional air electrodes for application in rechargeable alkaline zinc-air flow batteries were developed and electrochemically characterized. These electrodes achieved good bifunctional catalytic activity toward oxygen reduction reaction (ORR) as well as oxygen evolution reaction (OER) with a charge/discharge efficiency of over 50% at current densities of 50 mA cm^{-2} . The employed precious metal-free oxide catalysts, which reached this high catalytic activity, were NiCo_2O_4 spinel and $\text{La}_{0.6}\text{Sr}_{0.4}\text{Co}_{0.2}\text{Fe}_{0.8}\text{O}_3$ perovskite, but during the project it was found that the spinel was not sufficiently stable for repeated cycling operation. The commercially acquired $\text{La}_{0.6}\text{Sr}_{0.4}\text{Co}_{0.2}\text{Fe}_{0.8}\text{O}_3$ perovskite proved to be the best choice of all the investigated catalysts, both regarding the activity as well as the stability. With this catalyst reproducible and comparable performances in both small and larger-scaled electrodes up to 60 cm^2 were achieved. Incorporating these catalysts was successfully achieved by using corrosion resistant carbon nanofibers for good electrical connectivity of the low-conductive oxide catalyst particles, hydrophobic PTFE as binder material and nickel foam as mechanically stable current collector. In addition, by adding fine nickel powder a better catalytic activity toward OER was obtained.

After optimization of the electrode composition including the balancing of the hydrophobicity of the electrode, these custom-made air electrodes were electrochemically characterized in half-cell and full unit cell set-ups with focus on the long-term performance. The best small-scale air electrode with 4 cm^2 was operated for 1800 h and over 800 charge/discharge cycles at 50 mA cm^{-2} in a full unit zinc-air cell with flowing electrolyte. No significant degradation of the ORR and OER potentials were observed for nearly 1000 h and a voltage efficiency of $> 50\%$ was maintained for 700 cycles.

For minimizing dendrite growth on the zinc electrode, the zinc-air flow cells were charged by pulsed currents. The optimized air electrodes were not harmed by the pulse interrupt charging method, although doubled/tripled charging current densities were applied. The maximum charging potentials were about 2.1 V vs. Zn/Zn^{2+} , which proves the viability of this method for

operation of full zinc-air flow batteries without accelerated degradation of the air electrode. The flowing electrolyte with surface flow velocities of up to 8 cm s^{-1} did not harm the air electrode by shearing off the catalyst layers from the current collector. In fact, a more constant charge potential was observed during OER due to the out-take of generated oxygen bubbles and due to reduced concentration gradients within the constantly mixed electrolyte .

Scaling-up of the manufacturing process was successfully performed for electrode sizes up to 100 cm^2 . A first long-term cycling test had to be stopped due to high electrolyte leakage in the open set-up, but through the addition of a closed air compartment and by applying a slight gas pressure to counteract the hydrostatic pressure of the electrolyte within the cell, 60 cm^2 -sized air electrodes reached 300 h of operation in full unit-cell zinc-air flow cell. Moreover, these larger air electrodes achieved nearly the same charge/discharge performances as the air electrode in the small set-up with charging potentials of $< 2.0 \text{ V}$ and discharge potentials of about 1.0 V vs. Zn/Zn^{2+} . In addition, electrolyte leakage in an open set-up can be prevented by employing PTFE filter foils with $10 \mu\text{m}$ pore size on the air supplied side.

Additional characterization of the catalysts as well as end-of-life investigations of the electrodes were carried out by means of scanning electron microscopy (SEM), energy dispersive X-ray spectroscopy (EDX), X-ray diffraction experiments (XRD), light microscopy and contact angle measurements. By this, the composition of the NiCo_2O_4 catalyst, the homogeneous distribution of the perovskite catalyst on carbon nanofiber support, the morphology of the electrode surface as well as its hydrophobicity were investigated. After operation the electrodes appeared cracked with micrometer-sized holes in the carbon nanofiber network and the hydrophobicity was significantly reduced. Electrochemical impedance spectroscopy (EIS) of the air electrode was applied for obtaining knowledge of the mechanisms within the electrode. By observing the change in charge transfer resistance (R_{ct}) over time, information on the kinetics of ORR and OER and thus conclusions on changes regarding the catalytic sites (three-phase zones) could be obtained. A change in R_{ct} was, for example, apparent in the "activation" period within the first 50 h of operation. The slow improvement of charge/discharge potentials and the reduction in R_{ct} was attributed to a gradually improved wettability of the electrode with electrolyte.

For most of the tested air electrodes, regardless of the operating conditions (flow, air supply, size), the end-of-life was reached because of too low oxygen reduction potentials during discharge, whereas the OER potentials remained constant for the whole operation time. As the ORR is very sensitive to the electrode structure due to the requirement of three-phase zones

(gas/electrolyte/conductive catalyst), mechanical and chemical degradation effects are mainly apparent in the slowly decreasing discharge potentials. This is caused by a slow flooding of the air electrode resulting in increasingly long diffusion paths for the gas to the catalytic sites so that ORR becomes diffusion limited. SEM imaging of the electrodes after operation confirmed that on the one hand mechanical degradation caused by bubble formation during oxygen evolution slowly degraded the fine porous structure. On the other hand, contact angle measurements exhibited a significant reduction in hydrophobicity, especially of the electrolyte facing side of the air electrode. This change was slowly over the course of 200-300 h.

Improvements in long-term stability have to be tackled in this regard, both by manufacturing even more robust structures with more stable materials (e.g., substitute PTFE binder) and by keeping the anodic charging potentials during OER as low as possible. Especially for the small air electrode, changes in hydrophobicity - primarily on the electrolyte facing side by PTFE degradation - was found to be the main cause of initially slowly improving (about first 50 h) but then gradually decreasing ORR performance. Because of the rather low charging potentials of below 2.0 V, carbon corrosion was minimized in this current density range as the nearly colorless electrolyte proved and also the catalyst itself exhibited high stability throughout repeated cycling in this broad potential range. Thus, further optimization has to be tackled in regard to the hydrophobic binder material.

Although many problems could be suppressed with flowing electrolyte, inhomogeneous zinc morphology proved to be a major challenge, especially in the up-scaled cell under the conditions of long-term operation of a few hundred hours. For reaching operation times of > 1000 h also for the larger sized zinc-air cell, the design of the test cell as well as the zinc electrode have to be improved. Maintenance intervals have to be minimized in order to circumvent the issues related to dry-out and incomplete sealing of the cell, which were the main cause of decreasing performance or sudden end-of-life of the larger-sized air electrodes.

7 Materials and Instruments

7.1 Chemicals

All chemicals were used as purchased without further purification.

- Carbon nanofibers (CNF): Electrovac AG (Austria), type HTF150FF-LHT, 150 nm, lowheat
- Nickel foam (Type 2): Alantum Corporation (Germany), pore size 580 μm , area density 420 g m^{-2} , thickness 2.0 mm
- Nickel foam (Type 2): Alantum Corporation (Germany), pore size 450 μm , area density 420 g m^{-2} , thickness 1.6 mm
- Nickel mesh: G. BOPP + CO. AG (Switzerland); w=0.510 mm, d=0.150 mm, >99.7%
- Nickel cloth: G. BOPP + CO. AG (Switzerland); broad mesh 200x600 mesh; >99.7%
- Polytetrafluorethylene (PTFE) suspension (Type 1): 3M Dyneon; TF 5032; 68.6 wt% \pm 0.1%, 5 wt% emulsifier, 160 nm; used for electrodes E1-E62
- Polytetrafluorethylene (PTFE) suspension (Type 2): 3M Dyneon; TF5135 GZ; 58 wt%, 5.5 wt% emulsifier, 190 nm; used for electrodes > E63
- Polytetrafluorethylene powder: DuPont; type 601X
- 2-propanol ACS grade \geq 99.8% (Sigma-Aldrich)
- Ultrapure 18 M Ω H₂O
- Potassium hydroxide (KOH): Sigma-Aldrich, pellets \geq 85%
- Nickel(II)nitrate hexahydrate (Ni(NO₃)₂ · 6 H₂O): Sigma-Aldrich; purum p.a., crystallized, \geq 97%
- Cobalt(II)nitrate hexahydrate (Co(NO₃)₂ · 6 H₂O): Sigma-Aldrich; A.C.S. reagent, 98+%

- Lanthanum strontium cobalt ferrite ($\text{La}_{0.6}\text{Sr}_{0.4}\text{Co}_{0.2}\text{Fe}_{0.8}\text{O}_3$): Sigma Aldrich, surface area $10\text{-}14\text{ m}^2\text{ g}^{-1}$, size $d_{50}=0.4\text{-}0.8\text{ }\mu\text{m}$
- $(\text{La}_{0.8}\text{Sr}_{0.2})_{0.95}\text{MnO}_{3-x}$: fuelcellmaterials (USA); surface area $18.1\text{ m}^2\text{ g}^{-1}$, size $d_{50}=0.48\text{ }\mu\text{m}$
- Nickel powder (Type 1): Sigma-Aldrich; $< 50\text{ }\mu\text{m}$, 99.7% trace metals basis, used in electrodes E1-E62
- Nickel powder (Type 2): Novamet Specialty Products Corp. (USA); Type 255, $2.2\text{-}2.8\text{ }\mu\text{m}$ particle size; used for electrodes $> \text{E63}$
- Black carbon VXC 72: Cabot Corporation
- Nitrogen (N_2): 5.0, Air Liquide (AlphagazTM)
- Oxygen (O_2): 5.0, Air Liquide (AlphagazTM)
- Synthetic Air ($\text{N}_2 + \text{O}_2$): 5.0, $\text{O}_2\ 20\pm 1\%$, Air Liquide (AlphagazTM)
- Zinc foil: Alfa Aesar; 1.6 mm thick, 99% metals basis
- Carbon paper (hydrophobic): not labeled, probably Sigracet or Toray paper
- PTFE-coated glass fiber cloth (white): HighTechflon Gbr (Germany); air permeable, mass 300 g m^{-2} , 0.35 mm
- PTFE-coated glass fiber cloth (brown): HighTechflon Gbr (Germany); air permeable, 15% PTFE, mass 240 g m^{-2} , 0.2 mm
- PTFE filter foil (filtering sheets): BOLA GmbH (Germany); type I: 0.2 mm thickness, $10\text{ }\mu\text{m}$ pore size; type II: 1.0 mm thickness, $10\text{ }\mu\text{m}$ pore size

7.2 Materials

- Poly(methyl methacrylate) (PMMA) plate: for test cell housing, thickness 1 cm or 2 cm
- Ethylene propylene diene monomer rubber (EPDM): gasket material; thickness 0.1 cm
- SMP (silane modified polymer): wedi (Germany); polymer adhesive sealant based on SMP, type 610

7.3 Instruments

- Hydrogen Reference Electrode (RHE): Gaskatel GmbH (Germany), type: HydroFlex®
- Battery Cell Test System: BaSyTec GmbH (Germany); type CTS Lab
- Ultrasonic Finger: Hielscher GmbH (Germany), type: UP 400S; 4 A/200-240 V
- Press: Fontune (Netherlands); max. 20 t/300 °C
- Muffle Furnace: Elsklo, Type LNT15G/1320 °C/5.5 kW/Dicon
- Scanning Electron Microscope: Tescan, type: Vega3
- Secondary Electron Detector: Tescan, type: Low Vacuum Secondary Electron Detector 500 PA (Software: VegaTC)
- Energy Dispersive X-ray detector: Oxford Instruments; type: INCA x-act (Software: Inca)
- Sputter Coater (Au): Cressington; type: 108 auto 4 Experimental 69
- Contact Angle Measurement (Drop Shape Analyzer): Krüss; type: DSA100
- X-Ray Diffractometer: Bruker, type: D8 Advance; $\text{CuK}\alpha$, LYNXEYE detector, 20.00 – 100.00 [2θ], step size [2θ]: 0.0200, step time: 2 s/step (Rietveld software: X'Pert HighScore Plus by PANalytical and Topas by Bruker)
- Potentiostat for cyclic voltammetry: Gamry Instruments, type: Reference 600 (Software: Gamry Instruments Framework)
- Disk Electrode Tip: Pine Research Instrumentation, type: AFE5T050GC; glassy carbon area: 0.196 cm², max. 3000 rpm

8 References

- [1] Mukrimin Sevket Guney and Yalcin Tepe. “Classification and assessment of energy storage systems”. In: *Renewable and Sustainable Energy Reviews* 75.2016 (2017), pp. 1187–1197.
- [2] International Energy Agency. *Key World Energy Statistics 2017*. Tech. rep. 2017.
- [3] International Energy Agency. *Renewables Information 2017: Overview*. Tech. rep. 2017.
- [4] Stocker, V. Bex T.F., D. Qin, G.-K. Plattner, M. Tignor, S.K. Allen, J. Boschung, A. Nauels, Y. Xia, and P.M. Midgley (eds.) *IPCC, 2013: Summary for Policymakers*. Tech. rep. Cambridge, 2013.
- [5] Mathew Aneke and Meihong Wang. “Energy storage technologies and real life applications – A state of the art review”. In: *Applied Energy* 179 (2016), pp. 350–377.
- [6] Grigorios L. Kyriakopoulos and Garyfallos Arabatzis. “Electrical energy storage systems in electricity generation: Energy policies, innovative technologies, and regulatory regimes”. In: *Renewable and Sustainable Energy Reviews* 56 (2016), pp. 1044–1067.
- [7] Naga Srujana Goteti, Eric Hittinger, and Eric Williams. “How much wind and solar are needed to realize emissions benefits from storage?” In: *Energy Systems* (2017).
- [8] Christian Bussar et al. “Large-scale integration of renewable energies and impact on storage demand in a European renewable power system of 2050—Sensitivity study”. In: *Journal of Energy Storage* 6 (2016), pp. 1–10.
- [9] Mihaela Pacesila, Stefan Gabriel Burcea, and Sofia Elena Colesca. “Analysis of renewable energies in European Union”. In: *Renewable and Sustainable Energy Reviews* 56 (2016), pp. 156–170.
- [10] European Commission. *Roadmap 2050*. Tech. rep. April. 2012, pp. 1–9.
- [11] Sam Koochi-Kamali et al. “Emergence of energy storage technologies as the solution for reliable operation of smart power systems: A review”. In: *Renewable and Sustainable Energy Reviews* 25 (2013), pp. 135–165.

-
- [12] EASE/EERA. *European Energy Storage Technology Development Roadmap. 2017 Update*. Tech. rep. 2017.
- [13] Omid Palizban and Kimmo Kauhaniemi. “Energy storage systems in modern grids—Matrix of technologies and applications”. In: *Journal of Energy Storage* 6 (2016), pp. 248–259.
- [14] Sbc Energy Institute. *Hydrogen-Based Energy Conversion - More than storage: System flexibility*. Tech. rep. 2014, p. 9.
- [15] T.M.I. Mahlia et al. “A review of available methods and development on energy storage; technology update”. In: *Renewable and Sustainable Energy Reviews* 33 (2014), pp. 532–545.
- [16] Behnam Zakeri and Sanna Syri. “Electrical energy storage systems: A comparative life cycle cost analysis”. In: *Renewable and Sustainable Energy Reviews* 42 (2015), pp. 569–596.
- [17] S. Ould Amrouche et al. “Overview of energy storage in renewable energy systems”. In: *International Journal of Hydrogen Energy* 41.45 (2016), pp. 20914–20927.
- [18] J.D. Holladay et al. “An overview of hydrogen production technologies”. In: *Catalysis Today* 139.4 (2009), pp. 244–260.
- [19] Yanguang Li and Jun Lu. “Metal–Air Batteries: Will They Be the Future Electrochemical Energy Storage Device of Choice?” In: *ACS Energy Letters* 2.6 (2017), pp. 1370–1377.
- [20] Cyrus Wadia, Paul Albertus, and Venkat Srinivasan. “Resource constraints on the battery energy storage potential for grid and transportation applications”. In: *Journal of Power Sources* 196.3 (2011), pp. 1593–1598.
- [21] Jaephil Cho, Sookyung Jeong, and Youngsik Kim. “Commercial and research battery technologies for electrical energy storage applications”. In: *Progress in Energy and Combustion Science* 48 (2015), pp. 84–101.
- [22] Elaheh Davari and Douglas G. Ivey. “Bifunctional electrocatalysts for Zn–air batteries”. In: *Sustainable Energy & Fuels* 2.1 (2018), pp. 39–67.
- [23] Peng Gu et al. “Rechargeable zinc–air batteries: a promising way to green energy”. In: *Journal of Materials Chemistry A* 5.17 (2017), pp. 7651–7666.
- [24] Yanguang Li and Hongjie Dai. “Recent advances in zinc–air batteries”. In: *Chemical Society Reviews* 43.15 (2014), pp. 5257–5275.
- [25] O. Haas and J. Van Wesemael. “SECONDARY BATTERIES – METAL-AIR SYSTEMS | Zinc–Air: Electrical Recharge”. In: *Encyclopedia of Electrochemical Power Sources*. Elsevier, 2009, pp. 384–392.

- [26] Jing Pan et al. “Advanced Architectures and Relatives of Air Electrodes in Zn-Air Batteries”. In: *Advanced Science* 5.4 (2018), p. 1700691.
- [27] A. Khor et al. “Review of zinc-based hybrid flow batteries: From fundamentals to applications”. In: *Materials Today Energy* 8 (2018), pp. 80–108.
- [28] Jing Fu et al. “Electrically Rechargeable Zinc-Air Batteries: Progress, Challenges, and Perspectives”. In: *Advanced Materials* 29.7 (2017), p. 1604685.
- [29] Dong Un Lee et al. “Recent progress and perspectives on bi-functional oxygen electrocatalysts for advanced rechargeable metal–air batteries”. In: *Journal of Materials Chemistry A* 4.19 (2016), pp. 7107–7134.
- [30] M. Xu et al. “Rechargeable Zn-air batteries: Progress in electrolyte development and cell configuration advancement”. In: *Journal of Power Sources* 283 (2015), pp. 358–371.
- [31] Pucheng Pei, Keliang Wang, and Ze Ma. “Technologies for extending zinc–air battery’s cyclelife: A review”. In: *Applied Energy* 128 (2014), pp. 315–324.
- [32] Aroa R. Mainar et al. “A brief overview of secondary zinc anode development: The key of improving zinc-based energy storage systems”. In: *International Journal of Energy Research* 42.3 (2018), pp. 903–918.
- [33] Aroa R. Mainar et al. “An overview of progress in electrolytes for secondary zinc-air batteries and other storage systems based on zinc”. In: *Journal of Energy Storage* 15 (2018), pp. 304–328.
- [34] Xiaopeng Han et al. “Metal-Air Batteries: From Static to Flow System”. In: *Advanced Energy Materials* 8.27 (2018), p. 1801396.
- [35] Keith F. Blurton and Anthony F. Sammells. “Metal/air batteries: Their status and potential — a review”. In: *Journal of Power Sources* 4.4 (1979), pp. 263–279.
- [36] Luis F. Arenas et al. “The characteristics and performance of hybrid redox flow batteries with zinc negative electrodes for energy storage”. In: *Renewable and Sustainable Energy Reviews* 90 (2018), pp. 992–1016.
- [37] A.J. Appleby and M. Jacquier. “The C.G.E. circulating zinc/air battery: A practical vehicle power source”. In: *Journal of Power Sources* 1.1 (1976), pp. 17–34.
- [38] Dengjie Chen et al. “Nonstoichiometric Oxides as Low-Cost and Highly-Efficient Oxygen Reduction/Evolution Catalysts for Low-Temperature Electrochemical Devices”. In: *Chemical Reviews* 115.18 (2015), pp. 9869–9921.

-
- [39] Vincenzo Caramia and Benedetto Bozzini. “Materials science aspects of zinc–air batteries: a review”. In: *Materials for Renewable and Sustainable Energy* 3.2 (2014), p. 28.
- [40] Ludwig Jörissen. “Bifunctional oxygen/air electrodes”. In: *Journal of Power Sources* 155.1 (2006), pp. 23–32.
- [41] Jang-Soo Lee et al. “Metal-Air Batteries with High Energy Density: Li-Air versus Zn-Air”. In: *Advanced Energy Materials* 1.1 (2011), pp. 34–50.
- [42] Nika Mahne et al. “Mechanism and performance of lithium-oxygen batteries—a perspective”. In: *Chemical Science* 8.10 (2017), pp. 6716–6729.
- [43] Jonathan Goldstein, Ian Brown, and Binyamin Koretz. “New developments in the Electric Fuel Ltd. zinc/air system”. In: *Journal of Power Sources* 80.1 (1999), pp. 171–179.
- [44] Yanguang Li et al. “Advanced zinc-air batteries based on high-performance hybrid electrocatalysts”. In: *Nature Communications* 4.1 (2013), p. 1805.
- [45] Jing Fu et al. “Flexible Rechargeable Zinc-Air Batteries through Morphological Emulation of Human Hair Array”. In: *Advanced Materials* 28.30 (2016), pp. 6421–6428.
- [46] Mohammed Harun Chakrabarti et al. “Prospects of applying ionic liquids and deep eutectic solvents for renewable energy storage by means of redox flow batteries”. In: *Renewable and Sustainable Energy Reviews* 30 (2014), pp. 254–270.
- [47] L. Vieira, a. H. Whitehead, and B. Gollas. “Mechanistic Studies of Zinc Electrodeposition from Deep Eutectic Electrolytes”. In: *Journal of the Electrochemical Society* 161.1 (2013), pp. D7–D13.
- [48] Babu R. Chalamala et al. “Redox Flow Batteries: An Engineering Perspective”. In: *Proceedings of the IEEE* 102.6 (2014), pp. 976–999.
- [49] Minjoon Park et al. “Material design and engineering of next-generation flow-battery technologies”. In: *Nature Reviews Materials* 2.1 (2017), p. 16080.
- [50] L.F. Arenas, C. Ponce de León, and F.C. Walsh. “Engineering aspects of the design, construction and performance of modular redox flow batteries for energy storage”. In: *Journal of Energy Storage* 11 (2017), pp. 119–153.
- [51] B. Amunátegui et al. “Electrochemical energy storage for renewable energy integration: zinc-air flow batteries”. In: *Journal of Applied Electrochemistry* 48.6 (2018), pp. 627–637.

- [52] Marina Bockelmann, Ulrich Kunz, and Thomas Turek. “Electrically rechargeable zinc-oxygen flow battery with high power density”. In: *Electrochemistry Communications* 69 (2016), pp. 24–27.
- [53] Junqing Pan et al. “Preliminary study of alkaline single flowing Zn–O₂ battery”. In: *Electrochemistry Communications* 11.11 (2009), pp. 2191–2194.
- [54] Hongyun Ma et al. “Development and Characterization of an Electrically Rechargeable Zinc-Air Battery Stack”. In: *Energies* 7.10 (2014), pp. 6549–6557.
- [55] S. Müller et al. “Development of a 100 W rechargeable bipolar zinc/oxygen battery”. In: *Journal of Applied Electrochemistry* 28.3 (1998), pp. 305–310.
- [56] Keliang Wang et al. “Advanced rechargeable zinc-air battery with parameter optimization”. In: *Applied Energy* 225 (2018), pp. 848–856.
- [57] Damon E. Turney et al. “Development and testing of an economic grid-scale flow-assisted zinc/nickel-hydroxide alkaline battery”. In: *Journal of Power Sources* 264 (2014), pp. 49–58.
- [58] Dong Un Lee et al. “Self-Assembled NiO/Ni(OH)₂ Nanoflakes as Active Material for High-Power and High-Energy Hybrid Rechargeable Battery”. In: *Nano Letters* 16.3 (2016), pp. 1794–1802.
- [59] Fangyi Cheng and Jun Chen. “Metal–air batteries: from oxygen reduction electrochemistry to cathode catalysts”. In: *Chemical Society Reviews* 41.6 (2012), p. 2172.
- [60] Johannes Stamm et al. “Modeling nucleation and growth of zinc oxide during discharge of primary zinc-air batteries”. In: *Journal of Power Sources* 360 (2017), pp. 136–149.
- [61] Yasumasa Ito et al. “An indicator of zinc morphology transition in flowing alkaline electrolyte”. In: *Journal of Power Sources* 211 (2012), pp. 119–128.
- [62] Nima Shaigan, Wei Qu, and Tabitha Takeda. “Morphology Control of Electrodeposited Zinc from Alkaline Zincate Solutions for Rechargeable Zinc Air Batteries”. In: *ECS Transactions*. Vol. 28. 32. 2010, pp. 35–44.
- [63] Christian Zelger et al. “Rota-Hull Cell Study on Pulse Current Zinc Electrodeposition from Alkaline Electrolytes”. In: *Electrochimica Acta* 213 (2016), pp. 208–216.
- [64] Aleksandra Gavrilović-Wohlmuther et al. “Effects of Electrolyte Concentration, Temperature, Flow Velocity and Current Density on Zn Deposit Morphology”. In: *Journal of Energy and Power Engineering* 9.11 (2015), pp. 1019–1028.

-
- [65] Keliang Wang et al. “Dendrite growth in the recharging process of zinc–air batteries”. In: *Journal of Materials Chemistry A* 3.45 (2015), pp. 22648–22655.
- [66] Yinlong Zhu, Wei Zhou, and Zongping Shao. “Perovskite/Carbon Composites: Applications in Oxygen Electrocatalysis”. In: *Small* 13.12 (2017), p. 1603793.
- [67] Shiva Gupta et al. “Bifunctional Perovskite Oxide Catalysts for Oxygen Reduction and Evolution in Alkaline Media”. In: *Chemistry - An Asian Journal* 11.1 (2016), pp. 10–21.
- [68] Wesley T Hong et al. “Toward the rational design of non-precious transition metal oxides for oxygen electrocatalysis”. In: *Energy & Environmental Science* 8.5 (2015), pp. 1404–1427.
- [69] Jin Suntivich et al. “Design principles for oxygen-reduction activity on perovskite oxide catalysts for fuel cells and metal–air batteries”. In: *Nature Chemistry* 3.7 (2011), pp. 546–550.
- [70] Zhi Wei She et al. “Combining theory and experiment in electrocatalysis: Insights into materials design”. In: *Science* 355.6321 (2017).
- [71] Isabela C. Man et al. “Universality in Oxygen Evolution Electrocatalysis on Oxide Surfaces”. In: *ChemCatChem* 3.7 (2011), pp. 1159–1165.
- [72] Jin Suntivich et al. “A Perovskite Oxide Optimized for Oxygen Evolution Catalysis from Molecular Orbital Principles”. In: *Science* 334.6061 (2011), pp. 1383–1385.
- [73] Jaka Sunarso et al. “Oxygen reduction reaction activity of La-based perovskite oxides in alkaline medium: A thin-film rotating ring-disk electrode study”. In: *Journal of Physical Chemistry C* 116.9 (2012), pp. 5827–5834.
- [74] Chunyu Zhu et al. “Solution combustion synthesis of LaMO₃ (M = Fe, Co, Mn) perovskite nanoparticles and the measurement of their electrocatalytic properties for air cathode”. In: *International Journal of Hydrogen Energy* 38.30 (2013), pp. 13238–13248.
- [75] Shuxin Zhuang et al. “Preparation of homogeneous nanoporous La_{0.6}Ca_{0.4}CoO₃ for bi-functional catalysis in an alkaline electrolyte”. In: *Electrochemistry Communications* 13.4 (2011), pp. 321–324.
- [76] Hey Woong Park et al. “Electrospun porous nanorod perovskite oxide/nitrogen-doped graphene composite as a bi-functional catalyst for metal air batteries”. In: *Nano Energy* 10 (2014), pp. 192–200.

- [77] Rosalba A. Rincón et al. “Evaluation of Perovskites as Electrocatalysts for the Oxygen Evolution Reaction”. In: *ChemPhysChem* 15.13 (2014), pp. 2810–2816.
- [78] S K Tiwari, S P Singh, and R N Singh. “Effects of Ni, Fe, Cu, and Cr Substitutions for Co in La_{0.8}Sr_{0.2}CoO₃ on Electrocatalytic Properties for Oxygen Evolution”. In: *Journal of Electrochemical Society* 143.5 (1996), pp. 1505–1510.
- [79] Seyoung Ahn et al. “Synthesis and electrochemical performance of La_{0.7}Sr_{0.3}Co_{1-x}Fe_xO₃ catalysts for zinc air secondary batteries”. In: *Physica Scripta T* T139 (2010), p. 014014.
- [80] Jae Il Jung et al. “A bifunctional perovskite catalyst for oxygen reduction and evolution”. In: *Angewandte Chemie - International Edition* 53.18 (2014), pp. 4582–4586.
- [81] Jae-Il Jung et al. “Fabrication of Ba_{0.5}Sr_{0.5}Co_{0.8}Fe_{0.2}O_{3-δ} Catalysts with Enhanced Electrochemical Performance by Removing an Inherent Heterogeneous Surface Film Layer”. In: *Advanced Materials* 27.2 (2015), pp. 266–271.
- [82] Jae-Il Jung et al. “Optimizing nanoparticle perovskite for bifunctional oxygen electrocatalysis”. In: *Energy & Environmental Science* 9.1 (2016), pp. 176–183.
- [83] Jian Wang et al. “Ba_{0.5}Sr_{0.5}Co_{0.8}Fe_{0.2}O_{3-δ} on N-doped mesoporous carbon derived from organic waste as a bi-functional oxygen catalyst”. In: *International Journal of Hydrogen Energy* 41.25 (2016), pp. 10744–10754.
- [84] C. Alegre et al. “Bifunctional oxygen electrode based on a perovskite/carbon composite for electrochemical devices”. In: *Journal of Electroanalytical Chemistry* 808 (2018), pp. 412–419.
- [85] Karina Elumeeva et al. “Perovskite-based bifunctional electrocatalysts for oxygen evolution and oxygen reduction in alkaline electrolytes”. In: *Electrochimica Acta* 208 (2016), pp. 25–32.
- [86] Xiaohong Li et al. “A novel bifunctional oxygen GDE for alkaline secondary batteries”. In: *Electrochemistry Communications* 34 (2013), pp. 228–230.
- [87] Derek Pletcher et al. “Comparison of the Spinels Co₃O₄ and NiCo₂O₄ as Bifunctional Oxygen Catalysts in Alkaline Media”. In: *Electrochimica Acta* 188 (2016), pp. 286–293.
- [88] I. Abidat et al. “Electrochemically induced surface modifications of mesoporous spinels (Co₃O_{4-δ}, MnCo₂O_{4-δ}, NiCo₂O_{4-δ}) as the origin of the OER activity and stability in alkaline medium”. In: *Journal of Materials Chemistry A* 3.33 (2015), pp. 17433–17444.

-
- [89] Chengyu Ma et al. “Facile synthesis of NiCo₂O₄ nanosphere-carbon nanotubes hybrid as an efficient bifunctional electrocatalyst for rechargeable Zn–air batteries”. In: *International Journal of Hydrogen Energy* 41.21 (2016), pp. 9211–9218.
- [90] Aroa R. Mainar et al. “Manganese oxide catalysts for secondary zinc air batteries: from electrocatalytic activity to bifunctional air electrode performance”. In: *Electrochimica Acta* 217 (2016), pp. 80–91.
- [91] Ruiguo Cao et al. “Recent Progress in Non-Precious Catalysts for Metal-Air Batteries”. In: *Advanced Energy Materials* 2.7 (2012), pp. 816–829.
- [92] F. Bidault et al. “Review of gas diffusion cathodes for alkaline fuel cells”. In: *Journal of Power Sources* 187.1 (2009), pp. 39–48.
- [93] F. Bidault et al. “An improved cathode for alkaline fuel cells”. In: *International Journal of Hydrogen Energy* 35.4 (2010), pp. 1783–1788.
- [94] Vladimir Neburchilov et al. “A review on air cathodes for zinc–air fuel cells”. In: *Journal of Power Sources* 195.5 (2010), pp. 1271–1291.
- [95] Ilena Grimmer et al. “Ethanol tolerant precious metal free cathode catalyst for alkaline direct ethanol fuel cells”. In: *Electrochimica Acta* 228 (2017), pp. 325–331.
- [96] Seung-Wook Eom et al. “Electrochemical evaluation of La_{1-x}CaxCoO₃ cathode material for zinc air batteries application”. In: *Journal of Electroceramics* 23.2-4 (2009), pp. 382–386.
- [97] M. Cifrain and K.V Kordesch. “Advances, aging mechanism and lifetime in AFCs with circulating electrolytes”. In: *Journal of Power Sources* 127 (2004), pp. 234–242.
- [98] M. C. Wu et al. “Facile preparation of high-performance MnO₂/KB air cathode for Zn-air batteries”. In: *Electrochimica Acta* 222 (2016), pp. 1438–1444.
- [99] Dong Un Lee et al. “Advanced Extremely Durable 3D Bifunctional Air Electrodes for Rechargeable Zinc-Air Batteries”. In: *Advanced Energy Materials* 4.6 (2014), p. 1301389.
- [100] Stephen W T Price et al. “The fabrication of a bifunctional oxygen electrode without carbon components for alkaline secondary batteries”. In: *Journal of Power Sources* 259 (2014), pp. 43–49.
- [101] Rod Borup et al. “Scientific Aspects of Polymer Electrolyte Fuel Cell Durability and Degradation”. In: *Chemical Reviews* 107.10 (2007), pp. 3904–3951.

- [102] Chun Zhou et al. “Chemical durability studies of perfluorinated sulfonic acid polymers and model compounds under mimic fuel cell conditions”. In: *Macromolecules* 40.24 (2007), pp. 8695–8707.
- [103] J.-F. Drillet et al. “Influence of CO₂ on the stability of bifunctional oxygen electrodes for rechargeable zinc/air batteries and study of different CO₂ filter materials”. In: *Physical Chemistry Chemical Physics* 3.3 (2001), pp. 368–371.
- [104] Gwenaëlle Toussaint et al. “Development of a Rechargeable Zinc-Air Battery”. In: *ECS Transactions*. Vol. 28. 32. 2010, pp. 25–34.
- [105] Zhiming Cui et al. “High-Performance Pd₃Pb Intermetallic Catalyst for Electrochemical Oxygen Reduction”. In: *Nano Letters* 16.4 (2016), pp. 2560–2566.
- [106] Longjun Li et al. “Hierarchical pore-in-pore and wire-in-wire catalysts for rechargeable Zn- and Li-air batteries with ultra-long cycle life and high cell efficiency”. In: *Energy & Environmental Science* 8.11 (2015), pp. 3274–3282.
- [107] Yanjun Ding et al. “A Metal-Amino Acid Complex-Derived Bifunctional Oxygen Electrocatalyst for Rechargeable Zinc-Air Batteries”. In: *Small* 12.39 (2016), pp. 5414–5421.
- [108] Sambhaji S. Shinde et al. “Scalable 3-D Carbon Nitride Sponge as an Efficient Metal-Free Bifunctional Oxygen Electrocatalyst for Rechargeable Zn-Air Batteries”. In: *ACS Nano* 11.1 (2017), pp. 347–357.
- [109] Jintao Zhang et al. “A metal-free bifunctional electrocatalyst for oxygen reduction and oxygen evolution reactions”. In: *Nature Nanotechnology* 10.5 (2015), pp. 444–452.
- [110] Jie Hu et al. “Silver decorated LaMnO₃ nanorod/graphene composite electrocatalysts as reversible metal-air battery electrodes”. In: *Applied Surface Science* 402 (2017), pp. 61–69.
- [111] Moni Prabu et al. “Zinc-Air Battery: Understanding the Structure and Morphology Changes of Graphene-Supported CoMn₂O₄ Bifunctional Catalysts Under Practical Rechargeable Conditions”. In: *ACS Applied Materials & Interfaces* 6.19 (2014), pp. 16545–16555.
- [112] Moni Prabu, Prakash Ramakrishnan, and Sangaraju Shanmugam. “CoMn₂O₄ nanoparticles anchored on nitrogen-doped graphene nanosheets as bifunctional electrocatalyst for rechargeable zinc-air battery”. In: *Electrochemistry Communications* 41 (2014), pp. 59–63.

-
- [113] Moni Prabu, Kriangsak Ketpang, and Sangaraju Shanmugam. “Hierarchical nanostructured NiCo₂O₄ as an efficient bifunctional non-precious metal catalyst for rechargeable zinc–air batteries”. In: *Nanoscale* 6.6 (2014), p. 3173.
- [114] Hongyun Ma and Baoguo Wang. “A bifunctional electrocatalyst α -MnO₂-LaNiO₃ / carbon nanotube composite for rechargeable zinc–air batteries”. In: *RSC Advances* 4.86 (2014), pp. 46084–46092.
- [115] Tian Yi Ma et al. “Phosphorus-Doped Graphitic Carbon Nitrides Grown In Situ on Carbon-Fiber Paper: Flexible and Reversible Oxygen Electrodes”. In: *Angewandte Chemie - International Edition* 54.15 (2015), pp. 4646–4650.
- [116] Yi Cheng Lee et al. “Hierarchical meso-macroporous LaMnO₃ electrode material for rechargeable zinc-air batteries”. In: *Journal of the Taiwan Institute of Chemical Engineers* 45.5 (2014), pp. 2334–2339.
- [117] Dong Un Lee et al. “Highly Active and Durable Nanocrystal-Decorated Bifunctional Electrocatalyst for Rechargeable Zinc-Air Batteries”. In: *ChemSusChem* 8.18 (2015), pp. 3129–3138.
- [118] Dong Un Lee et al. “Synergistic bifunctional catalyst design based on perovskite oxide nanoparticles and intertwined carbon nanotubes for rechargeable zinc-air battery applications”. In: *ACS Applied Materials and Interfaces* 7.1 (2015), pp. 902–910.
- [119] Gengtao Fu et al. “Novel Hydrogel-Derived Bifunctional Oxygen Electrocatalyst for Rechargeable Air Cathodes”. In: *Nano Letters* 16.10 (2016), pp. 6516–6522.
- [120] Gengtao Fu et al. “Hierarchically mesoporous nickel-iron nitride as a cost-efficient and highly durable electrocatalyst for Zn-air battery”. In: *Nano Energy* 39 (2017), pp. 77–85.
- [121] Bing Li et al. “Co₃O₄ nanoparticles decorated carbon nanofiber mat as binder-free air-cathode for high performance rechargeable zinc-air batteries”. In: *Nanoscale* 7.5 (2015), pp. 1830–1838.
- [122] Bing Li et al. “Eggplant-derived microporous carbon sheets: towards mass production of efficient bifunctional oxygen electrocatalysts at low cost for rechargeable Zn–air batteries”. In: *Chem. Commun.* 51.42 (2015), pp. 8841–8844.
- [123] Bing Li et al. “Mussel-inspired one-pot synthesis of transition metal and nitrogen co-doped carbon (M/N–C) as efficient oxygen catalysts for Zn-air batteries”. In: *Nanoscale* 8.9 (2016), pp. 5067–5075.

- [124] Xien Liu et al. “Integrating NiCo Alloys with Their Oxides as Efficient Bifunctional Cathode Catalysts for Rechargeable Zinc-Air Batteries”. In: *Angewandte Chemie International Edition* 54.33 (2015), pp. 9654–9658.
- [125] Qin Liu et al. “Scalable Fabrication of Nanoporous Carbon Fiber Films as Bifunctional Catalytic Electrodes for Flexible Zn-Air Batteries”. In: *Advanced Materials* 28.15 (2016), pp. 3000–3006.
- [126] Nengneng Xu et al. “Self-assembly formation of Bi-functional Co₃O₄/MnO₂-CNTs hybrid catalysts for achieving both high energy/power density and cyclic ability of rechargeable zinc-air battery”. In: *Scientific Reports* 6.1 (2016), p. 33590.
- [127] Nengneng Xu et al. “Morphology controlled La₂O₃/Co₃O₄/MnO₂-CNTs hybrid nanocomposites with durable bi-functional air electrode in high-performance zinc-air energy storage”. In: *Applied Energy* 175 (2016), pp. 495–504.
- [128] Qing Wang et al. “3D carbon nanoframe scaffold-immobilized Ni₃FeN nanoparticle electrocatalysts for rechargeable zinc-air batteries’ cathodes”. In: *Nano Energy* 40 (2017), pp. 382–389.
- [129] Zilong Wang et al. “Co(II)_{1-x}Co(0)_x/3Mn(III)_{2x}/3S Nanoparticles Supported on B/N-Codoped Mesoporous Nanocarbon as a Bifunctional Electrocatalyst of Oxygen Reduction/Evolution for High-Performance Zinc-Air Batteries”. In: *ACS Applied Materials and Interfaces* 8.21 (2016), pp. 13348–13359.
- [130] Zhijuan Wang et al. “Core-shell carbon materials derived from metal-organic frameworks as an efficient oxygen bifunctional electrocatalyst”. In: *Nano Energy* 30 (2016), pp. 368–378.
- [131] Xiaoqiang Wu et al. “Silver-Copper Nanoalloy Catalyst Layer for Bifunctional Air Electrodes in Alkaline Media”. In: *ACS Applied Materials and Interfaces* 7.32 (2015), pp. 17782–17791.
- [132] Xiaoqiang Wu et al. “A silver-copper metallic glass electrocatalyst with high activity and stability comparable to Pt/C for zinc-air batteries”. In: *Journal of Materials Chemistry A* 4.9 (2016), pp. 3527–3537.
- [133] Afriyanti Sumboja et al. “Manganese Oxide Catalyst Grown on Carbon Paper as an Air Cathode for High-Performance Rechargeable Zinc-Air Batteries”. In: *ChemPlusChem* 80.8 (2015), pp. 1341–1346.

-
- [134] Afriyanti Sumboja et al. “Durable rechargeable zinc-air batteries with neutral electrolyte and manganese oxide catalyst”. In: *Journal of Power Sources* 332 (2016), pp. 330–336.
- [135] Youichi Shimizu et al. “Bi-functional Oxygen Electrode Using Large Surface Area Perovskite-type Oxide Catalyst for Rechargeable Metal-Air Batteries”. In: *Chemistry Letters* 21.6 (1992), pp. 1033–1036.
- [136] Kyu-Nam Jung et al. “Doped Lanthanum Nickelates with a Layered Perovskite Structure as Bifunctional Cathode Catalysts for Rechargeable Metal–Air Batteries”. In: *ACS Applied Materials & Interfaces* 5.20 (2013), pp. 9902–9907.
- [137] F. W. Thomas Goh et al. “A Near-Neutral Chloride Electrolyte for Electrically Rechargeable Zinc-Air Batteries”. In: *Journal of the Electrochemical Society* 161.14 (2014), A2080–A2086.
- [138] Ziyang Guo et al. “Ruthenium oxide coated ordered mesoporous carbon nanofiber arrays: a highly bifunctional oxygen electrocatalyst for rechargeable Zn–air batteries”. In: *Journal of Materials Chemistry A* 4.17 (2016), pp. 6282–6289.
- [139] H. B. Yang et al. “Identification of catalytic sites for oxygen reduction and oxygen evolution in N-doped graphene materials: Development of highly efficient metal-free bifunctional electrocatalyst”. In: *Science Advances* 2.4 (2016), e1501122.
- [140] Fanlu Meng et al. “In Situ Coupling of Strung Co₄N and Intertwined N-C Fibers toward Free-Standing Bifunctional Cathode for Robust, Efficient, and Flexible Zn-Air Batteries”. In: *Journal of the American Chemical Society* 138.32 (2016), pp. 10226–10231.
- [141] Moon Gyu Park et al. “3D Ordered Mesoporous Bifunctional Oxygen Catalyst for Electrically Rechargeable Zinc-Air Batteries”. In: *Small* 12.20 (2016), pp. 2707–2714.
- [142] Li-Na Han et al. “Ultra-durable two-electrode Zn–air secondary batteries based on bi-functional titania nanocatalysts: a Co²⁺ dopant boosts the electrochemical activity”. In: *Journal of Materials Chemistry A* 4.20 (2016), pp. 7841–7847.
- [143] Jie Yin et al. “NiO/CoN Porous Nanowires as Efficient Bifunctional Catalysts for Zn-Air Batteries”. In: *ACS Nano* 11.2 (2017), pp. 2275–2283.
- [144] Yuhong Qian et al. “A metal-free ORR/OER bifunctional electrocatalyst derived from metal-organic frameworks for rechargeable Zn-Air batteries”. In: *Carbon* 111 (2017), pp. 641–650.

- [145] Chang-Yuan Su et al. “Atomic Modulation of FeCo-Nitrogen-Carbon Bifunctional Oxygen Electrodes for Rechargeable and Flexible All-Solid-State Zinc-Air Battery”. In: *Advanced Energy Materials* 7.13 (2017), p. 1602420.
- [146] Stefan Mueller et al. “Development of Rechargeable Monopolar and Bipolar Zinc/Air Batteries”. In: *CHIMIA International Journal for Chemistry* 49.1 (1995), pp. 27–32.
- [147] Keliang Wang et al. “Morphology control of zinc regeneration for zinc-air fuel cell and battery”. In: *Journal of Power Sources* 271 (2014), pp. 65–75.
- [148] S. Müller, K. Striebel, and O. Haas. “La_{0.6}Ca_{0.4}CoO₃: a stable and powerful catalyst for bifunctional air electrodes”. In: *Electrochimica Acta* 39.11-12 (1994), pp. 1661–1668.
- [149] Qiwen Tang et al. “One step synthesis of carbon-supported Ag/MnyOx composites for oxygen reduction reaction in alkaline media”. In: *Applied Catalysis B: Environmental* 104.3-4 (2011), pp. 337–345.
- [150] Qiumei Wu et al. “Electrocatalytic activity and stability of Ag-MnOx/C composites toward oxygen reduction reaction in alkaline solution”. In: *Electrochimica Acta* 123 (2014), pp. 167–175.
- [151] Marcel Risch et al. “La_{0.8}Sr_{0.2}MnO_{3-δ} Decorated with Ba_{0.5}Sr_{0.5}Co_{0.8}Fe_{0.2}O_{3-δ}: A Bifunctional Surface for Oxygen Electrocatalysis with Enhanced Stability and Activity”. In: *Journal of the American Chemical Society* 136.14 (2014), pp. 5229–5232.
- [152] M. Bursell, M. Pirjamali, and Y. Kiros. “La_{0.6}Ca_{0.4}CoO₃, La_{0.1}Ca_{0.9}MnO₃ and LaNiO₃ as bifunctional oxygen electrodes”. In: *Electrochimica Acta* 47.10 (2002), pp. 1651–1660.
- [153] M. Sakthivel, S. Bhandari, and J.-F. Drillet. “On Activity and Stability of Rhombohedral LaNiO₃ Catalyst towards ORR and OER in Alkaline Electrolyte”. In: *ECS Electrochemistry Letters* 4.6 (2015), A56–A58.
- [154] Masayoshi Yuasa et al. “Bi-Functional Oxygen Electrodes Using LaMnO₃/LaNiO₃ for Rechargeable Metal-Air Batteries”. In: *Journal of The Electrochemical Society* 158.5 (2011), A605.
- [155] E. Fabbri et al. “Developments and perspectives of oxide-based catalysts for the oxygen evolution reaction”. In: *Catalysis Science and Technology* 4.11 (2014), pp. 3800–3821.

9 List of Figures

| | | |
|-----|--------------------------------------------------------------------------------------------------------------------------------------------------------------------------------------------------------------------------------------------------------------------------------------------------------------------------------------|----|
| 1.1 | Classification of different types of electrical energy storage according to Aneke <i>et al.</i> [5]. This thesis focuses on electrochemical energy storage with batteries. | 2 |
| 1.2 | Power requirement of different services (a) in comparison to the power delivered by different electrical storage systems (b) in regard to the discharge time. Schematics adapted from [5] and [14]. | 4 |
| 3.1 | The zinc-air system combines knowledge from the field of electrochemical engi- neering, electroplating, fuel cell and (flow) battery technology. | 14 |
| 3.2 | Schematic of the zinc-air cell including the chemical reactions occurring during discharge. When zincate ($\text{Zn}(\text{OH})_4^{2-}$) reaches supersaturation it precipitates in form of ZnO according to the reaction $\text{Zn}(\text{OH})_4^{2-} \longrightarrow \text{ZnO} + \text{H}_2\text{O} + 2\text{OH}^-$. . . | 15 |
| 3.3 | Schematic list of the ideal characteristics of a redox flow battery according to [50]. | 23 |
| 3.4 | Side reactions and unwanted effects on the zinc electrode: corrosion, passivation, shape change and dendrite growth (adapted from [28]). | 31 |
| 3.5 | Proposed mechanism for OER and ORR on perovskite oxide surfaces with rate determining steps (RDS) indicated. Images of the reaction mechanisms adapted from [67–69]. | 35 |
| 3.6 | Schematic of the ORR in protic ionic liquids via formation of superoxide and perhydroxyl radicals (adapted from [30]). | 37 |
| 3.7 | Perovskite structure shown as BaTiO_3 with Ba in green, Ti in grey and oxygen in red. | 38 |
| 3.8 | Spinel structure shown as NiCo_2O_4 with Ni in blue, Co in pink and oxygen in red. | 44 |
| 3.9 | Summary of various design parameters needed for achieving high-performing air electrodes. | 47 |

| | | |
|------|-------------------------------------------------------------------------------------------------------------------------------------------------------------------------------------------------------------------------------------------------------------------------------------------------------------------------------------------------------------------|----|
| 3.10 | ORR and OER polarization curves with power density and voltage efficiency of the air electrode at various current densities. A marks the activation loss region, B the ohmic loss region and C the mass-transport limited region, which is beyond the recorded current densities (own data, adapted from [28]). | 54 |
| 4.1 | Image of five 100 cm ² sized air electrodes after manufacture. | 63 |
| 4.2 | Images of the two flow test cells: left image - electrode holder with 2 x 2 cm left out space for attachment of the electrode; middle - assembled small flow cell; right - assembled 100 cm ² blue test cell. | 64 |
| 4.3 | Images of the BaSyTec test rig: left image - side front view with computer, 24 fixed test places with valves and electric plugs and 8 mobile test places (free cables), potentiostat at the top, power supply for DC pump on the right; right image - view of the backside with gas supply, and heated water supply from the Julabo thermostats (bottom). | 65 |
| 4.4 | Images of the two flow test set-ups: left - small scale with 0.5 L reservoir and open cell; right - closed blue 100 cm ² -sized test cell with 1 L reservoir. | 66 |
| 5.1 | Electrode manufacture and electrochemical performance of E1. | 73 |
| 5.2 | Electrode manufacture, testing and electrochemical performance of E9. | 74 |
| 5.3 | NiCo ₂ O ₄ -catalyzed electrodes E20, E15 (additional (La _{0.8} Sr _{0.2}) _{0.95} MnO _{3-x} perovskite) and E22 (additional Ag–MnO ₂ /CNF catalyst) and the electrochemical performance of E20. | 76 |
| 5.4 | Electrochemical measurement of E10, E16 and E18 using (La _{0.8} Sr _{0.2}) _{0.95} MnO _{3-x} perovskite catalyst at increasing current densities (supplied with synthetic air). | 80 |
| 5.5 | Results of (La _{0.8} Sr _{0.2}) _{0.95} MnO _{3-x} -catalyzed electrode E28. | 82 |
| 5.6 | Long-term operation of E34 catalyzed with LaNiO ₃ | 84 |
| 5.7 | Results of Ag–MnO ₂ /CNF-catalyzed and Pt-catalyzed air electrodes. | 85 |
| 5.8 | Results of the electrochemical characterization of E25 catalyzed with NiCo ₂ O ₄ /CNF and NiCo ₂ O ₄ /Ni powder. | 87 |
| 5.9 | SEM images of E25 after operation (backside). Clearly visible is the incorporated nickel foam and the fine carbon nanofibers within the paste. | 87 |
| 5.10 | Long-term cycling operation with 2 h cycles (alternating 1 h charge, 1 h discharge) of three different bi-catalyzed bifunctional air electrodes (NiCo ₂ O ₄ +perovskite). | 89 |
| 5.11 | Graphical abstract to the publication in <i>Electrochimica Acta</i> | 91 |

| | | |
|------|---------------------------------------------------------------------------------------------------------------------------------------------------------------------------------------------------------------------------------------------------------------------------------------------------------------------------------------------|-----|
| 5.12 | Graphical abstract to the publication in the Journal of Applied Electrochemistry. | 93 |
| 5.13 | Electrochemical characterization of E58_1 with additional carbon paper backing operated in the closed set-up supplied with compressed air (CA). | 95 |
| 5.14 | Electrochemical characterization of E58_2 with additional carbon paper backing operated in the open set-up with no active air supply. | 95 |
| 5.15 | Rotating disk electrode measurement of NiCo ₂ O ₄ spinel catalyst. | 97 |
| 5.16 | Results of the electrochemical characterization of E59 (no catalyst) and comparison between CVs of NiCo ₂ O ₄ and Ni powder. | 98 |
| 5.17 | Long-term cycling measurement of E66_1 with carbon paper backing and E66_2 without additional hydrophobic layer. | 100 |
| 5.18 | Electrochemical characterization of E69 with additional PTFE-coated glass fiber cloth backing operated with CA supply and images of electrodes with this backing layer. | 101 |
| 5.19 | Results of the electrochemical characterization of E _{0.2mm} with additional PTFE filter backing layer (0.2 mm thickness, 10 μm pore size) measured in the open set-up with no active gas supply (red) and in the closed set-up with CA (blue). | 103 |
| 5.20 | Image of E _{0.2mm} after manufacture (a) with the PTFE filter foil on the gas-facing side, and (b) the built-in electrode after several days of measurement in the open set-up with no electrolyte droplets visible on the backside. | 104 |
| 5.21 | Electrochemical characterization of E77, where one half was only used as cathode (ORR) and the other as anode (OER). | 105 |
| 5.22 | Results of the electrochemical characterization of the 60 cm ² -sized electrodes E86 and E87 with additional PTFE filter backing layer (0.2 mm thickness, 10 μm pore size) measured in the up-scaled blue test cell with flowing electrolyte with one side open set-up (red) and the second closed with active CA supply (blue). | 106 |
| 5.23 | Image of 100 cm ² -sized test cell with closed (a) and (d) and with open set-up (c) and (e). Top-view into the cell shown in (b). | 107 |
| 5.24 | Results of the electrochemical characterization of the 60 cm ² -sized electrodes E88 measured with a zinc electrode (unit zinc-air cell) in the up-scaled test cell with flowing electrolyte (1.5-2 cm s ⁻¹). | 108 |
| 5.25 | Graphical abstract to the publication in Batteries & Supercaps. | 110 |

10 List of Tables

| | | |
|-----|---------------------------------------------------------------------------------------------------------------------------------------------------------------------------------------------------------------------------------------------|----|
| 3.1 | Chemical reactions in an alkaline rechargeable zinc-air flow battery (discharge left to right, charge right to left) | 13 |
| 3.2 | Comparison of the advantages and disadvantages of alkaline aqueous electrolyte to ionic liquids. | 22 |
| 3.3 | Technical design specification of the Spanish zinc-air flow battery pilot plant. . . | 26 |
| 3.4 | Four and two electron mechanism in alkaline electrolyte: O ₂ is either directly reduced to OH ⁻ or via formation of peroxide intermediates. | 34 |
| 3.5 | Comparative list of zinc-air batteries found in literature. | 50 |
| 5.1 | All utilized materials and methods (and combinations thereof), which were investigated in the first stage of the project. | 71 |
| 5.2 | Summary of NiCo ₂ O ₄ catalyzed electrodes using the dip-coating method. Charge (OER) and discharge (ORR) potentials vs. RHE for the best performance at 20 mA cm ⁻² are listed. | 77 |
| 5.3 | Summary of NiCo ₂ O ₄ catalyzed electrodes (both 50 wt%) synthesized by the batch method. Charge potentials (OER) vs. RHE at 20 mA cm ⁻² are listed. | 78 |
| 5.4 | Summary of perovskite-catalyzed electrodes listing charge (OER) and discharge (ORR) potentials vs. RHE for the best performance at 20 mA cm ⁻² | 78 |
| 5.5 | Summary of Ag–MnO ₂ /CNF-catalyzed and Pt-catalyzed electrodes listing charge (OER) and discharge (ORR) potentials vs. RHE for the best performance at 20 mA cm ⁻² | 86 |
| 5.6 | Summary of NiCo ₂ O ₄ /CNF + NiCo ₂ O ₄ /Ni powder + perovskite electrodes listing start charge (OER) and discharge (ORR) potentials vs. RHE at 30 mA cm ⁻² (first cycling). | 88 |

| | | |
|------|----------------------------------------------------------------------------------------------------------------------------------------------------------------------------------------------------------------------------------------------------------------------------------------------------------------------------------------------------------------|-----|
| 11.1 | Charge/discharge cycling for beginning of operation with a step-wise raise of current density. Every five 20 min cycles the current density is increased. The maximum current density was 50 mA cm^{-2} . The lower cut-off voltage for discharge was 0.6 V and the maximum potential set to 2.2 V | 137 |
| 11.2 | Test protocol for long-term charge/discharge cycling with pulse charging. The pulse charging is recorded with two different registration rates in order to reduce the number of data points. The command CTSSRange is necessary for setting the internal resistance of the potentiostat in order to avoid continuous switching of the internal relays. | 140 |
| 11.3 | Test protocol for ORR polarization curve up to 50 mA cm^{-2} for a 4 cm^2 -sized air electrode. Lower cut-off potential was $0.8 \text{ V vs Zn/Zn}^{2+}$ | 141 |
| 11.4 | Test protocol for OER polarization curve up to 50 mA cm^{-2} for a 4 cm^2 -sized air electrode. Maximum potential (cut-off) was $2.4 \text{ V vs Zn/Zn}^{2+}$ | 142 |

11 Appendix A: Test Protocols for Electrochemical Characterization

In the following tables several exemplary test protocols written for the BaSyTec software are presented. The measurements were carried out in galvanostatic mode and the listed currents are always given for the standard 4 cm^2 -sized air electrode, *i.e.* 200 mA corresponds to a current density of 50 mA cm^{-2} . For larger sized electrodes the current densities were raised accordingly. Tables 11.1 and 11.2 were applied for charge/discharge cycling tests, alternating between ORR and OER. Tables 11.3 and 11.4 were used for recording polarization curves. It has to be mentioned that each channel of the BaSyTec potentiostat was restricted to about 3 A. Therefore, especially for pulse charging, the maximum current densities had to be lowered and the cycle length prolonged in order to balance charge and discharge capacity. The potential of the counter electrode or the cell voltage was recorded by using another BaSyTec channel and by simultaneously starting a program containing only "Pause" with a set-time of several hundred hours and a registration rate (*i.e.* recording) of $t = 30\text{ s}$.

Table 11.1: Charge/discharge cycling for beginning of operation with a step-wise raise of current density. Every five 20 min cycles the current density is increased. The maximum current density was 50 mA cm^{-2} . The lower cut-off voltage for discharge was 0.6 V and the maximum potential set to 2.2 V.

| Line | Command | Parameter | Cut-Off | Recording |
|------|--------------------|----------------------------------------------------------------------|---------------------|------------------|
| 1 | Cycle-start | | | |
| 2 | Pause | | $t > 2\text{ min}$ | $t = 5\text{ s}$ |
| 3 | Ramp-i | $I1 = -0\text{ mA}$, Slope = -1 mA/s , $I2 = -4\text{ mA}$ | $t > 4\text{ s}$ | $t = 1\text{ s}$ |
| 4 | Discharge | $I = 4\text{ mA}$ | $t > 10\text{ min}$ | $t = 5\text{ s}$ |
| 5 | Pause | | $t > 2\text{ min}$ | $t = 5\text{ s}$ |
| 6 | Ramp-i | $I1 = 0\text{ mA}$, Slope = 1 mA/s , $I2 = 4\text{ mA}$ | $t > 4\text{ s}$ | $t = 1\text{ s}$ |

| | | | | |
|----|--------------------|-----------------------------------------------------------------------------|----------------------|-------------------|
| 7 | Charge | $I = 4 \text{ mA}$ | $t > 10 \text{ min}$ | $t = 5 \text{ s}$ |
| 8 | Cycle-end | Count = 5 | | |
| 9 | Cycle-start | | | |
| 10 | Pause | | $t > 2 \text{ min}$ | $t = 5 \text{ s}$ |
| 11 | Ramp-i | $I1 = -0 \text{ mA}$, Slope = -1 mA/s , $I2 = -20 \text{ mA}$ | $t > 20 \text{ s}$ | $t = 1 \text{ s}$ |
| 12 | Discharge | $I = 20 \text{ mA}$ | $t > 10 \text{ min}$ | $t = 5 \text{ s}$ |
| 13 | Pause | | $t > 2 \text{ min}$ | $t = 5 \text{ s}$ |
| 14 | Ramp-i | $I1 = 0 \text{ mA}$, Slope = 1 mA/s , $I2 = 20 \text{ mA}$ | $t > 20 \text{ s}$ | $t = 1 \text{ s}$ |
| 15 | Charge | $I = 20 \text{ mA}$ | $t > 10 \text{ min}$ | $t = 5 \text{ s}$ |
| 16 | Cycle-end | Count = 5 | | |
| 17 | Cycle-start | | | |
| 18 | Pause | | $t > 2 \text{ min}$ | $t = 5 \text{ s}$ |
| 19 | Ramp-i | $I1 = -0 \text{ mA}$, Slope = -1 mA/s , $I2 = -40 \text{ mA}$ | $t > 40 \text{ s}$ | $t = 1 \text{ s}$ |
| 20 | Discharge | $I = 40 \text{ mA}$ | $t > 10 \text{ min}$ | $t = 5 \text{ s}$ |
| 21 | Pause | | $t > 2 \text{ min}$ | $t = 5 \text{ s}$ |
| 22 | Ramp-i | $I1 = 0 \text{ mA}$, Slope = 1 mA/s , $I2 = 40 \text{ mA}$ | $t > 40 \text{ s}$ | $t = 1 \text{ s}$ |
| 23 | Charge | $I = 40 \text{ mA}$ | $t > 10 \text{ min}$ | $t = 5 \text{ s}$ |
| 24 | Cycle-end | Count = 5 | | |
| 25 | Cycle-start | | | |
| 26 | Pause | | $t > 2 \text{ min}$ | $t = 5 \text{ s}$ |
| 27 | Ramp-i | $I1 = -0 \text{ mA}$, Slope = -1 mA/s , $I2 = -80 \text{ mA}$ | $t > 80 \text{ s}$ | $t = 1 \text{ s}$ |
| 28 | Discharge | $I = 80 \text{ mA}$ | $t > 10 \text{ min}$ | $t = 5 \text{ s}$ |
| 29 | Pause | | $t > 2 \text{ min}$ | $t = 5 \text{ s}$ |
| 30 | Ramp-i | $I1 = 0 \text{ mA}$, Slope = 1 mA/s , $I2 = 80 \text{ mA}$ | $t > 80 \text{ s}$ | $t = 1 \text{ s}$ |
| 31 | Charge | $I = 80 \text{ mA}$ | $t > 10 \text{ min}$ | $t = 5 \text{ s}$ |
| 32 | Cycle-end | Count = 5 | | |
| 33 | Cycle-start | | | |
| 34 | Pause | | $t > 2 \text{ min}$ | $t = 5 \text{ s}$ |
| 35 | Ramp-i | $I1 = -0 \text{ mA}$, Slope = -0.5 mA/s , $I2 = -120 \text{ mA}$ | $t > 240 \text{ s}$ | $t = 1 \text{ s}$ |
| 36 | Discharge | $I = 120 \text{ mA}$ | $t > 10 \text{ min}$ | $t = 5 \text{ s}$ |
| 37 | Pause | | $t > 2 \text{ min}$ | $t = 5 \text{ s}$ |
| 38 | Ramp-i | $I1 = 0 \text{ mA}$, Slope = 0.5 mA/s , $I2 = 120 \text{ mA}$ | $t > 240 \text{ s}$ | $t = 1 \text{ s}$ |

| | | | | |
|----|--------------------|-----------------------------------------------------------------------------|----------------------|--------------------|
| 39 | Charge | $I = 120 \text{ mA}$ | $t > 10 \text{ min}$ | $t = 5 \text{ s}$ |
| 40 | Cycle-end | Count = 5 | | |
| 41 | Cycle-start | | | |
| 42 | Pause | | $t > 2 \text{ min}$ | $t = 5 \text{ s}$ |
| 43 | Ramp-i | $I1 = -0 \text{ mA}$, Slope = -0.5 mA/s , $I2 = -200 \text{ mA}$ | $t > 400 \text{ s}$ | $t = 1 \text{ s}$ |
| 44 | Discharge | $I = 200 \text{ mA}$ | $t > 10 \text{ min}$ | $t = 5 \text{ s}$ |
| 45 | Pause | | $t > 2 \text{ min}$ | $t = 5 \text{ s}$ |
| 46 | Ramp-i | $I1 = 0 \text{ mA}$, Slope = 0.5 mA/s , $I2 = 200 \text{ mA}$ | $t > 400 \text{ s}$ | $t = 1 \text{ s}$ |
| 47 | Charge | $I = 200 \text{ mA}$ | $t > 10 \text{ min}$ | $t = 5 \text{ s}$ |
| 48 | Cycle-end | Count = 5 | | |
| 49 | Pause | | $t > 5 \text{ h}$ | $t = 30 \text{ s}$ |
| 50 | Stop | | | |

Table 11.2: Test protocol for long-term charge/discharge cycling with pulse charging. The pulse charging is recorded with two different registration rates in order to reduce the number of data points. The command CTSRange is necessary for setting the internal resistance of the potentiostat in order to avoid continuous switching of the internal relays.

| Line | Command | Parameter | Cut-Off | Recording |
|------|--------------------|--------------------------------------------------------------------------------|----------------------------------------------------------------|--------------------|
| 1 | Cycle-start | | | |
| 2 | Pause | | $t > 2 \text{ min}$ | $t = 5 \text{ s}$ |
| 3 | Ramp-i | $I_1 = -0 \text{ mA}$, Slope = -1 mA/s , $I_2 = -200 \text{ mA}$ | $t > 200 \text{ s}$ $U < 0.5 \text{ V} \& t > 5 \text{ s}$ | $t = 1 \text{ s}$ |
| 4 | Discharge | $I = 200 \text{ mA}$ | $t > 60 \text{ min}$ $U < 0.5 \text{ V} \& t > 5 \text{ s}$ | $t = 30 \text{ s}$ |
| 5 | Pause | | $t > 2 \text{ min}$ | $t = 5 \text{ s}$ |
| 6 | Cycle-start | | | |
| 7 | Cycle-start | | | |
| 8 | Charge | $I = 0 \text{ mA}$, CTSRange = 3 | $t > 50 \text{ ms}$ | $t = 1 \text{ ms}$ |
| 9 | Charge | $I = 400 \text{ mA}$, CTSRange = 3 | $t > 50 \text{ ms}$ $U > 2.3 \text{ V} \& t > 5 \text{ s}$ | $t = 1 \text{ ms}$ |
| 10 | Cycle-end | Count = 10 | | |
| 11 | Cycle-start | | | |
| 12 | Charge | $I = 0 \text{ mA}$, CTSRange = 3 | $t > 50 \text{ ms}$ | $t = 10 \text{ s}$ |
| 13 | Charge | $I = 400 \text{ mA}$, CTSRange = 3 | $t > 50 \text{ ms}$ $U > 2.3 \text{ V} \& t > 5 \text{ s}$ | $t = 10 \text{ s}$ |
| 14 | Cycle-end | Count = 490 | | |
| 15 | Cycle-end | Count = 72 | | |
| 16 | Cycle-end | Count = 25 | | |
| 17 | Pause | | $t > 5 \text{ h}$ | $t = 30 \text{ s}$ |
| 18 | Stop | | | |

Table 11.3: Test protocol for ORR polarization curve up to 50 mA cm^{-2} for a 4 cm^2 -sized air electrode. Lower cut-off potential was $0.8 \text{ V vs Zn/Zn}^{2+}$.

| Line | Command | Parameter | Cut-Off | Recording |
|------|--------------------|-----------------------------------------------------------------------------|----------------------|-------------------|
| 1 | Cycle-start | | | |
| 2 | Pause | | $t > 15 \text{ min}$ | $t = 1 \text{ s}$ |
| 3 | Ramp-i | $I1 = -0 \text{ mA}$, Slope = -1 mA/s , $I2 = -4 \text{ mA}$ | $t > 4 \text{ s}$ | $t = 1 \text{ s}$ |
| 4 | Discharge | $I = 4 \text{ mA}$ | $t > 10 \text{ min}$ | $t = 1 \text{ s}$ |
| 5 | Ramp-i | $I1 = -4 \text{ mA}$, Slope = -1 mA/s , $I2 = -8 \text{ mA}$ | $t > 4 \text{ s}$ | $t = 1 \text{ s}$ |
| 6 | Discharge | $I = 8 \text{ mA}$ | $t > 10 \text{ min}$ | $t = 1 \text{ s}$ |
| 7 | Ramp-i | $I1 = -8 \text{ mA}$, Slope = -1 mA/s , $I2 = -12 \text{ mA}$ | $t > 4 \text{ s}$ | $t = 1 \text{ s}$ |
| 8 | Discharge | $I = 12 \text{ mA}$ | $t > 10 \text{ min}$ | $t = 1 \text{ s}$ |
| 9 | Ramp-i | $I1 = -12 \text{ mA}$, Slope = -1 mA/s , $I2 = -20 \text{ mA}$ | $t > 8 \text{ s}$ | $t = 1 \text{ s}$ |
| 10 | Discharge | $I = 20 \text{ mA}$ | $t > 10 \text{ min}$ | $t = 1 \text{ s}$ |
| 11 | Ramp-i | $I1 = -20 \text{ mA}$, Slope = -1 mA/s , $I2 = -40 \text{ mA}$ | $t > 20 \text{ s}$ | $t = 1 \text{ s}$ |
| 12 | Discharge | $I = 40 \text{ mA}$ | $t > 10 \text{ min}$ | $t = 1 \text{ s}$ |
| 13 | Ramp-i | $I1 = -40 \text{ mA}$, Slope = -1 mA/s , $I2 = -80 \text{ mA}$ | $t > 40 \text{ s}$ | $t = 1 \text{ s}$ |
| 14 | Discharge | $I = 80 \text{ mA}$ | $t > 10 \text{ min}$ | $t = 1 \text{ s}$ |
| 15 | Ramp-i | $I1 = -80 \text{ mA}$, Slope = -1 mA/s , $I2 = -120 \text{ mA}$ | $t > 40 \text{ s}$ | $t = 1 \text{ s}$ |
| 16 | Discharge | $I = 120 \text{ mA}$ | $t > 10 \text{ min}$ | $t = 1 \text{ s}$ |
| 17 | Ramp-i | $I1 = -120 \text{ mA}$, Slope = -1 mA/s , $I2 = -140 \text{ mA}$ | $t > 20 \text{ s}$ | $t = 1 \text{ s}$ |
| 18 | Discharge | $I = 140 \text{ mA}$ | $t > 10 \text{ min}$ | $t = 1 \text{ s}$ |
| 19 | Ramp-i | $I1 = -140 \text{ mA}$, Slope = -1 mA/s , $I2 = -160 \text{ mA}$ | $t > 20 \text{ s}$ | $t = 1 \text{ s}$ |
| 20 | Discharge | $I = 160 \text{ mA}$ | $t > 10 \text{ min}$ | $t = 1 \text{ s}$ |
| 21 | Ramp-i | $I1 = -160 \text{ mA}$, Slope = -1 mA/s , $I2 = -200 \text{ mA}$ | $t > 40 \text{ s}$ | $t = 1 \text{ s}$ |
| 22 | Discharge | $I = 200 \text{ mA}$ | $t > 10 \text{ min}$ | $t = 1 \text{ s}$ |
| 23 | Cycle-end | Count = 2 | | |
| 24 | Pause | | $t > 1 \text{ h}$ | $t = 1 \text{ s}$ |
| 25 | Stop | | | |

Table 11.4: Test protocol for OER polarization curve up to 50 mA cm^{-2} for a 4 cm^2 -sized air electrode. Maximum potential (cut-off) was $2.4 \text{ V vs Zn/Zn}^{2+}$.

| Line | Command | Parameter | Cut-Off | Recording |
|------|--------------------|--------------------------------------------------------------------------|----------------------|--------------------|
| 1 | Cycle-start | | | |
| 2 | Pause | | $t > 15 \text{ min}$ | $t = 1 \text{ s}$ |
| 3 | Ramp-i | $I1 = 0 \text{ mA}$, Slope = 1 mA/s , $I2 = 4 \text{ mA}$ | $t > 4 \text{ s}$ | $t = 1 \text{ s}$ |
| 4 | Charge | $I = 4 \text{ mA}$ | $t > 10 \text{ min}$ | $t = 1 \text{ s}$ |
| 5 | Ramp-i | $I1 = 4 \text{ mA}$, Slope = 1 mA/s , $I2 = 8 \text{ mA}$ | $t > 4 \text{ s}$ | $t = 1 \text{ s}$ |
| 6 | Charge | $I = 8 \text{ mA}$ | $t > 10 \text{ min}$ | $t = 1 \text{ s}$ |
| 7 | Ramp-i | $I1 = 8 \text{ mA}$, Slope = 1 mA/s , $I2 = 12 \text{ mA}$ | $t > 4 \text{ s}$ | $t = 1 \text{ s}$ |
| 8 | Charge | $I = 12 \text{ mA}$ | $t > 10 \text{ min}$ | $t = 1 \text{ s}$ |
| 9 | Ramp-i | $I1 = 12 \text{ mA}$, Slope = 1 mA/s , $I2 = 20 \text{ mA}$ | $t > 8 \text{ s}$ | $t = 1 \text{ s}$ |
| 10 | Charge | $I = 20 \text{ mA}$ | $t > 10 \text{ min}$ | $t = 1 \text{ s}$ |
| 11 | Ramp-i | $I1 = 20 \text{ mA}$, Slope = 1 mA/s , $I2 = 40 \text{ mA}$ | $t > 20 \text{ s}$ | $t = 1 \text{ s}$ |
| 12 | Charge | $I = 40 \text{ mA}$ | $t > 10 \text{ min}$ | $t = 1 \text{ s}$ |
| 13 | Ramp-i | $I1 = 40 \text{ mA}$, Slope = 1 mA/s , $I2 = 80 \text{ mA}$ | $t > 40 \text{ s}$ | $t = 1 \text{ s}$ |
| 14 | Charge | $I = 80 \text{ mA}$ | $t > 10 \text{ min}$ | $t = 1 \text{ s}$ |
| 15 | Ramp-i | $I1 = 80 \text{ mA}$, Slope = 1 mA/s , $I2 = 120 \text{ mA}$ | $t > 40 \text{ s}$ | $t = 1 \text{ s}$ |
| 16 | Charge | $I = 120 \text{ mA}$ | $t > 10 \text{ min}$ | $t = 1 \text{ s}$ |
| 17 | Ramp-i | $I1 = 120 \text{ mA}$, Slope = 1 mA/s , $I2 = 140 \text{ mA}$ | $t > 20 \text{ s}$ | $t = 1 \text{ s}$ |
| 18 | Charge | $I = 140 \text{ mA}$ | $t > 10 \text{ min}$ | $t = 1 \text{ s}$ |
| 19 | Ramp-i | $I1 = 140 \text{ mA}$, Slope = 1 mA/s , $I2 = 160 \text{ mA}$ | $t > 20 \text{ s}$ | $t = 1 \text{ s}$ |
| 20 | Charge | $I = 160 \text{ mA}$ | $t > 10 \text{ min}$ | $t = 1 \text{ s}$ |
| 21 | Ramp-i | $I1 = 160 \text{ mA}$, Slope = 1 mA/s , $I2 = 200 \text{ mA}$ | $t > 40 \text{ s}$ | $t = 1 \text{ s}$ |
| 22 | Charge | $I = 200 \text{ mA}$ | $t > 10 \text{ min}$ | $t = 1 \text{ s}$ |
| 23 | Cycle-end | Count = 2 | | |
| 24 | Pause | | $t > 5\text{h}$ | $t = 30 \text{ s}$ |
| 25 | Stop | | | |

12 Appendix B: Dissemination

12.1 List of Publications

12.1.1 Peer-Reviewed Journal Articles

- **B. Pichler**, K. Mayer, V. Hacker, *Long-term Operation of Perovskite-catalyzed Bifunctional Air Electrodes in Rechargeable Zinc-Air Flow Batteries*, Batteries & Supercapacitors. doi: 10.1002/batt.201800094 (accepted to Special Issue on "Bifunctional Catalysts for Metal–Air Batteries", October 2018)
- **B. Pichler**, B.S. Berner, N. Rauch, C. Zelger, H.-J. Pauling, B. Gollas, V. Hacker, *The impact of operating conditions on component and electrode development for zinc-air flow batteries*, Journal of Applied Electrochemistry, 48 (2018) 1043–1056. doi:10.1007/s10800-018-1233-z.
- **B. Pichler**, S. Weinberger, L. Rešček, I. Grimmer, F. Gebetsroither, B. Bitschnau, V. Hacker, *Bifunctional electrode performance for zinc-air flow cells with pulse charging*, Electrochimica Acta, 251 (2017) 488–497. doi:10.1016/j.electacta.2017.08.128.
- I. Grimmer, P. Zorn, S. Weinberger, C. Grimmer, **B. Pichler**, B. Cermenek, F. Gebetsroither, A. Schenk, F.-A. Mautner, B. Bitschnau, V. Hacker, *Ethanol tolerant precious metal free cathode catalyst for alkaline direct ethanol fuel cells*, Electrochimica Acta. 228 (2017) 325–331. doi:10.1016/j.electacta.2017.01.087.
- C. Chaiburi, B. Cermenek, **B. Pichler**, C. Grimmer, A. Schenk, V. Hacker, *Ethanol - Tolerant Pt-free Cathode Catalysts for the Alkaline Direct Ethanol Fuel Cell*, Journal of New Materials for Electrochemical Systems 19 (2017) 199–207. <http://new-mat.org/ejournal/index.php/jnmes/article/view/282>.

- C. Grimmer, R. Zacharias, M. Grandi, **B. Pichler**, I. Kaltenboeck, F. Gebetsroither, J. Wagner, B. Cermenek, S. Weinberger, A. Schenk, V. Hacker, *A membrane-free and practical mixed electrolyte direct borohydride fuel cell*, Journal of the Electrochemical Society, 163 (2016) F278–F283. doi:10.1149/2.1111603jes
- A. Schenk, C. Grimmer, M. Perchthaler, S. Weinberger, **B. Pichler**, C. Heinzl, C. Scheu, F.-A. Mautner, B. Bitschnau, V. Hacker, *Platinum–cobalt catalysts for the oxygen reduction reaction in high temperature proton exchange membrane fuel cells – Long term behavior under ex-situ and in-situ conditions*, J. Power Sources. 266 (2014) 313–322. doi:10.1016/j.jpowsour.2014.05.023.

12.1.2 Selected Reviewed Conference Proceedings

- B. Pichler, V. Hacker, C. Zelger, W. Taucher-Mautner, B. Gollas, H. J. Pauling, *Development of zinc-air flow batteries by investigating compact zinc deposition and improving air electrode cycling stability*, Proceedings of 7th Transport Research Arena, Vienna, Austria (2018)
- B. Pichler, S. Weinberger, L. Reščec, V. Hacker, *Development of Stable Bifunctional Air Electrodes for Zinc-Air Flow Batteries*, ECS Transactions, 80 (2017) 371–375. doi:10.1149/08010.0371ecst.

12.1.3 Presentations at Conferences and Meetings

- B. Pichler, V. Hacker, C. Zelger, W. Taucher-Mautner, B. Gollas, H. J. Pauling, *Development of zinc-air flow batteries by investigating compact zinc deposition and improving air electrode cycling stability*, 7th Transport Research Arena, Vienna, Austria (2018)
- B. Pichler, S. Weinberger, L. Reščec, V. Hacker, *Development of stable bifunctional air electrodes for zinc-air flow batteries*, IEA Annex 31 Meeting, Washington D.C., USA (2017)
- B. Pichler, S. Weinberger, L. Reščec, V. Hacker, *Development of stable bifunctional air electrodes for zinc-air flow batteries*, 232nd Meeting of the Electrochemical Society, National Harbor (MD), USA (2017)
- B. Pichler, L. Reščec, V. Hacker, *Investigations on long-term behavior of bifunctional air electrodes for zinc-air flow batteries*, 6th Regional Symposium on Electrochemistry of South-East Europe, Balatonkenese, Hungary (2017)

12.1.4 Poster

- B. Pichler, H.-J. Pauling, V. Hacker, *Manufacture and Operation of 60 cm² Zinc-Air Flow Batteries with Bifunctional Air Electrodes*, 4th International Workshop on Hydrogen and Fuel Cells, Graz, Austria (2018)
- B. Pichler, N. Rauch, V. Hacker, *Influence of operating conditions on the long-term performance of bifunctional air electrodes*, Second International Zinc/Air Battery Workshop, Trondheim, Norway (2018)
- B. Pichler, L. Reščec, V. Hacker, *Development of bifunctional electrodes for rechargeable zinc/air flow batteries*, 649. WE-Heraeus-Seminar: In-operando characterization of energy materials, Bad Honnef, Germany (2017)
- B. Pichler, L. Reščec, V. Hacker, *Bifunctional air electrodes for rechargeable zinc/air flow batteries*, 13th Minisymposium Chemical and Process Engineering, Innsbruck, Austria (2017)
- B. Pichler, L. Reščec, V. Hacker, *Characterization of Bifunctional Air Electrodes for Zinc/Air Flow Batteries used in Energy Storage*, 2nd International Workshop on Hydrogen and Fuel Cells, Graz, Austria (2016)
- B. Pichler, S. Weinberger, V. Hacker, *Design of bifunctional air electrodes for Zn/air redox flow batteries*, 67th Annual Meeting of the International Society of Electrochemistry, Den Haag, Netherlands (2016)
- B. Pichler, S. Weinberger V. Hacker, *Influence of pulse charging on air electrodes for Zn/Air batteries*, First International Zinc/Air Battery Workshop, Ulm, Germany (2016)
- B. Pichler, V. Hacker, *Design of bifunctional air electrodes for rechargeable zinc/air redox flow systems*, 12th Minisymposium Chemical and Process Engineering, Graz, Austria (2016)
- B. Pichler, A. Schenk, C. Grimmer, M. Perchthaler, V. Hacker, *Synthesis of Platinum-Iron/Carbon Catalysts for the Oxygen Reduction Reaction in High-Temperature PEFC*, 7th International Summer School on Advanced Studies of Polymer Electrolyte Fuel Cells, Graz Austria (2014)

- B. Pichler, A. Schenk, C. Grimmer, M. Perchthaler, V. Hacker, *Platinum Nickel Co-Catalysts for the Oxygen Reduction Reaction on PEM Fuel Cells*, 15. Österreichische Chemietage, Graz, Austria (2013)
- B. Pichler, A. Schenk, C. Grimmer, M. Perchthaler, V. Hacker, *Manufacture and Stability Enhancement of Platinum Nickel Co-Catalysts for HT-PEM Fuel Cells*, 6th International Summer School On Advanced Studies of Polymer Electrolyte Fuel Cells, Yokohama, Japan (2013)

12.1.5 Book Chapters

- G. Voitic, **B. Pichler**, A. Basile, A. Iulianelli, K. Malli, S. Bock, V. Hacker, *Hydrogen Production (Chapter 10)* in *Fuel Cells and Hydrogen: From Fundamentals to Applied Research*. V Hacker & S. Mitsushima. (Hrsg.), Amsterdam, S. 215-242 (2018), eBook ISBN: 9780128115374
- T.W. Napporn, L. Karpenko-Jereb, **B. Pichler**, V. Hacker; *Polymer Electrolyte Fuel Cells (Chapter 4)* in *Fuel Cells and Hydrogen: From Fundamentals to Applied Research*. V Hacker & S. Mitsushima. (Hrsg.), Amsterdam, S. 63-90 (2018), eBook ISBN: 9780128115374



Contents lists available at ScienceDirect

Electrochimica Acta

journal homepage: www.elsevier.com/locate/electacta

Bifunctional electrode performance for zinc-air flow cells with pulse charging



Birgit Pichler^{a,*}, Stephan Weinberger^a, Lucas Rešćec^a, Ilena Grimmer^a, Florian Gebetsroither^a, Brigitte Bitschnau^b, Viktor Hacker^a

^a Graz University of Technology, Institute of Chemical Engineering and Environmental Technology, Fuel Cell Group, NAWI Graz, Inffeldgasse 25C, 8010 Graz, Austria

^b Graz University of Technology, Institute of Physical and Theoretical Chemistry, NAWI Graz, Stremayrgasse 9/I, 8010 Graz, Austria

ARTICLE INFO

Article history:

Received 4 July 2017
Received in revised form 31 July 2017
Accepted 22 August 2017

Keywords:

zinc-air flow cells
bi-catalyzed bifunctional air electrode
long-term cycling with pulse charging
NiCo₂O₄ spinel
La_{0.6}Sr_{0.4}Co_{0.2}Fe_{0.8}O₃ perovskite

ABSTRACT

Bifunctional air electrodes with tuned composition consisting of two precious metal-free oxide catalysts are manufactured for application in rechargeable zinc-air flow batteries and electrochemically tested via long-term pulse charge and discharge cycling experiments at 50 mA cm⁻² (mean). NiCo₂O₄ spinel, synthesized via direct impregnation on carbon nanofibers or nickel powder and characterized by energy dispersive X-ray spectroscopy and X-ray diffraction experiments, shows high activity toward oxygen evolution reaction with low charge potentials of < 2.0 V vs. Zn/Zn²⁺. La_{0.6}Sr_{0.4}Co_{0.2}Fe_{0.8}O₃ perovskite exhibits bifunctional activity and outperforms the NiCo₂O₄ spinel in long-term stability tenfold. By combining the catalysts in one bi-catalyzed bifunctional air electrode, stable performances of more than 1000 h and 450 cycles are achieved when supplied with oxygen and over 650 h and 300 cycles when supplied with synthetic air. In addition, the pulse charging method, which is beneficial for compact zinc deposition, is successfully tested on air electrodes during long-term operation. The oxygen evolution potentials during pulse, i.e. at tripled charge current density of 150 mA cm⁻², are only 0.06–0.08 V higher compared to constant charging current densities. Scanning electron microscopy confirms that mechanical degradation caused by bubble formation during oxygen evolution results in slowly decreasing discharge potentials.

© 2017 Elsevier Ltd. All rights reserved.

1. Introduction

An increasing share of electrical energy generated by fluctuating sources such as wind and solar power leads to growing interest in efficient and easily scalable energy storage systems with fast response times. One promising option is the rechargeable zinc-air battery due to its use of the environmentally friendly, abundant and safe active storage material zinc [1]. However, despite extensive research on all components, as summarized in recent review publications [2–5], mainly small primary zinc-air batteries are commercially available so far. Many different approaches concerning the recharge capability have been pursued in order to overcome the two main challenges, which are *i*) dendrite-free zinc

deposition on the negative electrode and *ii*) long and efficient cycling capability of the air electrode. This resulted in several different types of zinc-air battery systems depending on the desired applications [1,5–7], one of those being the stationary zinc-air flow battery [8,9]. In comparison to other redox flow batteries, which have two completely soluble redox partners (i.e. the all-vanadium system), in zinc-air batteries only one active material has to be stored and no membrane is needed to separate different electrolytes [10]. Nevertheless, improvements in long-term cycling behavior of the applied catalysts and the whole air electrode assembly are crucial, if rechargeable zinc-air flow battery systems are to be utilized in stationary applications.

In the zinc-air flow battery, oxygen is reduced during discharge to hydroxide ions at the positive air electrode (oxygen reduction reaction; ORR) and zinc at the negative electrode is dissolved into the flowing electrolyte and stored in a tank as zincate (Zn(OH)₄²⁻). In contrast to small secondary zinc-air batteries, no subsequent precipitation of zincate to zinc oxide (ZnO) is desired. During charging, while zinc is redeposited from the electrolyte, the oxygen evolution reaction (OER) occurs on the positive electrode, whereby

* Corresponding author. Tel.: +43 316 873 8797, fax: +43 316 873 8782.

E-mail addresses: birgit.pichler@tugraz.at (B. Pichler),

stephan.weinberger@tugraz.at (S. Weinberger), rescec@tugraz.at (L. Rešćec),

ilena.grimmer@tugraz.at (I. Grimmer), florian.gebetsroither@tugraz.at

(F. Gebetsroither), bitschnau@tugraz.at (B. Bitschnau), viktor.hacker@tugraz.at

(V. Hacker).

the flow battery design allows transport of the generated oxygen out of the cell by the electrolyte stream and critical bubble coalescence is reduced [11]. However, due to the flowing electrolyte, only compact zinc deposition morphologies (layer- and boulder-like) are favorable, as non-compact types such as dendritic, filamentous-mossy or heavy-spongy can result in short-circuiting and capacity losses by mechanical detachment of active material [12–14]. A recent study by Zelger et al. [12] showed by means of rotating cylinder Hull experiments the compact deposition of zinc at different electrolyte flow rates by using the pulse charging method. In these experiments the time ratio between pulse (on-time 50 ms) and pause (100 ms) was 1:2 (duty cycle $\gamma = 0.33$), which means that tripled current densities have to be applied during the pulse (j_p) in order to reach the same mean charge current density (j_m). Although the pulse charging method is advantageous for the negative zinc electrode, the high current densities applied can have a deteriorating influence on the positive air electrode in the zinc-air battery, mainly due to a more vigorous oxygen evolution and due to increased electrode material corrosion at high OER potentials. The compatibility of air electrodes with the pulse charging method needs to be investigated in order to test if it is a feasible operation mode of whole zinc-air cells.

In principle, there are three different ways to achieve a bifunctional system in regard to ORR/OER by either using *i*) two different electrodes i.e. one for ORR and one for OER, *ii*) a bifunctional catalyst with high catalytic activity toward ORR as well as OER employed in a single active layer, or *iii*) one bifunctional air electrode with two different catalysts employed in two spatially separated active layers as investigated in this work [15]. The performance and long-term stability of a bifunctional air electrode is thereby dependent on several factors such as inherent catalyst activity, hydrophobicity/hydrophilicity and mechanical and chemical durability. The approach via separate layers is especially promising, because different conditions are needed during ORR and OER in terms of gas diffusivity and electrolyte wettability, as the ORR takes place on a three-phase reaction zone between catalyst-electrolyte-gas and the OER on a two-phase boundary (catalyst-electrolyte) [5,15]. Therefore, it is favorable to spatially separate ORR and OER sites in the air electrode.

In this work, well-known precious metal-free oxide catalysts of the spinel-type (NiCo_2O_4) and perovskite-type ($\text{La}_{0.6}\text{Sr}_{0.4}\text{Co}_{0.2}\text{Fe}_{0.8}\text{O}_3$) were used in a bifunctional air electrode. Both catalysts are inexpensive compared to Pt/C or IrO_2 and RuO_2 and exhibit bifunctional catalytic activity toward ORR and OER [15–20]. They were implemented into an electrode by a combination of PTFE as hydrophobic binder with (electro-)chemically resistant and electrically conductive support materials such as carbon nanofibers and nickel powder, all supported on a mechanically stable nickel foam current collector. Especially when using oxide catalysts, which have low intrinsic electrical conductivity, a finely tuned selection of the support materials is crucial for reaching high performances [17].

Regarding the electrochemical measurements, zinc-air batteries are commonly tested with charge/discharge current densities in the range of 5–50 mA cm^{-2} [7,20–26], thereby avoiding dendritic zinc deposition during charging. Hence, a comparably high current density of 50 mA cm^{-2} was chosen in order to test the long-term stability of the air electrodes during prolonged cycling experiments. Because of the beneficial effects of pulse charging on zinc deposition, special focus was placed on the influence of pulse charging in regard to the long-term stability of the positive electrode by monitoring the respective maximum potentials during charging. As measurements performed with air [23,24,26] as well as with pure oxygen [20–22,25] have been published, additionally, the difference in performance between these two measurement types were investigated and compared.

2. Experimental

2.1. Catalyst preparation

All chemicals were used as purchased without further purification.

NiCo_2O_4 spinel supported on carbon nanofibers (CNF; HTF150FF-LHT, 150 nm, lowheat; Electrovac AG, Austria) and supported on Ni powder ($< 50 \mu\text{m}$; Sigma Aldrich) was separately prepared by a impregnation-calcination method [27]. First, 7 g support material were dispersed in 200 mL ultrapure water (18 $\text{M}\Omega\text{cm}$)/ethanol 1:1 (v:v) using an ultrasonic probe. 3.62 g $\text{Ni}(\text{NO}_3)_2 \cdot 6\text{H}_2\text{O}$ (Sigma Aldrich) and 7.26 g $\text{Co}(\text{NO}_3)_2 \cdot 6\text{H}_2\text{O}$ (Sigma Aldrich) in the Ni:Co molar ratio 1:2 were dissolved in the support material dispersion with an ultrasonic probe for 1 h. Under vigorous stirring at 80 °C (heating mantle) the solvent was slowly evaporated within approximately 10 h. The obtained dry powder was ground in a mortar and calcined at 375 °C in air atmosphere (no gas flow) for 2 h (heating rate 5 °C min^{-1}) in a chamber furnace and afterwards cooled down at room temperature. It has to be noted, that probably due to larger fractions of less graphitized carbon in the CNF powder, significant losses of support material – catalyzed by the deposited metal – were detected during calcination. In regard to the obtained yield, the catalyst weight percentage of NiCo_2O_4 on CNF was calculated to be 48 wt%, which was confirmed by ICP-OES measurement (Supplementary Table S1). The NiCo_2O_4 loading on Ni powder was 30 wt%. The two supported catalysts obtained by this procedure are noted in the following as $\text{NiCo}_2\text{O}_4/\text{CNF}$ and $\text{NiCo}_2\text{O}_4/\text{Ni}$, respectively.

$\text{La}_{0.6}\text{Sr}_{0.4}\text{Co}_{0.2}\text{Fe}_{0.8}\text{O}_3$ perovskite (d_{50} 0.4–0.8 μm , 10–14 $\text{m}^2 \text{g}^{-1}$; Sigma-Aldrich) was homogeneously dispersed on carbon nanofiber support material (75 wt% on CNF) by ultrasonic mixing in ultrapure water/2-propanol (99.5%; Sigma-Aldrich) 1:1 (v:v) for 1 h, followed by evaporation of the solvent at 80 °C under vigorous stirring (Supplementary Fig. S1b)).

2.2. Air electrode preparation

Nickel foam (pore size 450 μm , area density 420 g m^{-2} , thickness 1.6 mm; Alantum Corporation, Germany) was used as current collector (Supplementary Fig. S1a) and provides spatial separation of ORR (good gas accessibility) and OER (electrolyte wettability) sites. Before use, it was cleaned with 2-propanol and ultrapure water. A PTFE suspension (TF5032; Dyneon GmbH) served as hydrophobic binder material. For the bi-catalyzed air electrode, two separate electrode pastes – one for each side of the Ni foam – were prepared by mixing the catalyst powders with binder in 10 mL g^{-1} powder ultrapure water/2-propanol 1:1 (v:v). The mixture for the electrolyte side (for OER) contained the spinel catalyst and consisted of 55 wt% $\text{NiCo}_2\text{O}_4/\text{CNF}$, 25 wt% $\text{NiCo}_2\text{O}_4/\text{Ni}$ and 20 wt% PTFE. The second mixture, used for the gas side (ORR), contained 80 wt% $\text{La}_{0.6}\text{Sr}_{0.4}\text{Co}_{0.2}\text{Fe}_{0.8}\text{O}_3/\text{CNF}$ and 20 wt% PTFE. During mixing and slow evaporation of the solvent, a paste was obtained and spread onto the Ni foam. For a stable connection between the Ni foam and the catalyst-binder paste, the electrode was pressed and sintered at 300 °C with a pressure of 150 kg cm^{-2} for 20 min in air atmosphere resulting in a final electrode thickness of 0.7 mm with a catalyst loading of approximately 10 mg cm^{-2} NiCo_2O_4 and 25 mg cm^{-2} $\text{La}_{0.6}\text{Sr}_{0.4}\text{Co}_{0.2}\text{Fe}_{0.8}\text{O}_3$. In order to ensure comparability, 24 cm^2 or 48 cm^2 electrodes were manufactured in one batch and then cut into smaller electrodes (Supplementary Fig. S2b)).

In addition, electrodes catalyzed either with NiCo_2O_4 or $\text{La}_{0.6}\text{Sr}_{0.4}\text{Co}_{0.2}\text{Fe}_{0.8}\text{O}_3$ were manufactured for comparison to the bi-catalyzed bifunctional air electrodes. For this, twice the amount of each electrode paste was prepared and spread on both sides of

the Ni foam, obtaining a final catalyst loading of approximately 19 mg cm^{-2} NiCo_2O_4 in case of the NiCo_2O_4 -only electrode and 45 mg cm^{-2} $\text{La}_{0.6}\text{Sr}_{0.4}\text{Co}_{0.2}\text{Fe}_{0.8}\text{O}_3$ for $\text{La}_{0.6}\text{Sr}_{0.4}\text{Co}_{0.2}\text{Fe}_{0.8}\text{O}_3$ -only air electrode, respectively.

2.3. Electrochemical measurements

All electrochemical measurements of air electrodes were performed in a half-cell set-up using one air electrode as working electrode and a second one as counter electrode allowing simultaneous observation of the degradation behavior of two electrodes (shown in the schematic in Supplementary Fig. S2a)). Both air electrodes were separately referenced to Zn foil (1.6 mm thickness, $\sim 8 \text{ cm}^2$ surface area; AlfaAesar) using a Luggin capillary with a distance of 2 mm to the electrode in order to obtain near electrolyte resistance free potentials. The measurements were performed using a multi-channel BaSyTec Cell Test System with corresponding software in stationary 8 M KOH (> 90% flakes, Sigma Aldrich) electrolyte with 0.5 M ZnO (p.a.; Merck) at ambient temperature, thereby allowing to reference versus zinc as first-order electrode. In the measured potential window between ORR and OER no zinc is dissolved or electrochemically deposited, hence a constant zinc concentration is maintained during the measurement. All potentials listed within this paper are given in regard to Zn/Zn^{2+} . The air electrodes were vertically mounted in an in-house designed PMMA test cell using a polymeric alkali resistant sealing, leaving a square surface area of 4 cm^2 in contact with the electrolyte. The same electrode surface area was open at the back,

where it was continuously supplied either with 25 mL min^{-1} synthetic air (SA; 80% N_2 /20% O_2 ; Messer Group GmbH) or 5 mL min^{-1} pure oxygen (5.5; Messer Group GmbH). The vertical set-up was chosen to promote oxygen bubble removal [11]. To counter the hydrostatic pressure from the electrolyte, the gas exhaust was immersed 5 cm into water. The working electrode was long-term tested by charge/discharge cycling with a duration of 1 h each (2 h per cycle). During discharging 50 mA cm^{-2} were applied and pulse charging was performed with 24,000 pulses with 150 mA cm^{-2} (j_p) during the 50 ms pulse and no current during the 100 ms pause. This corresponds to a mean current density j_m of 50 mA cm^{-2} . About every 100 cycles a current-potential polarization curve for ORR and OER was recorded with ten steps between $4\text{--}50 \text{ mA cm}^{-2}$. Each step was kept for 10 min.

2.4. Physical characterization

Scanning electron microscopy (SEM) was performed on a Vega 3 (Tescan) at 20.0 kV with a secondary electron detector. Corresponding energy dispersive X-ray spectroscopy (EDX) mapping was performed with an X-ray detector and software by Oxford instruments. X-ray diffraction patterns (XRD) of the NiCo_2O_4 catalyst powders were performed on a D8 Advance X-ray diffractometer (Bruker) using $\text{CuK}\alpha$ irradiation. XRD data were collected in the range of $20\text{--}100^\circ 2\theta$, using a step size of $0.02^\circ 2\theta$ and a counting time of 2 s per step. Rietveld-analysis was performed with the software X'Pert HighScore Plus (PANalytical) and with Topas (Bruker).

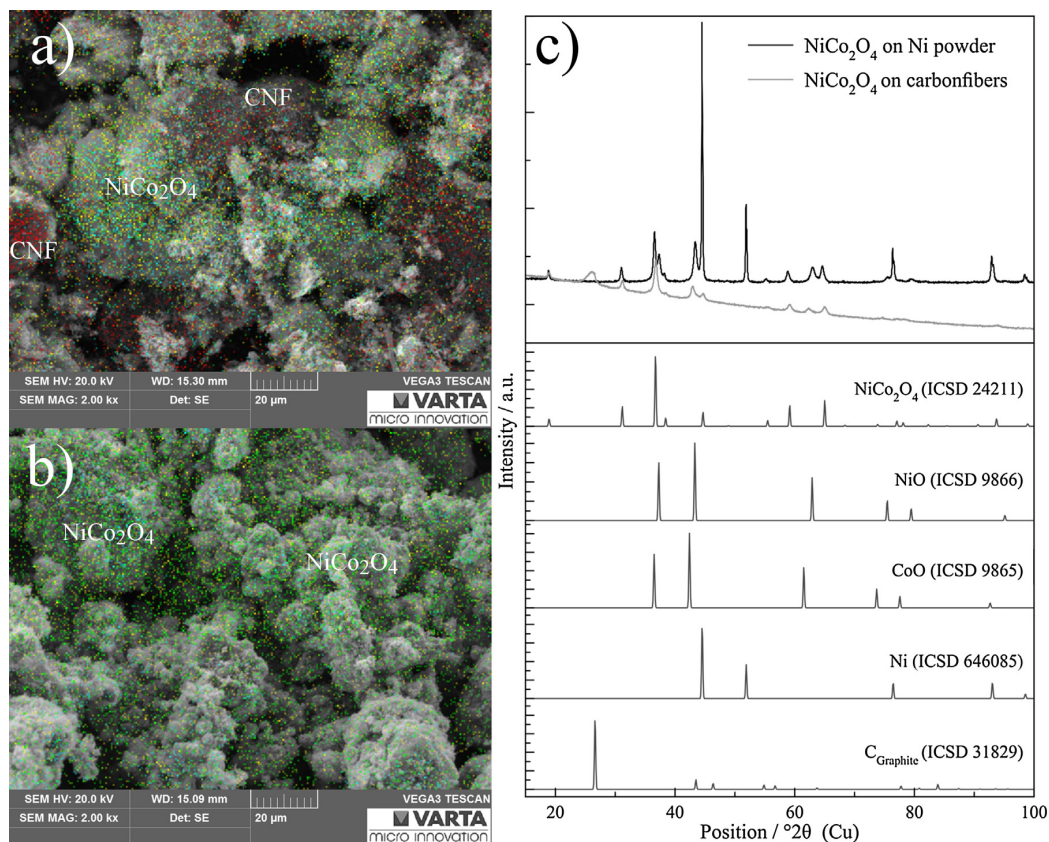


Fig. 1. EDX mapping of **a)** $\text{NiCo}_2\text{O}_4/\text{CNF}$ and **b)** $\text{NiCo}_2\text{O}_4/\text{Ni}$ displaying nickel (green), cobalt (yellow), oxygen (cyan) and carbon (red), **c)** XRD results of the $\text{NiCo}_2\text{O}_4/\text{CNF}$ and $\text{NiCo}_2\text{O}_4/\text{Ni}$, where all peaks can be assigned to NiCo_2O_4 , NiO and support material (Ni or carbon). (For interpretation of the references to colour in this figure legend, the reader is referred to the web version of this article.)

3. Results and discussion

3.1. Catalyst characterization

The low formation temperature of the NiCo_2O_4 spinel catalyst of about 400°C [28] enables direct formation of the spinel on the support material, whereby the Ni powder support provides good electrical conductivity and CNFs were chosen as carbon support as they exhibit superior electrochemical stability at highly oxidative potentials compared to other carbon materials such as Vulcan XC72, because of higher fractions of conjugated graphitic structures [5]. SEM images in connection with EDX mapping (Fig. 1a) and b)) show high particle surface areas for both catalysts and confirm a homogeneous distribution of nickel, cobalt and oxygen on the CNF support (carbon in red in Fig. 1a)) as well as of cobalt and oxygen on the Ni powder support (Fig. 1b)).

The XRD pattern of $\text{NiCo}_2\text{O}_4/\text{CNF}$ (Fig. 1c)) shows peaks attributed to cubic NiCo_2O_4 spinel (lattice constant $a = 8.116(1) \text{ \AA}$, literature value ICSD-24211 $a = 8.114 \text{ \AA}$) as well as of NiO. By means of Rietveld analysis (see Supplementary Fig. S3) the share of NiO in proportion to NiCo_2O_4 was determined to be about 31 vol% in the irradiated volume of the sample. A closer look at the obtained lattice constant for cubic NiO ($a = 4.2133(6) \text{ \AA}$) shows that this value lies between the ICSD literature values of pure cubic NiO ($a = 4.17\text{--}4.18 \text{ \AA}$) and CoO ($a = 4.252\text{--}4.262 \text{ \AA}$). This indicates that in this case, nickel and cobalt, which did not form a spinel during calcination, are present in the form of $\text{Ni}_{1-x}\text{Co}_x\text{O}$ or as NiO and CoO in approximately equal amounts. In the XRD analysis of $\text{NiCo}_2\text{O}_4/\text{Ni}$ (Fig. 1c)), the share of formed NiCo_2O_4 spinel (lattice constant $a = 8.158 \text{ \AA}$) is difficult to determine as it is not possible to distinguish between NiO formed by Ni salt decomposition or by surface oxidation of the Ni support. Rietveld-analysis shows a distribution of about 32 vol% NiCo_2O_4 , 36 vol% NiO and 32 vol% Ni. However, the obtained lattice constant of $a = 4.173 \text{ \AA}$ is assigned to pure NiO with no shift toward CoO, showing that close to all of the deposited cobalt salt formed into NiCo_2O_4 spinel during calcination.

3.2. Electrochemical measurements

3.2.1. Long-term performance of NiCo_2O_4 -only and $\text{La}_{0.6}\text{Sr}_{0.4}\text{Co}_{0.2}\text{Fe}_{0.8}\text{O}_3$ -only bifunctional air electrodes

High bifunctional catalytic activity of NiCo_2O_4 spinel catalyst toward OER and ORR has been reported in literature by several groups [19,20], but also the respective oxides, i.e. NiO and CoO, are known to have good catalytic activity especially toward OER [24,29,30]. Moreover, many different types of perovskites with good ORR and OER activity have been successfully tested and reported [15,17,31]. In this work, both types of oxide catalysts were investigated in air electrodes, confirming their good performance as presented in the following.

In Fig. 2a) the pulse charging/discharging cycling measurement of the NiCo_2O_4 -catalyzed air electrode supplied with synthetic air ($\text{NiCo}_2\text{O}_4/\text{SA}$) is depicted. The electrode showed over the whole operation period of 43 h stable pulse charging OER potentials of around 2.0 V with a pulse maximum potential of 2.05 V and a pause minimum potential of 1.94 V. The initial charge/discharge potential gap ΔV was only 0.88 V, which is significantly below 1.0 V. Between 10 h and 40 h of operation, the ORR discharge potential decreased steadily from 1.16 V to 0.80 V. Within the first 10 h of operation this effect is not visible. A similar degradation behavior was observed by Pletcher et al. [20] during their long-term measurement and was also mentioned by Jörissen [15], who assessed NiCo_2O_4 a stable OER activity but deteriorating ORR performance over time.

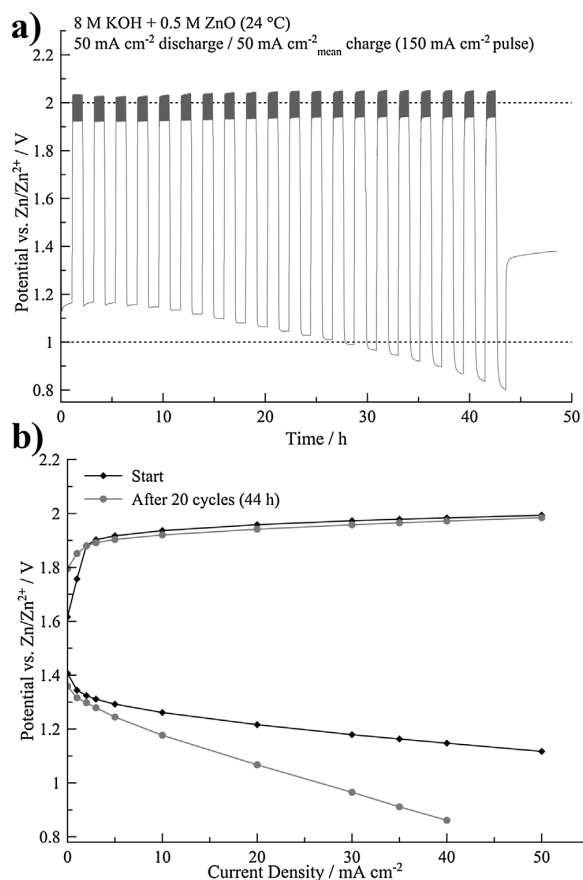


Fig. 2. Electrochemical long-term cycling with pulse charging of a NiCo_2O_4 -catalyzed air electrode supplied with synthetic air ($\text{NiCo}_2\text{O}_4/\text{SA}$): a) course of the potential shown over the whole measuring time; b) current-potential polarization curves for ORR and OER.

ORR/OER polarization curves recorded at the end and the beginning of operation are depicted in Fig. 2b). The curves initially exhibited a flat profile and little ohmic losses with increasing current density, showing good electrical conductivity within the electrode. An interesting effect were the different open circuit potentials (OCP) after charging or discharging, respectively [20,28]. The OCP gap between ORR and OER observed with the spinel catalyst is due to different Ni and Co oxidation states within the spinel structure (see Supplementary Fig. S4). During repeated cycling Co changes between oxidation states +II/+III and subsequently between +III/+IV and Ni between oxidation states +II/+III, respectively [19]. All these redox processes are in the potential range between 1.4–1.8 V vs. Zn/Zn^{2+} (which corresponds to about 1.0–1.4 V vs. reversible hydrogen electrode). For a prolonged time the catalyst stays in the oxidized state after charging or vice versa in the reduced state after discharging [20]. These perpetual redox processes induced irreversible changes within the spinel structure, causing the spinel's fast deteriorating performance toward ORR.

The results of the $\text{La}_{0.6}\text{Sr}_{0.4}\text{Co}_{0.2}\text{Fe}_{0.8}\text{O}_3/\text{SA}$ electrode long-term operation of about 700 h, i.e. 300 cycles, are depicted in Fig. 3a) and b). The course of its long-term behavior can also be seen in Fig. 3c), where the ORR/OER current-potential curves measured after every 100 cycles are depicted. In contrast to the NiCo_2O_4 -catalyzed electrodes, the initial performance regarding ORR and OER was low, exhibiting a high charge/discharge ΔV of 1.30 V with the

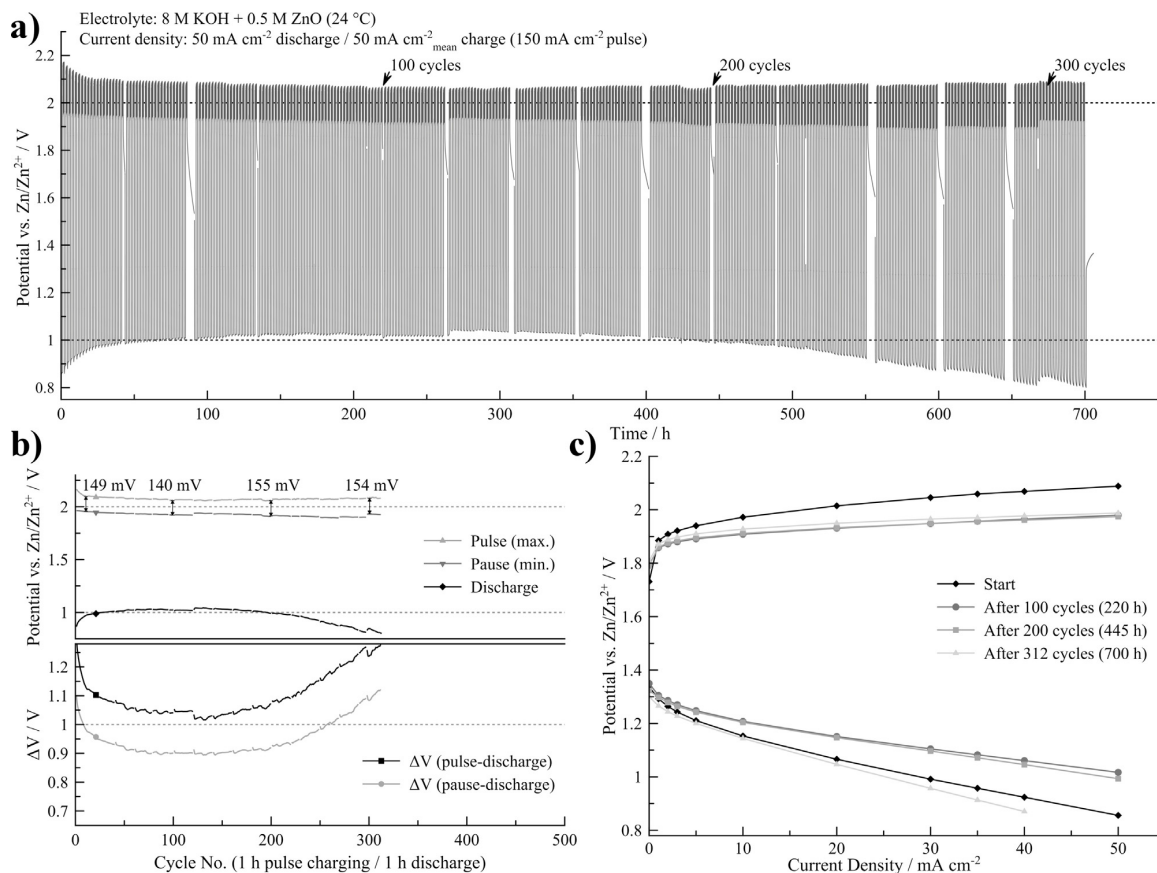


Fig. 3. Electrochemical long-term cycling with pulse charging of a $\text{La}_{0.6}\text{Sr}_{0.4}\text{Co}_{0.2}\text{Fe}_{0.8}\text{O}_3$ -catalyzed air electrode supplied with synthetic air ($\text{La}_{0.6}\text{Sr}_{0.4}\text{Co}_{0.2}\text{Fe}_{0.8}\text{O}_3/\text{SA}$): **a)** course of the potential shown over the whole measuring time; **b)** maximum and minimum potentials and the respective potential difference for each cycle; **c)** current-potential polarization curves for ORR and OER measured every 100 cycles.

maximum pulse charging potential at 2.17 V and the ORR potential at 0.87 V. However, within the first 40 h of operation, the discharge potential increased up to 1.0 V and the charging potential converged closely to 2.0 V. This confirms the need of longer operating times in order to be able to evaluate the performance of air electrodes. As similar perovskites exhibited good catalytic activity for ORR and OER [18,32], the reason for the improving performance are attributed to altered wettability inside of the electrode's structure occurring within the first 40 h. For an operational period of about 400 h or 170 cycles the charge/discharge performance remained constant surpassing the $\text{NiCo}_2\text{O}_4/\text{SA}$ electrode's stability by tenfold. After that, the discharge potential slowly decreased over the course of 250 h until the lower abort potential of 0.8 V was reached. However, in contrast to the $\text{NiCo}_2\text{O}_4/\text{SA}$ electrode, the measured OER potentials were about 0.03–0.04 V higher during charging and also the ΔV between pulse and pause as indicated in Fig. 3b) was slightly larger, thus confirming the superior catalytic activity of the NiCo_2O_4 spinel toward OER. Nevertheless, the stability during prolonged cycling is a beneficial asset of the perovskite catalyst.

3.2.2. Long-term performance of bi-catalyzed bifunctional air electrodes supplied with synthetic air or oxygen

As described in section 3.2.1, NiCo_2O_4 spinel proved to be an excellent OER catalyst with low potentials of around 2.0 V and initially high but fast deteriorating discharge performance. In

comparison, $\text{La}_{0.6}\text{Sr}_{0.4}\text{Co}_{0.2}\text{Fe}_{0.8}\text{O}_3$ perovskite exhibited lower OER activity but much higher stability. The combination of those two oxide catalysts was tested in bi-catalyzed bifunctional electrodes and the performance comparatively investigated by supplying the electrodes with either synthetic air or pure oxygen.

Fig. 4 depicts the collected results of the long-term pulse charge cycling measurement of the bi-catalyzed/ O_2 electrode, which exhibited the highest long-term stability of all of the tested electrodes with an operation time of more than 1000 h. Within the first 20 h of operation (i.e. 10 cycles) the discharge potential decreased from 1.25 V to 1.17 V. This trend matches with the first initial discharge performance drop observed for the $\text{NiCo}_2\text{O}_4/\text{SA}$ electrode. Overall the discharge potential was stable for more than 700 h (1 month) and 325 cycles after the initial ORR performance drop. During this time, the charge potentials during pulsing (visible as darker black bar in Fig. 4a)) remained between 1.89–1.91 V (i.e. pause potential) and 2.0–2.05 V (i.e. pulse potential) with a slightly increasing potential gap as indicated in Fig. 4b). Furthermore, the charge/discharge potential gap ΔV was between 0.71 V (pause-discharge) and 0.83–0.87 V (pulse-discharge), i.e. significantly below 1.0 V. The drop in discharge potential after 700 h was caused by blockage of the gas outlet and slow filling of the gas-side with electrolyte droplets, hindering the gas accessibility of the electrode. After maintenance of the test cell including rinsing of the electrolyte-exposed side with ultrapure water, the

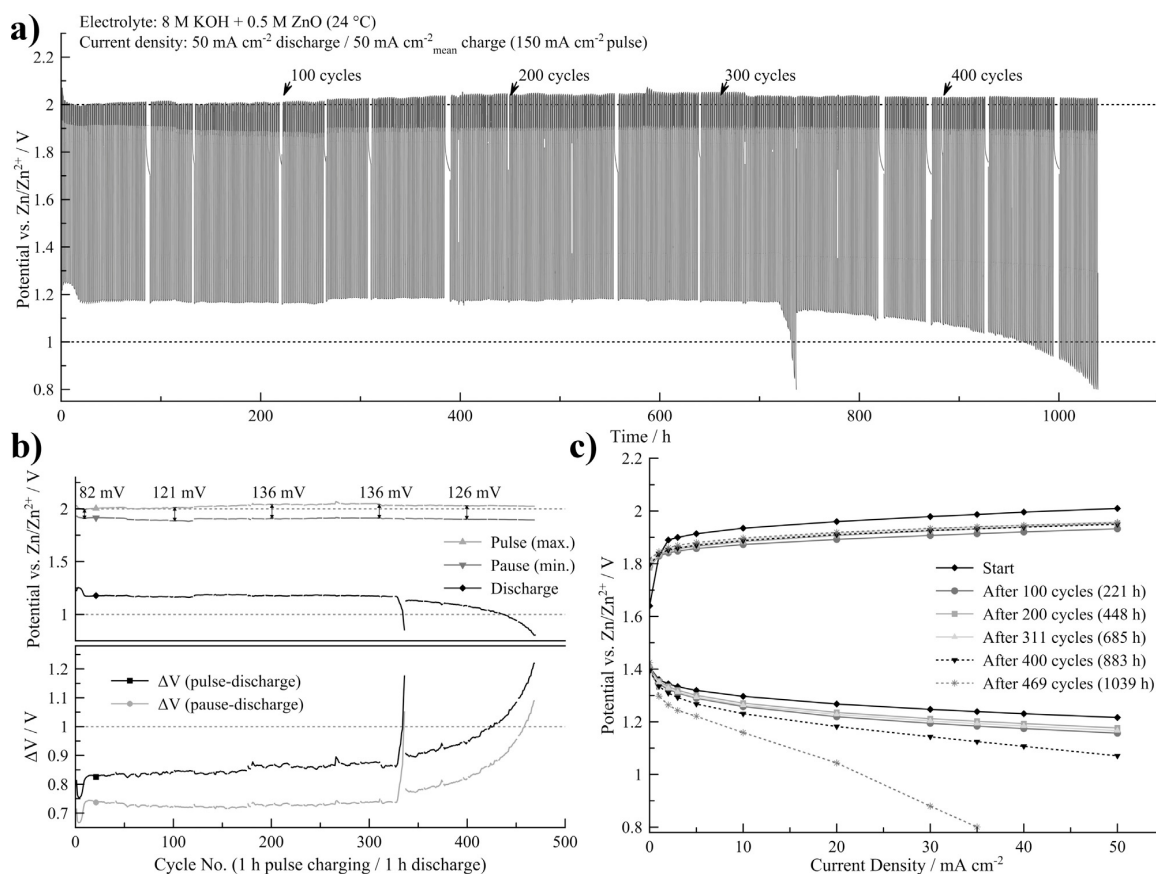


Fig. 4. Electrochemical long-term cycling with pulse charging of a bi-catalyzed bifunctional air electrode supplied with oxygen (bi-catalyzed/ O_2): **a**) course of the potential shown over the whole operation time; **b**) maximum and minimum potentials and the respective potential difference for each cycle; **c**) current-potential polarization curves for ORR and OER measured every 100 cycles.

discharge performance was restored close to the previous potential (1.13 V), showing the robustness of the air electrode build. In the course of the following 250 h the discharge potential slowly decreased, exhibiting the same behavior as observed with the $La_{0.6}Sr_{0.4}Co_{0.2}Fe_{0.8}O_3/SA$ electrode.

With ORR/OER polarization curves, as depicted in Fig. 4c), the electrodes performance at different current densities is determined. Regarding the ORR, the polarization curves slightly decreased from the initial performance to stable values for a period of 300 cycles. The OCP was slightly above 1.4 V. Activation losses up to 10 mA cm^{-2} were observed as indicated by the first steeper drop in the polarization curve. The linear ohmic potential drop between 10 mA cm^{-2} and 50 mA cm^{-2} was 0.08 V at the beginning of operation and 0.10 V after 300 cycles, showing good electrical conductivity within the electrode provided by the Ni foam. Regarding the OER, the shape of the polarization curves was flat with charge potentials of always $< 2.0 \text{ V}$. No degradation of OER performance was visible during operation.

Besides long-term cycling measurements of the bi-catalyzed/ O_2 electrode, a similar electrode was tested with synthetic air (SA) supply. The results of these measurements are shown in Fig. 5 and emphasize the significantly lower discharge performance of the bi-catalyzed/SA electrode by about 0.17 V compared to the bi-catalyzed/ O_2 electrode. The disparity is due to the difference in oxygen partial pressure with a high percentage of inert nitrogen in the SA, while flushing the electrode with the same

absolute amount of oxygen (5 mL min^{-1}). At the beginning of operation there was a similar drop in discharge potential of about 0.14 V as observed with the bi-catalyzed/ O_2 electrode, but the discharge potential subsequently stabilized after 10 h measuring time. The performance remained stable for more than 400 h and close to 200 cycles, exhibiting a ORR discharge potential of 1.0 V and very stable pulse charge potential of 2.01–2.03 V (pulse) and 1.89–1.92 V (pause) (Fig. 5b)). After that, a slow degradation in ORR activity in the course of about 250 h was apparent until the abort potential of 0.8 V was reached. As both electrodes exhibited similar degradation rates within the last few hundred hours while maintaining constant OER potentials, the same degradation mechanism came into effect. This includes pronounced wetting of the electrode, thereby reducing the number of three-phase boundaries and lowering gas accessibility, which is also indicated by the SEM images in Fig. 7. The overall shorter operation time of the bi-catalyzed/SA electrode is caused by the high amount of inert nitrogen in the gas feed, which reduces the oxygen accessibility to the few remaining catalytic sites with short diffusion paths.

The shape of ORR/OER current-potential curves depicted in Fig. 5c) is similar to the bi-catalyzed/ O_2 electrode. A decreasing ORR discharge performance was apparent, but the OER potentials remained below 2.0 V and were stable until the end of operation.

A comparative summary of the investigated electrodes is listed in Table 1. The potential gap ΔV for the bi-catalyzed/SA and the

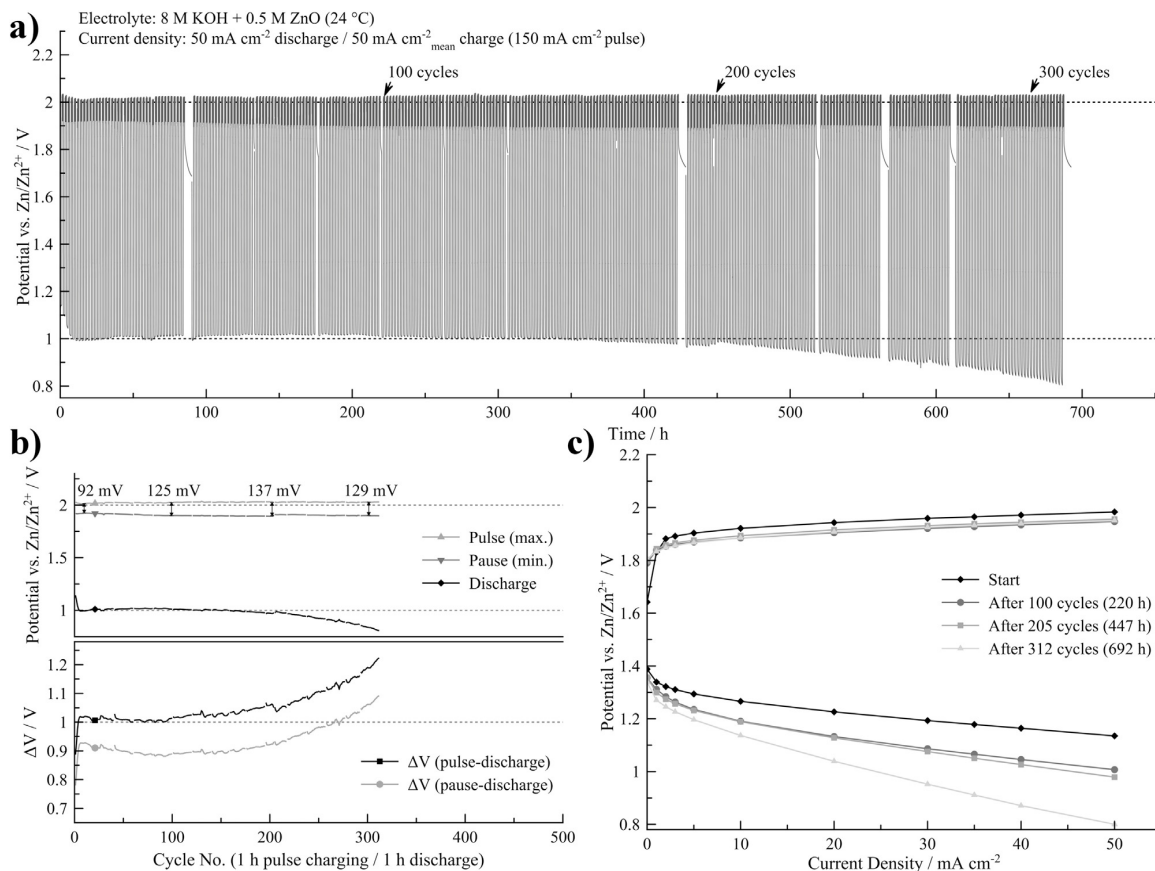


Fig. 5. Electrochemical long-term cycling with pulse charging of a bi-catalyzed bifunctional air electrode supplied with synthetic air (bi-catalyzed/SA): **a)** course of the potential shown over the whole measuring time; **b)** maximum and minimum potentials and the respective potential difference for each cycle; **c)** current-potential polarization curves for ORR and OER measured every 100 cycles.

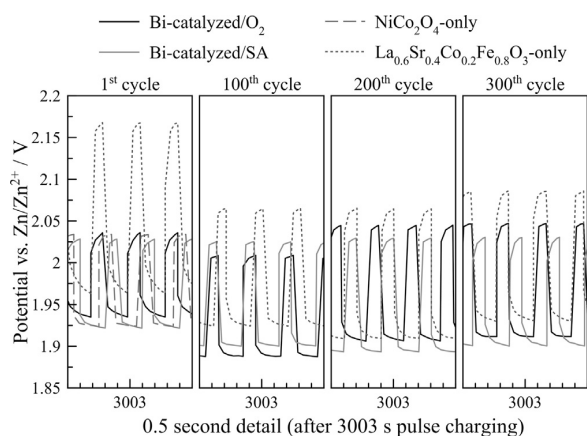


Fig. 6. Comparison of the four different electrodes depicting the potential during pulse charging with 50 ms pulse (high potential) at 150 mA cm⁻² and 100 ms pause (low potential) after every 100th cycle.

La_{0.6}Sr_{0.4}Co_{0.2}Fe_{0.8}O₃/SA electrode was 0.98 V after 200 cycles, which corresponds to a potential charge/discharge efficiency of 51% for this half-cell reaction. For the bi-catalyzed/O₂ electrode ΔV was even below 0.8 V, i.e. as high as 60% potential efficiency.

Nevertheless, one has to keep in mind, that supplying electrodes with air is more economically reasonable in the zinc-air flow battery than supply with pure oxygen.

3.2.3. Pulse charging

Pulse charging is an advantageous method in order to obtain compact zinc morphologies on the zinc electrode, which is necessary for preventing capacity losses and short-circuiting by dendrite formation. However, because of the high oxidative pulse currents, degradative stress is induced on the air electrode by this method. Therefore, special attention lies on the performance of air electrodes during prolonged pulse charge/discharge cycling. The detailed behavior during pulse charging of the four investigated electrodes is shown in Fig. 6. The NiCo₂O₄ spinel-catalyzed electrodes exhibited stable and low pulse potentials of < 2.05 V demonstrating the superior OER performance of the spinel catalyst compared to the La_{0.6}Sr_{0.4}Co_{0.2}Fe_{0.8}O₃ perovskite. The lower OER potentials can be beneficial for improving the electrode's long-term stability as these highly oxidative potentials promote degradative effects, e.g. carbon corrosion.

The shape of the two bi-catalyzed electrodes was nearly the same as of the NiCo₂O₄/SA electrode with comparable potential profiles in the course of 1st to 300th cycle. The profile itself was nearly rectangular indicating fast potential response times of the electrodes. All in all, the high current densities of 150 mA cm⁻²

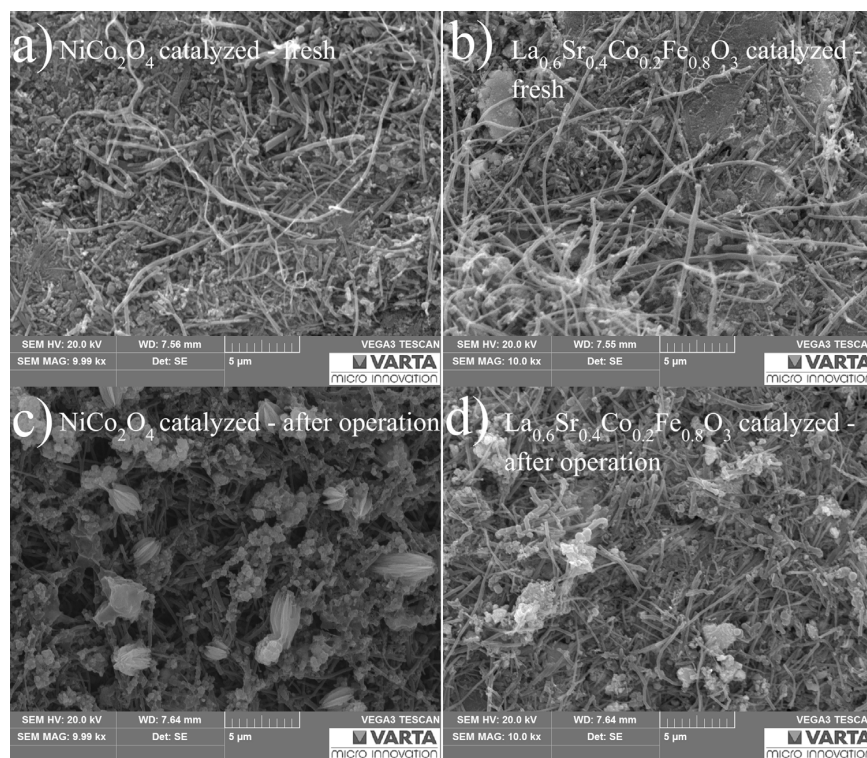


Fig. 7. SEM images of the bi-catalyzed/ O_2 electrode before and after long-term operation: **a**) and **c**) show the $NiCo_2O_4$ spinel catalyzed side, which faced the electrolyte and **b**) and **d**) depicts the $La_{0.6}Sr_{0.4}Co_{0.2}Fe_{0.8}O_3$ perovskite surface, which was flushed with gas during operation.

Table 1

Comparison of the charge/discharge potential difference (ΔV) of the four electrodes at the beginning of operation and after 200 cycles.

| | ΔV at $20\text{ mA cm}^{-2}/V$ | | ΔV at $50\text{ mA cm}^{-2}/V$ | |
|-------------------------------------------|----------------------------------------|------------------|----------------------------------------|------------------|
| | Start | After 200 cycles | Start | After 200 cycles |
| bi-catalyzed/ O_2 | 0.69 | 0.67 | 0.79 | 0.78 |
| bi-catalyzed/SA | 0.72 | 0.79 | 0.85 | 0.98 |
| $NiCo_2O_4$ /SA | 0.74 | – | 0.88 | – |
| $La_{0.6}Sr_{0.4}Co_{0.2}Fe_{0.8}O_3$ /SA | 0.95 | 0.79 | 1.23 | 0.98 |

during the 50 ms pulse resulted in only about 0.06–0.08 V higher charge potentials compared to constant current charging, showing that it is possible to obtain good long-term stability with this charging method.

3.3. End of life characterization

Fig. 7 depicts SEM images of a bi-catalyzed air electrode before and after operation. The $NiCo_2O_4$ spinel- and the $La_{0.6}Sr_{0.4}Co_{0.2}Fe_{0.8}O_3$ perovskite-catalyzed surfaces have a similar appearance after pressing and sintering (**Fig. 7a**) and **b**) showing a complex distribution of materials. The carbon nanofibers are distinguishable and form an electrically conductive network whilst providing channels for gas supply within the electrode. EDX mapping of the spinel catalyzed surface of a freshly manufactured air electrode (depicted in Supplementary Fig. S5) proves the homogeneous distribution of catalyst and support materials. After electrochemical charge/discharge measurements of more than 1000 h the KOH electrolyte was washed out of the electrode by soaking it five

times with ultrapure water followed by slow drying. Even after washing, electrolyte residues can be seen as oval-shaped deposits on the surface of the spinel side, which was facing the electrolyte (**Fig. 7c**). They are not visible on the perovskite side (**Fig. 7d**), which generally appears unaltered by the electrochemical testing. In contrast to this, the spinel side exhibits about 1–3 μm sized holes in the surface, which were shaped by the emerging gas bubbles during oxygen evolution whilst charging. The carbon network is significantly reduced and mainly the roundly shaped catalyst particles are left. Through the holes, electrolyte penetrated deeper into the electrode over time, thereby slowly changing its wettability [33]. In the end, electrolyte leakage occurred and the ORR potentials decreased due to hindered gas diffusion within the electrolyte-filled gas channels. In contrast to this, the OER potentials during pulse charging stayed in the same range during the whole operation time, indicating no change in the number of two-phase boundaries between catalyst and electrolyte.

4. Conclusion

The investigated bifunctional air electrodes for the use in zinc-air flow batteries exhibited stable long-term performances during pulse charging and discharge measurements (2 h per cycle). Stable charge and discharge potentials for more than 700 h (1 month) and 325 cycles were achieved with a bi-catalyzed bifunctional air electrode supplied with oxygen. The potential gap ΔV between O_2 -reduction minimum potential and O_2 -evolution maximum pulse potential was thereby 0.83–0.87 V at 50 mA cm^{-2} . When supplied with air, which is preferable for future applications in zinc-air flow batteries, a stable long-term performance of 1.0 V potential gap ΔV

for more than 400 h and close to 200 cycles was obtained. The pulse charging method, which is advantageous for compact zinc deposition, was successfully applied and tested for air electrodes. The resulting OER potentials during pulsing, i.e. at tripled charge current density of 150 mA cm^{-2} , were only 0.06–0.08 V higher, compared to constant charging current densities.

In-house synthesized NiCo_2O_4 spinel catalyst supported on either carbon nanofibers or nickel powder was found to be an excellent catalyst toward OER with charge potentials $< 2.0 \text{ V vs. Zn/Zn}^{2+}$ and initially also toward ORR, but deteriorating discharge performance was observed within the first 40 h of operation. Commercial $\text{La}_{0.6}\text{Sr}_{0.4}\text{Co}_{0.2}\text{Fe}_{0.8}\text{O}_3$ perovskite showed initially improving and stable charge/discharge performance, but thereby exhibiting about 0.04 V higher OER potentials. Hence, the two oxide catalysts were combined within one Ni foam-supported bifunctional electrode, where the NiCo_2O_4 spinel catalyst faced the electrolyte and the $\text{La}_{0.6}\text{Sr}_{0.4}\text{Co}_{0.2}\text{Fe}_{0.8}\text{O}_3$ perovskite side was supplied with oxygen or air. With these electrodes operation times of more than 1000 h (oxygen) and 750 h (synthetic air) were achieved.

SEM imaging of the electrodes after operation confirmed the end of life by mechanical degradation caused by bubble formation during oxygen evolution. The resulting slowly declining discharge potentials over the course of 250 h indicate a reduction of three-phase boundaries for ORR and increasingly long diffusion paths for the gas. In order to gain further insights, long-term stability and degradation effects within an up-scaled zinc-air flow cell are under investigation.

Acknowledgements

Funding by the Austrian Federal Ministry of Transport, Innovation and Technology (BMVIT) and The Austrian Research Promotion Agency (FFG) through the program “e!MISSION.at Energieforschungsprogramm” (No. 848933) is gratefully acknowledged. We also want to thank our cooperation partners from the Institute of Chemistry and Technology of Materials at Graz University of Technology and our industry partners VARTA Micro Innovation GmbH (Austria) and TSR-Kat (Germany). ICP-OES measurements were kindly performed by Helmar Wiltsche (Institute of Analytical Chemistry and Food Chemistry, Graz University of Technology). Ni foam was generously provided by Alantum Europe GmbH, Germany.

Appendix A. Supplementary data

Supplementary data associated with this article can be found, in the online version, at <http://dx.doi.org/10.1016/j.electacta.2017.08.128>.

References

- [1] M. Xu, D.G. Ivey, Z. Xie, W. Qu, Rechargeable Zn-air batteries: Progress in electrolyte development and cell configuration advancement, *J. Power Sources* 283 (2015) 358–371, doi:<http://dx.doi.org/10.1016/j.jpowsour.2015.02.114>.
- [2] P. Pei, K. Wang, Z. Ma, Technologies for extending zinc-air battery's cyclife: A review, *Appl. Energy* 128 (2014) 315–324, doi:<http://dx.doi.org/10.1016/j.apenergy.2014.04.095>.
- [3] V. Caramia, B. Bozzini, Materials science aspects of zinc-air batteries: a review, *Mater. Renew. Sustain. Energy* 3 (2014) 28, doi:<http://dx.doi.org/10.1007/s40243-014-0028-3>.
- [4] Y. Li, H. Dai, Recent advances in zinc-air batteries, *Chem. Soc. Rev.* 43 (2014) 5257–5275, doi:<http://dx.doi.org/10.1039/C4CS00015C>.
- [5] J. Fu, Z.P. Cano, M.G. Park, A. Yu, M. Fowler, Z. Chen, Electrically Rechargeable Zinc-Air Batteries: Progress, Challenges, and Perspectives, *Adv. Mater.* 29 (2017) 1604685, doi:<http://dx.doi.org/10.1002/adma.201604685>.
- [6] S. Suren, S. Kheawhom, Development of a High Energy Density Flexible Zinc-Air Battery, *J. Electrochem. Soc.* 163 (2016) A846–A850, doi:<http://dx.doi.org/10.1149/2.0361606jes>.
- [7] J. Fu, F.M. Hassan, J. Li, D.U. Lee, A.R. Ghannoum, G. Lui, M.A. Hoque, Z. Chen, Flexible Rechargeable Zinc-Air Batteries through Morphological Emulation of Human Hair Array, *Adv. Mater.* (2016) 6421–6428, doi:<http://dx.doi.org/10.1002/adma.201600762>.
- [8] J. Pan, L. Ji, Y. Sun, P. Wan, J. Cheng, Y. Yang, M. Fan, Preliminary study of alkaline single flowing Zn-O₂ battery, *Electrochem. Commun.* 11 (2009) 2191–2194, doi:<http://dx.doi.org/10.1016/j.elecom.2009.09.028>.
- [9] M. Bockelmann, U. Kunz, T. Turek, Electrically rechargeable zinc-oxygen flow battery with high power density, *Electrochem. Commun.* 69 (2016) 24–27, doi:<http://dx.doi.org/10.1016/j.elecom.2016.05.013>.
- [10] J. Cho, S. Jeong, Y. Kim, Commercial and research battery technologies for electrical energy storage applications, *Prog. Energy Combust. Sci.* 48 (2015) 84–101, doi:<http://dx.doi.org/10.1016/j.pecs.2015.01.002>.
- [11] K. Wang, P. Pei, Z. Ma, H. Chen, H. Xu, D. Chen, H. Xing, Growth of oxygen bubbles during recharge process in zinc-air battery, *J. Power Sources* 296 (2015) 40–45, doi:<http://dx.doi.org/10.1016/j.jpowsour.2015.07.039>.
- [12] C. Zelger, J. Laumen, A. Laskos, B. Gollas, Rota-Hull Cell Study on Pulse Current Zinc Electrodeposition from Alkaline Electrolytes, *Electrochim. Acta* 213 (2016) 208–216, doi:<http://dx.doi.org/10.1016/j.electacta.2016.07.108>.
- [13] K. Wang, P. Pei, Z. Ma, H. Xu, P. Li, X. Wang, Morphology control of zinc regeneration for zinc-air fuel cell and battery, *J. Power Sources* 271 (2014) 65–75, doi:<http://dx.doi.org/10.1016/j.jpowsour.2014.07.182>.
- [14] K. Wang, P. Pei, Z. Ma, H. Chen, H. Xu, D. Chen, X. Wang, Dendrite growth in the recharging process of zinc-air battery, *J. Mater. Chem. A* (2015) 22648–22655, doi:<http://dx.doi.org/10.1039/C5TA06366C>.
- [15] L. Jörissen, Bifunctional oxygen/air electrodes, *J. Power Sources* 155 (2006) 23–32, doi:<http://dx.doi.org/10.1016/j.jpowsour.2005.07.038>.
- [16] M.Y. Oh, J.S. Jeon, J.J. Lee, P. Kim, K.S. Nahm, The bifunctional electrocatalytic activity of perovskite $\text{La}_{0.6}\text{Sr}_{0.4}\text{Co}_{0.3}\text{Fe}_{0.7}$ for oxygen reduction and evolution reactions, *Rsc Adv.* 5 (2015) 19190–19198, doi:<http://dx.doi.org/10.1039/c4ra16097e>.
- [17] K. Elumeeva, J. Masa, J. Sierau, F. Tietz, M. Muhler, W. Schuhmann, Perovskite-based bifunctional electrocatalysts for oxygen evolution and oxygen reduction in alkaline electrolytes, *Electrochim. Acta* 208 (2016) 25–32, doi:<http://dx.doi.org/10.1016/j.electacta.2016.05.010>.
- [18] Y. Miyahara, K. Miyazaki, T. Fukutsuka, T. Abe, Catalytic Roles of Perovskite Oxides in Electrochemical Oxygen Reactions in Alkaline Media, *J. Electrochem. Soc.* 161 (2014) F694–F697, doi:<http://dx.doi.org/10.1149/2.019406jes>.
- [19] I. Abidat, N. Bouchenafa-Saib, A. Habrioux, C. Comminges, C. Canaff, J. Rousseau, T.W. Napporn, D. Dambournet, O. Borkiewicz, K.B. Kokoh, Electrochemically induced surface modifications of mesoporous spinels (Co_3O_4 – δ , MnCo_2O_4 – δ , NiCo_2O_4 – δ) as the origin of the OER activity and stability in alkaline medium, *J. Mater. Chem. A* 3 (2015) 17433–17444, doi:<http://dx.doi.org/10.1039/C5TA04437E>.
- [20] D. Pletcher, X. Li, S.W.T. Price, A.E. Russell, T. Sönmez, S.J. Thompson, Comparison of the Spinels Co_3O_4 and NiCo_2O_4 as Bifunctional Oxygen Catalysts in Alkaline Media, *Electrochim. Acta* 188 (2016) 286–293, doi:<http://dx.doi.org/10.1016/j.electacta.2015.10.020>.
- [21] Y. Li, M. Gong, Y. Liang, J. Feng, J.E. Kim, H. Wang, G. Hong, B. Zhang, H. Dai, Advanced zinc-air batteries based on high-performance hybrid electrocatalysts, *Nat Commun.* 4 (2013) 1805, doi:<http://dx.doi.org/10.1038/ncomms2812>.
- [22] M. Prabhu, K. Ketpang, S. Shanmugam, Hierarchical nanostructured NiCo_2O_4 as an efficient bifunctional non-precious metal catalyst for rechargeable zinc-air batteries, *Nanoscale* 6 (2014) 3173, doi:<http://dx.doi.org/10.1039/c3nr05835b>.
- [23] D.U. Lee, J.Y. Choi, K. Feng, H.W. Park, Z. Chen, Advanced extremely durable 3D bifunctional air electrodes for rechargeable zinc-air batteries, *Adv. Energy Mater.* 4 (2014), doi:<http://dx.doi.org/10.1002/aenm.201301389>.
- [24] X. Liu, M. Park, M.G. Kim, S. Gupta, G. Wu, J. Cho, Integrating NiCo Alloys with Their Oxides as Efficient Bifunctional Cathode Catalysts for Rechargeable Zinc-Air Batteries, *Angew. Chemie – Int. Ed.* 54 (2015) 9654–9658, doi:<http://dx.doi.org/10.1002/anie.201503612>.
- [25] P.C. Li, Y.J. Chien, C.C. Hu, Novel configuration of bifunctional air electrodes for rechargeable zinc-air batteries, *J. Power Sources* 313 (2016) 37–45, doi:<http://dx.doi.org/10.1016/j.jpowsour.2016.02.063>.
- [26] A.R. Mainar, L.C. Colmenares, O. Leonet, F. Alcaide, J.J. Iruin, S. Weinberger, V. Hacker, E. Iruin, I. Urdanpilleta, J.A. Blazquez, Manganese oxide catalysts for secondary zinc air batteries: from electrocatalytic activity to bifunctional air electrode performance, *Electrochim. Acta* 217 (2016) 80–91, doi:<http://dx.doi.org/10.1016/j.electacta.2016.09.052>.
- [27] S.W.T. Price, S.J. Thompson, X. Li, S.F. Gorman, D. Pletcher, A.E. Russell, F.C. Walsh, R.G.A. Wills, The fabrication of a bifunctional oxygen electrode without carbon components for alkaline secondary batteries, *J. Power Sources* 259 (2014) 43–49, doi:<http://dx.doi.org/10.1016/j.jpowsour.2014.02.058>.
- [28] X. Li, D. Pletcher, A.E. Russell, F.C. Walsh, R.G.A. Wills, S.F. Gorman, S.W.T. Price, S.J. Thompson, A novel bifunctional oxygen GDE for alkaline secondary batteries, *Electrochem. Commun.* 34 (2013) 228–230, doi:<http://dx.doi.org/10.1016/j.elecom.2013.06.020>.
- [29] X. Liu, W. Liu, M. Ko, M. Park, M.G. Kim, P. Oh, S. Chae, S. Park, A. Casimir, G. Wu, J. Cho, Metal (Ni, Co)-Metal Oxides/Graphene Nanocomposites as Multifunctional Electrocatalysts, *Adv. Funct. Mater.* 25 (2015) 5799–5808, doi:<http://dx.doi.org/10.1002/adfm.201502217>.
- [30] C. Zhu, D. Wen, S. Leubner, M. Oschatz, W. Liu, M. Holzschuh, F. Simon, S. Kaskel, A. Eychmüller, Nickel cobalt oxide hollow nanospheres as advanced electrocatalysts for the oxygen evolution reaction, *Chem. Commun. (Camb)* 51 (2015) 7851–7854, doi:<http://dx.doi.org/10.1039/c5cc01558h>.

- [31] S. Gupta, W. Kellogg, H. Xu, X. Liu, J. Cho, G. Wu, Bifunctional Perovskite Oxide Catalysts for Oxygen Reduction and Evolution in Alkaline Media, *Chem. – An Asian J.* 11 (2016) 10–21, doi:<http://dx.doi.org/10.1002/asia.201500640>.
- [32] I. Grimmer, P. Zorn, S. Weinberger, C. Grimmer, B. Pichler, B. Cermenek, F. Gebetsroither, A. Schenk, F.-A. Mautner, B. Bitschnau, V. Hacker, Ethanol tolerant precious metal free cathode catalyst for alkaline direct ethanol fuel cells, *Electrochim. Acta* (2017), doi:<http://dx.doi.org/10.1016/j.electacta.2017.01.087>.
- [33] Z. Ma, P. Pei, K. Wang, X. Wang, H. Xu, Y. Liu, G. Peng, Degradation characteristics of air cathode in zinc air fuel cells, *J. Power Sources* 274 (2015) 56–64, doi:<http://dx.doi.org/10.1016/j.jpowsour.2014.10.030>.

Supplementary

Bifunctional electrode performance for zinc-air flow cells with pulse charging

Birgit Pichler*₁, Stephan Weinberger₁, Lucas Reščec₁, Ilena Grimmer₁, Florian Gebetsroither₁, Brigitte Bitschnau₂, Viktor Hacker₁

₁ Graz University of Technology, Institute of Chemical Engineering and Environmental Technology, Fuel Cell Group, NAWI Graz, Inffeldgasse 25C, 8010 Graz, Austria

₂ Graz University of Technology, Institute of Physical and Theoretical Chemistry, NAWI Graz, Stremayrgasse 9/I, 8010 Graz, Austria

*Corresponding author: Birgit Pichler, birgit.pichler@tugraz.at, phone: +43 316 873 8797

Table S1: Nickel and cobalt weight percentages on carbon nanofibers (CNF) as obtained by ICP-OES measurements; by adding 12.5 wt% for oxygen in NiCo₂O₄ the total catalyst loading is 48 wt% for NiCo₂O₄/CNF.

| | Cobalt (228.616 nm) | Nickel (231.604 nm) | Oxygen (in NiCo ₂ O ₄) |
|-----------------|---------------------|---------------------|-----------------------------------------------|
| ICP OES results | 24 ± 2 wt% | 11.5 ± 0.9 wt% | |
| Calculated | | | 12.5 wt% |

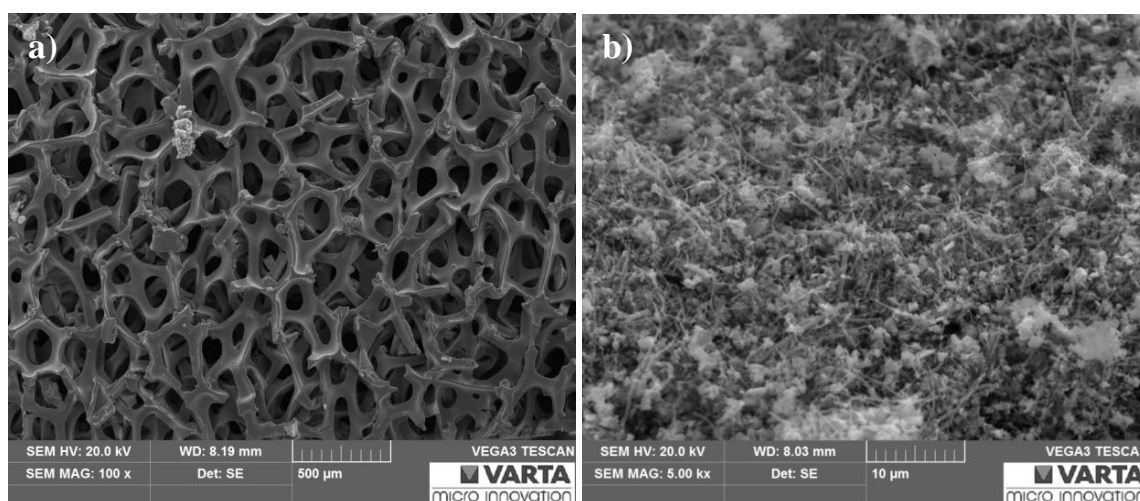


Fig. S1: **a)** SEM image of the pressed Ni foam current collector used as electrode backbone and **b)** SEM image of the La_{0.6}Sr_{0.4}Co_{0.2}Fe_{0.8}O₃ perovskite catalyst homogeneously dispersed on carbon nanofibers.

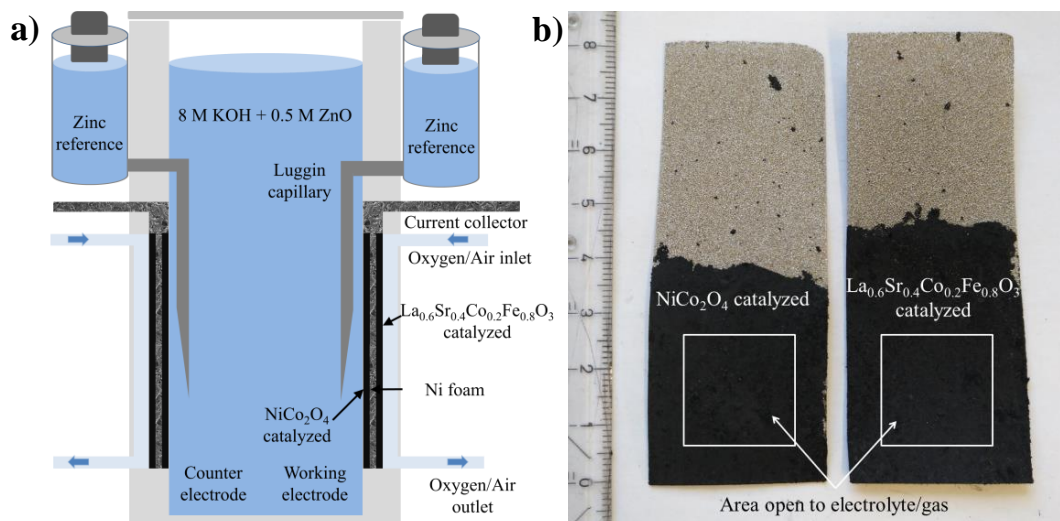


Fig. S2: **a)** Schematic of the measurement set-up with two air electrodes and **b)** image of a pressed and sintered bifunctional air electrode (back and front side shown) cut-out from a 48 cm² electrode (white rectangles indicate the area left open during the electrochemical characterization).

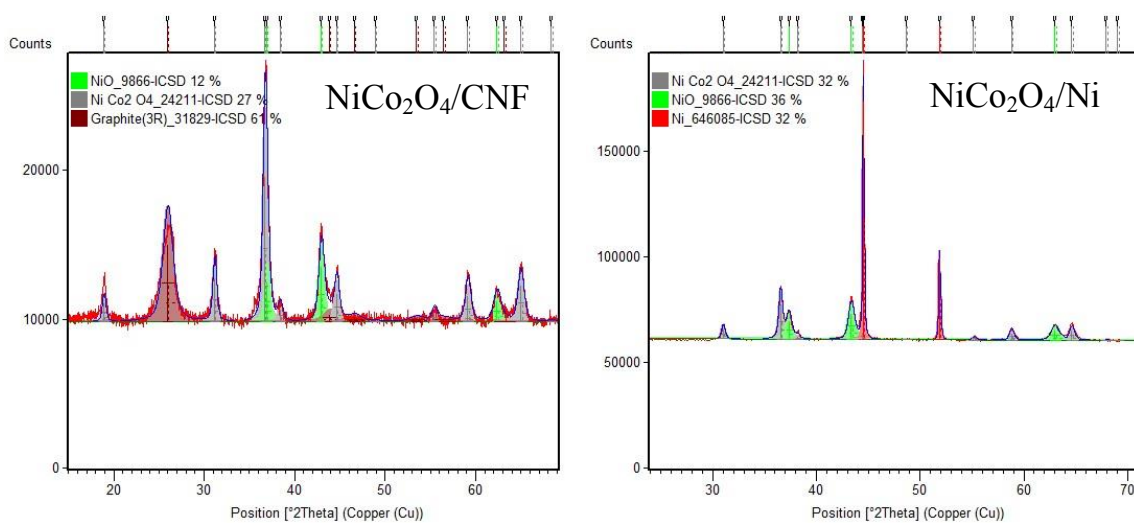


Fig. S3: Graphical representation of the Rietveld analysis of NiCo_2O_4 spinel catalyst supported on carbon nanofibers and nickel powder depicting the different volume percentages of the irradiated sample volume.

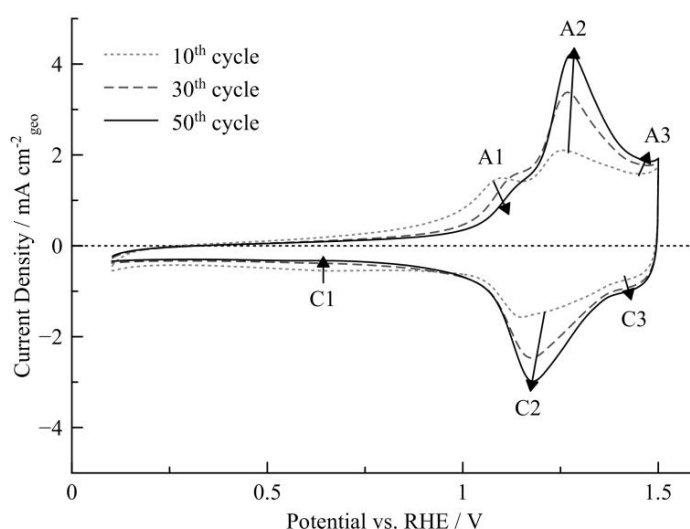


Fig. S4: Cyclic voltammogram of NiCo₂O₄/CNF catalyst (loading 73 $\mu\text{g cm}^{-2}_{\text{geo}}$) in N₂-flushed 1 M KOH (sweep rate 50 mV s⁻¹, 30°C): the redox peaks A1/C1 and A3/C3 are assigned to the oxidation/reduction of Co(II) \rightleftharpoons Co(III) \rightleftharpoons Co(IV) and A2/C2 is ascribed to Ni(II) \rightleftharpoons Ni(III) oxidation/reduction, respectively (interpreted according to Abidat et.al.¹).

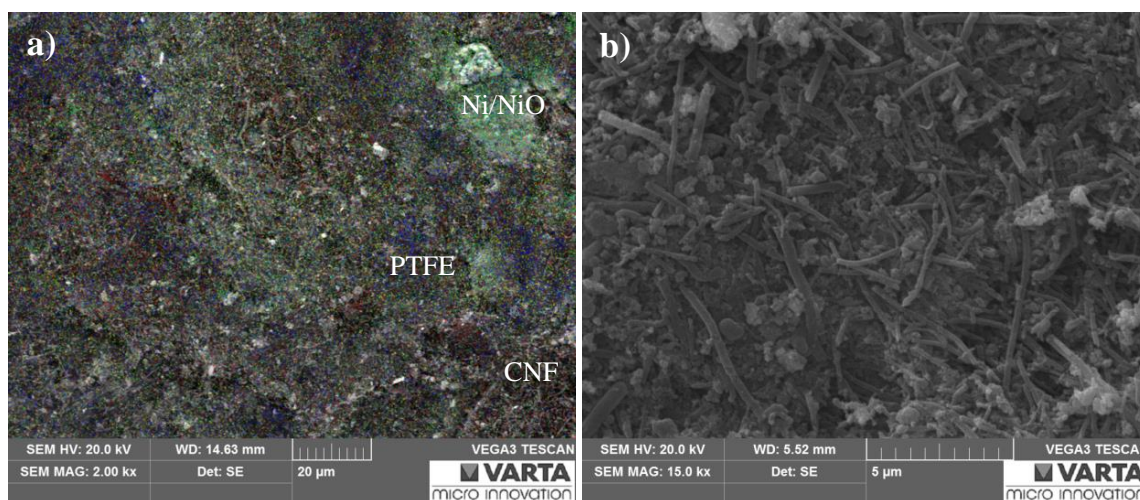


Fig. S5: NiCo₂O₄-catalyzed surface of an air electrode: **a)** EDX mapping displaying nickel (green), cobalt (yellow), oxygen (cyan) and carbon (red) and fluor (dark blue). Homogenous distribution of catalyst and support material is visible with the PTFE binder in dark blue (fluor) and an integrated Ni particle as seen in the upper right corner; **b)** SEM image showing the CNFs on the pressed electrode surface with a complex distribution of the different materials.

¹ I. Abidat, N. Bouchenafa-Saib, A. Habrioux, C. Comminges, C. Canaff, J. Rousseau, T.W. Napporn, D. Dambournet, O. Borkiewicz, K.B. Kokoh, Electrochemically induced surface modifications of mesoporous spinels (Co₃O_{4- δ} , MnCo₂O_{4- δ} , NiCo₂O_{4- δ}) as the origin of the OER activity and stability in alkaline medium, J. Mater. Chem. A. 3 (2015) 17433–17444. doi:10.1039/C5TA04437E.



The impact of operating conditions on component and electrode development for zinc-air flow batteries

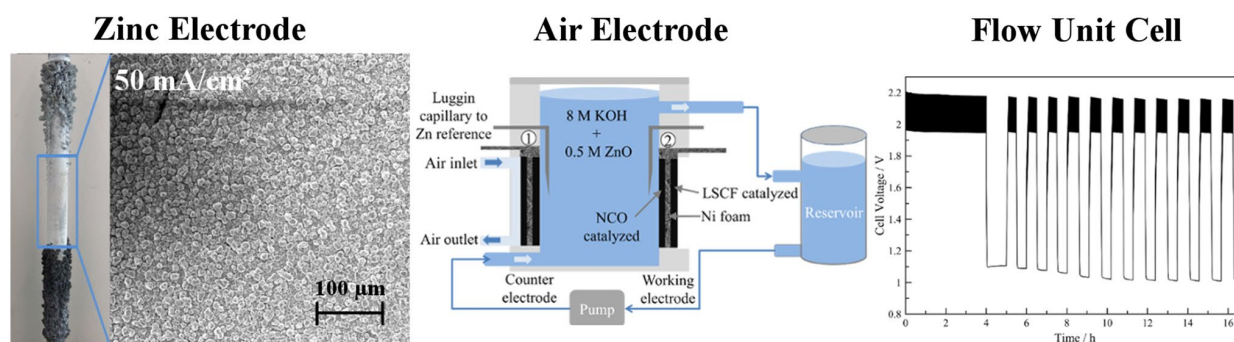
Birgit Pichler¹ · Bernhard S. Berner² · Nikolaus Rauch¹ · Christian Zelger² · Hans-Jürgen Pauling³ · Bernhard Gollas² · Viktor Hacker¹

Received: 5 April 2018 / Accepted: 1 July 2018
© The Author(s) 2018

Abstract

Rechargeable zinc-air flow batteries are investigated as possible technology for fast responding large-scale electrical energy storage due to the use of inexpensive, non-toxic and abundant materials, and compact system design. The operating ranges for several parameters such as flow rate ($2\text{--}8\text{ cm s}^{-1}$), concentration of electrolyte (6 or 8 M KOH), charge/discharge current densities (up to 100 mA cm^{-2} mean), and active or passive air supply as well as their influence on the performance and stability of the electrodes are investigated and compared. Bi-catalyzed bifunctional air electrodes are tested by means of half-cell measurements achieving minimum 200 charge/discharge cycles at 50 mA cm^{-2} with the longest operation time being 800 h. At this current density, charge/discharge efficiencies are in the range of 50% for all tested air electrodes. End-of-life characterization by means of scanning electron microscopy reveals mechanical degradation of the electrode material. On the negative zinc electrode, zinc deposition morphology on different current collector materials (nickel, brass, and steel) is investigated using Rota-Hull cylinders showing nickel to be the most suitable material. The pulse interrupt current method is thereby successfully applied for compact zinc deposition in a broad current density range without any electrolyte additive. Subsequent scale-up of the rechargeable zinc-air flow battery and unit cell operation is finally performed for proof-of-concept.

Graphical Abstract



Keywords Zinc-air flow battery · Bifunctional air electrode · Pulse interrupt currents · Compact zinc morphology · Flow operation

Electronic supplementary material The online version of this article (<https://doi.org/10.1007/s10800-018-1233-z>) contains supplementary material, which is available to authorized users.

✉ Birgit Pichler
birgit.pichler@tugraz.at

Extended author information available on the last page of the article

1 Introduction

Electrical energy storage (EES) with fast response times of below 1 s is crucial for balancing energy supply and demand from intermittent electricity generators such as wind and solar power systems. Secondary batteries are suited for

this bridging power application with power ranging from 100 kW to 10 MW [1–5] due to their ability to rapidly respond to load changes. In addition, because of low self-discharge rates, the standby losses are small. However, in stationary units, high costs in comparison to the capacity, low energy density, and the negative ecological impact due to the use of scarce (Li-ion batteries) or toxic materials (i.e., lead-acid batteries, NiCd batteries) still prevent wide-spread installation of large-scale battery storage modules [1]. Also, for a competitive large-scale EES system, life-times of at least 10 years with about each 5 h charge and discharge per day are required [6].

Flow batteries allow deep discharge [4] and a higher flexibility concerning capacity and power using external tanks for storing the dissolved electroactive species [3, 7]. Therefore, the scale-up of a flow battery as stationary electrical energy storage system can be achieved in a cost-effective way [6]. Different zinc-based hybrid flow batteries have been developed during the last decades [3, 7–9]. Among them is the most developed zinc-bromine flow battery, which was mainly researched during the 1980s with module storage capacities of up to 500 kWh [3]. It is characterized by inexpensive materials and cycling efficiencies of about 75% [3, 10]. Another type is the zinc-air flow battery [9, 11, 12], which is investigated in this work and has already been demonstrated in varying forms in a few commercial and pilot systems (for example, US companies *Fluidic Energy* and *EOS Energy Storage* [13, 14], EU projects ZAESS and POWAIR [15–18]). Although the zinc-air flow battery is still far behind the development of the zinc-bromine system, it has the advantage to be free of potentially hazardous bromine species by substituting the positive electrode with a reversible air electrode. On this air electrode, oxygen from the surrounding air is reduced to hydroxide ions into the highly alkaline electrolyte during discharging and, reversely, oxygen is generated during charging (Table 1) [14, 15].

Although the high energy density of zinc-air batteries [19, 20] is less relevant in stationary flow systems, using a metal-air configuration can still significantly reduce the capital costs per kWh as only one active material has to be stored. Zinc is compared to lithium less hazardous and much more abundant, easily recyclable and thus less costly with only US \$2 per kg [14, 19]. Furthermore, no ion-exchange membrane is necessary to separate anolyte and catholyte [11]. The cost of a commercialized system is projected to

be about US \$160 per kWh depending on the utilized air electrode catalysts [14]. Nevertheless, the zinc-air system suffers, as most metal-air batteries, from low roundtrip efficiencies of below 50% due to the sluggish oxygen reaction kinetics and short cycle life mainly caused by material degradation [13, 14, 20]. Not only material and catalyst selection for an optimal air electrode design plays a crucial role to overcome these issues but also the operating conditions have a significant impact on the longevity of the electrodes. This is also true for the zinc electrode, where mechanically unstable growth morphologies of zinc are commonly observed in current density ranges close to and far below the limiting current density [21]. The detachment of zinc particles from the electrode results in capacity losses, while the growth of zinc dendrites can lead to short circuits and damaging of the air electrode. It is thus essential to optimize and control the operating conditions of the zinc-air flow battery for the processes at both electrodes.

In this work, we show the influence of different operating conditions both on the long-term performance of bifunctional air electrodes as well as on the growth morphology of zinc on several current collector materials. The recharge capability of the zinc electrode is studied with pulse interrupt currents (PIC) on rotating electrodes in order to achieve dendrite-free zinc deposits [21, 22]. Concerning the positive electrode, of the many catalysts reported for zinc-air batteries [14, 23–26], well-known oxide catalysts—the NiCo_2O_4 spinel and the $\text{La}_{0.6}\text{Sr}_{0.4}\text{Co}_{0.2}\text{Fe}_{0.8}\text{O}_3$ perovskite [27–30]—were chosen and both employed in the investigated air electrodes. They bi-functionally catalyze the discharging reaction, i.e., oxygen reduction reaction—ORR, and the charging reaction, i.e., oxygen evolution reaction—OER. With such an air electrode, the system can be operated in a structurally more compact two-electrode arrangement with one zinc and only one air electrode, which reduces the complexity of the system compared to a three-electrode set-up [12, 16, 23]. Long-term operation of the air electrodes in half-cell set-up with minimum 200 charge/discharge cycles was performed at comparably high current densities of 50 mA cm^{-2} [3, 14, 31]. The investigated effects presented in this work concerning the air electrode are (i) the influence of charging with pulse interrupt currents (PIC), (ii) a comparison of open set-up to active gas supply, (iii) a test using an up-scaled electrode with 16 cm^2 electrode size, (iv) a comparison of 6 M KOH electrolyte to 8 M KOH, and (v) the influence of

Table 1 Electrochemical reactions in a zinc-air battery-charging reaction from left to right [14, 15]

| | Reaction | Potential vs SHE ^a (V) |
|------------------|----------------------------------------------------------------------------------------------------------------|-----------------------------------|
| Zn electrode | $\text{Zn}(\text{OH})_4^{2-} + 2\text{e}^- \rightleftharpoons \text{Zn} + 4\text{OH}^-$ | $E_{00} = -1.26$ |
| Air electrode | $4\text{OH}^- \rightleftharpoons \text{O}_2 + 2\text{H}_2\text{O} + 4\text{e}^-$ | $E_{00} = 0.4$ |
| Overall reaction | $2\text{Zn}(\text{OH})_4^{2-} \rightleftharpoons 2\text{Zn} + 4\text{OH}^- + \text{O}_2 + 2\text{H}_2\text{O}$ | $E_{\text{cell,eq}} = 1.66$ |

^aStandard hydrogen electrode

flowing electrolyte at different flow rates. The course of the potentials during discharging and charging as well as energy efficiency are used to characterize the stability of the electrodes. Finally, the gained knowledge on operation of both electrodes is applied in a full cell set-up with flowing electrolyte for demonstration. With these experiments, we hope to facilitate the assessment of optimal operating conditions and to take the zinc-air flow battery one step further from component development to full cell operation.

2 Experimental

2.1 Rota-Hull and rotating cylinder experiments of the zinc anode

Electrolytes were prepared with potassium hydroxide from Carl Roth GmbH ($\geq 85\%$, p. a.) and zinc oxide from Sigma-Aldrich ($> 99\%$, puriss.). First, a solution with deionized water and 8 M potassium hydroxide was prepared, and then different amounts of zinc oxide were dissolved to obtain zincate concentrations c of 0.2 and 0.5 M.

The Rota-Hull cell (Eco Chemie B. V., Netherlands) has been described previously [21, 32] and consisted of a cylinder cathode and of a cylindrical platinized titanium mesh anode, placed concentrically around the cathode. Rota-Hull cell experiments were performed at 23 and 60 °C with a zincate concentration of 0.5 M. The rotational rates of the RCH cathodes are specified as linear velocities of the rotating cylinder surface w [cm s^{-1}]. Constant direct current was generated by the power and control unit of the Rota-Hull cell, while pulse current was fed into the Rota-Hull control unit from a PGSTAT128N (Metrohm Autolab B. V., Netherlands). Rotating cylinder experiments were carried out with a Pine Research Instruments Model AFMSRCE (USA) connected to the PGSTAT128N.

All cylinder electrodes in Rota-Hull experiments were 12 cm long with 6 mm diameter l (exposed electrode area $A = 15 \text{ cm}^2$) from brass (CuZn39Pb3, Metrohm INULA GmbH, Austria) or steel (C45 grade, material number 1.0503, Franz Grossschädel Stahlgroßhandel GmbH, Austria). The nickel electrodes in rotating cylinder experiments were 1.00 cm long and had a diameter of $l = 15 \text{ mm}$ with an exposed electrode area $A = 4.71 \text{ cm}^2$. Nickel cylinders for Rota-Hull and rotating cylinder experiments were prepared by electrodepositing 10 μm of Ni onto brass, copper, or steel cylinders from a sulfamate bath (Atotech, Germany) at a current density of 2.5 A dm^{-2} and 50 °C under stirring. All brass and steel cylinders were pre-treated before zinc deposition. Brass was abraded with SiC grinding paper (800 mesh). Steel was treated first in aqueous 50 g L^{-1} UniClean 154 (Atotech, Germany) for 10 min at 65 °C and then for 3 min in aqueous 120 g L^{-1} UniClean 675 (Atotech, Germany) at 70 °C under stirring.

Current efficiencies in the Rota-Hull experiments were calculated from the gravimetrically determined mass of zinc or in the case of the rotating cylinder experiments by coulometry of the potentiostatic zinc dissolution.

2.2 Catalyst and air electrode preparation

All chemicals were used as purchased without further purification. The synthesis procedure of NiCo_2O_4 spinel (NCO) supported on either untreated carbon nanofibers (CNF) or nickel powder and the electrode manufacturing process using two different oxide catalysts has already been described in detail in a previous publication [27]. The procedure is shortly described in the following for electrode sizes up to 100 cm^2 .

NiCo_2O_4 spinel (NCO) was synthesized by an impregnation-calcination route by dissolving $\text{Ni}(\text{NO}_3)_2 \cdot 6\text{H}_2\text{O}$ (Sigma-Aldrich) and $\text{Co}(\text{NO}_3)_2 \cdot 6\text{H}_2\text{O}$ (Sigma-Aldrich) in the Ni:Co molar ratio of 1:2 in ultrapure water/2-propanol 1:1 (v:v). After addition of support material—either CNF (HTF150FF-LHT, 150 nm, lowheat; Electrovac AG, Austria) or nickel powder ($< 50 \mu\text{m}$, Sigma-Aldrich)—the dispersion was treated with ultrasounds for 1 h. The solvent was evaporated under vigorous stirring at 80 °C. The dry powder was ground in a mortar and calcined at 375 °C for 2 h (air, heating rate 5 °C min^{-1}). The final product was NCO/CNF ($\sim 45 \text{ wt}\%$ on CNF) and 30 wt% NCO/Ni powder. The second catalyst was a commercially acquired $\text{La}_{0.6}\text{Sr}_{0.4}\text{Co}_{0.2}\text{Fe}_{0.8}\text{O}_3$ perovskite (LSCF, d_{50} 0.4–0.8 μm , 10–14 $\text{m}^2 \text{g}^{-1}$; Sigma-Aldrich). To achieve a better distribution of the powder on CNF support, the perovskite was homogeneously dispersed with CNF in a weight ratio of 3:1 in ultrapure water/2-propanol 1:1 (v:v) using an ultrasonic probe (LSCF/CNF).

For electrode manufacturing, two different electrode pastes were prepared by mixing the catalyst/support powders with PTFE (TF5032, suspension; Dyneon GmbH) in ultrapure water/2-propanol 1:1 (v:v). Paste one consisted of 50% NCO/CNF, 20% NCO/Ni powder, and 20% PTFE (wt%). The second paste comprised 80% LSCF/CNF and 20% PTFE (wt%). The pastes were separately spread on opposite sides of nickel foam (pore size 450 μm , area density 420 g m^{-3} , thickness 1.6 mm; Alantum Corporation, Germany) using about 30–40 mg of the dry catalyst/support/PTFE mixture per cm^2 of nickel foam. Nickel foam was chosen as current collector as it provides good electrical conductivity within the electrode and gives mechanical strength to the build. The catalyst loadings were 10 mg cm^{-2} NiCo_2O_4 and 25 mg cm^{-2} $\text{La}_{0.6}\text{Sr}_{0.4}\text{Co}_{0.2}\text{Fe}_{0.8}\text{O}_3$.

2.3 Electrochemical measurements of air electrodes and full cell

Electrochemical characterization of the air electrodes in half-cell set-up was performed with a BaSyTec Cell Test

System (Germany) in custom-made PMMA test cells with EPDM gaskets. Always two air electrodes were measured at the same time, one operated as working electrode and the second as counter electrode as depicted in Fig. 1. Both electrodes were separately referenced against a piece of zinc foil (1.6 mm, $\sim 8 \text{ cm}^2$ surface area; Alfa Aesar) via a Luggin capillary. The standard measurement was performed with 4 cm^2 sized electrodes at room temperature ($24 \text{ }^\circ\text{C}$) in 8 M KOH with 0.5 M ZnO electrolyte and actively supplied with 25 mL min^{-1} synthetic air (80% N_2 /20% O_2) via the closed gas compartment. The gas exhaust was immersed in 5 cm of water to counter the hydrostatic pressure of the liquid electrolyte. The utilized electrode mounts were adapted to the different tests by increasing the electrode size from standard 4 cm^2 to 16 cm^2 or by removing the closed gas compartment for measuring with passive air supply. Furthermore, a DC centrifugal pump (WPDC-02.5L-1.00M-12-VP; Rotek, Austria) was added to the set-up for operation with flowing electrolyte. The surface flow velocities w were 5, 6, and 8 cm s^{-1} , which correspond in this set-up to 1.5, 1.8, and 2.1 L min^{-1} . Long-term operation was performed with 2 h cycles consisting of 1 h discharge (ORR) and 1 h charging (OER). 1 h pulse charging with the PIC method was performed with 150 mA cm^{-2} pulse for $t_{\text{on}} = 50 \text{ ms}$ and no current for 150 ms (duty cycle $\gamma = 0.33$), resulting in a mean current density (j_m) of 50 mA cm^{-2} . Every hundred cycles ORR/OER polarization curves were recorded for additional information on the performance at lower current densities.

Full cell operation was demonstrated in a scaled-up set-up with two 100 cm^2 bifunctional air electrodes (overall 200 cm^2) and with 100 cm^2 of nickel foam (thickness 1 mm) electrodeposited with zinc as negative electrode, which was mounted between the two air electrodes with 1 cm distance to each. The air electrodes were open to the ambient air with no active gas supply. The tank size was increased to 5 L. A volume of 4.5 L of 6 M KOH electrolyte with 0.325 M ZnO

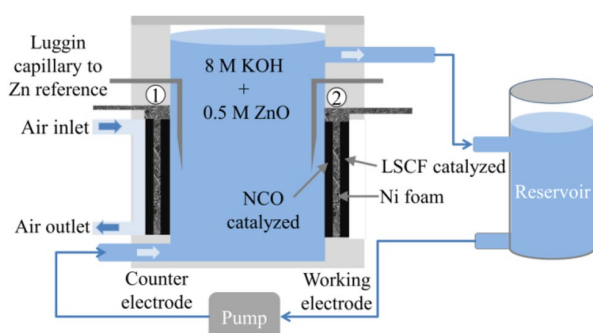


Fig. 1 Schematic drawing of the electrochemical measurement set-up for air electrode half-cell measurements depicting the closed set-up with active synthetic air supply (1) and the open set-up (2); images of the half-cell and full cell set-ups are shown in Supplementary Fig. S1

was pumped through the vertical cell with a surface flow velocity of 2 cm s^{-1} , which corresponds to 1.9 L min^{-1} . If 0.2 M zinc is set as the minimum concentration, this cell configuration has a theoretical capacity of 30 Ah [7]. The zinc electrodeposition was done by the PIC method for 4 h using $t_{\text{on}} = 50 \text{ ms}$ with 50 mA cm^{-2} and 50 ms pause (duty cycle $\gamma = 0.5$). This corresponds to a j_m of 25 mA cm^{-2} on the zinc electrode and 12.5 mA cm^{-2} at the air electrode. Approximately 12.2 g (0.19 mol) of zinc was deposited during this time. The zinc-air cell was cycled with 35 min pulse charging with the same conditions as during the coating, followed by 30 min discharge at 25 mA cm^{-2} $_{\text{Zn electrode}}$.

2.4 Materials characterization

A system VEGA3 ESEM Tescan 500 PA (Czech Republic) equipped with an energy dispersive X-ray detector from Oxford Instruments (UK) was used for scanning electron microscopy and EDX. Prior to characterization by SEM, the air electrodes were thoroughly soaked with ultrapure water before drying preventing morphology changes by crystallizing KOH.

3 Results and discussion

3.1 Zinc electrode

3.1.1 Zinc morphology on different current collector materials with pulse interrupt current (PIC) plating

A number of different growth morphologies have been reported for zinc electrodeposition from alkaline aqueous electrolytes [33]. They have been attributed to different current density regimes and range from filamentous mossy (nucleation and activation control) over compact morphologies such as layer-like (activation control) and boulder (mixed activation and diffusion control) to dendritic (diffusion control) and heavy spongy under mass-transport control (diffusion and convection resulting from hydrogen bubble stirring). In addition to the factors that govern the limiting current density during deposition (zincate concentration, convection, temperature), also the topography of the substrate surface and the crystallographic misfit of the substrate material to that of zinc have been reported to play a crucial role for the type of growth morphology. Three different zinc morphologies can be clearly distinguished on the Rota-Hull cylinder cathode in Fig. 2. Here, the zinc has been deposited by pulse interrupt current (PIC) for 100 min on nickel with an average current density j_m of 50 mA cm^{-2} . At low current densities, the filamentous mossy morphology is observed, at medium current densities the compact boulder type, and at high current densities dendritic zinc.

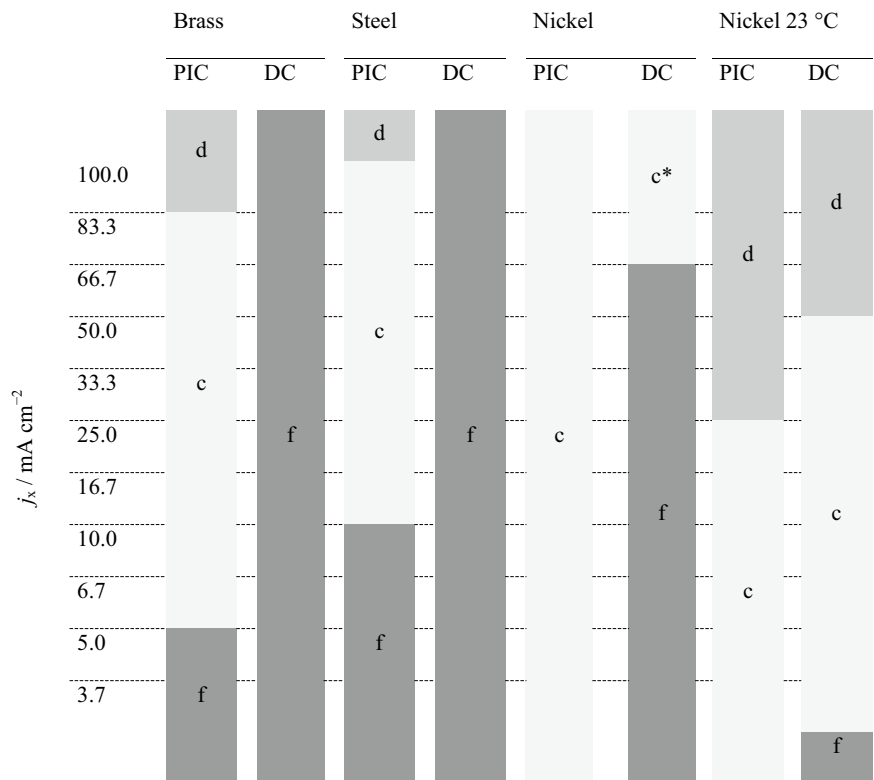
Fig. 2 Zinc deposited on a Rota-Hull cathode cylinder (Ni-coated brass) from 8 M KOH/0.5 M ZnO showing three distinct morphologies (bottom to top, low to high local current density): filamentous, compact, and dendritic. Deposition conditions were $T=60\text{ }^\circ\text{C}$, $w=3\text{ cm s}^{-1}$, $Q=300\text{ C cm}^{-2}$, $\gamma=0.33$, $t_{\text{on}}=50\text{ ms}$, $j_m=50\text{ mA cm}^{-2}$



In order to test the impact of the substrate material and type of current, zinc was deposited for 15 min by PIC and by constant DC on brass, steel, and nickel with an average current density j_m of 33.33 mA cm^{-2} . All current efficiencies

were in the range of 95–100%. The resulting zinc morphologies are depicted schematically in Fig. 3. Most important, constant DC at $60\text{ }^\circ\text{C}$ produces the filamentous mossy morphology (denoted as *f* in Fig. 3) almost irrelevant of the substrate material, while PIC leads to wide current density ranges with compact morphology (denoted as *c*). This is clear evidence for the beneficial effect of high pulse current densities on nucleation, meaning also high overpotentials. Slow and selective nucleation has been reported to result in mossy initiation [33]. At a temperature of $23\text{ }^\circ\text{C}$, the results on nickel are slightly different. Clearly, the dendritic morphology is produced by PIC and constant DC already at considerably lower current densities compared to $60\text{ }^\circ\text{C}$. This can be explained by the limiting current density, which decreases with temperature due to the increasing electrolyte viscosity and consequently a smaller zincate diffusion coefficient. Also the type of substrate material influences the current density boundaries between the different growth morphologies. At low current density, zinc deposits tend to grow at $\langle 0001 \rangle$ (filamentous mossy). For steel, iron (110) is the bcc close-packed plane with an interatomic distance of 0.2482 nm , which is smaller than the 0.2665-nm distance of the zinc (0001) basal plane. This represents a larger negative misfit than those between zinc and fcc copper (111) with 0.2556 nm . The negative misfit between zinc and nickel (111) with 0.2492 nm is similar to that between zinc and

Fig. 3 Morphologies of Zn (*f* filamentous mossy, *c* compact, *c** compact with few dendrites, *d* dendritic) deposited with pulse interrupt current and conventional DC from 8 M KOH/0.5 M ZnO on brass, steel, and nickel Rota-Hull cylinders. Deposition conditions were $T=60\text{ }^\circ\text{C}$ and $23\text{ }^\circ\text{C}$, $t=15\text{ min}$, $\gamma=0.5$, $t_{\text{on}}=50\text{ ms}$, $j_m=33.33\text{ mA cm}^{-2}$, and $w=6\text{ cm s}^{-1}$



iron. In all cases, the negative misfits have been reported to result in the Volmer–Weber-type growth of 3D islands producing boulder, dendritic, or heavy spongy morphology [33]. The different growth behavior of Zn on brass, steel, and nickel must therefore be caused by something else. The local partial current density distribution of the hydrogen evolution side reaction depends on the respective overpotentials of the materials for this reaction. Presumably, the latter is lower for nickel. Consequently, a larger area towards the high local current density end of the nickel electrode is blocked for zinc deposition by hydrogen bubbles. This results in a shift of partial current density for zinc deposition towards the lower current density end of the electrode preventing the formation of the mossy morphology. It cannot be ruled out that slight differences in the surface roughness of the three substrates might affect the growth morphology as well. Based on the results obtained here, nickel seems to be the most suitable current collector material.

The local current densities shown along the length of the Rota-Hull cylinders are based on the primary current density distribution calculated from the geometry of the cell [34, 35]. The practical current density distribution, which is affected also by the charge transfer kinetics and mass-transport limitations together with the resulting side reactions, might deviate significantly from the primary one. In order to verify that the morphology ranges observed along the Rota-Hull cylinder can be attributed to certain current density ranges, rotating cylinder experiments with defined current densities were carried out. The results are shown in Fig. 4. On the left-hand side is a picture of the Rota-Hull cylinder schematically shown in Fig. 3 (PIC zinc deposition on nickel at 60 °C), where the compact boulder zinc morphology had been observed over the whole current density range. On the right-hand side, SEM images of zinc deposited on rotating cylinders at the indicated current densities under otherwise identical conditions are shown. The compact boulder-type zinc morphology could be reproduced at current densities of 50 and 60 mA cm⁻². At 100 mA cm⁻², the morphology still is boulder type, but the very coarse-grained pyramidal boulders are regarded as dendrite precursors. In all cases, the current efficiencies were in the range of 96–97%.

Compact zinc has been described as a transient morphology in electrodeposition from alkaline electrolytes [36, 37]. After a certain deposition time with compact morphology, either mossy or dendritic growth is initiated. The consequence of this initiation time is also apparent from the results shown in Fig. 5. Zinc was electrodeposited by PIC in Rota-Hull cell experiments on brass and on nickel cylinders for periods of 15 and 150 min or 30 and 300 C cm⁻², respectively. On both substrates, the range of local current densities with compact zinc based on the primary current density distribution is significantly narrower at longer deposition times and 60 °C. The same effect is observed on nickel also

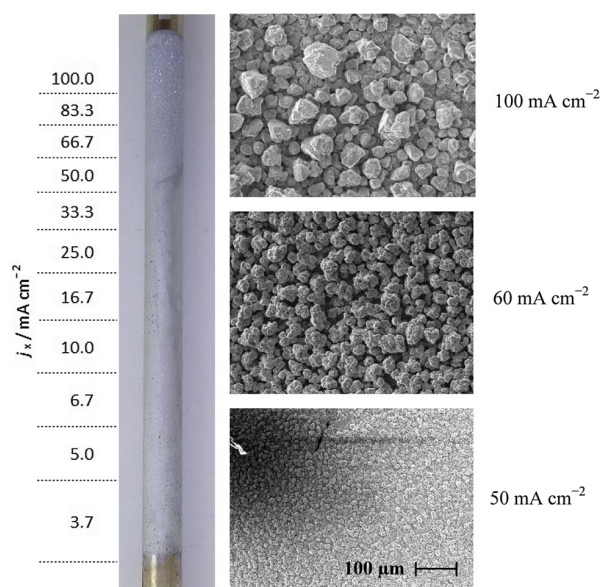


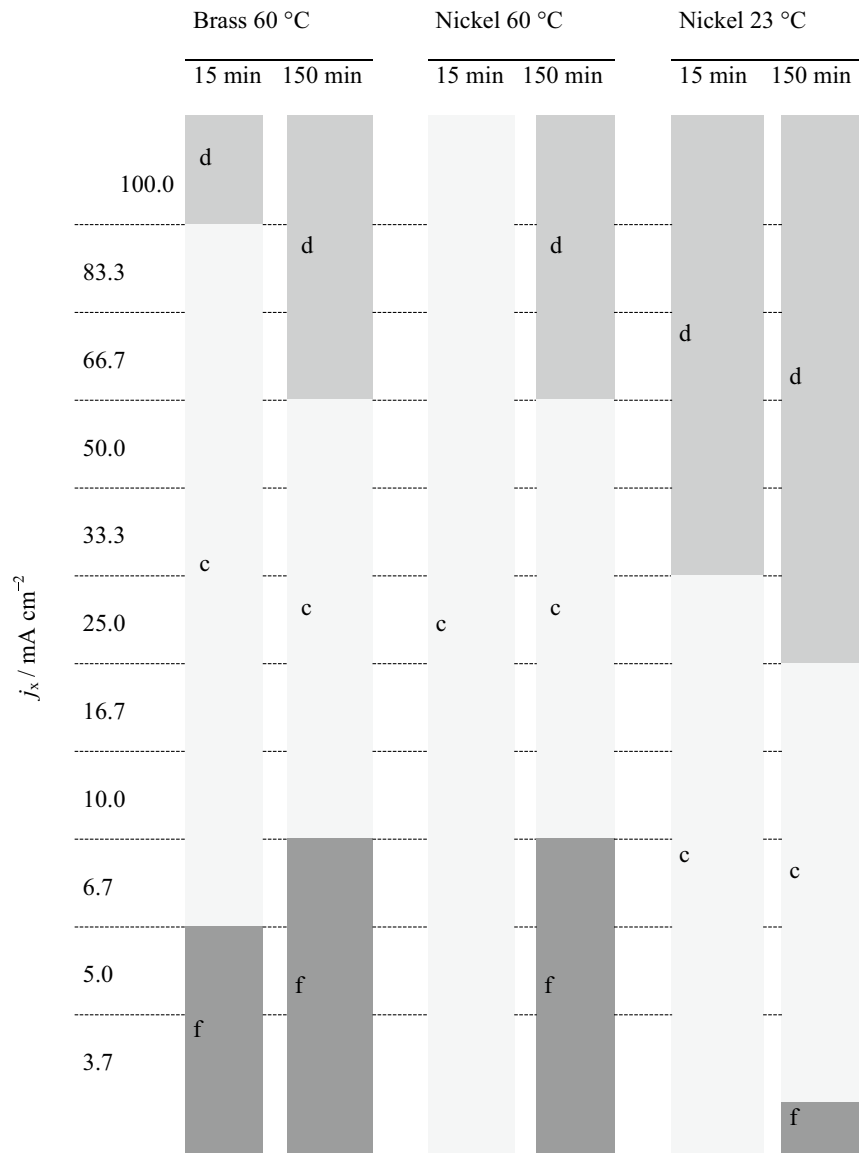
Fig. 4 Morphologies of Zn deposited on a Ni-coated Rota-Hull cathode cylinder from 8 M KOH/0.5 M ZnO indicating the local current densities based on a primary current density distribution (left), and SEM images (500×) of Zn morphologies (right) deposited at defined current densities on Ni-coated cylinder electrodes under the same conditions ($T=60$ °C, $t=15$ min, $\gamma=0.5$, $t_{\text{on}}=50$ ms, $j_m=33.33$ mA cm⁻², and $w=6$ cm s⁻¹)

for an electrolyte temperature of 23 °C. Again, the dendritic morphology is produced already at significantly lower local current densities for short and long deposition times, due to the lower limiting current. The current efficiencies are lower for brass increasing with deposition time from 95 to 98% and higher for nickel, again increasing with deposition time from 97 to 99%. This probably reflects the extent of hydrogen evolution decreasing in the order brass > nickel > zinc.

3.1.2 Dissolution/deposition cycling experiments with PIC plating

The growth behavior of zinc during deposition/dissolution cycling is critical for the operation of the zinc-air flow battery. This behavior was tested with PIC deposition (charging) at 50, 60, and 70 mA cm⁻² average current densities and constant DC dissolution (discharging) at 100, 120, and 140 mA cm⁻² under turbulent flow conditions on nickel rotating cylinder electrodes as shown in Fig. 6. After 1000 s of PIC zinc deposition followed by 4 cycles of 100 s constant DC dissolution/200 s PIC deposition, compact zinc was still observed for 50 and 60 mA cm⁻² average current densities, while dendritic zinc had grown at 70 mA cm⁻² average current density. The diffusion limiting current j_{lim} for the rotating cylinder electrodes under these conditions is

Fig. 5 Morphologies of Zn long- (150 min) and short-term (15 min) deposited on brass and Ni-coated brass Rota-Hull cylinders from 8 M KOH/0.5 M ZnO with $T=60\text{ }^{\circ}\text{C}$ and $23\text{ }^{\circ}\text{C}$, $w=6\text{ cm s}^{-1}$, $t_{\text{on}}=50\text{ ms}$, $\gamma=0.5$, $j_{\text{m}}=33.33\text{ mA cm}^{-2}$



52.7 mA cm^{-2} and can be calculated from Eq. 1 [32]. Here n is the number of transferred electrons per zincate ion (2), F is the Faraday constant ($96,485\text{ C mol}^{-1}$), c is the zincate concentration (0.5 M), l is the cylinder diameter (11.3 mm), ν is the kinematic viscosity ($9.625 \times 10^{-3}\text{ cm}^2\text{ s}^{-1}$), and D the diffusion coefficient of the zincate ion ($6.38 \times 10^{-6}\text{ cm}^2\text{ s}^{-1}$).

$$j_{\text{lim}} = 0.079 \times n \times F \times c \times l^{-0.3} \times \nu^{0.70} \times v_{\text{kin}}^{-0.344} \times D^{0.644}. \quad (1)$$

It is noteworthy that even for an average current density of 60 mA cm^{-2} , which is above the limiting current density, the compact zinc morphology has been obtained. The “cumulated” current efficiencies determined from amperometric dissolution of the final zinc deposit were 96% for

50 mA cm^{-2} , 95% for 60 mA cm^{-2} , and 94% for 70 mA cm^{-2} average deposition current density.

3.2 Air electrode

3.2.1 PIC charging with active or passive air supply

Charging with pulse interrupt currents (PIC) is a beneficial method for obtaining compact zinc morphologies during charging as described in Sect. 3.1. Thereby unfavorable morphologies such as dendritic or mossy leading to shorts and loss of active material are avoided [21]. However, the high pulse currents could lead to accelerated degradation at the air electrode due to a much more vigorous oxygen bubble formation during OER and higher oxidative potentials.

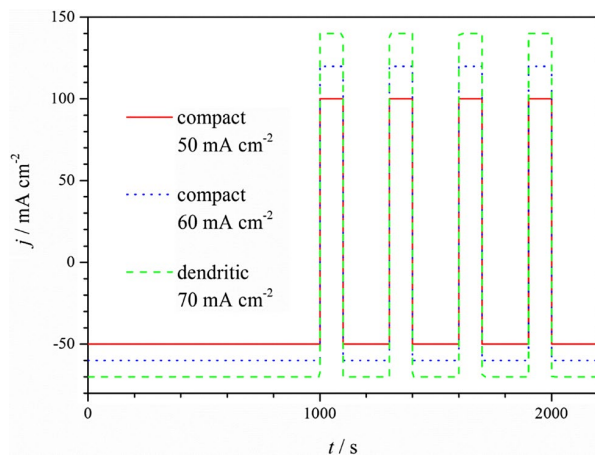


Fig. 6 Cycling scheme and resulting Zn morphologies on nickel rotating cylinders for $j_m = 50, 60,$ and 70 mA cm^{-2} pulse interrupt current charging and constant DC discharge currents in 8 M KOH/0.5 M ZnO with $T=60 \text{ }^\circ\text{C}$, $w=6 \text{ cm s}^{-1}$, $t_{\text{on}} = 50 \text{ ms}$, $\gamma=0.5$

In the following, air electrodes charged with the PIC method (E_{PIC} and $E_{\text{PIC_open}}$) are compared to the long-term behavior of an electrode charged with constant current (E_{const}) at 50 mA cm^{-2} . The results of these half-cell measurements are depicted in Fig. 7.

E_{const} achieved 600 h (300 cycles) until the lower cut-off potential of 0.8 V vs Zn/Zn²⁺ was reached. For 200 cycles, the potential difference between charge and discharge was below 1.0 V. When charging with PIC, the

electrode E_{PIC} could be operated for more than 800 h (380 cycles) and in the open set-up $E_{\text{PIC_open}}$ 500 h (220 cycles) were achieved. Although the overall operation time varied significantly, all three electrodes showed nearly the same performance from 100 to 400 h indicating stable three-phase zones within the electrodes for ORR. The PIC method resulted in only slightly higher charging potentials of about 2.05 V. The potential difference between pulse and pause increased from 101 to 176 mV for E_{PIC} and for $E_{\text{PIC_open}}$ from 115 to 159 mV over the course of the measurement. Overall, the maximum charging potentials were very stable for all three electrodes with the E_{const} exhibiting low OER potentials of about 1.94 V.

The energy efficiency [2, 38, 39] or roundtrip efficiency [24] for the air electrodes was calculated according to Eq. 2 with the applied current density j , the time t , and the measured potential V at charge c and discharge d , respectively.

$$\text{Energy efficiency [\%]} = \frac{j_d \times t_d \times V_d}{j_c \times t_c \times V_c} \times 100 \quad (2)$$

Depending on the applied current densities, the roundtrip efficiencies of all three air electrodes are higher than 65% at 5 mA cm^{-2} , about 60% at 20 mA cm^{-2} and in the range of 50% at 50 mA cm^{-2} even after 200 cycles as summarized in Table 2. This is in agreement to reported values of other zinc-air battery systems [14, 28, 40–43]. The charge/discharge potentials are nearly the same for all

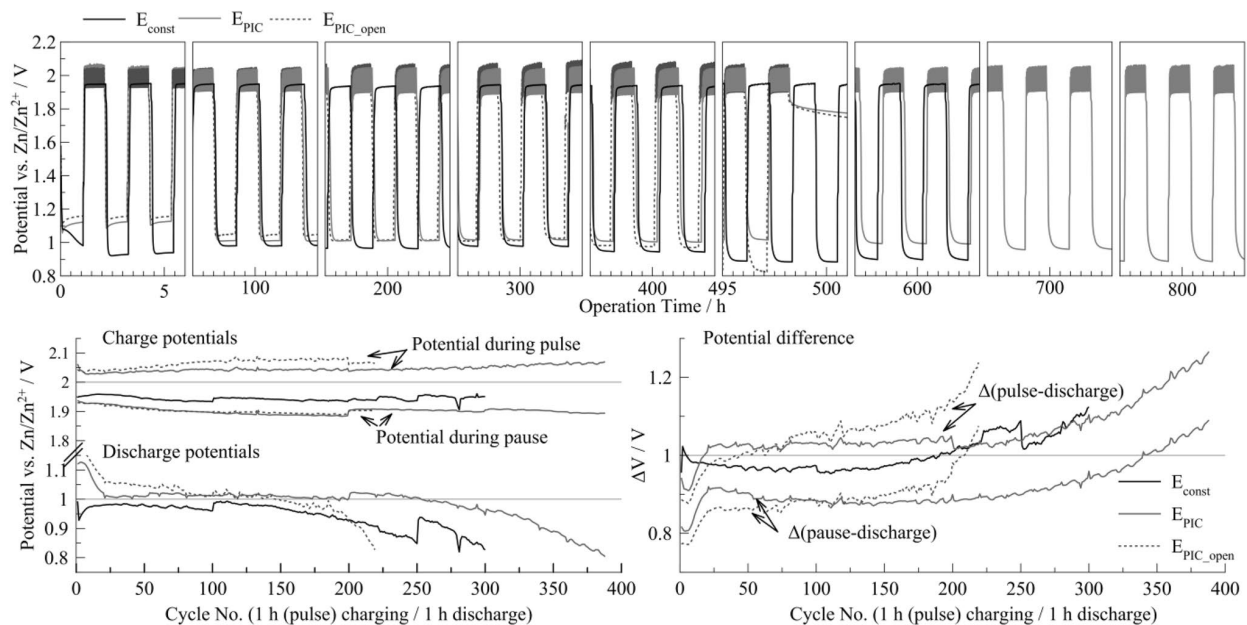


Fig. 7 Performance of three bifunctional air electrodes during long-term cycling operated at constant current density of 50 mA cm^{-2} (E_{const}) or charged with PIC method (pulsed charging at 50 mA cm^{-2} mean) with active synthetic air supply (E_{PIC}) or open to ambient air ($E_{\text{PIC_open}}$)

three electrodes indicating that the PIC method is applicable in full cell operation without any harming effect on the air electrode. In fact, the E_{PIC} with active gas supply exhibited the highest performance after 200 cycles and the longest overall operation time.

Keeping stable three-phase boundaries for ORR within the electrode during repeated charging and discharging is one of the most challenging issues in a rechargeable zinc-air battery, especially in connection with slow PTFE degradation and reduced hydrophobicity [14] (see Supplementary Fig. S3). As summarized by Pei et al. [16], several failure mechanisms are plausible. One is the slow flooding of the electrode caused by increasing penetration of electrolyte into the electrode's pore structure. In consequence, oxygen diffusion is hindered during ORR. This degradation mechanism is further enhanced through the charging reaction as the oxygen bubbles generated within the electrode during OER mechanically destroy the fine porous structure. The effect was observed with scanning electron microscopy (SEM) when comparing a fresh electrode to E_{const} and $E_{\text{PIC_open}}$ after operation as depicted in Fig. 8. The surface of the electrodes is much rougher after the testing and the carbon fiber network appears washed out. The oxidative potentials during OER and the highly alkaline environment can lead to carbon corrosion [14] of the crude CNF indicated by a slightly orange-colored electrolyte observed after 100 h of testing. In general, the right selection of carbon support has a severe impact on the durability of bifunctional air electrodes [44, 45]. Furthermore, because of the constant synthetic air gas flow on the electrode's backside of E_{const} and E_{PIC} , a drying-out effect can occur leading to precipitation of KOH and ZnO within the pore structure. In consequence, sufficient gas supply is hindered during discharging. In comparison, the open set-up was more prone to leakage of electrolyte as no gas pressure could be applied. In consequence, fine droplets were visible on the electrode side facing the surrounding air after about 50 h, which then formed a continuous film. However even with this film, the current–potential curves up to 50 mA cm^{-2} (depicted in Supplementary Fig. S2) showed no diffusion limitation. In the closed set-up with active gas flow, these electrolyte droplets were taken out with the air flow.

The results show that the favorable PIC method can be applied in a full zinc-air cell without damaging the air electrode. When comparing the open and the closed set-up, the

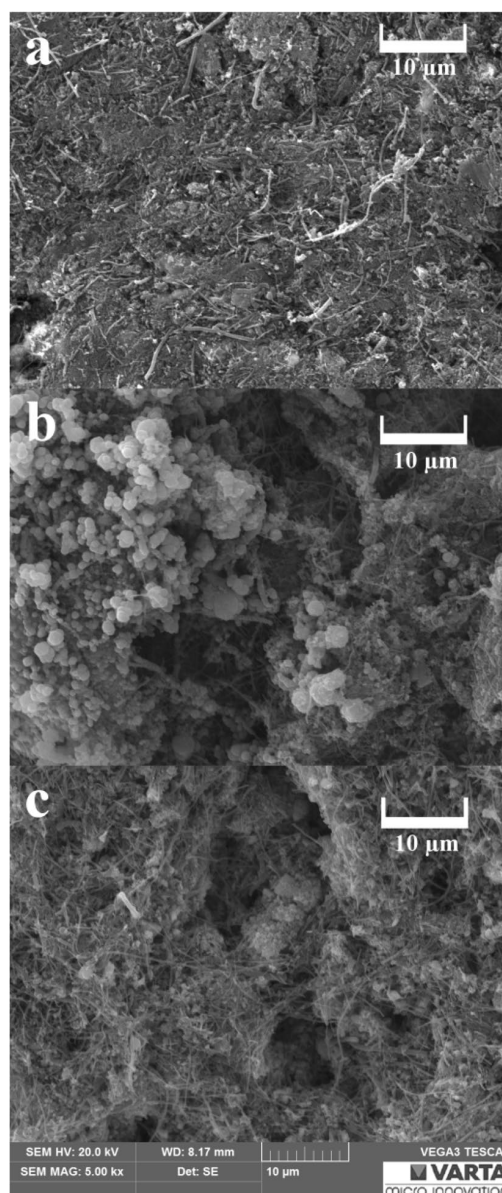


Fig. 8 SEM images of the NCO-catalyzed side facing the electrolyte during operation of **a** a fresh electrode before electrochemical characterization, **b** of E_{const} after operation, and **c** $E_{\text{PIC_open}}$ after operation

Table 2 Charge/discharge potential differences and the calculated air electrode efficiencies from the recorded current–potential curves (see Supplementary Fig. S2) at the start of operation and after 200 cycles

| ΔV (V) and efficiency (%) | At $\pm 5 \text{ mA cm}^{-2}$ | | At $\pm 20 \text{ mA cm}^{-2}$ | | At $\pm 50 \text{ mA cm}^{-2}$ | |
|-----------------------------------|-------------------------------|------------------|--------------------------------|------------------|--------------------------------|------------------|
| | Start | After 200 cycles | Start | After 200 cycles | Start | After 200 cycles |
| E_{const} | 0.61 (68%) | 0.63 (66%) | 0.71 (63%) | 0.79 (58%) | 0.83 (58%) | 1.02 (47%) |
| E_{PIC} | 0.65 (66%) | 0.61 (67%) | 0.78 (60%) | 0.76 (60%) | 0.95 (53%) | 0.96 (51%) |
| $E_{\text{PIC_open}}$ | 0.64 (67%) | 0.61 (67%) | 0.75 (62%) | 0.78 (59%) | 0.87 (56%) | 1.03 (48%) |

closed set-up results in prolonged operation times, due to more control of the wetting behavior by varying the air flow or by increasing the air pressure. However, the system has to be designed in a more complex way than the open set-up. Nevertheless, when considering the need of scale-up, active air supply can be helpful to achieve even current distribution over the whole electrode area during operation. This can further be enhanced by implementation of flow fields as used in fuel cells.

3.2.2 Scale-up to 16 cm²

Although high activities and good stabilities for zinc-air cells have been reported by many groups [12, 46, 47], the usual active surface areas of tested air electrodes are smaller than 5 cm². However, for stationary large-scale applications scale-up of the electrode size is crucial. This includes not only the scalability of the electrode production process but also the stability of these electrodes. During operation, the fine balance of gas accessibility and electrolyte permeability is altered due to the increased hydrostatic pressure. The long-term measurement of a 16 cm² sized electrode, i.e., four times bigger surface area than E_{const} , with active synthetic air supply is depicted in Fig. 9. The ORR/OER roundtrip efficiency of $E_{16 \text{ cm}^2}$ was 54% after 40 cycles at 30 mA cm⁻² ($\Delta V = 0.90$ V). In consequence to the increasing performance over time indicating improved wetting of the electrode, the current density was raised to 50 mA cm⁻² after 100 h total operation time as shown in Fig. 9. In the first cycle at 50 mA cm⁻² the efficiency was 51%, and even 52% after 400 h total testing time and after changing to 6 M KOH electrolyte. The change of electrolyte had no significant effect on the performance of the air electrode. Between 6 and 8 M, the ionic conductivity of KOH electrolyte is high with its maximum of 650 mS cm⁻¹ (25 °C) at a concentration of 7 M (or ~30 wt% KOH) [13, 48]. Although even higher molarities would allow to dissolve more ZnO (i.e., about 1.2 M ZnO in 12 M KOH at room temperature)

and thus increase the volumetric energy density of the flow battery system, the resulting increase of viscosity and corrosiveness would further complicate the system management [15, 19, 48].

After total 200 cycles (517 h operation time), the efficiency was still 51% ($\Delta V = 0.95$ V) at 50 mA cm⁻². The measurement was stopped due to increased leakage of electrolyte and too low ORR potentials after 280 charge/discharge cycles. Overall, the performances of $E_{16 \text{ cm}^2}$ and E_{const} are nearly the same showing that the scale-up from 4 to 16 cm² was successfully achieved.

3.2.3 Flowing electrolyte

Because of the high flow velocities necessary for obtaining compact zinc morphologies, a 4 cm² air electrode (E_{flow}) was long-term cycled with surface flow velocities up to 8 cm s⁻¹ (which corresponds to 2.1 L min⁻¹ with this cell geometry). The measurement is depicted in Fig. 10 showing the first 15 h of testing in the left graph and the following 400 h, i.e., overall 200 cycles at 8 cm s⁻¹ on the right-hand graph. The lower operation time of 450 h compared to the other electrodes is caused by the longer shut-off times during the measurement of E_{flow} . After every restart, the first ORR cycle exhibited low potentials; however, after the first charging the ORR potentials improved again indicating that the three-phase boundaries were restored. This effect indicates that during shut-off times the electrode soaked with KOH, but the electrolyte was then displaced again by the generated oxygen during OER. Altogether, the E_{flow} electrode exhibited stable ORR and OER potentials for more than 400 h, even with the high shear forces affecting the electrode's surface. In fact, the flowing electrolyte had the positive effect to remove the generated oxygen bubbles during OER resulting in more stable charging potentials as shown in Supplementary Fig. S4. Increase of flow velocity from 5 to 8 cm s⁻¹ (i.e., 1.5–2.1 L min⁻¹) did not affect the performance as can be seen in Fig. 10 (left) between 10 and 17 h of operation.

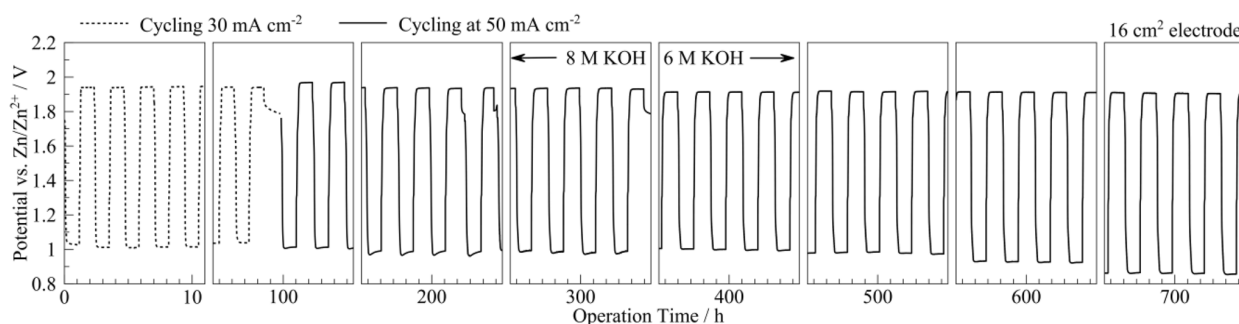


Fig. 9 Performance of a 16 cm² bifunctional air electrode during long-term cycling operated at 30 and 50 mA cm⁻² in 8 or 6 M KOH electrolyte (actively supplied with synthetic air)

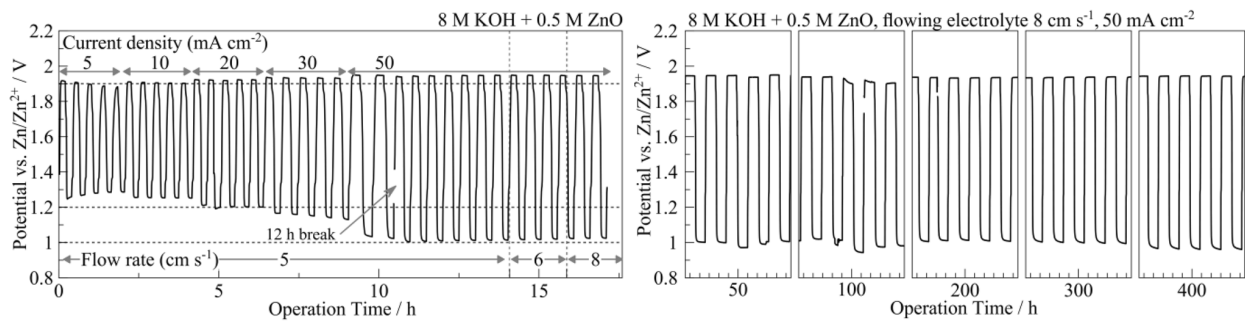


Fig. 10 Performance of a 4 cm² bifunctional air electrode during long-term cycling with flowing electrolyte ($w=5\text{--}8\text{ cm s}^{-1}$, i.e. 1.5–2.1 L min⁻¹) and increasing current density up to 50 mA cm⁻² (supplied with synthetic air)

This indicates that the fine Ni foam provides sufficient stability for the catalyst/CNF/PTFE network and that in this build slow material removal is prevented. The results show that the air electrode can withstand the stressing conditions (high surface flow velocities, PIC charging) needed for compact zinc deposition. Nevertheless, it has to be considered that too high flow velocities reduce the energy efficiency of the whole system due to the power needed for pumping [49, 50]. The air electrode efficiency after 50 h of long-term operation was 50%, 52% after 200 h, and still 50% after 400 h of operation. The measurement was stopped after 450 h due to increased electrolyte leakage.

After these promising results with pulse interrupt current charging for both the reversible air electrode and the zinc electrode, it was highly interesting to test the effect of PIC charging in the unit cell with flowing KOH electrolyte.

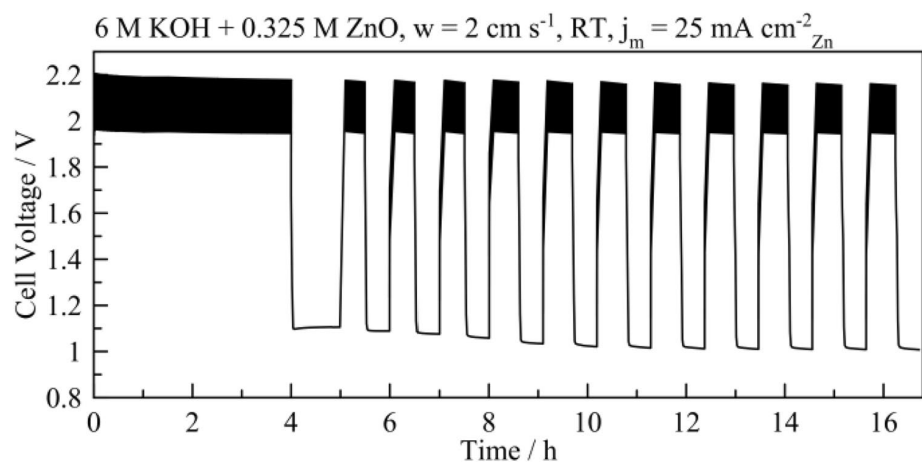
3.3 Full cell operation with 100 cm² air electrodes and zinc pulse interrupt current plating

The first full cell operation at room temperature with flowing 6 M KOH electrolyte is shown in Fig. 11, depicting the unit

cell voltage over time. After PIC deposition of zinc onto the nickel foam within the first 4 h, the cell was cycled for 17 h, showing stable charge cell voltages over the whole operation time and, after an initial decrease, also stable discharge voltages at > 1 V. During the first full cycle, the efficiency of the complete zinc-air cell is 51% at 25 mA cm⁻²_{Zn}. This value includes, in contrast to the efficiencies listed in Table 2, also the ohmic resistances and the zinc overpotentials. However, these losses are much smaller in comparison to the ORR/OER overpotentials [51]. At the last cycle, the efficiency was 47%.

The results show that although the manufacturing of 100 cm² air electrodes was successfully achieved, further optimization of the set-up is still necessary in order to prevent electrolyte leakage. The leakage posed a rather minor problem in small electrodes up to 16 cm²; however, the open set-up used for full cell operation in combination with the big air electrode surface area of 200 cm² (cell height of 16 cm) allowed too much loss of electrolyte so that the electrode could not be operated further. Suggestions for improvement would be the backing of the air electrodes with an additional PTFE layer or an additional gas diffusion layer

Fig. 11 Performance of a zinc-air flow unit cell with 100 cm² zinc-coated nickel foam as negative electrode and two 100 cm² sized bi-catalyzed bifunctional air electrodes open to the ambient air



(GDL) as known from fuel cell technology [52]. By achieving this, the next step would be the increase of surface flow velocity from 2 to 6 cm s⁻¹ by reducing the electrode distance. Nevertheless, this measurement can be seen as proof-of-concept that the knowledge gained by the investigations on both electrodes can be applied for unit cell operation.

4 Conclusion

Separate study of the operating conditions of both half-cells in the rechargeable zinc-air flow battery allows faster transfer to larger-scaled full cells. In full cells often only the cell voltage is measured, which makes it more challenging to differentiate and attribute the various effects occurring at anode and cathode. Determining the operating range for various parameters allows further optimization of the cell performance. The investigated parameters discussed in this paper and their effects on the half- and full-cell performances are summarized as follows:

- In the range of 10–50 mA cm⁻² average current density, compact zinc morphologies are obtained for pulse interrupt current (PIC) charging times as long as 150 min in additive-free 0.5 M ZnO/8 M KOH at 60 °C. At 23 °C, the average current density producing compact zinc decreases to a range between 3.7 and 16.7 mA cm⁻². Charge/discharge cycling using PIC results in compact dendrite-free zinc deposits up to 60 mA cm⁻² mean current density j_m (120 mA cm⁻² pulse current density, flow rate 6 cm s⁻¹, and 60 °C). Nickel is preferred over brass and stainless steel as substrate material in producing compact zinc deposits.
- On the air electrode, applying the PIC charging waveform, the charging potentials stay below 2.1 V even with pulse currents of 150 mA cm⁻². Long-term results show that there is no accelerated degradation of the air electrode by that method [27].
- Scaling-up of the utilized manufacturing process was successful for electrode sizes up to 100 cm². Up-scaling from 4 to 16 cm² resulted in comparable operation times. For long-term operation of bigger sized electrodes, additional backing is required.
- 8 and 6 M KOH electrolytes are both suitable for operation of the flow cell.
- High electrolyte flow rates of up to 8 cm s⁻¹ on the electrode surface do not damage the air electrode and result in more stable charging potentials due to the outtake of generated oxygen bubbles.
- The open set-up with passive air supply can lead to faster electrolyte leakage and to oxygen diffusion limitations at current densities > 50 mA cm⁻². However, the build of

the cell and the peripheral systems can be designed in a more compact way.

Long operation times of up to 800 h charge/discharge cycling at 50 mA cm⁻²_{mean} were demonstrated for bifunctional air electrodes. For all tested electrodes, regardless of the operating conditions (flow, air supply, size), end-of-life was reached because of too low oxygen reduction potentials during discharge. As the ORR is very sensitive to the electrode structure due to the requirement of three-phase zones (gas/electrolyte/conductive catalyst), mechanical and chemical degradation effects are mainly apparent in the slowly decreasing discharge potentials. Improvements in long-term stability have to be tackled in this regard, either by manufacturing even more robust structures with more stable materials (e.g., substitute PTFE binder) or by keeping the anodic charging potentials during OER as low as possible.

Acknowledgements Open access funding provided by Graz University of Technology. Funding by the Austrian Federal Ministry of Transport, Innovation and Technology (BMVIT) and The Austrian Research Promotion Agency (FFG) through the program “e!MISSION.at Energieforschungsprogramm” (No. 848933) is gratefully acknowledged. We also want to thank our industry partners VARTA Micro Innovation GmbH (Austria) and RECAT (Germany). Nickel foam was generously provided by Alantum Europe GmbH, Germany.

Open Access This article is distributed under the terms of the Creative Commons Attribution 4.0 International License (<http://creativecommons.org/licenses/by/4.0/>), which permits unrestricted use, distribution, and reproduction in any medium, provided you give appropriate credit to the original author(s) and the source, provide a link to the Creative Commons license, and indicate if changes were made.


References

1. Chen H, Cong TN, Yang W, Tan C, Li Y, Ding Y (2009) Progress in electrical energy storage system: a critical review. *Prog Nat Sci* 19:291–312. <https://doi.org/10.1016/j.pnsc.2008.07.014>
2. Li X, Zhang H, Mai Z, Zhang H, Vankelecom I (2011) Ion exchange membranes for vanadium redox flow battery (VRB) applications. *Energy Environ Sci* 4:1147. <https://doi.org/10.1039/c0ee00770f>
3. Alotto P, Guarnieri M, Moro F (2014) Redox flow batteries for the storage of renewable energy: a review. *Renew Sustain Energy Rev* 29:325–335. <https://doi.org/10.1016/j.rser.2013.08.001>
4. Leung PK, Li X, Ponce de León C, Berlouis L, Low CTJ, Walsh FC (2012) Progress in redox flow batteries, remaining challenges and their applications in energy storage. *RSC Adv* 2:10125–10156. <https://doi.org/10.1039/c2ra21342g>
5. Dunn B, Kamath H, Tarascon J-M (2011) Electrical energy storage for the grid: a battery of choices. *Science* 334:928–935. <https://doi.org/10.1126/science.1212741>
6. Perry ML, Weber AZ (2016) Advanced redox-flow batteries: a perspective. *J Electrochem Soc* 163:A5064–A5067. <https://doi.org/10.1149/2.0101601jes>
7. Arenas LF, Ponce de León C, Walsh FC (2017) Engineering aspects of the design, construction and performance of modular

- redox flow batteries for energy storage. *J Energy Storage* 11:119–153. <https://doi.org/10.1016/j.est.2017.02.007>
8. Skyllas-Kazacos M, Chakrabarti MH, Hajimolana S, Mjalli FS, Saleem M (2011) Progress in flow battery research and development. *J Electrochem Soc* 158:R55. <https://doi.org/10.1149/1.3599565>
 9. Li X, Ponce de León C, Walsh FC, Wills RGA, Pletcher D (2015) Zinc-based flow batteries for medium- and large-scale energy storage. In: *Advances in batteries for medium and large-scale energy storage*. Elsevier, New York, pp 293–315
 10. Poullikkas A (2013) A comparative overview of large-scale battery systems for electricity storage. *Renew Sustain Energy Rev* 27:778–788. <https://doi.org/10.1016/j.rser.2013.07.017>
 11. Pan J, Ji L, Sun Y, Wan P, Cheng J, Yang Y, Fan M (2009) Preliminary study of alkaline single flowing Zn-O₂ battery. *Electrochim Commun* 11:2191–2194. <https://doi.org/10.1016/j.elecom.2009.09.028>
 12. Bockelmann M, Kunz U, Turek T (2016) Electrically rechargeable zinc-oxygen flow battery with high power density. *Electrochim Commun* 69:24–27. <https://doi.org/10.1016/j.elecom.2016.05.013>
 13. Xu M, Ivey DG, Xie Z, Qu W (2015) Rechargeable Zn-air batteries: progress in electrolyte development and cell configuration advancement. *J Power Sources* 283:358–371. <https://doi.org/10.1016/j.jpowsour.2015.02.114>
 14. Davari E, Ivey DG (2018) Bifunctional electrocatalysts for Zn-air batteries. *Sustain Energy Fuels* 2:39–67. <https://doi.org/10.1039/C7SE00413C>
 15. Fu J, Cano ZP, Park MG, Yu A, Fowler M, Chen Z (2017) Electrically rechargeable zinc-air batteries: progress, challenges, and perspectives. *Adv Mater* 29:1604685. <https://doi.org/10.1002/adma.201604685>
 16. Pei P, Wang K, Ma Z (2014) Technologies for extending zinc-air battery's cyclife: a review. *Appl Energy* 128:315–324. <https://doi.org/10.1016/j.apenergy.2014.04.095>
 17. POWAIR - Zinc-Air Flow Batteries for Electrical Power Distribution Networks. <http://www.powair.eu/index.php>. Accessed 17 Jan 2018
 18. ZAESS - Zinc Air Energy Storage System. <http://www.zaess.eu/>. Accessed 17 Jan 2018
 19. Caramia V, Bozzini B (2014) Materials science aspects of zinc-air batteries: a review. *Mater Renew Sustain Energy* 3:28. <https://doi.org/10.1007/s40243-014-0028-3>
 20. Gilligan GE, Qu D (2015) Zinc-air and other types of metal-air batteries. *Adv Battery Medium Large Scale Energy Storage*. <https://doi.org/10.1016/B978-1-78242-013-2.00012-1>
 21. Zelger C, Laumen J, Laskos A, Gollas B (2016) Rota-Hull cell study on pulse current zinc electrodeposition from alkaline electrolytes. *Electrochim Acta* 213:208–216. <https://doi.org/10.1016/j.electacta.2016.07.108>
 22. Wang K, Pei P, Ma Z, Chen H, Xu H, Chen D, Wang X (2015) Dendrite growth in the recharging process of zinc-air batteries. *J Mater Chem A* 3:22648–22655. <https://doi.org/10.1039/C5TA06366C>
 23. Jörissen L (2006) Bifunctional oxygen/air electrodes. *J Power Sources* 155:23–32. <https://doi.org/10.1016/j.jpowsour.2005.07.038>
 24. Chen D, Chen C, Baiyee ZM, Shao Z, Ciucci F (2015) Nonstoichiometric oxides as low-cost and highly-efficient oxygen reduction/evolution catalysts for low-temperature electrochemical devices. *Chem Rev* 115:9869–9921. <https://doi.org/10.1021/acs.chemrev.5b00073>
 25. Hong WT, Risch M, Stoerzinger KA, Grimaud A, Suntivich J, Shao-Horn Y (2015) Toward the rational design of non-precious transition metal oxides for oxygen electrocatalysis. *Energy Environ Sci* 8:1404–1427. <https://doi.org/10.1039/C4EE03869J>
 26. Gupta S, Kellogg W, Xu H, Liu X, Cho J, Wu G (2016) Bifunctional perovskite oxide catalysts for oxygen reduction and evolution in alkaline media. *Chem An Asian J* 11:10–21. <https://doi.org/10.1002/asia.201500640>
 27. Pichler B, Weinberger S, Reščec L, Grimmer I, Gebetsroither F, Bitschnau B, Hacker V (2017) Bifunctional electrode performance for zinc-air flow cells with pulse charging. *Electrochim Acta* 251:488–497. <https://doi.org/10.1016/j.electacta.2017.08.128>
 28. Pletcher D, Li X, Price SWT, Russell AE, Sönmez T, Thompson SJ (2016) Comparison of the spinels Co₃O₄ and NiCo₂O₄ as bifunctional oxygen catalysts in alkaline media. *Electrochim Acta* 188:286–293. <https://doi.org/10.1016/j.electacta.2015.10.020>
 29. Elumeeva K, Masa J, Sierau J, Tietz F, Muhler M, Schuhmann W (2016) Perovskite-based bifunctional electrocatalysts for oxygen evolution and oxygen reduction in alkaline electrolytes. *Electrochim Acta* 208:25–32. <https://doi.org/10.1016/j.electacta.2016.05.010>
 30. Alegre C, Modica E, Aricò AS, Baglio V (2018) Bifunctional oxygen electrode based on a perovskite/carbon composite for electrochemical devices. *J Electroanal Chem* 808:412–419. <https://doi.org/10.1016/j.jelechem.2017.06.023>
 31. Sumboja A, Ge X, Zheng G, Goh FWT, Hor TSA, Zong Y, Liu Z (2016) Durable rechargeable zinc-air batteries with neutral electrolyte and manganese oxide catalyst. *J Power Sources* 332:330–336. <https://doi.org/10.1016/j.jpowsour.2016.09.142>
 32. Low CTJ, Roberts EPL, Walsh FC (2007) Numerical simulation of the current, potential and concentration distributions along the cathode of a rotating cylinder Hull cell. *Electrochim Acta* 52:3831–3840. <https://doi.org/10.1016/j.electacta.2006.10.056>
 33. Wang RY, Kirk DW, Zhang GX (2006) Effects of deposition conditions on the morphology of zinc deposits from alkaline zincate solutions. *J Electrochem Soc* 153:C357–C364. <https://doi.org/10.1149/1.2186037>
 34. West AC, Matlosz M, Landolt D (1992) Primary current distribution in the Hull cell and related trapezoidal geometries. *J Appl Electrochem* 22:301–303. <https://doi.org/10.1007/BF01030192>
 35. Madore C, Matlosz M, Landolt D (1992) Experimental investigation of the primary and secondary current distribution in a rotating cylinder Hull cell. *J Appl Electrochem* 22:1155–1160. <https://doi.org/10.1007/BF01297417>
 36. Gallaway JW, Desai D, Gaikwad A, Corredor C, Banerjee S, Steingart D (2010) A lateral microfluidic cell for imaging electrodeposited zinc near the shorting condition. *J Electrochem Soc* 157:A1279. <https://doi.org/10.1149/1.3491355>
 37. Ito Y, Wei X, Desai D, Steingart D, Banerjee S (2012) An indicator of zinc morphology transition in flowing alkaline electrolyte. *J Power Sources* 211:119–128. <https://doi.org/10.1016/j.jpowsour.2012.03.056>
 38. Shin S-H, Yun S-H, Moon S-H (2013) A review of current developments in non-aqueous redox flow batteries: characterization of their membranes for design perspective. *RSC Adv* 3:9095. <https://doi.org/10.1039/c3ra00115f>
 39. Ma H, Wang B, Fan Y, Hong W (2014) Development and characterization of an electrically rechargeable zinc-air battery stack. *Energies* 7:6549–6557. <https://doi.org/10.3390/en7106549>
 40. Gu P, Zheng M, Zhao Q, Xiao X, Xue H, Pang H (2017) Rechargeable zinc-air batteries: a promising way to green energy. *J Mater Chem A* 2017:1–16. <https://doi.org/10.1039/C7TA01693J>
 41. Li Y, Dai H (2014) Recent advances in zinc-air batteries. *Chem Soc Rev* 43:5257–5275. <https://doi.org/10.1039/C4CS00015C>
 42. Prabu M, Ketpang K, Shanmugam S (2014) Hierarchical nanostructured NiCo₂O₄ as an efficient bifunctional non-precious metal catalyst for rechargeable zinc-air batteries. *Nanoscale* 6:3173. <https://doi.org/10.1039/c3nr05835b>

43. Li PC, Chien YJ, Hu CC (2016) Novel configuration of bifunctional air electrodes for rechargeable zinc-air batteries. *J Power Sources* 313:37–45. <https://doi.org/10.1016/j.jpowsour.2016.02.063>
44. Bogolowski N, Ngaleu O, Sakthivel M, Drillet JF (2017) Long-life bifunctional BaSrCoFeO₃/C gas diffusion electrode. *Carbon N Y* 119:511–518. <https://doi.org/10.1016/j.carbon.2017.04.051>
45. Li PC, Hu CC, You TH, Chen PY (2017) Development and characterization of bi-functional air electrodes for rechargeable zinc-air batteries: effects of carbons. *Carbon N Y* 111:813–821. <https://doi.org/10.1016/j.carbon.2016.10.057>
46. Li X, Pletcher D, Russell AE, Walsh FC, Wills RGA, Gorman SF, Price SWT, Thompson SJ (2013) A novel bifunctional oxygen GDE for alkaline secondary batteries. *Electrochem Commun* 34:228–230. <https://doi.org/10.1016/j.elecom.2013.06.020>
47. Lee DU, Choi JY, Feng K, Park HW, Chen Z (2014) Advanced extremely durable 3D bifunctional air electrodes for rechargeable zinc-air batteries. *Adv Energy Mater*. <https://doi.org/10.1002/aenm.201301389>
48. Mainar R, Leonet A, Bengoechea O, Boyano M, de Meataz I, Kvasa I, Guerfi A, Alberto A, Blázquez J (2016) Alkaline aqueous electrolytes for secondary zinc-air batteries: an overview. *Int J Energy Res* 40:1032–1049. <https://doi.org/10.1002/er.3499>
49. Amunátegui B, Ibáñez A, Sierra M, Pérez M (2017) Electrochemical energy storage for renewable energy integration: zinc-air flow batteries. *J Appl Electrochem* 2017:1–11. <https://doi.org/10.1007/s10800-017-1133-7>
50. Chalamala BR, Soundappan T, Fisher GR, Anstey MR, Viswanathan VV, Perry ML (2014) Redox flow batteries: an engineering perspective. *Proc IEEE* 102:1–24. <https://doi.org/10.1109/JPROC.2014.2320317>
51. Lee J-S, Tai Kim S, Cao R, Choi N-S, Liu M, Lee KT, Cho J (2011) Metal-air batteries with high energy density: Li-air versus Zn-air. *Adv Energy Mater* 1:34–50. <https://doi.org/10.1002/aenm.201000010>
52. Lapique F, Belhadj M, Bonnet C, Pauchet J, Thomas Y (2016) A critical review on gas diffusion micro and macroporous layers degradations for improved membrane fuel cell durability. *J Power Sources* 336:40–53. <https://doi.org/10.1016/j.jpowsour.2016.10.037>

Affiliations

Birgit Pichler¹  · Bernhard S. Berner² · Nikolaus Rauch¹ · Christian Zelger² · Hans-Jürgen Pauling³ · Bernhard Gollas² · Viktor Hacker¹

Bernhard S. Berner
berner@student.tugraz.at

Nikolaus Rauch
nrauch@student.tugraz.at

Christian Zelger
christian.zelger@tugraz.at

Hans-Jürgen Pauling
hj.pauling@recat.de

Bernhard Gollas
bernhard.gollas@tugraz.at

Viktor Hacker
viktor.hacker@tugraz.at

¹ Institute of Chemical Engineering and Environmental Technology, Fuel Cell Group, Graz University of Technology, Inffeldgasse 25C, 8010 Graz, Austria

² Institute for Chemistry and Technology of Materials, Graz University of Technology, Stremayrgasse 9, 8010 Graz, Austria

³ RECAT GmbH, Ochsenburger Straße 19, 75056 Sulzfeld, Germany

Supplementary to

The impact of operating conditions on component and electrode development for zinc-air flow batteries

¹Birgit Pichler*, ²Bernhard S. Berner, ¹Nikolaus Rauch, ²Christian Zelger, ³Hans-Jürgen Pauling, ²Bernhard Gollas, ¹Viktor Hacker

¹ Graz University of Technology, Institute of Chemical Engineering and Environmental Technology, Fuel Cell Group, Inffeldgasse 25C, 8010 Graz, Austria

² Graz University of Technology, Institute for Chemistry and Technology of Materials, Stremayrgasse 9, 8010 Graz, Austria

³ RECAT GmbH, Ochsenburger Straße 19, 75056 Sulzfeld, Germany

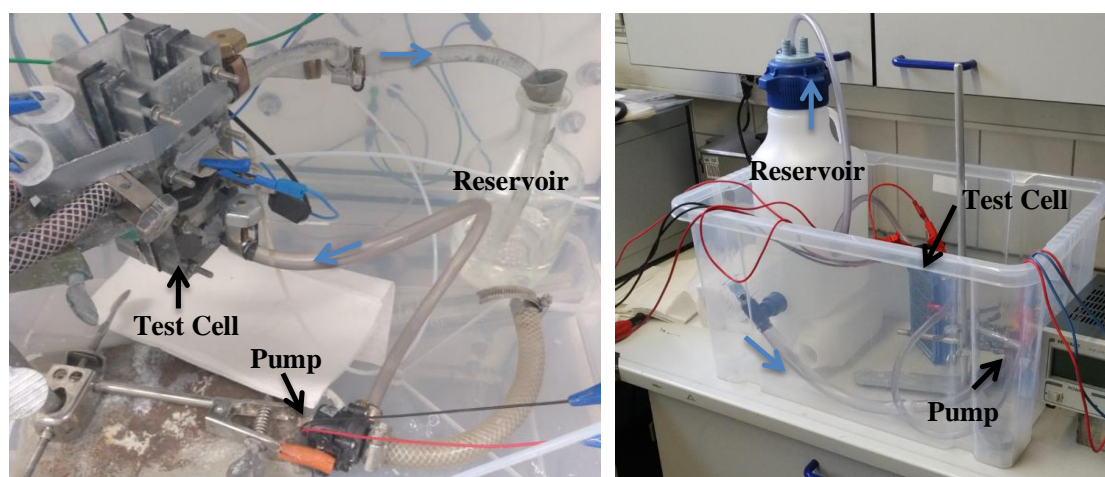
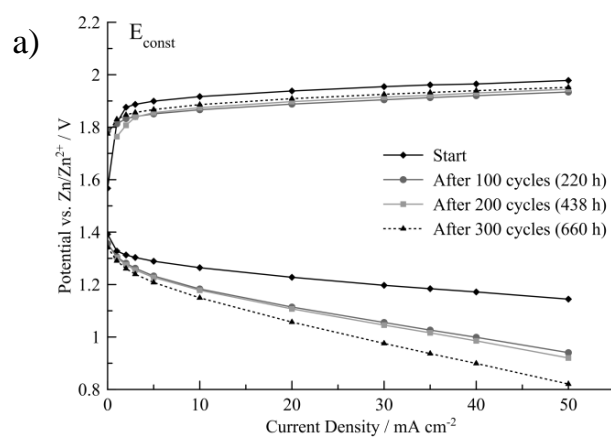


Fig. S1 Image of the air electrode half-cell set-up (left) and the full-cell set-up (right) showing the pump, the reservoir and the test cell, respectively



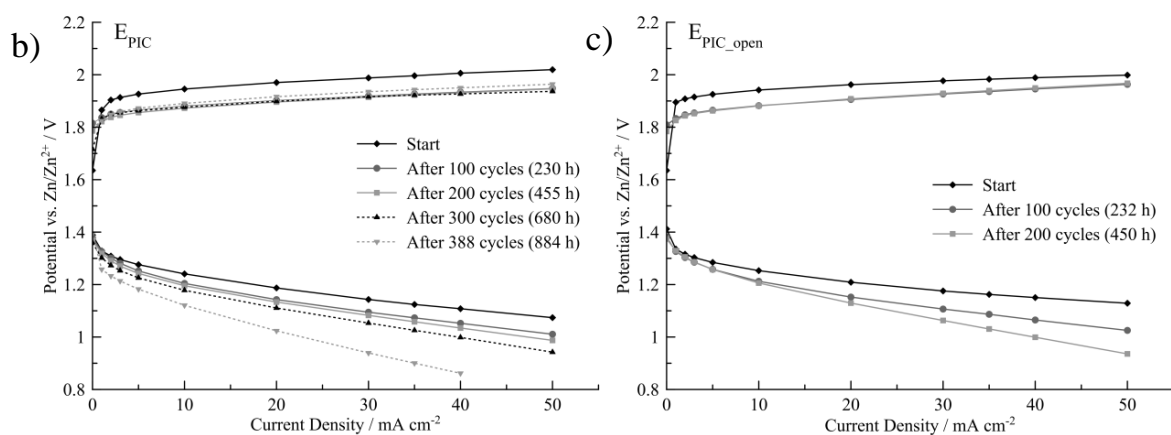


Fig. S2 Current-potential curves for oxygen reduction reaction and oxygen evolution reaction of E_{const} (a), E_{PIC} (b) and $E_{\text{PIC_open}}$ (c) after every hundred charge/discharge cycles

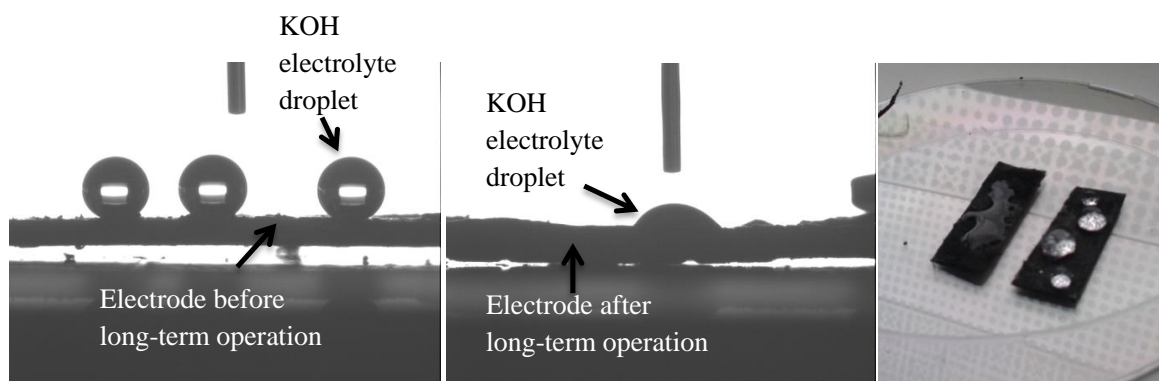


Fig. S3 Contact angle measurements of a bi-catalyzed bifunctional air electrode before (left) and after (middle) operation with the difference in hydrophobicity being also apparent in the picture (right)

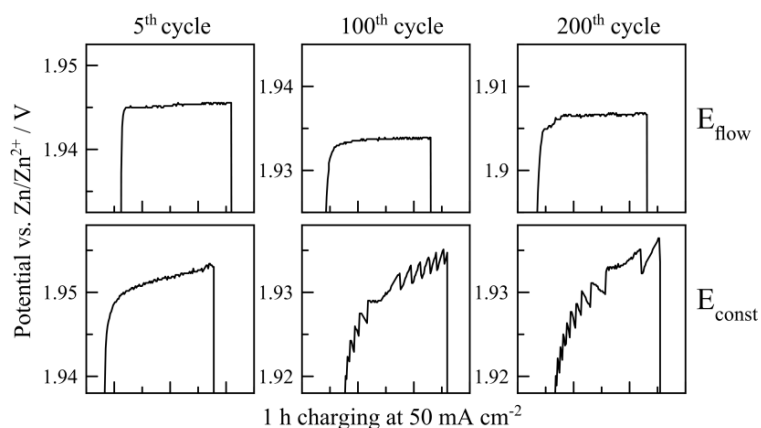


Fig. S4 Potential course of one charging cycle of E_{flow} (top) and E_{const} (bottom) indicating the easier oxygen bubble outtake with the flowing electrolyte

Long-term Operation of Perovskite-catalyzed Bifunctional Air Electrodes in Rechargeable Zinc-Air Flow Batteries

Birgit Pichler,^{*[a]} Kurt Mayer,^[a] and Viktor Hacker^[a]

Abstract: Rechargeable zinc-air flow batteries are investigated as promising stationary energy storage system due to compact system design and low cost materials. Bifunctional air electrodes employing $\text{La}_{0.6}\text{Sr}_{0.4}\text{Co}_{0.2}\text{Fe}_{0.8}\text{O}_3$ perovskite catalyst for O_2 -reduction and O_2 -evolution are manufactured in small scale (4 cm^2) and in up-scaled sizes ($50 - 55\text{ cm}^2$) and tested in unit cell configuration with flowing electrolyte. Stable operation of 1000 h is achieved in the small set-up with an overall 1800 h of operation over 700 cycles at high voltage efficiencies of $> 50\%$ (air electrode) at 50 mA cm^{-2} . The up-scaled flow cell reaches nearly the same performance for 320 h and 130 h, respectively, proving the successful scale-up. Slowly decreasing hydrophobicity is found to be the main reason of initially increasing but then decreasing performance. This is confirmed by electrochemical impedance spectroscopy. Although many problems are suppressed with flowing electrolyte, zinc morphology proves to be the major challenge especially in larger cells in long-term operation of a few hundred hours.

Introduction

Fast and inexpensive storage of electrical energy generated by intermittent sources is becoming more and more relevant due to increasing installation capacities of wind and solar power systems^[1–3]. Stationary flow batteries either using fully soluble redox couples (e.g. all-vanadium) or zinc-based hybrid systems (e.g. Zn-Br₂) have been developed with low costs as an important goal with the DOE target for stationary energy storage being below USD\$ 150 per kWh^[4–9]. Metal-air cell configurations, using for example zinc as the abundant and low cost (\sim USD\$ 2 per kg^{−1})^[7] active storing metal, are thereby of increasing interest as summarized in recent review publications^[10–15]. When flow-assisted (i.e. zinc-air flow battery, ZAFB), these hybrid systems are regarded as “next-generation” flow battery^[12] due to compact system design with only one low cost electrolyte (\sim 4 \$US kWh^{−1})^[7] and one external tank containing the metal zinc in form of zincate (instead of ZnO as in stationary batteries). Also, there is no need for costly separators or anion exchange membranes^[7]. The energy density of the hybrid system is limited by the amount of zinc storable as zincate in alkaline solution (\sim 0.8 M in 8.2 M (35 wt%) KOH)^[11] on the one hand and on the other hand by the area of the zinc

electrode^[7]. A detailed analysis of a large-scale demonstration ZAFB was recently published by Amunatgeui et al.^[16], who concluded that this system is mainly suited for low power and long duration energy storage.

Zinc-air flow batteries employ a bifunctional air electrode for oxygen reduction reaction (ORR) in discharge mode and for oxygen evolution reaction (OER) during charging, thus electrochemically converting freely available oxygen from the ambient air. So far, mainly three-electrode configurations using a separate charge and discharge air electrode have been employed^[16–18], nevertheless, the two-electrode configuration with one zinc electrode and only one air electrode would be preferred because of the more compact cell design and the easier handling of the electrical circuitry^[16].

Numerous catalysts with high activity have been reported in literature to be able to bifunctionally catalyze ORR and OER, but activity measurements are often performed ex-situ by means of cyclic voltammetry using rotating ring disk electrodes or demonstrated with shorter in-situ tests of about 100 h (compare to Table S1 in the supporting information). Thereby long-term stability and degradation mechanisms are often less studied. The bifunctional catalysts for alkaline media can be classified^[10] as **i)** precious metal (e.g. Pt and IrO₂, commonly utilized for benchmarking but not really bifunctional^[13]), **ii)** transition metal oxide catalysts^[19], such as spinels (AB₂O₄)^[20] and perovskites (ABO₃), but also single metal oxides (NiO_x, CoO_x, MnO_x)^[21] and **iii)** carbon-based materials for example carbon nanotubes and (reduced) graphene oxide^[10]. Many different perovskite catalysts^[19,22–24] have been investigated, whereby the B-site is generally regarded as the active site. In addition, the doping with heteroatoms has a high impact on catalytic activity as well as on the stability during potential cycling^[24].

A few alkaline zinc-air flow battery systems have been reported^[16,17,25–27], but more work needs to be done in regard to implementation of the abovementioned catalysts into stable electrode structures for achieving operation times of hundreds of hours. Nevertheless, by utilizing a flowing electrolyte, common problems of static zinc-air batteries can be reduced, mainly on the zinc electrode by suppressing dendrite growth, shape change and passivation due to a more even zinc distribution and lower concentration gradients. Thus, operation at increased current densities is possible^[7]. Obtaining compact zinc morphologies can further be enhanced by applying pulsating currents during charging^[28–30]. Nevertheless, reduced cycle life, either caused by air electrode degradation or by irreversible changes on the zinc electrode, especially in up-scaled cells, is still a major hindrance for bringing the zinc-air (flow) battery closer to application.

[a] Birgit Pichler, Kurt Mayer, Prof. Viktor Hacker
Institute of Chemical Engineering and Environmental Technology
Graz University of Technology
Inffeldgasse 25C, 8010 Graz, Austria
E-mail: birgit.pichler@tugraz.at; viktor.hacker@tugraz.at

In this work we present durable bifunctional air electrodes manufactured via a scalable process for application in flow-assisted zinc-air batteries. The electrodes employed commercial $\text{La}_{0.6}\text{Sr}_{0.4}\text{Co}_{0.2}\text{Fe}_{0.8}\text{O}_3$ perovskite as catalyst^[22,23], which allowed more reproducible optimization of the electrode build. Thus, the straightforward manufacturing process also allows easy implementation and characterization of other types of (oxide) catalysts. So far, there are no standardized characterization procedures for zinc-air batteries, also because it usually depends on the focus of the study, e.g. testing of zinc electrodes is often performed with capacity dependent cycles. In this work, the air electrodes were tested at a comparatively high but for stationary systems practically applicable^[5] current density of 50 mA cm^{-2} and long cycle times ($\geq 2 \text{ h}$) in a small 4 cm^2 set-up and in a bigger cell with 50 cm^2 . Insight on degradation mechanisms was gained by electrochemical impedance spectroscopy. Although full unit cells were tested, this work focused its investigations and optimizations regarding longevity and catalytic activity on the bifunctional air electrode.

Results and Discussion

Electrode Manufacture

Bifunctional air electrodes for ORR and OER were manufactured via an easily scalable ($4 - 55 \text{ cm}^2$)^[29] manufacturing process, employing a $\text{La}_{0.6}\text{Sr}_{0.4}\text{Co}_{0.2}\text{Fe}_{0.8}\text{O}_3$ perovskite as catalyst in this work. However, the process can be readily adapted for implementation of other catalysts. Nickel foam was utilized as current collector material as it provides good stability and flexibility to the electrode build. By using two separate electrode pastes containing the catalyst – one on each side of the nickel foam - the electrochemical activity of the electrode toward OER on the electrolyte side (two-phase zones between electrolyte and catalyst) and toward ORR on the air supplied side (three-phase boundaries between oxygen/catalyst/electrolyte required) was optimized separately. OER activity, for example, was much enhanced by the addition of fine nickel powder on the electrolyte facing side as the $\text{Ni}(\text{OH})_2/\text{NiOOH}$ redox couple worked as reaction promoting mediator^[12]. Thereby, nickel got repeatedly

oxidized/reduced, i.e. during cycling always oxidation/reduction of the $\text{Ni}(\text{OH})_2/\text{NiOOH}$ redox couple took place before ORR/OER (two-step reaction) as was recently studied by Cano et al.^[31]. The beneficial effect on the OER performance through the addition of fine Ni powder was also apparent by the lower charging potentials of these electrodes compared to previously investigated $\text{La}_{0.6}\text{Sr}_{0.4}\text{Co}_{0.2}\text{Fe}_{0.8}\text{O}_3$ perovskite-only air electrodes^[32].

In the electrode build, an optimized amount of PTFE was utilized as hydrophobic binder material and the added carbon nanofibers (CNF) provided good oxygen accessibility and electrical conductivity by forming a fibrous electrically conductive network. Although less defined and homogenous than carbon nanotubes, the comparatively low-cost CNF had the benefit to exhibit good stability at high anodic potentials compared to other common carbon-type electrode additives such as Vulcan XC72 due to higher graphitized regions^[24]. Although carbon-free electrodes have been developed, for example by Li et al.^[33], in order to prevent degradation by carbon corrosion, carbon-materials exhibit a synergistic ORR promoting effect especially together with lowly electrically conductive perovskite^[24]. Thus, the discharge performance of the air electrode is significantly enhanced.

Regarding the zinc electrode, in the small test cell a zinc plate (together with air electrode 1, E1) was utilized to ensure sufficient zinc availability on the zinc electrode. In the larger cell, a copper plate coated with a thin layer of pre-deposited zinc (with air electrode 2, E2) was employed in order to prevent contact losses at the clamping. However, Cu in contact with electrolyte was prone to oxidation/reduction during cycling thus proving to be unpractical in this regard, so that in the third cell in combination with air electrode E3, a copper wire, which was soldered onto the backside of a zinc plate, was utilized as current collector. For achieving compact zinc morphologies and for reducing dendrite formation, pulse interrupt currents were applied during charging, thus prolonging the cycle life of the zinc electrode without the addition of modifying additives into the electrolyte.

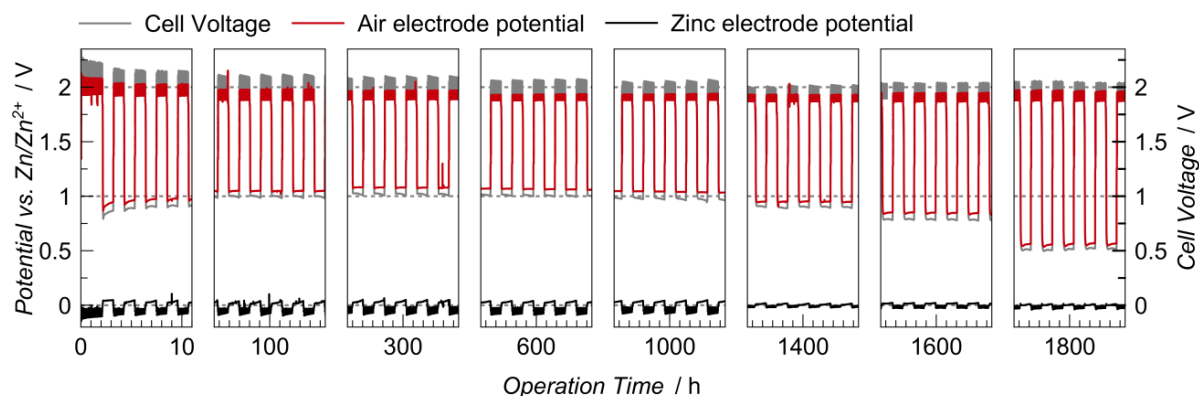


Figure 1. Electrochemical long-term charge/discharge cycling of a zinc-air flow cell with 4 cm^2 bifunctional air electrode (E1) operated at 50 mA cm^{-2} (air) with pulse charging, actively supplied with air at RT and with flowing $8 \text{ M KOH} + 0.5 \text{ M ZnO}$ electrolyte (8 cm s^{-1} surface flow velocity). Besides cell voltage (right y-axis) the air and the zinc electrode's potentials were separately recorded against Zn/Zn^{2+} reference (left y-axis).

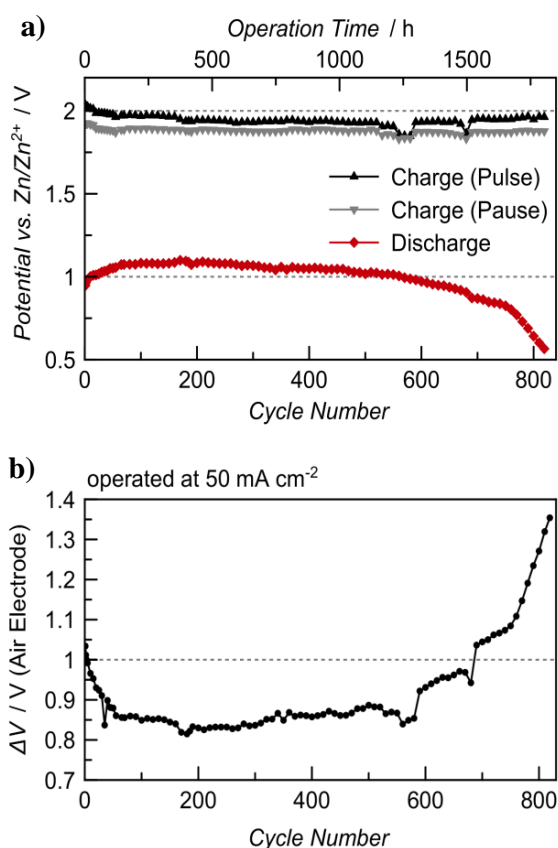


Figure 2. Potential course of the air electrode E1 during long-term operation, **a)** showing the maximum and minimum potentials during pulse charging (100 mA cm^{-2} pulse for 50 ms, 50 ms pause) and the ORR potentials during discharge and **b)** the ΔV between charge (mean value) and discharge.

Electrochemical Characterization of 4 cm^2 Air Electrode E1

The electrochemical characterization results of a unit cell zinc-air flow battery with 4 cm^2 sized air electrode (E1) is shown in Figure 1, which depicts the air electrode potential and the zinc potential vs. Zn/Zn^{2+} as well as the cell voltage every few hundred hours of testing. The performance of the air electrode alone is depicted in more detail in Figure 2. As can be seen in Figure 1, stable air electrode potentials in the range of 1.0 V (discharge) and 2.0 V vs. Zn/Zn^{2+} (during pulse charging indicated by the thick bars) were achieved between 100 h and 1000 h of operation. Overall, it was possible to charge/discharge cycle the air electrode for 1820 h (i.e. over 800 cycles) until the lower cut-off potential of 0.5 V vs. Zn/Zn^{2+} was reached. Including shut-off times, where the air electrode was kept in static electrolyte and continuously fed with low air flow, the air electrode was mounted in the set-up for 136 days (about 4.5 months).

During the whole operation time (except the first 50 h), the charging potentials of the air electrode were stable between 1.93–1.95 V vs. Zn/Zn^{2+} during the 100 mA cm^{-2} pulse and 1.87–1.89 V vs. Zn/Zn^{2+} during pause (no current), showing that the OER two-phase zones between catalyst and electrolyte

were constant during operation and that product oxygen was effectively removed from the electrode's surface with the flowing electrolyte. The potential difference between charge and discharge of the air electrode (ΔV) was below 1.0 V for 700 cycles and even as low as 0.82 V after 200 cycles (depicted in Figure 2b), which corresponds to a voltage efficiency of 57% (air electrode only). A detailed list of the potentials and ΔV obtained with this cell is listed in Table S2 in the supporting information.

At the beginning of operation, zinc was pre-deposited by pulse charging onto the zinc electrode from the dissolved ZnO containing electrolyte (first inlet in Figure 1), and the procedure repeated from time to time to prevent zinc depletion over time. Nevertheless, after 1050 h of continuous operation, no zinc was left of the initial 4 cm^2 sized zinc plate, which is attributed to uneven current distribution during deposition, as well as unbalanced charge/discharge capacities^[11]. In consequence, a new, slightly larger sized (9 cm^2) zinc plate was mounted in the cell, resulting in smaller zinc overpotentials as can be seen in the 1400 h inlet in Figure 1. However, zinc dendrites were visibly growing on the edges of the new zinc electrode, whereas the middle, directly opposite the air electrode, was slowly depleted. There were no short-circuits because of the distance of 2 cm between air and zinc electrode. As the small flow cell set-up was open on the top, repeated renewing of the zinc electrode without complete disassembly of the cell was possible.

Regarding the air electrode, its surface exhibited initially high hydrophobicity, so that it was kept in electrolyte for 1 h prior to operation. Nevertheless, an "activation" behavior was visible within the first 50 h of operation as can be seen in the first inlet of Figure 1 and in Figure 2. The separate referencing of air, zinc and cell potentials allowed for better attribution of the effects occurring within the cell. For example, the cell voltage often decreased within one discharge cycle, which can rather be ascribed to increasing zinc electrode potential than to the air electrode, which in fact, exhibited slightly improving ORR potential within the 1 h discharge during each cycle.

After about 400 h of operation the electrolyte had a slightly orange color, indicating carbon corrosion to a certain degree^[10], but no further change of color was observed thereafter (see image in the supporting information Figure S9). Also, inwards bulging of the air electrode caused by the 10–15 mbar pressure from the immersed gas exhaust became apparent over time, leading to small electrolyte leakage between electrode's edges and the softened polymeric sealing after about 750 h (shown in Figure S1 in the supporting information). Initially, small droplets were taken out with the air flow, however, after 1000 h of operation the effect became more pronounced. In combination with slowly declining hydrophobicity, this resulted finally in decreasing discharge performance with the ORR potential dropping below 1.0 V after 1250 h (560 cycles) and to the end of testing after 1800 h.

After 1800 h the air electrode was washed on both sides with pure KOH (with no ZnO) and with deionized water in order to

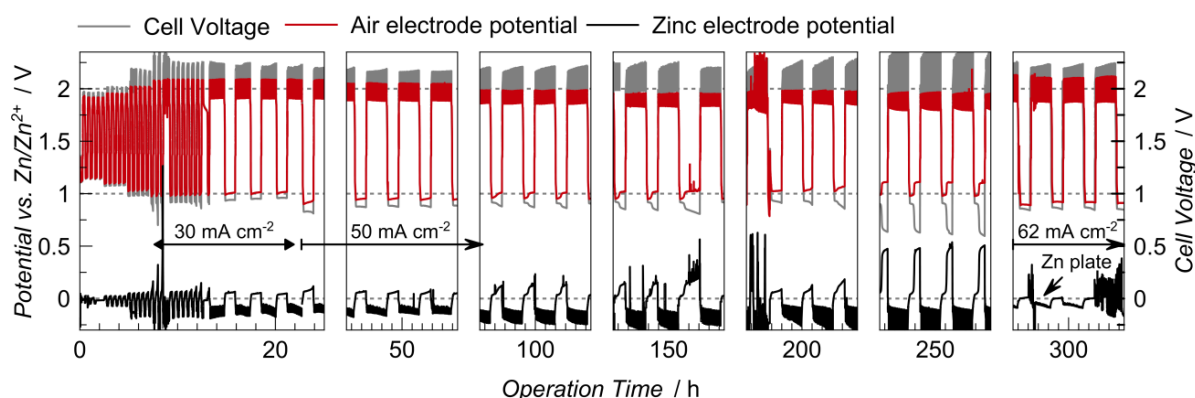


Figure 3. Electrochemical long-term charge/discharge cycling of a zinc-air flow cell with 50 cm^2 bifunctional air electrode (E2) operated at 50 mA cm^{-2} (air) with pulse charging (50 mA cm^{-2} pulse), actively supplied with air at RT and with flowing $8 \text{ M KOH} + 0.5 \text{ M ZnO}$ electrolyte (2 cm s^{-1} surface flow velocity).

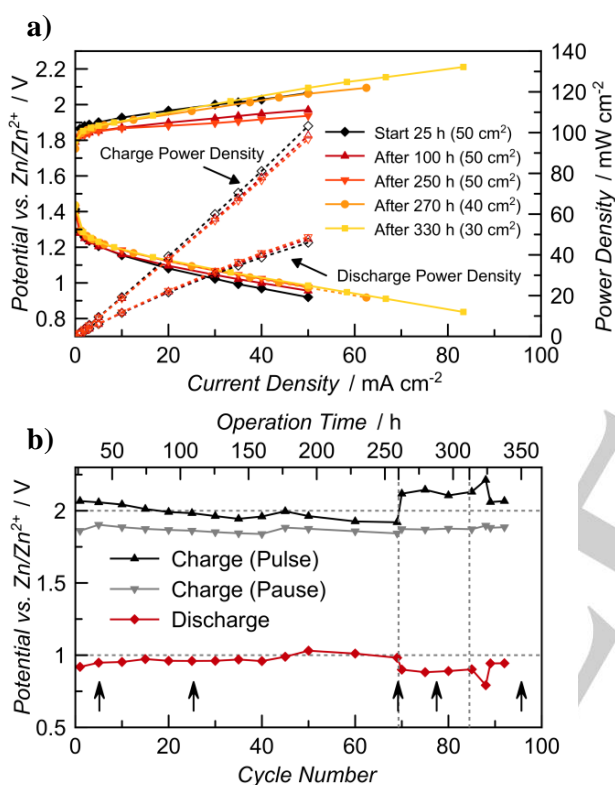


Figure 4. Characterization of 50 cm^2 air electrode E2 showing **a)** polarization curves measured for ORR and OER including the power density of the air electrode needed for charging and obtained during discharge (dashed lines) and **b)** maximum and minimum potentials during pulse charging (50 mA cm^{-2} pulse for 50 ms , 50 ms pause) and the ORR potentials (black arrows indicate the breaks for recording polarization curves and EIS, the dashed vertical lines the both times the cell had to be opened).

remove any precipitates (carbonates, ZnO , hydroxides^[34,35]) within the electrode. Although no crystallized deposits were visible, the high ORR performance was not restored by that procedure. This is mainly attributed to the degraded hydrophobicity of the electrode^[14] as shown in Figure 7.

Electrochemical Characterization of 50 cm^2 Air Electrode E2

In an up-scaled zinc-air flow cell set-up, a 50 cm^2 air electrode (E2) was mounted together with a $7 \times 8 \text{ cm}$ sized copper plate which was priorly coated with about 0.5 g of electrodeposited zinc in order to reduce the zinc corrosion problem encountered in the small cell and to prevent contact loss at the clamping. As in the small set-up, the cell voltage as well as both half-cell potentials were measured. The air electrode was actively supplied with air from a compressor and the air exhaust immersed in 15 cm of water. As a result of the smaller in- and outlets of this cell, only lower electrolyte flow rates of 2 cm s^{-1} were possible.

The result of the long-term cycling measurement of this zinc-air flow cell employing E2 is shown in Figure 3 and the course of the air electrode potentials in Figure 4b. Because of the current restrictions of the potentiostat, the pulse charging was - compared to E1 - performed at half the current density (50 mA cm^{-2} pulse) but double the time length (2 h instead of 1 h ; 3 h overall cycle length). The successfully up-scaled zinc-air flow battery was operated for 320 h (92 cycles). Similar performances to the small E1 cell were obtained, as a comparison of the two 100 h inlets of Figure 1 and Figure 3 shows. E2 also exhibited the same "activation" effect with gradually improving performance at the beginning of operation. As shown in the first inlet of Figure 3, within the first 10 h of the measurement the current density was slowly increased up to 30 mA cm^{-2} (20 min cycles) in order to minimize degradation effects by uneven current distributions. Only after that it was raised to 50 mA cm^{-2} . After the first 50 h of operation, the potential course of the air electrode shows similar charge/discharge potentials as E1 with the ORR at $\sim 1.0 \text{ V}$ and the pulse charging $< 2.0 \text{ V vs. Zn/Zn}^{2+}$ as depicted in Figure 4b.

To gain further insight into the mechanisms within the up-scaled cell, polarization curves (depicted in Figure 4a) as well as impedance spectra (Figure 5 and Figure 6) were recorded. In the polarization curves the ORR and OER kinetic activation region up to 5 mA cm^{-2} and the linear ohmic region are visible.

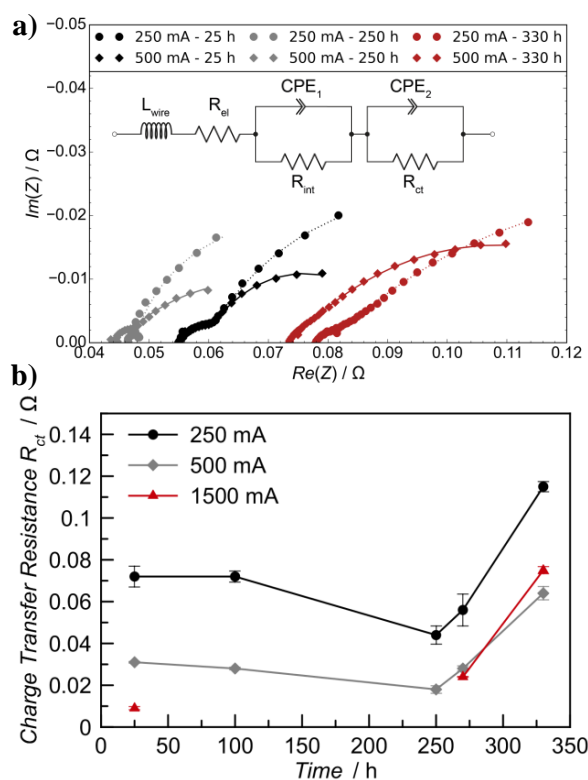


Figure 5. EIS measurements at OER of 50 cm² air electrode E2 showing **a)** Nyquist plots at different currents (● 250 mA, ◆ 500 mA, — 25 h, — 250 h, — 330 h). The different electrolyte resistances arise due to the replacement of the copper plate with a zinc plate. At the top the equivalent circuit used for fitting the OER and ORR spectra, respectively, is pictured. The line plots are the fitting results of the equivalent circuit (see Table S4 in supporting information). **b)** The trend of the charge transfer resistance R_{ct} at different currents and times (● 250 mA, ◆ 500 mA, ▲ 1500 mA).

The corresponding power densities show the very high losses caused by the overpotentials of ORR and OER. Double the charging power is required as is regained during discharge. Further potentials values and ΔV of the polarization curves are listed in Table S3 in the supporting information.

Electrochemical impedance spectroscopy (EIS), shown in Figure 5 for OER and Figure 6 for ORR, revealed that the charge transfer resistance, R_{ct} , which represents the kinetics of the OER and ORR, respectively^[36–39], followed the same behavior as the overpotentials and the trend of the potentials depicted in Figure 4. In case of OER, R_{ct} slightly decreased within the first 250 h (see Figure 5b), which indicates that the kinetics of the OER was improved and therefore the overpotential dropped. Reasons can be the good transport of product water away from the air electrode, through the still very hydrophobic structure. Because of the improved wetting within the electrode, more active sites at the catalyst were available^[38]. This corresponds well with the decreasing ΔV measured for E2 within this 250 h as depicted in Figure 4b. Further interpretation of the EIS data can be found in the supporting information in Figures S3–S6 and Tables S4 and S5.

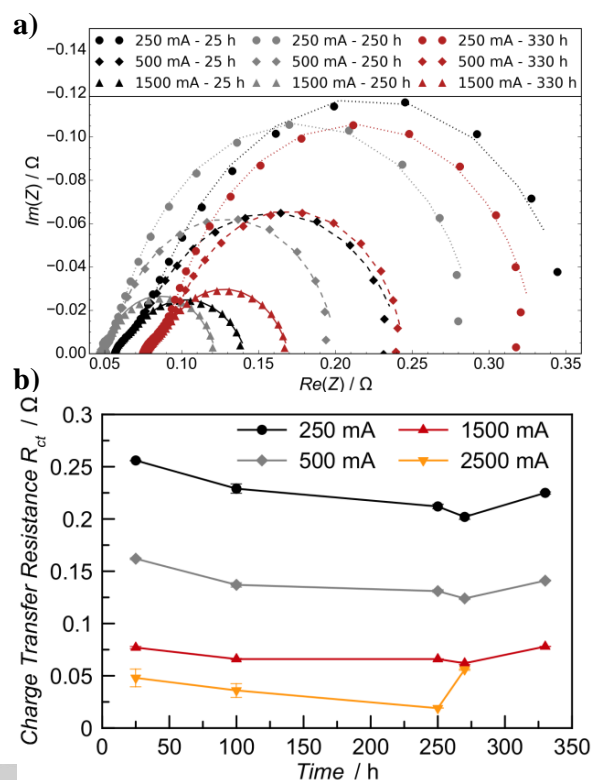


Figure 6. EIS measurements at ORR of 50 cm² air electrode E2 showing **a)** Nyquist plots at different currents (● 250 mA, ◆ 500 mA, ▲ 1500 mA, — 25 h, — 250 h, — 330 h, fitting results in Table S5 in supporting information) and **b)** the trend of the R_{ct} at different times and currents (● 250 mA, ◆ 500 mA, ▲ 1500 mA, ▼ 2500 mA).

Due to the long recording times and the applied constant charging current (no pulse charging) during the measurement of the polarization curves (~ 2 h) as well as the EIS (~ 5 h) each time, the zinc deposited unevenly on the copper current collector plate, which resulted in ever higher overpotentials after 100 h (visible in Figure 3 between 50–250 h). In consequence, copper was open to electrolyte and an oxidation peak on the zinc electrode and a reduction peak on the air electrode side became more and more apparent, which is attributed to Cu oxidation and reduction in the highly alkaline media resulting in mixed potentials^[40–42]. The effect became so pronounced (see 250 h inlet in Figure 3) that the cell had to be completely disassembled (see image in Figure S2 in the supporting information) and a new zinc plate (7 x 8 cm) was implemented. Thereby the air electrode was slightly damaged but could be resealed (new surface area 40 cm²).

After reassembly the measurements were continued but although the ORR performance stayed the same the charging potential significantly increased. EIS confirmed a significant increase of R_{ct} after reassembly, as depicted in the Figure 5b, resulting in slower kinetics of the OER and higher overpotentials. This behavior can be attributed to residual hydroxides, ZnO and carbonates precipitated in the emptied cell during maintenance

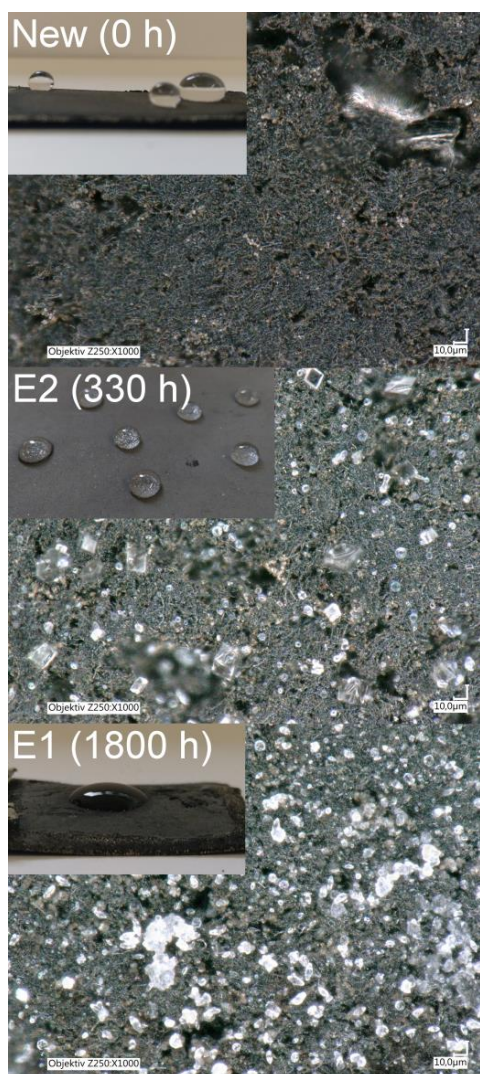


Figure 7. Light microscopy images and photographs (left upper corners) of the electrolyte facing side of a new electrode and E2 and E1 after operation depicting the change in hydrophobicity. Also, ZnO and electrolyte residues, which could not be completely removed by washing, are visible as white deposits. Images of the air supplied side are shown in Figure S7 in the supporting information.

as a drying period after resealing was necessary^[43]. Looking at R_{ct} of the ORR, it is also in good accordance with the results presented in Figure 4. Within the first 250 h values of R_{ct} were nearly unchanged, but after disassembly the resistance increased like in the OER case (see Figure 6b). These results support the hypothesis that precipitates are the cause for the lack of performance at the end as the maintenance interval severely disrupted the balance within the air electrode. After 312 h, due to problems with the zinc half-cell potential measurement, a second disassembly and reassembly was done whereby the sealing around the air electrode had to be renewed, which reduced the open area to 30 cm². A last set of polarization curves and impedance spectra were recorded, but because of

zinc deposits on the Luggin capillary as well as leakages at the edges of the air electrode including dry-out at the gas inlet as shown in supporting information Figure S9, the measurement was stopped.

The aforementioned changes in hydrophobicity over the course of long-term operation are also visible in Figure 7, where three light microscopy images and three photographs of a new electrode, of E2 after 330 h of operation and of E1 after 1800 h of operation are shown. It is clear that the hydrophobicity gradually decreases although the structure of the electrode does not appear to be altered significantly. Whereas the electrolyte droplets readily beaded off the new electrode, the droplets on E2 – although still defined after 320 h of operation – already slightly soaked into the electrode. After 1800 h of operation (E1), the soaking effect is most severe, while the fine structure of the carbon fibers appears primarily unchanged. On perovskite as well as carbon-based catalysts the ORR proceeds to some degree via the two electron pathway, whereby H₂O₂ is formed as the intermediate product^[10,21,24]. A reason for PTFE degradation can hence be attributed to H₂O₂ or HO[•] radical attack of the F-C chain, an effect known from PEM fuel cells^[44,45].

Electrochemical Characterization of 55 cm² Air Electrode E3

As the constant charging currents during recording of polarization curves and electrochemical impedance spectra resulted in unstable zinc potentials, a new air electrode (E3; 55 cm² sized) was mounted in the up-scaled flow set-up. As zinc electrode, a new zinc plate was utilized with a copper current collector soldered on the backside of the plate. The continuous long-term cycling measurement of the zinc-air cell with air electrode E3 at increasing current densities is depicted in Figure 8, showing stable cell voltages as well as half-cell potentials over a duration of 130 h and 48 cycles. The obtained air electrode performance during pulse charging and discharge is comparable to E1 and E2 and even after 120 h a slight improvement in the air electrode's performance was observed as summarized in Table 1. In contrast to this, the zinc electrode showed increasing overpotentials over time, which can be attributed to uneven zinc deposition over the whole zinc plate surface area with agglomeration of zinc on the lower part. This was probably caused by the lower flow rates of 2 cm s⁻¹. Higher flow-rates as used in the small set-up are thus preferable and can result in a prolonged cycle life of the zinc electrode.

After 130 h the measurement was stopped for a few days but restarting of the cell was prevented by too severe zinc corrosion and thus leakage of the cell on the side of the zinc electrode (probably accelerated by corrosion currents between zinc and copper current collector). Nevertheless, very good and stable potentials for the bifunctional air electrode were obtained even at high current densities of 50 mA cm⁻², showing the feasibility of the manufacturing process for larger-sized electrodes. The high catalytic activity toward ORR/OER of the La_{0.6}Sr_{0.4}Co_{0.2}Fe_{0.8}O₃ perovskite could be successfully transferred from the small electrode to over ten times larger sized electrodes (i.e. 50 – 55 cm²).

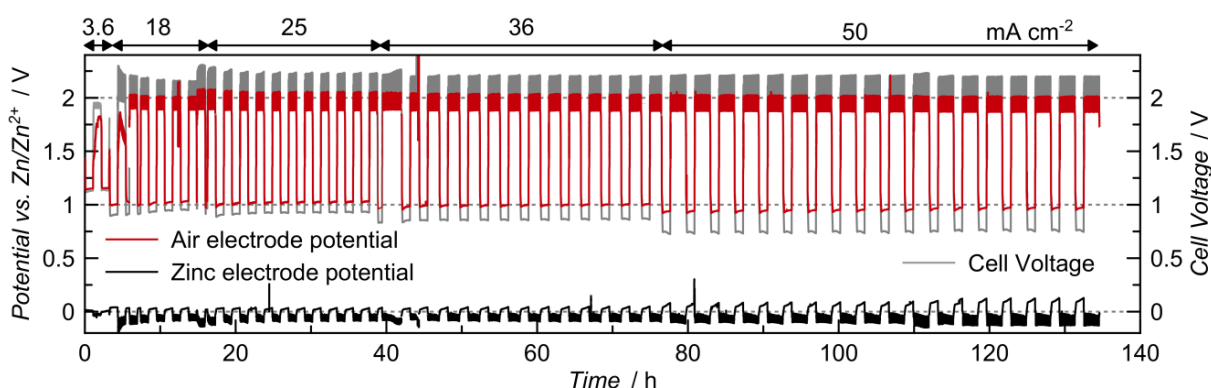


Figure 8. Electrochemical long-term charge/discharge cycling of a zinc-air flow cell with 55 cm² bifunctional air electrode (E3) operated up to 50 mA cm⁻²(air) with pulse charging (50 mA cm⁻² pulse), actively supplied with air at RT and with flowing 8 M KOH + 0.5 M ZnO electrolyte (2 cm s⁻¹ surface flow velocity). Fluctuations within the first 5 h of operation were caused by slight blockage of the air electrode's Luggin capillary.

Table 1. Potentials obtained during long-term charge/discharge cycling up to 50 mA cm⁻² discharge of the zinc-air flow cell with 55 cm² air electrode E3.

| | Potentials at 25 mA cm ⁻² (37 h) / V | | | Potentials at 36 mA cm ⁻² (75 h) / V | | | Potentials at 50 mA cm ⁻² (132 h) / V | | |
|------------------------------|----------------------------------------------------|------|-------------|----------------------------------------------------|------|-------------|-----------------------------------------------------|------|-------------|
| | OER ^[a] | ORR | ΔV | OER ^[a] | ORR | ΔV | OER ^[a] | ORR | ΔV |
| Cell Voltage | 2.10 | 0.93 | 1.17 | 2.08 | 0.86 | 1.22 | 2.07 | 0.75 | 1.32 |
| Air vs. Zn/Zn ²⁺ | 1.97 | 1.04 | 0.93 | 1.95 | 1.01 | 0.94 | 1.94 | 0.97 | 0.97 |
| Zinc vs. Zn/Zn ²⁺ | -0.06 | 0.03 | 0.09 | -0.06 | 0.05 | 0.11 | -0.08 | 0.13 | 0.21 |

[a] Mean value between pulse potential and pause potential (duty cycle $\gamma = 0.5$)

Conclusions

In this work, long-term operation of bifunctional air electrodes catalyzed with highly stable La_{0.6}Sr_{0.4}Co_{0.2}Fe_{0.8}O₃ perovskite were demonstrated for application in stationary zinc-air flow batteries. In a small set-up of 4 cm² a durability of 1000 h and an overall operation time of 1800 h with high voltage efficiencies of the air electrode of >50% at 50 mA cm⁻² over 700 cycles were achieved. The scale-up of the air electrode was successfully performed, and 50 and 55 cm² air electrodes were operated in an up-scaled flow set-up for 320 h and 130 h, respectively. They achieved similar charge and discharge performances and the same characteristic trends were observed in the small and in the bigger cell, respectively. Thereby, separate referencing of the half-cell as well as the cell potentials was essential for distinguishing the effects within the cell. Electrochemical impedance spectroscopy of the air electrode was applied for obtaining knowledge of the mechanisms within the electrode, whereby two distinctive processes could be distinguished. One is attributed to the interface of the solid to the electrolyte; the other one is related to the kinetics of the overall OER or ORR reaction. Looking closer at the latter, the charge transfer resistance for ORR and OER, respectively, decreased slightly

within the first 250 h of operation, leading to a better performance of the battery and to lower overpotentials. This can be attributed to a slowly changing hydrophobicity and thus an improved wetting of the electrode. After disassembly, the charge transfer resistance for ORR and OER increased significantly probably because of precipitation of ZnCO₃ or ZnO within the electrode during the maintenance, leading to a weak performance and to higher overpotentials.

Regarding end-of-life, especially of the small air electrode, changes in hydrophobicity primarily on the electrolyte facing side by PTFE degradation^[10] was found to be the main cause of initially slowly improving (about first 50 h) but then gradually decreasing ORR performance. Because of the rather low charging potentials of below 2.0 V, carbon corrosion was minimized in this current density range as the nearly colorless electrolyte proved and also the catalyst itself exhibited high stability throughout repeated cycling in this broad potential range. Thus, further optimization has to be tackled in regard to the hydrophobic binder material.

The zinc-air flow cell is a highly sensitive cell system, where the operation conditions have to be selected carefully and the disruption through, for example, maintenance minimized. Although many problems could be suppressed with flowing

electrolyte, inhomogeneous zinc morphology proved to be a major challenge, especially in the up-scaled cell under the conditions of long-term operation of a few hundred hours. This work mainly focused on the optimization of the air electrode, however, for further studies investigations on improving the zinc electrode have to be done by applying the methods, which were recently summarized by Mainar et al.^[35] and Turney et al.^[46]. Changing to a horizontal flow set-up^[14,17] is another way to tackle some of these issues. In addition, electrochemical engineering becomes more and more important the larger the unit-cell^[5], and is especially important when operating a stack. Changes in electrolyte conductivity and density have to be monitored^[47–49] and maintenance intervals minimized in order to circumvent the issues related to dry-out and sealing of the cell, which were the main cause of decreasing performance of the larger-sized air electrodes.

Experimental Section

All chemicals were used as purchased without further purification. Commercial $\text{La}_{0.6}\text{Sr}_{0.4}\text{Co}_{0.2}\text{Fe}_{0.8}\text{O}_3$ perovskite (LSCF; surface area $10 - 14 \text{ m}^2 \text{ g}^{-1}$, size $d_{50} = 0.4 - 0.8 \mu\text{m}$; Sigma-Aldrich) was homogeneously dispersed on carbon nanofibers (CNF; HTF150FF-LHT (lowheat), 70–150 nm diameter, $> 10 \mu\text{m}$ length, heat-treated at $1000 \text{ }^\circ\text{C}$, resistance $< 10^{-3} \Omega \text{ cm}^{-1}$, metal impurities $< 0.5 \text{ wt}\%$, N_2 specific surface area $43 \text{ m}^2 \text{ g}^{-1}$, Electrovac AG, Austria) in a weight ratio of 3:1 in ultra-pure water/2-propanol 1:1 (200 mL for 5 g of LSCF/CNF) for 1 h using an ultrasonic probe (UP400S; Hielscher, Germany). The solvent was slowly evaporated at $80 \text{ }^\circ\text{C}$ under vigorous stirring and the dry powder ground in a mortar (see SEM images in Figure S8 in the supporting information). Two separate electrode pastes were prepared using about 1–1.5 g per 25 cm^2 electrode area. Paste one contained 45 wt% LSCF/CNF, 40 wt% Ni powder (Type 255, 2.2–2.8 μm particle size; Novamet Specialty Products Corp., USA) and 15 wt% PTFE (Dispersion TF5135 GZ; 58 wt%, 5.5 wt% emulsifier, 190 nm; 3M Dyneon) and paste two 85 wt% LSCF/CNF and 15 wt% PTFE. The pastes were separately mixed in ultra-pure water/2-propanol 1:1 (about 10 mL per g paste) until a dough-like consistency was obtained. They were spread on opposite sides of nickel foam (thickness 1.6 mm, pore size 450 μm , area density 420 g m^{-2} ; Alantum Corporation, Germany), dried overnight and sinter-pressed at 150 kg cm^{-2} for 20 min at $300 \text{ }^\circ\text{C}$. The final catalyst loading was about 40 mg cm^{-2} LSCF.

Electrochemical characterization was performed using a custom-made vertical flow-cell set-up with a DC centrifugal pump (WPDC-02.5L-1.00M-12-VP; Rotek, Austria) with either a 0.5 L or 1 L electrolyte reservoir for the 4 cm^2 cell (E1) or the 50 cm^2 (E2) / 55 cm^2 (E3) cell, respectively. As electrolyte 8 M KOH ($> 85\%$ pellets; Carl Roth GmbH+Co.KG) with 0.5 M ZnO (99.99%; Alfa Aesar) was utilized, which was pumped from bottom to top with an electrode surface flow velocity of 8 cm s^{-1} in the small set-up and 2 cm s^{-1} in the big set-up. Assuming zincate concentrations of 0.5 M (discharged) and 0.2 M charged, this cell has a nominal capacity of about 16 Ah (see calculations in the supporting information). The air electrodes were always operated in three-electrode mode using the air electrode as working electrode, a zinc plate (E1 and E3) or zinc-plated copper plate (E2) as counter electrode and a zinc foil (1.6 mm thickness, AlfaAesar) as reference electrode, which was mounted in front of the air electrode via a Luggin capillary. In addition, the cell voltage between zinc and air electrode as well as the zinc electrode potential via a second zinc foil reference Luggin capillary set in front of the zinc electrode, were recorded. The distance between air and zinc electrode was in both set-

ups 2 cm. All current densities mentioned in this work are in respect to the open surface area of the air electrode to the electrolyte. The backside of the electrode was actively supplied with air from a compressor (25 mL min^{-1} for the 4 cm^2 and 350 mL min^{-1} for 50 cm^2 / 55 cm^2 sized electrode). It contained ambient CO_2 and was not humidified. The gas exhaust was immersed in 10–15 cm of water to counter the hydrostatic pressure of the electrolyte. For more details, images of the cells and the set-up can be found in the supporting information (Figure S1 and Figure S2).

Cycling experiments for the 4 cm^2 electrode E1 comprised 1 h charge and 1 h discharge (2 h per cycle) performed with a BaSyTec Cell Test System (CTS Lab) with corresponding software at 50 mA cm^{-2} (mean) with additional pulse charging at 100 mA cm^{-2} during a 50 ms pulse and no current during 50 ms pause (duty cycle $\gamma = 0.5$, 36,000 pulses per hour). Because of the current restriction of 3 A of the potentiostat the pulse charging times were prolonged for the larger sized electrodes accordingly to match the discharge capacity of 1 h (for example 2 h pulse charging at 25 mA cm^{-2} (mean) with 50 mA cm^{-2} pulses with $\gamma = 0.5$, then 1 h discharge at 50 mA cm^{-2}). Polarization curves were recorded in galvanostatic mode with 5 min steps. Electrochemical impedance spectroscopy was performed in three-electrode mode with the air electrode as working electrode on an IM6ex and a PP240 potentiostat (Zahner Elektrik) between 50 mHz and 10 kHz at 250 mA, 500 mA and 1500 mA for OER and -250 mA, -500 mA, -1500 mA and -2500 mA for ORR (three impedance measurements at each step) with amplitudes of 50–200 mA. For E2 the currents during EIS were kept the same although the surface area of the air electrode was decreased from 50 cm^2 to 40 and 30 cm^2 . Light microscopy was performed on a Keyence VHX-S500E.

Acknowledgements

Funding by the Austrian Federal Ministry of Transport, Innovation and Technology (BMVIT) and The Austrian Research Promotion Agency (FFG) through the program “e!MISSION.at Energieforschungsprogramm” (No. 848933) is gratefully acknowledged. We also want to thank our cooperation partners from the Institute of Chemistry and Technology of Materials at Graz University of Technology and our industry partners VARTA Micro Innovation GmbH (Austria). Special thanks go to our cooperation partner Hans-Jürgen Pauling from the German company RECAT GmbH for developing and providing the large-scale test cell.

Keywords: zinc-air flow battery • bifunctional air electrode • $\text{La}_{0.6}\text{Sr}_{0.4}\text{Co}_{0.2}\text{Fe}_{0.8}\text{O}_3$ perovskite • oxygen reduction reaction • oxygen evolution reaction

- [1] P. Alotto, M. Guarnieri, F. Moro, *Renew. Sustain. Energy Rev.* **2014**, *29*, 325–335.
- [2] J. Cho, S. Jeong, Y. Kim, *Prog. Energy Combust. Sci.* **2015**, *48*, 84–101.
- [3] G. L. Kyriakopoulos, G. Arabatzi, *Renew. Sustain. Energy Rev.* **2016**, *56*, 1044–1067.
- [4] L. F. Arenas, A. Loh, D. P. Trudgeon, X. Li, C. Ponce de León, F. C. Walsh, *Renew. Sustain. Energy Rev.* **2018**, *90*, 992–1016.
- [5] L. F. Arenas, C. Ponce de León, F. C. Walsh, *J. Energy Storage* **2017**, *11*, 119–153.

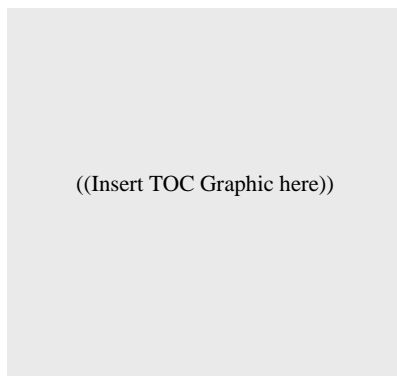
- [6] B. R. Chalamala, T. Soundappan, G. R. Fisher, M. R. Anstey, V. V. Viswanathan, M. L. Perry, *Proc. IEEE* **2014**, *102*, 1–24.
- [7] A. Khor, P. Leung, M. R. Mohamed, C. Flox, Q. Xu, L. An, R. G. A. Wills, J. R. Morante, A. A. Shah, *Mater. Today Energy* **2018**, *8*, 80–108.
- [8] P. K. Leung, T. Martin, A. A. Shah, M. R. Mohamed, M. A. Anderson, J. Palma, *J. Power Sources* **2017**, *341*, 36–45.
- [9] M. Park, J. Ryu, W. Wang, J. Cho, *Nat. Rev. Mater.* **2017**, *2*, 16080.
- [10] E. Davari, D. G. Ivey, *Sustain. Energy Fuels* **2018**, *2*, 39–67.
- [11] J. Fu, Z. P. Cano, M. G. Park, A. Yu, M. Fowler, Z. Chen, *Adv. Mater.* **2017**, *29*, 1604685.
- [12] X. Han, X. Li, J. White, C. Zhong, Y. Deng, W. Hu, T. Ma, *Adv. Energy Mater.* **2018**, *8*, 1801396.
- [13] J. Pan, Y. Y. Xu, H. Yang, Z. Dong, H. Liu, B. Y. Xia, *Adv. Sci.* **2018**, *5*, 1700691.
- [14] P. Pei, K. Wang, Z. Ma, *Appl. Energy* **2014**, *128*, 315–324.
- [15] M. Xu, D. G. Ivey, Z. Xie, W. Qu, *J. Power Sources* **2015**, *283*, 358–371.
- [16] B. Amunátegui, A. Ibáñez, M. Sierra, M. Pérez, *J. Appl. Electrochem.* **2018**, *48*, 627–637.
- [17] M. Bockelmann, U. Kunz, T. Turek, *Electrochem. commun.* **2016**, *69*, 24–27.
- [18] Y. Li, M. Gong, Y. Liang, J. Feng, J.-E. Kim, H. Wang, G. Hong, B. Zhang, H. Dai, *Nat. Commun.* **2013**, *4*, 1805.
- [19] W. T. Hong, M. Risch, K. A. Stoerzinger, A. Grimaud, J. Suntivich, Y. Shao-Horn, *Energy Environ. Sci.* **2015**, *8*, 1404–1427.
- [20] D. Pletcher, X. Li, S. W. T. Price, A. E. Russell, T. Sönmez, S. J. Thompson, *Electrochim. Acta* **2016**, *188*, 286–293.
- [21] D. Chen, C. Chen, Z. M. Baiyee, Z. Shao, F. Ciucci, *Chem. Rev.* **2015**, *115*, 9869–9921.
- [22] K. Elumeeva, J. Masa, J. Sierau, F. Tietz, M. Muhler, W. Schuhmann, *Electrochim. Acta* **2016**, *208*, 25–32.
- [23] J.-I. Jung, M. Risch, S. Park, M. G. Kim, G. Nam, H.-Y. Jeong, Y. Shao-Horn, J. Cho, *Energy Environ. Sci.* **2016**, *9*, 176–183.
- [24] Y. Zhu, W. Zhou, Z. Shao, *Small* **2017**, *13*, 1603793.
- [25] S. Müller, O. Haas, C. Schlatter, C. Comninellis, S. Mu, *J. Appl. Electrochem.* **1998**, *28*, 305–310.
- [26] J. Pan, L. Ji, Y. Sun, P. Wan, J. Cheng, Y. Yang, M. Fan, *Electrochem. commun.* **2009**, *11*, 2191–2194.
- [27] K. Wang, P. Pei, Y. Wang, C. Liao, W. Wang, S. Huang, *Appl. Energy* **2018**, *225*, 848–856.
- [28] H. E. Lin, C. H. Ho, C. Y. Lee, *Surf. Coatings Technol.* **2017**, *319*, 378–385.
- [29] B. Pichler, B. S. Berner, N. Rauch, C. Zelger, H. J. Pauling, B. Gollas, V. Hacker, *J. Appl. Electrochem.* **2018**, *48*, 1–14.
- [30] C. Zelger, J. Laumen, A. Laskos, B. Gollas, *Electrochim. Acta* **2016**, *213*, 208–216.
- [31] Z. P. Cano, M. G. Park, D. U. Lee, J. Fu, H. Liu, M. W. Fowler, Z. Chen, *J. Phys. Chem. C* **2018**, *122*, acs.jpcc.8b06243.
- [32] B. Pichler, S. Weinberger, L. Reščec, I. Grimmer, F. Gebetsroither, B. Bitschnau, V. Hacker, *Electrochim. Acta* **2017**, *251*, 488–497.
- [33] X. Li, D. Pletcher, A. E. Russell, F. C. Walsh, R. G. A. Wills, S. F. Gorman, S. W. T. Price, S. J. Thompson, *Electrochem. commun.* **2013**, *34*, 228–230.
- [34] J.-F. Drillet, F. Holzer, T. Kallis, S. Müller, V. M. Schmidt, *Phys. Chem. Chem. Phys.* **2001**, *3*, 368–371.
- [35] A. R. Mainar, L. C. Colmenares, J. A. Blázquez, I. Urdampilleta, *Int. J. Energy Res.* **2018**, *42*, 903–918.
- [36] D. U. Lee, J. Y. Choi, K. Feng, H. W. Park, Z. Chen, *Adv. Energy Mater.* **2014**, *4*, DOI 10.1002/aenm.201301389.
- [37] D. Thiele, A. Züttel, *J. Power Sources* **2008**, *183*, 590–594.
- [38] Z. Chen, A. Yu, D. Higgins, H. Li, H. Wang, Z. Chen, *Nano Lett.* **2012**, *12*, 1946–1952.
- [39] H. Arai, S. Müller, O. Haas, *J. Electrochem. Soc.* **2000**, *147*, 3584.
- [40] S. Dong, Y. Xie, G. Cheng, *Electrochim. Acta* **1992**, *37*, 17–22.
- [41] W. Z. Le, Y. Q. Liu, *Sensors Actuators, B Chem.* **2009**, *141*, 147–153.
- [42] W. Z. Teo, A. Ambrosi, M. Pumera, *Electrochem. commun.* **2013**, *28*, 51–53.
- [43] M. Prabu, P. Ramakrishnan, H. Nara, T. Momma, T. Osaka, S. Shanmugam, *ACS Appl. Mater. Interfaces* **2014**, *6*, 16545–16555.
- [44] R. Borup, J. Meyers, B. Pivovar, Y. S. Kim, R. Mukundan, N. Garland, D. Myers, M. Wilson, F. Garzon, D. Wood, et al., *Chem. Rev.* **2007**, *107*, 3904–3951.
- [45] C. Zhou, M. A. Guerra, Z. M. Qiu, T. A. Zawodzinski, D. A. Schiraldi, *Macromolecules* **2007**, *40*, 8695–8707.
- [46] D. E. Turney, J. W. Gallaway, G. G. Yadav, R. Ramirez, M. Nyce, S. Banerjee, Y. C. K. Chen-Wiegart, J. Wang, M. J. D'Ambrose, S. Kolhekar, et al., *Chem. Mater.* **2017**, *29*, 4819–4832.
- [47] R. J. Gilliam, J. W. Graydon, D. W. Kirk, S. J. Thorpe, *Int. J. Hydrogen Energy* **2007**, *32*, 359–364.
- [48] Aleksandra Gavrilović-Wohlmuther, Andreas Laskos, Christian Zelger, Bernhard Gollas, Adam Harding Whitehead, *J. Energy Power Eng.* **2015**, *9*, 1019–1028.
- [49] G. Li, K. Zhang, M. A. Mezaal, R. Zhang, L. Lei, *Int. J. Electrochem. Sci.* **2015**, *10*, 6672–6683.

Entry for the Table of Contents (Please choose one layout)

Layout 1:

ARTICLE

Text for Table of Contents



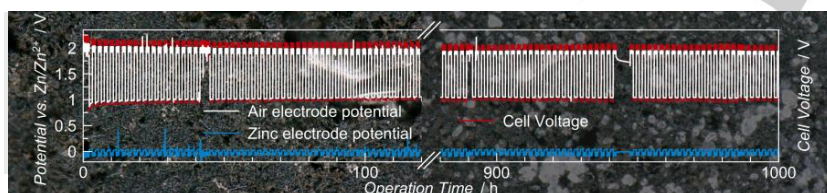
Author(s), Corresponding Author(s)*

Page No. – Page No.

Title

Layout 2:

ARTICLE



Birgit Pichler, Kurt Mayer, Viktor Hacker*

Page No. – Page No.

Long-term Operation of Perovskite-catalyzed Bifunctional Air Electrodes in Rechargeable Zinc-Air Flow Batteries

One more cycle: $\text{La}_{0.6}\text{Sr}_{0.4}\text{Co}_{0.2}\text{Fe}_{0.8}\text{O}_3$ perovskite is implemented as highly active bifunctional catalyst in optimized air electrode architecture and reaches 1000 h (500 cycles) of stable performance at 50 mA cm^{-2} (see picture). Up-scaled 50 cm^2 -sized zinc-air cells are investigated by means of electrochemical impedance spectroscopy and operated for 300 h. Loss of hydrophobicity is found to be the main reason for slowly decreasing performance of the air electrode.

Table S1 List of zinc-air batteries or bifunctional air electrodes tested at $\geq 50 \text{ mA cm}^{-2}$ or with flowing electrolyte reported in literature.

| Catalyst | Mode | CD ¹ / mA cm ⁻² | Size ² / cm ² | Time / h | Cycles | Charge ³ / V | Discharge ³ / V | Supply | Ref. |
|--------------------------------------------------------------------------------------------|--------------------|------------------------------------------|----------------------------------------|-------------|--------|----------------------------|-------------------------------|----------------|------|
| Fe/N/C and Ni | tri (flow) | 50 | 9 | 100 | 24 | ~2.2 | ~1 | air | [1] |
| CoO/N-CNT and NiFe LDH | tri | 50 | 1 | 40 | 10 | ~2.05 | ~1.19 | O ₂ | [2] |
| NiCo ₂ O ₄ -CNT | bi | 50 | 4 | 55 | 339 | ~2.3 | ~1 V | air | [3] |
| Histidine- derived Fe ₃ C NPs | tri | 50 | N/A | 30 | 27 | ~2.6 | ~1.2 | O ₂ | [4] |
| Co ₃ O ₄ /MnO ₂ - CNTs | bi | 100 | 4 | 20 | 2.5 | ~2.1 | ~1 | air | [5] |
| La ₂ O ₃ /Co ₃ O ₄ / MnO ₂ -CNTs | bi | 50 | 4 | 21 | 21 | ~2.2 | ~1.05 | air | [6] |
| Ni ₃ FeN/Co, N-CNF | bi | 50 | < 1 | 136 | ~ 70 | ~2.2 | ~0.8 | air | [7] |
| N-GCNT/ FeCo | bi | 120 | 1 | 40 | 240 | 2.25 | 0.73 | air | [8] |
| La _{0.6} Ca _{0.4} Co _{0.2} Fe _{0.8} O ₃ | Half cell (bi) | 100 | N/A | 80 | 240 | ~1.85 | ~0.8 | synth. air | [9] |
| La _{0.6} Ca _{0.4} CoO ₃ | Half cell (bi) | 50 | 1 | 300 | 100 | ~2 | ~1.1 | air | [10] |
| MnO ₂ and stainless steel | Half cell (tri) | 100 | ~30 ⁴ | 1000 | 500 | ~1.9 | ~1.1 | air | [11] |
| NiCo ₂ O ₄ | Half cell (bi) | 50 | 1.1 | 50 | 50 | ~1.95 | ~1.1 | O ₂ | [12] |
| Ag and Ni foam | tri (flow) | 20 | 5 | ~85 | 600 | ~2.5 | ~1.25 | O ₂ | [13] |
| MnO ₂ /NaBiO ₃ and Ni(OH) ₂ | tri (flow) | 20 | 22 | 750 | 150 | 1.78 | 1.32 | air | [14] |

¹ CD = current density; ² Size of air electrode open to gas/electrolyte; ³ Cell voltage or half-cell potential converted to vs. Zn/Zn²⁺; ⁴ Size of zinc electrode

Table S2 Potentials obtained during long-term charge/discharge cycling at 50 mA cm⁻² of the zinc-air flow cell with 4 cm² air electrode E1.

| | Potential after 10 h | | | Potential after 400 h | | | Potential after 1000 h | | | Potential after 1400 h | | |
|------------------------------|----------------------|------|-------------|-----------------------|------|-------------|------------------------|------|-------------|------------------------|------|-------------|
| | OER ¹ | ORR | ΔV | OER ¹ | ORR | ΔV | OER ¹ | ORR | ΔV | OER ¹ | ORR | ΔV |
| Cell Voltage | 2.05 | 0.91 | 1.14 | 1.99 | 1.00 | 0.99 | 1.97 | 0.96 | 1.01 | 1.95 | 0.90 | 1.05 |
| Air vs. Zn/Zn ²⁺ | 1.98 | 0.98 | 1.00 | 1.91 | 1.09 | 0.82 | 1.91 | 1.04 | 0.87 | 1.9 | 0.95 | 0.95 |
| Zinc vs. Zn/Zn ²⁺ | -0.05 | 0.04 | 0.09 | -0.05 | 0.05 | 0.10 | -0.04 | 0.04 | 0.08 | -0.01 | 0.02 | 0.03 |

¹ Mean value between pulse potential and pause potential (duty cycle $\gamma = 0.5$)

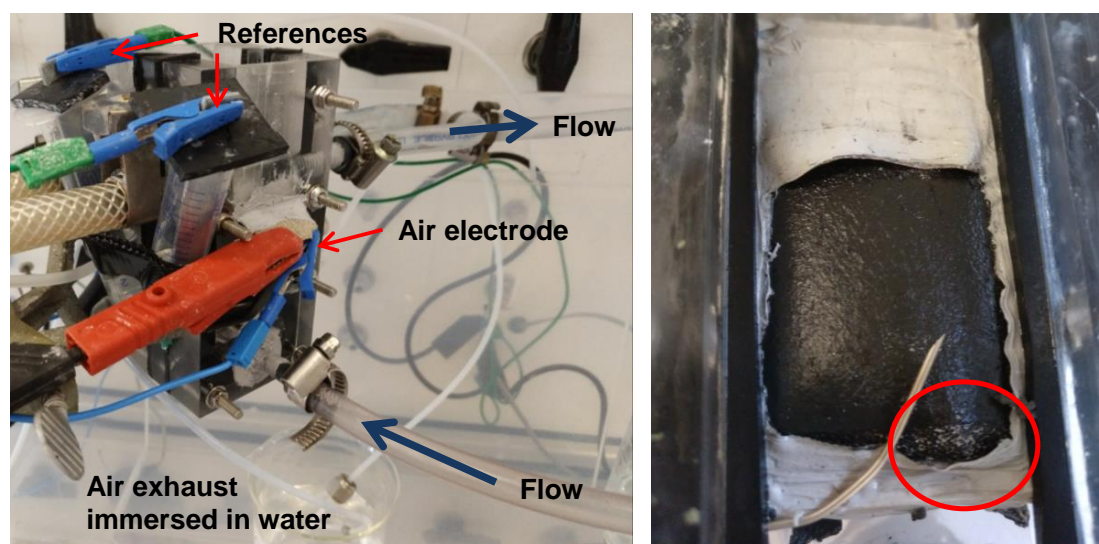


Figure S1 Unit cell zinc-air flow battery set-up for 4 cm² air electrode (left) and the bulged air electrode E1 (electrolyte side) after operation with the region marked where the electrolyte leakage occurred.

Table S3 List of the potential values obtained from the recorded polarization curves of the 50 cm² air electrode E2.

| Current Density / mA cm ⁻² | Potential after 25 h / V | | | Potential after 250 h / V | | |
|---------------------------------------|--------------------------|------|-------------|---------------------------|------|-------------|
| | OER | ORR | ΔV | OER | ORR | ΔV |
| 1 | 1.87 | 1.29 | 0.58 | 1.82 | 1.29 | 0.53 |
| 5 | 1.90 | 1.21 | 0.69 | 1.85 | 1.23 | 0.62 |
| 10 | 1.93 | 1.16 | 0.77 | 1.87 | 1.18 | 0.69 |
| 20 | 1.97 | 1.08 | 0.89 | 1.88 | 1.12 | 0.76 |
| 50 | 2.07 | 0.92 | 1.15 | 1.94 | 0.98 | 0.96 |

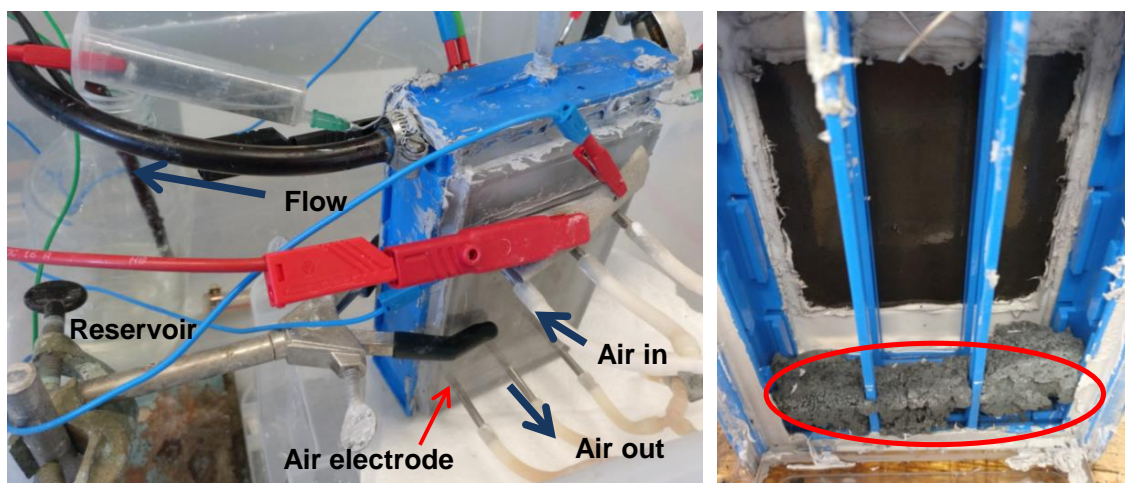


Figure S2 Unit cell zinc-air flow battery set-up for 50 cm² air electrode (left) and the air electrode E2 (electrolyte side) after first disassembly with the zinc deposit (red circle) on the bottom of the cell.

Electrochemical Impedance Spectroscopy (EIS)

EIS measurements were conducted in order to identify different processes inside a zinc-air battery during charging and discharging in regard to the air electrode. These investigations revealed that there are two distinctive processes due to the two semicircles shown in Nyquist plots at OER and ORR, respectively. Therefore, the equivalent circuit model used for simulating the Nyquist plots consists out of a resistance R_{el} , which is mostly composed of the electrolyte resistance but also contact resistances and the resistances of various components of the battery. In addition, two parallel circuits of resistance-constant phase elements (CPEs) are connected in series with R_{el} . The first smaller flattened semicircle in the high frequency spectrum resembles the interface resistance R_{int} from solid to electrolyte interface and the double layer capacitance between solid and electrolyte interface. The second much larger highly voltage dependent semicircle in the mid to low frequency region features the charge transfer resistance R_{ct} , which provides information of the kinetics of the overall ORR and OER reaction, respectively^[15–17]. In Figure S3 the equivalent circuit is presented.

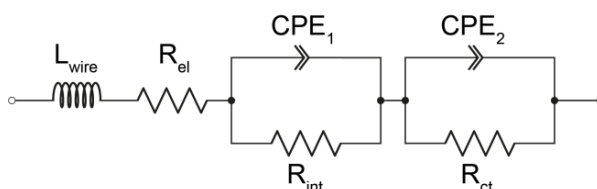


Figure S3 Equivalent circuit model of a zinc-air battery at OER and ORR. The inductance at the beginning has its seeds in the long cable lengths from the potentiostat to the battery and is not part of the battery itself.

Looking closer at the changes of R_{el} during operation (see Figure S4, Table S4 and S5), R_{el} decreased within the first 250 h. One possible reason is that the zinc covered copper plate gets more and more uncovered and therefore the resistance decreases as copper is a much better conductor than zinc. After 250 h a sharp increase in R_{el} could be observed due to the exchange of the copper plate to a zinc plate.

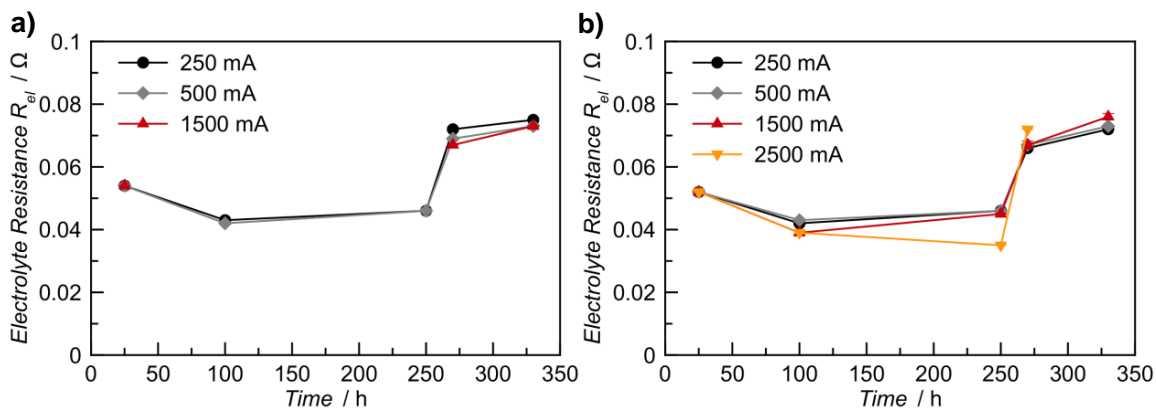


Figure S4 Changes of R_{el} during operation at a) OER and b) ORR, respectively.

Concerning the interfacial resistance R_{int} , an observation was made at OER. At the beginning of operation, there existed only one small semicircle at high frequencies. The longer the experiment lasted the more distorted this semicircle became. Already within the first 100 h it became two semicircles. One possible reason are the discussed mixed potentials due to the oxidation and reduction of copper, as the effect prolonged and increased over time like the observed overpotentials due to copper oxidation and reduction and disappeared after disassembly (see Figure S5).

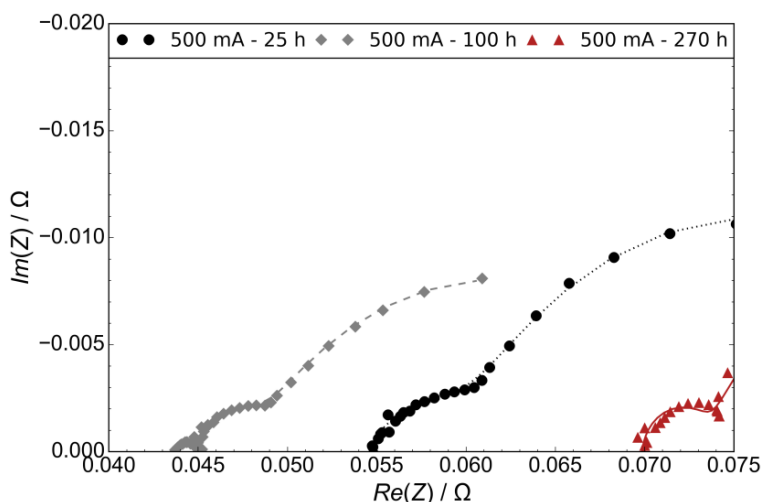


Figure S5 Changes of first semicircle during operation at OER. At the beginning (\bullet) one semicircle can be seen, after 100 h (\blacklozenge) the semicircle split into two and after disassembly and the exchange of the copper plate (\blacktriangle), one semicircle is visible again.

Investigating the double layer capacity of the second larger semicircle, statements about the active surface area can be made. As pictured in Figure S6, the double layer capacity stayed the same or increased within the first 250 h at OER as well as at ORR. This draws the conclusion that the active surface area gets bigger. After disassembly, the double layer capacity at OER as well as ORR dropped drastically, which corresponds to a decreasing active surface area. These phenomena can be explained by the coverage of the catalyst with precipitates of ZnCO_3 , ZnO or hydroxides.

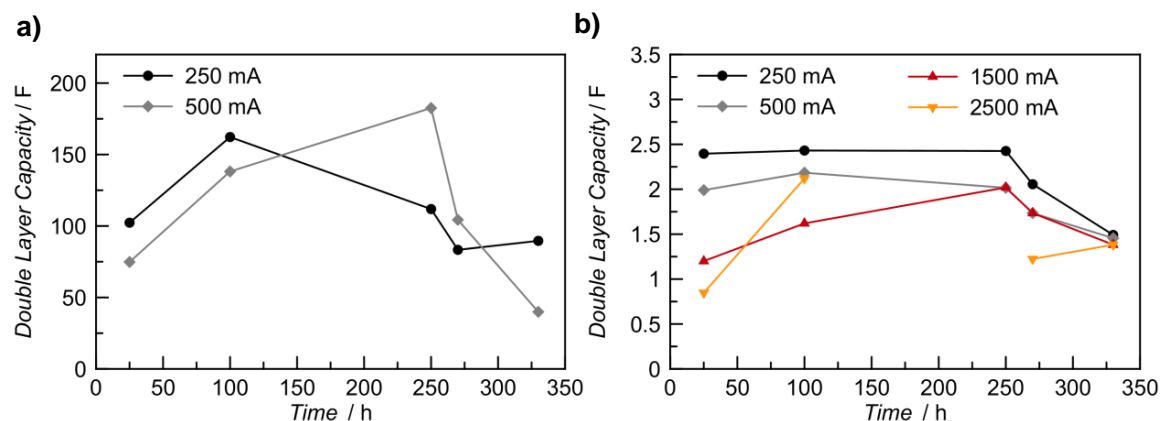


Figure S6 Double layer capacity over time at a) OER and b) ORR, respectively.

Table S4 List of fitting results of electrical components of equivalent circuit at OER.

| | 25 h | | 250 h | | 100 h | | 330 h | |
|----------------------------|---------------------|---------------------|---------------------|---------------------|---------------------|---------------------|--------|--------|
| | 250 mA | 500 mA | 250 mA | 500 mA | 250 mA | 500 mA | 250 mA | 500 mA |
| L_{wire} / H | $7.8 \cdot 10^{-7}$ | $7.7 \cdot 10^{-7}$ | $3.1 \cdot 10^{-6}$ | $2.9 \cdot 10^{-8}$ | $2.9 \cdot 10^{-7}$ | $3.0 \cdot 10^{-7}$ | | |
| $R_{el} / \text{m}\Omega$ | 54 | 54 | 46 | 44 | 75 | 73 | | |
| $R_{int} / \text{m}\Omega$ | 7 | 7 | 1 | 1 | 5 | 1 | | |
| $CPE-T_1$ | 10.38 | 10.60 | 7.17 | 13.05 | 1.29 | 18.30 | | |
| $CPE-P_1$ | 0.57 | 0.55 | 1 | 1 | 0.62 | 0.76 | | |
| $R_{ct} / \text{m}\Omega$ | 71 | 31 | 50 | 43 | 113 | 68 | | |
| $CPE-T_2$ | 58.25 | 61.83 | 88.65 | 76.55 | 28.33 | 25.55 | | |
| $CPE-P_2$ | 0.71 | 0.77 | 0.82 | 0.52 | 0.48 | 0.54 | | |

Table S5 List of fitting results of electrical components of equivalent circuit at ORR.

| | 25 h | | | 250 h | | | 330 h | | |
|----------------------------|-------------------|-------------------|-------------------|-----------|-----------|-------------------|-------------------|-------------------|-------------------|
| | 250 mA | 500 mA | 1500 mA | 250 mA | 500 mA | 1500 mA | 250 mA | 500 mA | 1500 mA |
| L_{wire} / H | $9 \cdot 10^{-7}$ | $9 \cdot 10^{-7}$ | $9 \cdot 10^{-7}$ | 10^{-7} | 10^{-7} | $9 \cdot 10^{-8}$ | $3 \cdot 10^{-7}$ | $3 \cdot 10^{-7}$ | $3 \cdot 10^{-7}$ |
| $R_{el} / \text{m}\Omega$ | 52 | 52 | 52 | 46 | 45 | 45 | 72 | 74 | 75 |
| $R_{int} / \text{m}\Omega$ | 54 | 29 | 15 | 37 | 25 | 13 | 33 | 31 | 16 |
| $CPE-T_1$ | 4.91 | 2.73 | 1.39 | 10.64 | 9.91 | 15.76 | 3.11 | 2.60 | 2.72 |
| $CPE-P_1$ | 0.42 | 0.49 | 0.59 | 0.45 | 0.43 | 0.41 | 0.50 | 0.51 | 0.52 |
| $R_{ct} / \text{m}\Omega$ | 256 | 163 | 76 | 213 | 133 | 65 | 226 | 141 | 79 |
| $CPE-T_2$ | 2.57 | 2.35 | 2.36 | 2.46 | 2.41 | 2.89 | 1.60 | 1.62 | 2.17 |
| $CPE-P_2$ | 0.91 | 0.83 | 0.72 | 0.96 | 0.93 | 0.83 | 0.94 | 0.93 | 0.80 |

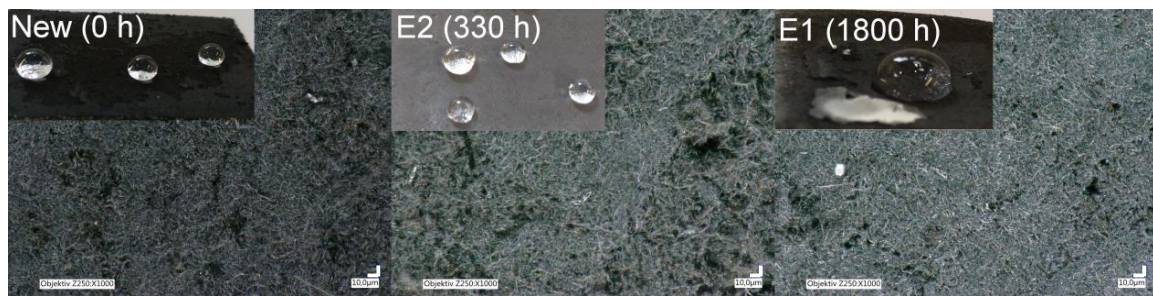


Figure S7 Light microscopy images and photography (left upper corners) of the air facing side of a new electrode and E2 as well as E1 after operation depicting the change in hydrophobicity, which is less severe than on the electrolyte-facing side. Also in contrast to the electrolyte side, no ZnO and electrolyte residues are visible. The CNF fine-structure appears unaltered.

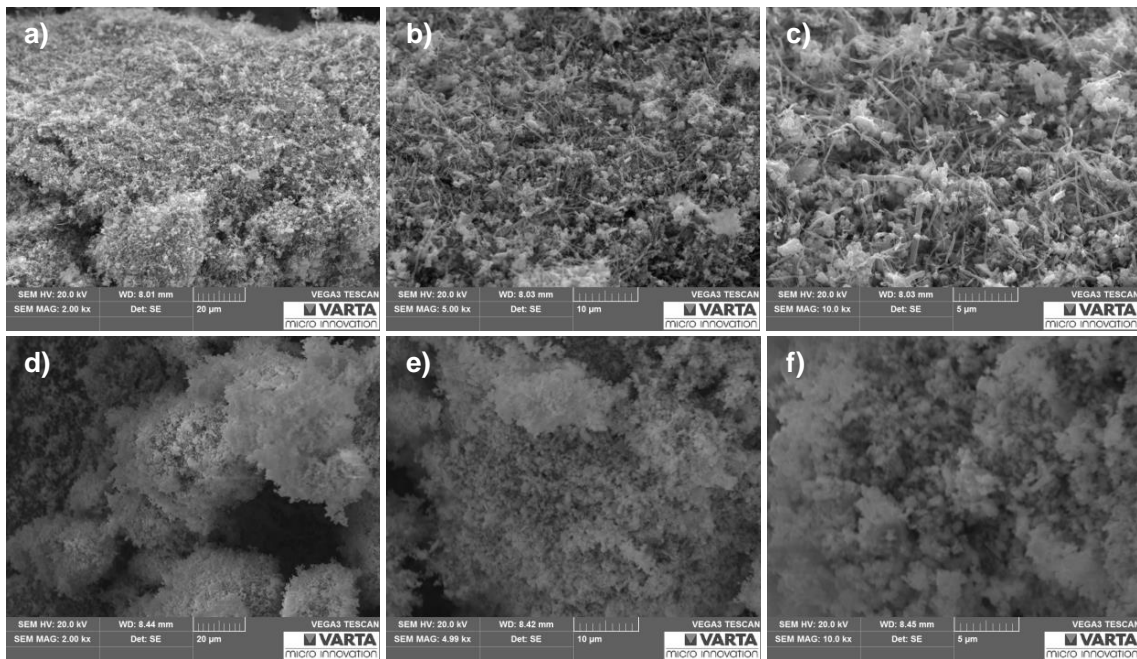


Figure S8 Scanning electron microscopy images (SEM) of the $\text{La}_{0.6}\text{Sr}_{0.4}\text{Co}_{0.2}\text{Fe}_{0.8}\text{O}_3$ homogeneously dispersed on carbon nanofibers (**a-c**) and only the $\text{La}_{0.6}\text{Sr}_{0.4}\text{Co}_{0.2}\text{Fe}_{0.8}\text{O}_3$ perovskite particles as commercially acquired without support material (**d-f**) measured on a VEGA3 ESEM Tescan 500 PA system (Czech Republic).

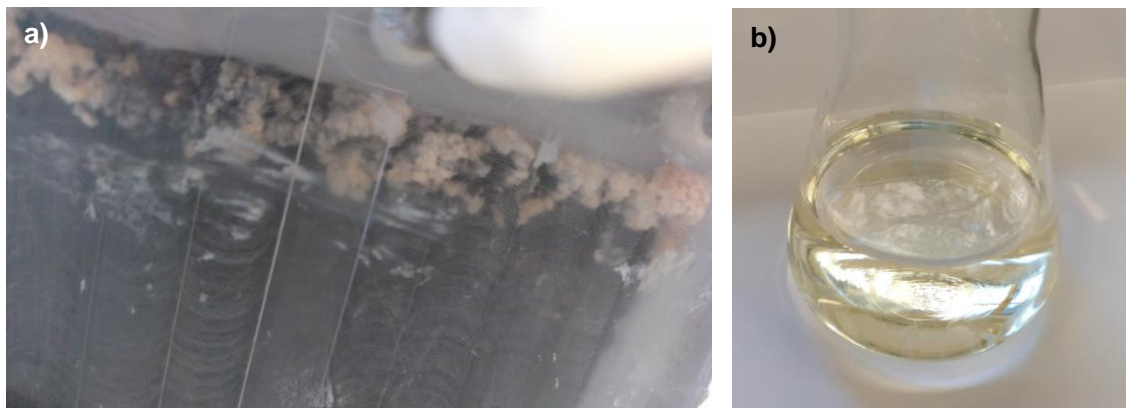


Figure S9 a) Image of the precipitation formed at the upper edge of the 50 cm² sized air electrode E2 after 250 h of operation, through leaking electrolyte at the sealing. The precipitate was easily soluble in water and could be removed by washing. The dry-out occurred only at the upper edge at the air inlet. **b)** Orange coloring of the used 8 M KOH electrolyte after operation indicating only slight carbon corrosion.

Calculations

A zinc-air flow battery is operated in a limited concentration span due to the low solubility of the zincate ($\text{Zn}(\text{OH})_4^{2-}$) in alkaline electrolyte. For example, if the electrolyte concentration varies between 0.2 M zincate in charged state and 0.5 M zincate in discharge state, 0.3 mol L^{-1} are available for cycling. That means, that a zinc-air flow battery providing an energy of 1 kWh (1000 A in 1 h if the discharge cell voltage is 1 V) requires an electrolyte volume of 56 L according to the calculations in equation 2 using Faraday's law (equation 1).

$$\frac{dn}{dt} = \frac{\varphi * I}{z * F} \quad \text{Eq. 1}$$

With n the mol of zinc, t the time, the current efficiency φ , which is estimated to be 0.9 due to parasitic side reactions, I the current, z the converted electrons (2 for zinc) and F the Faradaic constant (96 485 As mol^{-1}).

$$m_{\text{Zn}} = \frac{\varphi * I * M}{z * F} = \frac{0.9 * 1000 \text{ A} * 3600 \text{ s} * 65.38 \text{ g mol}^{-1}}{2 * 96485 \text{ As mol}^{-1}} = 1098 \text{ g Zn} \quad \text{Eq. 2}$$

1098 g_{Zn} correspond to 16.8 mol zinc, which is cycled between charge and discharge. As the concentration varies by 0.3 M this corresponds to 56 L. Overall the zinc-air system has an energy density (only considering the tank volume and not the volume of the stack) of 18 Wh L^{-1} . Assuming a zinc electrode area A of 200 cm^2 the thickness of the (uniformly) deposited zinc layer d in the charged state can be calculated using the density of zinc δ (7.14 g cm^{-3}) according to equation 3.

$$d_{\text{Zn}} = \frac{m_{\text{Zn}}}{\delta * A} = \frac{1098 \text{ g}}{7.14 \text{ g cm}^{-3} * 200 \text{ cm}^2} = 0.77 \text{ cm Zn} \quad \text{Eq. 3}$$

As the rechargeable zinc-air flow battery can be only discharged with 0.05 A cm^{-2} at 1 V, this cell theoretically delivers 10 A, which corresponds to 10 W. Thus, for an energy output of 1 kWh it has to be discharged for 100 h. This calculations are in good accordance with the specification values reported by Amunátegui^[18], who used three 250 L tanks for their nominal 1 kW / 4 kWh demonstration plant (depth of discharge 20%).

For example, the zinc-air cell tested in this work employed electrodes with a size of 50 cm^2 and had an electrolyte volume of 1 L with a concentration of 0.5 M ZnO. If cycled between 0.5 M and 0.2 M, 0.3 mol of Zn are available for cycling, which corresponds to 19.6 g zinc

($M = 65.38 \text{ g mol}^{-1}$). Using Faraday's law in equation 1 (assuming 100% conversion efficiency), this cell has a nominal capacity of 16.1 Ah. In addition, also using Faraday's equation, the conversion time t with a current density of 50 mA cm^{-2} ($= 2.5 \text{ A}$) can be calculated:

$$t = \frac{n * z * F}{I} = \frac{0.3 \text{ mol} * 2 * 96485 \text{ As mol}^{-1}}{2.5 \text{ A}} = 23156 \text{ s} = 6.4 \text{ h} \quad \text{Eq. 4}$$

This means that in 1 h about 0.05 mol Zn are converted ($= 3.1 \text{ g}$), which corresponds to a fraction of 16%.

References

- [1] K. Wang, P. Pei, Y. Wang, C. Liao, W. Wang, S. Huang, *Appl. Energy* **2018**, 225, 848–856.
- [2] Y. Li, M. Gong, Y. Liang, J. Feng, J.-E. Kim, H. Wang, G. Hong, B. Zhang, H. Dai, *Nat. Commun.* **2013**, 4, 1805.
- [3] C. Ma, N. Xu, J. Qiao, S. Jian, J. Zhang, *Int. J. Hydrogen Energy* **2016**, 41, 9211–9218.
- [4] Y. Ding, Y. Niu, J. Yang, L. Ma, J. Liu, Y. Xiong, H. Xu, *Small* **2016**, 12, 5414–5421.
- [5] N. Xu, Y. Liu, X. Zhang, X. Li, A. Li, J. Qiao, J. Zhang, *Sci. Rep.* **2016**, 6, 33590.
- [6] N. Xu, J. Qiao, X. Zhang, C. Ma, S. Jian, Y. Liu, P. Pei, *Appl. Energy* **2016**, 175, 495–504.
- [7] Q. Wang, L. Shang, R. Shi, X. Zhang, G. I. N. Waterhouse, L.-Z. Wu, C.-H. Tung, T. Zhang, *Nano Energy* **2017**, 40, 382–389.
- [8] C.-Y. Su, H. Cheng, W. Li, Z.-Q. Liu, N. Li, Z. Hou, F.-Q. Bai, H.-X. Zhang, T.-Y. Ma, *Adv. Energy Mater.* **2017**, 7, 1602420.
- [9] Y. Shimizu, H. Matsuda, N. Miura, N. Yamazoe, *Chem. Lett.* **1992**, 21, 1033–1036.
- [10] S. Zhuang, C. Huang, K. Huang, X. Hu, F. Tu, H. Huang, *Electrochem. commun.* **2011**, 13, 321–324.
- [11] G. Toussaint, P. Stevens, L. Akrou, R. Rouget, F. Fourgeot, in *ECS Trans.*, **2010**, pp. 25–34.
- [12] S. W. T. Price, S. J. Thompson, X. Li, S. F. Gorman, D. Pletcher, A. E. Russell, F. C. Walsh, R. G. A. Wills, *J. Power Sources* **2014**, 259, 43–49.
- [13] M. Bockelmann, U. Kunz, T. Turek, *Electrochem. commun.* **2016**, 69, 24–27.
- [14] J. Pan, L. Ji, Y. Sun, P. Wan, J. Cheng, Y. Yang, M. Fan, *Electrochem. commun.* **2009**, 11, 2191–2194.
- [15] D. U. Lee, J. Y. Choi, K. Feng, H. W. Park, Z. Chen, *Adv. Energy Mater.* **2014**, 4, DOI 10.1002/aenm.201301389.
- [16] D. Thiele, A. Züttel, *J. Power Sources* **2008**, 183, 590–594.
- [17] Z. Chen, A. Yu, D. Higgins, H. Li, H. Wang, Z. Chen, *Nano Lett.* **2012**, 12, 1946–1952.
- [18] B. Amunátegui, A. Ibáñez, M. Sierra, M. Pérez, *J. Appl. Electrochem.* **2018**, 48, 627–637.

Development of Stable Bifunctional Air Electrodes for Zinc-Air Flow Batteries

B. Pichler^a, S. Weinberger^a, L. Reščec^a, V. Hacker^a

^a Institute of Chemical Engineering and Environmental Technology, Graz University of Technology, 8010 Graz, Austria

Bifunctional air electrodes for the application in zinc-air flow batteries were manufactured in a scalable manufacturing process using precious metal-free oxide catalysts. During repeated charge/discharge cycling at 50 mA cm⁻² and with synthetic air supply stable performances over more than 450 h and 200 cycles were achieved. The energy efficiency was 49% at start and 45% after 200 cycles. In addition, the pulse charging method with 150 mA cm⁻² pulses was successfully applied on air electrodes.

Introduction

The increasing installation capacities of renewable but fluctuating electricity generators such as wind and solar power systems have raised the need for energy storage with short response times. Out of the many different types of electrochemical energy storage systems, the stationary zinc-air flow battery is promising due to its use of the safe, abundant and inexpensive active storing metal zinc (1). In this system zinc is dissolved into the flowing alkaline electrolyte during discharge and can be stored as zincate ion outside of the electrochemical cell. It is redeposited during charging, whereby compact zinc morphologies are preferred in order to avoid internal short-circuiting and loss of active material (2). As in other metal-air batteries, the reactions of the second electrode are the oxygen reduction reaction (ORR) during discharging using oxygen from the air and the oxygen evolution reaction (OER) during charging (1,3) (see Table I).

TABLE I. Electrochemical reactions in a zinc-air battery - charging reaction from left to right.

| | Reaction | Potential vs. SHE [V] |
|-------------------------|-------------------------------------------------------------------------------------------------------------|----------------------------------------|
| Zn electrode | $\text{Zn(OH)}_4^{2-} + 2 e^- \rightleftharpoons \text{Zn} + 4 \text{OH}^-$ | $E_{00} = -1.25 \text{ V}$ |
| Air electrode | $4 \text{OH}^- \rightleftharpoons \text{O}_2 + 2 \text{H}_2\text{O} + 4 e^-$ | $E_{00} = 0.4 \text{ V}$ |
| Overall reaction | $2 \text{Zn(OH)}_4^{2-} \rightleftharpoons 2 \text{Zn} + 4 \text{OH}^- + \text{O}_2 + 2 \text{H}_2\text{O}$ | $E_{\text{cell,eq.}} = 1.65 \text{ V}$ |

In practical applications, the recharge capability of the zinc-air cell is dependent on the compact zinc deposition and the mechanical and chemical long-term stability of the air electrode. Furthermore, the low cycling efficiencies of around 50% resulting from the slow ORR/OER reaction kinetics are challenging to overcome and rely on the activity of the chosen catalysts. In air electrodes non-precious metal oxides such as perovskites (e.g. La_{0.6}Sr_{0.4}Co_{0.2}Fe_{0.8}O₃, LaNiO₃) and spinels (e.g. NiCo₂O₄) can be utilized, due to their chemical stability in alkaline electrolyte (3,4). Although many oxide catalysts exhibit bifunctional catalytic activity toward ORR and OER, they are often not equally active toward both reactions. Hence, a combination of two catalysts in one electrode is beneficial, as was investigated in the course of the project (4). Furthermore, their

implementation into a stable and porous electrode structure with balanced gas diffusivity and electrolyte wettability is important in order to obtain a high number of three-phase zones between gas, electrolyte and catalyst. This was achieved by selecting suitable additives such as carbon nanofibers and nickel powder for electrical conductivity and PTFE as hydrophobic binder material. These materials need to be resistant toward the highly oxidative potentials of around 2 V vs. Zn/Zn^{2+} and the mechanical stress by the vigorous oxygen bubble formation during charging. In addition, nickel foam was found to be an applicable current collector material, which functions at the same time as mechanical backbone of the air electrode.

Experimental

Catalyst Synthesis and Electrode Manufacture

NiCo_2O_4 spinel was synthesized directly onto the carbon nanofibers (CNF) or nickel powder support via a straightforward impregnation-calcination synthesis route (4,5). The perovskite $\text{La}_{0.6}\text{Sr}_{0.4}\text{Co}_{0.2}\text{Fe}_{0.8}\text{O}_3$ was a commercial catalyst with defined particles size and composition. For better electrical conductivity it was homogeneously dispersed with CNF using an ultrasonic probe. These two catalysts were mixed to form pastes using PTFE as binder material and ultrapure water/2-propanol as solvent and subsequently spread onto the nickel foam current collector as described in Figure 1. After drying the electrode was pressed and sintered resulting in a final thickness of 0.7 mm (4).

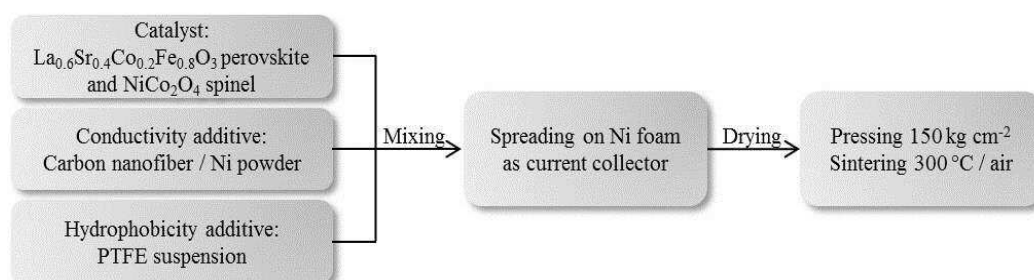


Figure 1. Manufacturing process of the bifunctional air electrodes.

Electrochemical Characterization

The described in-house manufactured electrodes were cut to a size of 4 cm^2 and electrochemically characterized in a half-cell set-up in 8 M KOH electrolyte with the addition of 0.5 M ZnO, whereby one air electrode was operated as working electrode and a second air electrode as counter electrode. They were referenced against zinc foil. Discharging was performed at a constant current density of 50 mA cm^{-2} for 2 h per cycle. Because of the beneficial effects for the deposition of compact zinc layers, charging was conducted with the pulse charging method by applying tripled current densities, i.e. 150 mA cm^{-2} , during a short pulse of 50 ms followed by a pause of 100 ms (24 000 pulses in 1 h). The influence of the pulse charging on the performance of the air electrodes was studied in order to confirm the viability of this method for full cell application.

Results and Discussion

The long-term cycling experiment with pulse charging, as depicted in Figure 2, was performed for overall 550 h and 228 cycles until the lower cut-off potential of 0.8 V vs. Zn/Zn^{2+} was reached. An initial decrease of ORR discharge potential of 0.05 V down to about 1.0 V was observed within the first 10 hours of cycling, which is attributed to decreasing catalytic activity of the spinel catalyst toward ORR upon repeated cycling (4). However, the ORR potential was then constant for more than 200 h of testing due to the stable catalytic activity of the perovskite. Within the subsequent 200 cycles (450 h) shown in Figure 2, the decrease of ORR discharge potential was 80 mV, indicating degradation resulting from altered wetting behavior of the electrode caused by the continuous cycling.

The maximum OER potentials during charging were stable throughout the measurement with a maximum of 2.04 V during the pulse. The potential difference between pulse and pause increased over time, which indicates alteration within the electrode's structure during testing. A summary of the obtained potential values and the respective potential differences (ΔV) is given in Table II.

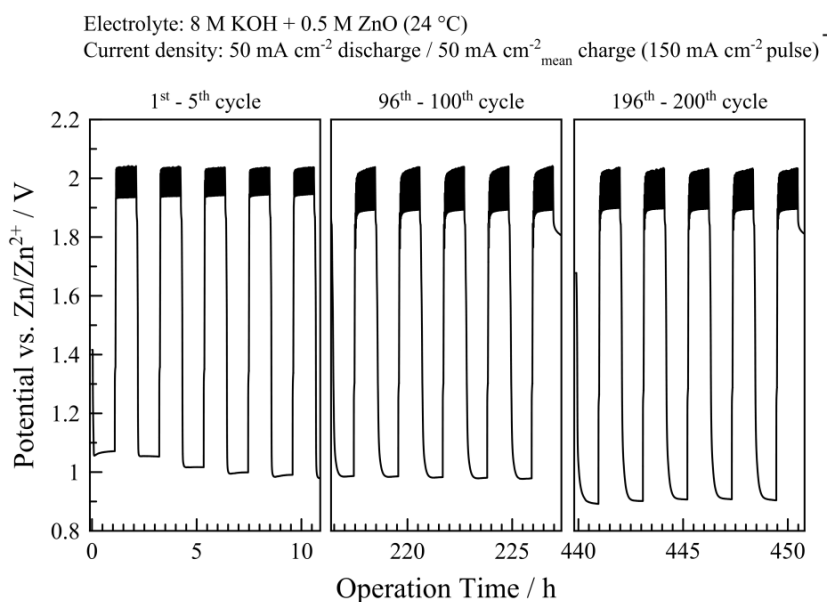


Figure 2. Charge and discharge cycles of the bifunctional electrode (black bars related to the pulse charging with 24.000 pulses per hour).

The good stability of the investigated electrode can be attributed to an optimized catalyst paste composition, whereby the added amount of hydrophobic PTFE has a strong influence on the ORR performance. Especially for the ORR, gas permeability and thus oxygen diffusivity is crucial due to the need of three-phase boundaries at the reaction sites, i.e. the catalyst/electrolyte/gas interface. Also the added carbon nanofibers enhance gas accessibility, while at the same time providing electrical conductivity within the electrode. In comparison to other carbon types such as Vulcan XC72, the CNFs show significantly higher oxidative stability and hence lower carbon corrosion. Mechanical strength, particularly against the oxygen bubble formation during charging, was provided by the nickel foam.

The end of testing was caused by too low ORR performance resulting in charge/discharge potential differences significantly over 1 V. The deterioration was due to the increased hydrophilicity of the electrode through the break up the fine CNF/PTFE-network resulting from mechanical stress induced by the oxygen bubble formation during repeated charging cycles. In consequence, the alkaline electrolyte was able to slowly fill the pores within the electrode. Because oxygen diffusion is much slower in liquid media, the gas accessibility to the catalyst sites was hindered and thus activity toward the oxygen reduction reaction became limited by gas diffusion.

TABLE II. Results of the long-term pulse charging/discharging measurement and potential differences

| Potential / V | 5 th Cycle | 100 th cycle | 200 th cycle |
|----------------------------|-----------------------|-------------------------|-------------------------|
| Discharge | 0.99 | 0.98 | 0.91 |
| Pulse | 2.04 | 2.04 | 2.03 |
| Pause | 1.95 | 1.89 | 1.90 |
| ΔV Pulse-Discharge | 1.05 | 1.06 | 1.12 |
| ΔV Pause-Discharge | 0.96 | 0.92 | 0.99 |
| ΔV Pulse-Pause | 0.09 | 0.15 | 0.13 |

The energy efficiency was calculated according to Equation 1 using the current density j applied for a defined time t and the measured potential V during charge (c) and discharge (d) (6).

$$\text{Energy efficiency [\%]} = [(j_d * V_d * \Delta t_d) / (j_c * V_c * \Delta t_c)] * 100 \quad [1]$$

After 5 cycles and after 10 h the energy efficiency was 49% and decreased then to 45% after 200 cycles, which is mainly due to decreasing ORR performance. Nevertheless, this value is still very low, and can be only improved by better catalyst utilization within the electrode.

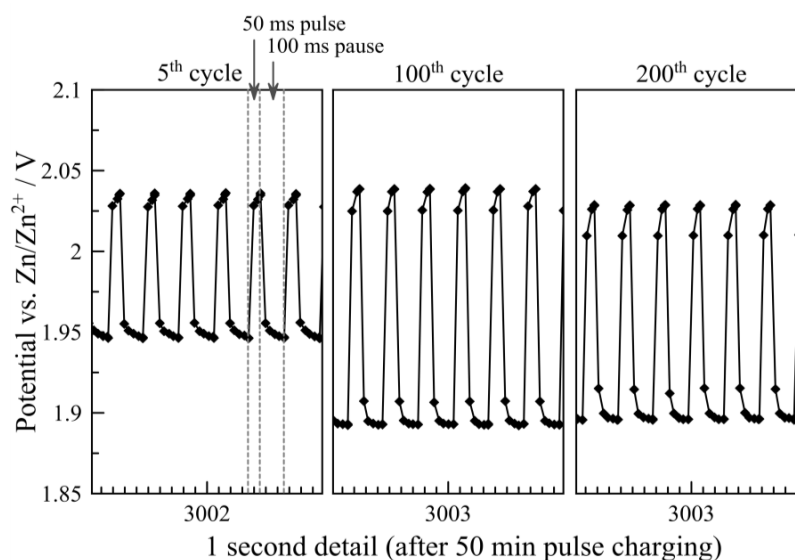


Figure 3. 1 s detail of the pulse potentials during charging each after 50 min of charging.

Figure 3 shows the detailed results of the pulse charging. Over the whole operation period the maximum potential was constantly between 2.04 V and 2.03 V and the pause potential even decreased by 60 mV. Furthermore, the shape of the measured potentials is not completely rectangular and during the pulse the maximum potential is not reached during the short 50 ms pulse. These measurements show that although the tripled current density (150 mA cm^{-2}) is applied, the maximum potentials are only slightly above 2 V, thereby verifying the applicability of the pulse charging method also for full cell zinc-air battery operation.

Conclusion and Outlook

The in-house manufactured bifunctional air electrodes exhibited high stability over several hundred hours at the comparably high current density of 50 mA cm^{-2} , bringing the zinc-air flow battery one step further to commercial application. Nevertheless, the energy efficiency still has to be improved and the degradation mechanisms need to be studied further in order to optimize the electrode build. Especially the many requirements for a well performing bifunctional air electrode regarding gas permeability, liquid electrolyte wettability as well as mechanical and electrochemical stability during charging put the emphasis on a finely balanced and optimized electrode design. The complete soaking of the electrode over time has to be prevented, which can be achieved mainly by increasing the mechanical stability. Future work will include scale-up of the electrode sizes as well as operation in flowing electrolyte.

Acknowledgments

Funding by the Austrian Federal Ministry of Transport, Innovation and Technology (BMVIT) and The Austrian Research Promotion Agency (FFG) through the program “e!MISSION.at Energieforschungsprogramm” (No. 848933) is gratefully acknowledged. We also want to thank our cooperation partners from the Institute of Chemistry and Technology of Materials at Graz University of Technology and our industry partners VARTA Micro Innovation GmbH (Austria) and TSR-Kat (Germany).

References

1. J. Fu et al., *Adv. Mater.* **28**, 6421-6428 (2016).
2. C. Zelger, J. Laumen, A. Laskos, and B. Gollas, *Electrochim. Acta*, **213**, 208–216 (2016).
3. L. Jörissen, *J. Power Sources*, **155**, 23–32 (2006).
4. B. Pichler et al., *Electrochim. Acta*, **251**, 488–497 (2017).
5. D. Pletcher et al., *Electrochim. Acta*, **188**, 286–293 (2016).
6. S.-H. Shin, S.-H. Yun, and S.-H. Moon, *RSC Adv.*, **3**, 9095 (2013).

Proceedings of 7th Transport Research Arena TRA 2018, April 16-19, 2018, Vienna, Austria

Development of zinc-air flow batteries by investigating compact zinc deposition and improving air electrode cycling stability

Birgit Pichler a^{*}, Viktor Hacker a, Christian Zelger b, Waltraud Taucher-Mautner b, Bernhard Gollas b, Hans-Jürgen Pauling c

^a*Institute of Chemical Engineering and Environmental Technology, Graz University of Technology, Inffeldgasse 25C, 8010 Graz, Austria*

^b*Institute for Chemistry and Technology of Materials, Graz University of Technology, Stremayrgasse 9, 8010 Graz, Austria*

^c*TSR-KAT GmbH, Ochsenburger Straße 19, 75056 Sulzfeld, Germany*

Abstract

The growing number of electric vehicles worldwide demands increasing electricity generation from renewable sources such as wind and solar in order to render these vehicles CO₂ neutral. However, these systems are very intermittent and need to be coupled with high capacity and fast responding energy storage systems. Zinc-air flow batteries are designed for this stationary application, using the inexpensive, safe and abundant metal zinc as active storing material. In the project *Luziflow* all battery components are investigated and improved regarding the efficiency during cycling and the long-term stability during operation. On the negative zinc electrode, new insights have been gained on dendrite-free zinc deposition during charging and with flowing electrolyte. On the positive air electrode stable bifunctional electrode designs with high catalytic activity have been applied in long-term operation. The final aim of the project *Luziflow* will be the scale-up to 100 cm² and full cell operation.

Keywords: renewable electricity for EV; electrical energy storage; zinc-air flow battery; project *Luziflow*

^{*} Birgit Pichler. Tel.: +43 316 873 8797;
E-mail address: birgit.pichler@tugraz.at

1. Introduction

Progress in battery technology is the key for widespread commercialization of electric vehicles (EV). Several factors, such as the price per kWh, power density, environmental impact and resource constraints of the required materials, determine which type of battery is suitable for portable and for stationary large-scale applications (Wadia, Albertus, and Srinivasan 2011). Despite significant developments in lithium-ion battery technology in the last decades, other battery technologies have come into focus in recent years such as lithium-sulfur, sodium-ion and metal-air batteries, which are especially promising due to their high theoretical energy density (Li and Dai 2014; Fu et al. 2017). In this type of battery only one active material – zinc, aluminum, magnesium, lithium – has to be stored, while the second reactant – oxygen – can be directly withdrawn from the surrounding air. Nevertheless, their application as secondary batteries is prevented by the limited recharge capability and efficiency. Rechargeable zinc-air systems are the most widely developed type of secondary metal-air batteries and are very flexible in their application. The battery design ranges from small sheet-like assemblies to large-scale flow systems (Gu et al. 2017).

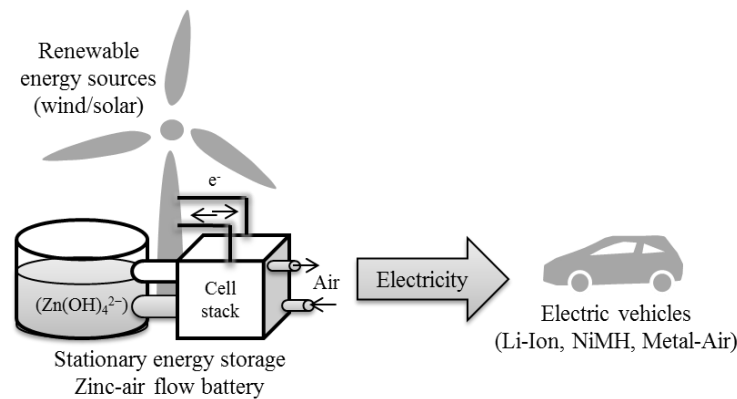


Fig 1 Importance of battery technology for electrical energy storage and EVs.

Although the work presented in the following is aimed at stationary energy storage, the findings can be transferred to small portable devices used for example in transportation. However, up until now, the power output and the recharge capability of the zinc-air battery are not sufficient for use in battery electric vehicles (BEV). Nevertheless, as shown in Figure 1, the use of CO_2 -neutral EVs is directly connected to electricity generation from renewable sources such as wind and solar. As these sources are very intermittent and unreliable, counteracting these fluctuations by flexible energy storage is required (Zhao et al. 2015). Stationary battery systems can function as bridging power to balance the fast load shifts (Chen et al. 2009).

1.1. Zinc-Air Flow Battery

Flow batteries have been intensively studied over the last years as potential energy storage systems with fast response times. Their biggest advantage is the flexibility of the system as it is possible to separately scale power and capacity by customizing the number of cells in the stack and the size of the external storage tanks. Of the many different types of flow batteries, the zinc-air system holds high potential for wide-spread application due to the use of the low-cost, abundant and environmentally friendly active materials (Fu et al. 2017). Furthermore, as only zinc has to be stored and the second reactant – oxygen – is withdrawn from the surrounding air, the system reaches high energy density (see Figure 2 and Table 1).

Table 1 Electrochemical reactions in a zinc-air battery - charging reaction from left to right.

| | Reaction | Potential vs. standard hydrogen electrode [V] |
|-------------------------|--------------------------------------------------------------------------------------------------------------------|-----------------------------------------------|
| Zn electrode | $\text{Zn}(\text{OH})_4^{2-} + 2 e^- \rightleftharpoons \text{Zn} + 4 \text{OH}^-$ | $E_{00} = -1.25 \text{ V}$ |
| Air electrode | $4 \text{OH}^- \rightleftharpoons \text{O}_2 + 2 \text{H}_2\text{O} + 4 e^-$ | $E_{00} = 0.4 \text{ V}$ |
| Overall reaction | $2 \text{Zn}(\text{OH})_4^{2-} \rightleftharpoons 2 \text{Zn} + 4 \text{OH}^- + \text{O}_2 + 2 \text{H}_2\text{O}$ | $E_{\text{cell,eq}} = 1.65 \text{ V}$ |

However, several technical challenges, such as the dendrite-free zinc deposition during charging and the insufficient long-term stability as well as low cycling efficiency of the air electrode, prevent the commercialization and practical application of the zinc-air flow battery (Fu et al. 2017). A summary of the challenges concerning the commercialization of the zinc-air flow battery is given in Table 2. In the course of the project *Luziflow* both electrode reactions are investigated and the system further improved in order to bring the rechargeable zinc-air flow battery one step closer to commercial application.

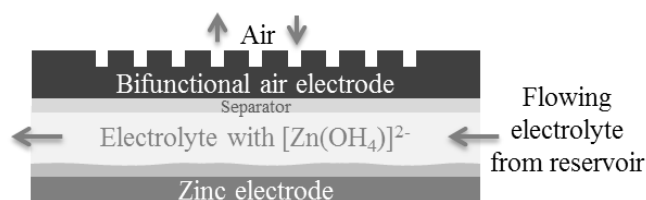


Fig 2 Schematic of a zinc-air flow battery cell.

On the zinc electrode important insights for achieving compact zinc electrodeposition have been gained (Zelger et al. 2016). Based on this knowledge, experiments with different flow rates using the pulse current method are performed in order to further optimize the operating parameters.

For well-performing air electrodes, precious metal-free oxide catalysts, such as spinels and perovskites, are tested. These catalysts are known to show good catalytic activity towards oxygen reduction reaction (ORR) during discharge and oxygen evolution reaction (OER) during charging. They are implemented into chemically and mechanically stable air electrodes and electrochemically characterized by long-term cycling experiments. Stable charge and discharge potentials for more than 200 cycles and several hundred hours have been achieved (Pichler et al. 2017). Further details of this work are described in the following. The final aim of the project *Luziflow* will be the assembly of both optimized electrodes in a 100 cm² flow cell in order to obtain knowledge on the practical operation of the zinc-air flow battery.

Table 2 Technical challenges regarding electrically rechargeable zinc-air (flow) batteries.

| Zinc electrode | | Air electrode | |
|----------------------------------------|------------------------------|----------------------------------------------------------|------------------------------------------|
| Dendrite-formation during charging | → Short-circuiting | High ORR/OER overpotentials | → Low energy efficiency (50-60%) |
| Non-compact morphologies | → Loss of active material | O ₂ bubble formation (mechanical degradation) | → Low long-term stability |
| H ₂ evolution side reaction | → Reduced current efficiency | Highly oxidative potentials during charging | → Degrading reversibility during cycling |

2. Zinc Electrode and Electrolyte Development – Results and Discussion

Challenges for the zinc electrode lie in the formation of zinc dendrites leading to cell shorting and capacity losses (Zelger et al. 2016). Two approaches are taken in the project *Luziflow* to meet these challenges. One is to use and optimize a pulsed charging current that yields dendrite-free zinc deposits from conventional additive-free alkaline electrolytes even at low zincate concentration and current densities of at least 50 mA cm⁻² (Djoufac Woumfo and Vittori 1991; Wang et al. 2014).

The second approach is the development of a novel pH neutral electrolyte consisting of aqueous zinc salt solutions mixed with ionic liquids or deep eutectic solvent components. Only dendrite-free zinc deposits have been obtained from such liquids, due to the specific properties of the electrochemical double layer (Simons et al. 2012; Liu, Abedin, and Endres 2013; Vieira, Whitehead, and Gollas 2013). It is also expected that this new electrolyte will have an energy density several-fold of that alkaline electrolytes offer due to the higher solubility of the respective zinc salts. In this project the effect of the pulsed charging current in alkaline electrolytes and that of pH neutral electrolyte mixtures on zinc deposition and dissolution under flow-cell conditions is studied by electrochemical and material characterization methods. The most promising electrolytes are tested in flow-cell cycling experiments. In the latter electrolytes also the self-discharge is quantified.

The electrodeposition of zinc was studied in a Rota-Hull cell at 60 °C, electrolyte flow velocities w of 3, 6, and 16 cm s⁻¹, and 0.2 M and 0.5 M zincate concentrations c in additive-free 8 M KOH electrolytes (Zelger et al. 2016). Depositions with continuous current predominantly produced the non-compact filamentous mossy zinc morphology. By contrast, under the same experimental conditions and the same average current density, pulse interrupt current Rota-Hull cell experiments produced compact zinc deposits at all electrolyte flow velocities and zincate concentrations. The filamentous mossy morphology was not observed. Compact zinc deposits were obtained with pulse current at local practical partial current densities between 3 and 34 mA cm⁻². Current efficiencies between 96% and 100% have been found for the highest practical current densities. Compact zinc deposits up to the mass-transport limited current could be achieved with pulse interrupt current under the most critical conditions used in this work ($c = 0.2$ M and $w = 3$ cm s⁻¹). Further adjustment of the applied current density and the pulse parameters might produce compact zinc deposits up to the mass-transport limit even for the whole range of zincate concentrations and electrolyte flow velocities. At low current densities, the absence of the filamentous mossy zinc morphology in pulse interrupt current experiments is ascribed to a beneficial effect of the off-time. Based on these results, pulse charging can thus increase the operating range and robustness of zinc-air redox flow batteries.

3. Air Electrode – Results and Discussion

3.1. Catalyst Synthesis and Electrode Manufacture

Because alkaline electrolytes are utilized in metal-air batteries, non-precious metal catalysts instead of scarce and costly platinum or iridium oxide/ruthenium oxide can be implemented into the air electrode build. This is an important factor for achieving a significant cost reduction of the battery system. Very promising and of high interest are different types of oxide catalysts such as perovskites (general formula ABO₃) and spinels (AB₂O₄). They are synthesized via a sol-gel process or with the direct impregnation/calcination method (Jörissen 2006; Pletcher et al. 2016). Oxide catalysts of varying composition were investigated. Of these La_{0.6}Sr_{0.4}Co_{0.2}Fe_{0.8}O₃ perovskite and NiCo₂O₄ spinel exhibited the most promising catalytic activity during ex-situ cyclic voltammetry measurements and also in in-situ electrode tests.

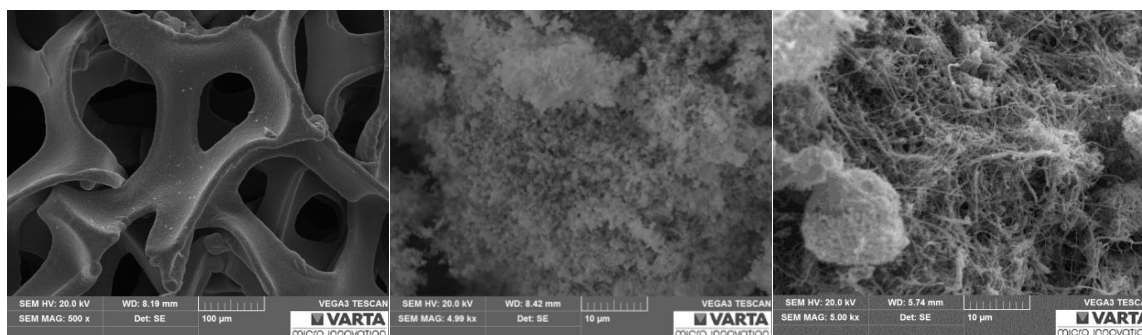


Fig 3 Scanning electron microscopy (SEM) images of nickel foam current collector (left), La_{0.6}Sr_{0.4}Co_{0.2}Fe_{0.8}O₃ perovskite catalyst (middle) and NiCo₂O₄ spinel catalyst on carbon nanofibers (right).

For manufacturing electrodes, these catalysts were mixed together with PTFE as hydrophobic binder material and carbon nanofibers (CNF), until a homogeneous paste was obtained. This paste was spread onto nickel foam functioning as current collector and mechanical backbone of the electrode. Scanning electron microscopy images showing the nickel foam current collector and the two investigated catalysts are presented in Figure 3. The fine nickel foam structure provides stability to the catalyst paste, whereas the finely grained perovskite with < 1 µm particle size (in the SEM image without CNF) and the slightly larger sized (about 10 µm) spinel catalyst are well connected to the electrically conductive wool-like carbon nanofibers. After pressing and sintering, the final electrodes were mounted in in-house made test cells for electrochemical characterization (Pichler et al. 2017).

3.2. Electrochemical Testing

Electrochemical measurements were performed on a 32-channel BaSyTec CTS Lab potentiostat with corresponding software. The long-term charge/discharge cycling tests (two hours per cycle) were performed at room temperature in 8 M KOH with 0.5 M ZnO electrolyte in a three-electrode set-up using a zinc plate as reference electrode. Charging was performed with pulsed currents, which is a beneficial method for obtaining compact and dendrite-free zinc deposition. Investigations focused on the degrading effect of the high pulse currents on the air electrode applying 150 mA cm^{-2} during the 50 ms pulse and no current during 100 ms pause, which corresponds to a mean current density of 50 mA cm^{-2} .

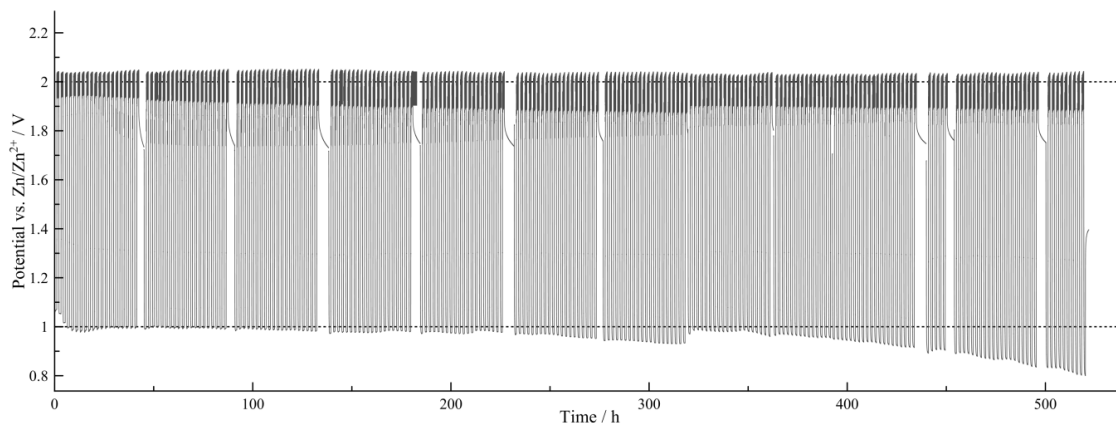


Fig 4 Long-term charge/discharge cycling test of a bi-catalyzed bifunctional air electrode supplied with synthetic air (50 mA cm^{-2} applied; 1 h pulse charging per cycle)

The long-term charge/discharge performance of a bi-catalyzed bifunctional air electrode is depicted in Figure 4. Stable performances over the course of 500 h and over 200 cycles (1 h discharge and 1 h pulse charging) were achieved. Detailed analysis of this measurement is given in Figure 5 a) showing the discharge potential around 1 V vs. Zn/Zn^{2+} and the charging potentials of about 2 V vs Zn/Zn^{2+} (higher potential corresponds to the pulse of 150 mA cm^{-2} , the lower to the potential during pause). The resulting potential difference shown in the lower graph of Figure 5 a), remains around 1 V for about 150 h, which corresponds to a cycling efficiency of 50%. The polarization curves depicted in Figure 5 b) confirm the very stable performance of the electrode towards oxygen evolution reaction (OER) during charging. However, oxygen reduction performance decreases slowly over time, indicating a change of gas accessibility towards the catalyst within the electrode.

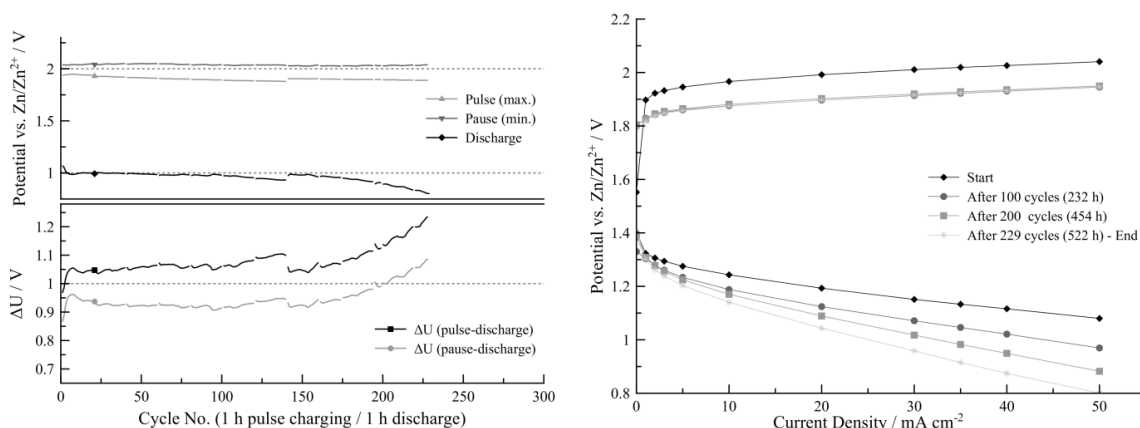


Fig 5 a) Details of the long-term cycling showing potential and charge/discharge potential difference for each cycle and b) polarization curves for ORR and OER recorded every 100 cycles.

3.3. End of Life Characterization

After the electrochemical testing the electrodes were investigated by contact angle measurements. As can be seen in Figure 6 the wetting behavior of the air electrode changed drastically during the repeated charge/discharge cycling. Due to the increased hydrophilicity the alkaline electrolyte was able to fill the pores within the electrode. As oxygen diffusion is much slower in liquid media, the gas accessibility to the catalyst sites is hindered and in consequence activity towards the oxygen reduction reaction becomes limited by gas diffusion. Further optimization of the electrode build is needed to overcome this issue.

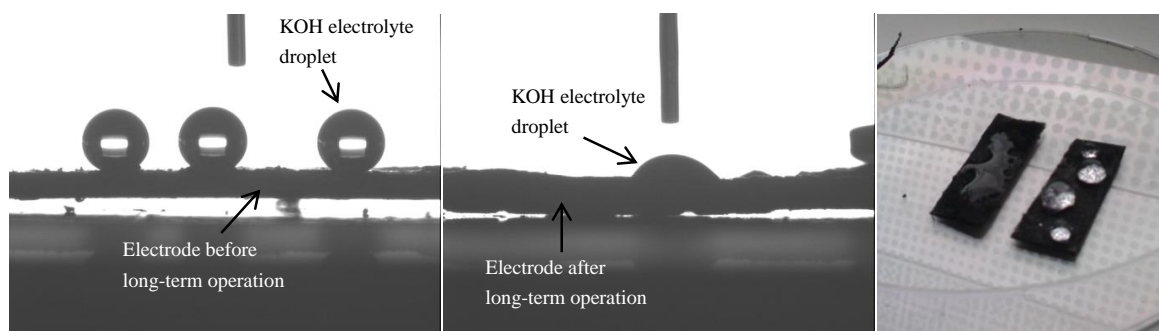


Fig 6 Images of the contact angle measurements of the bi-catalyzed bifunctional before (left) and after (middle) operation; the difference is also apparent in the picture (right) of electrodes before and after the testing.

4. Conclusion and Outlook

Zinc-air flow batteries are a promising battery technology for energy storage, but the system suffers from low cycling efficiencies and insufficient long-term stability. In the project *Luziflow*, strategies to overcome these issues have been investigated. Regarding the negative zinc electrode, dendrite-free zinc deposition was achieved at different electrolyte flow rates and varying current densities up to 34 mA cm^{-2} . High current efficiencies of $> 96\%$ were obtained (Zelger et al. 2016).

On the positive air electrode, operation times of several hundred hours and more than 200 cycles of charge/discharge at a comparably high current density of 50 mA cm^{-2} were achieved by optimizing the electrode build. An energy efficiency of 50% was reached, which corresponds well to performance values listed in literature (Sumboja et al. 2016; Fu et al. 2017). Degradation effects at the end of life were investigated by means of scanning electron microscopy, revealing slow mechanical decomposition of the electrode's structure caused by the charging process (Pichler et al. 2017).

Future work will comprise further optimization of the air electrode build, scale-up of both electrodes and final full cell operation with flowing electrolyte. With these steps, the project *Luziflow* will contribute to the development of the zinc-air system and take it one step further towards commercial application.

Acknowledgements

Funding of the project *Luziflow* by the Austrian Federal Ministry of Transport, Innovation and Technology (BMVIT) and The Austrian Research Promotion Agency (FFG) through the program "e!MISSION.at Energieforschungsprogramm" (No. 848933) is gratefully acknowledged. We also want to thank our industry partners VARTA Micro Innovation GmbH (Austria) and TSR-Kat (Germany). Nickel foam was generously provided by Alantum Europe GmbH, Germany.

5. References

- Chen, Haisheng, Thang Ngoc Cong, Wei Yang, Chunqing Tan, Yongliang Li, and Yulong Ding. 2009. "Progress in Electrical Energy Storage System: A Critical Review." *Progress in Natural Science* 19 (3). National Natural Science Foundation of China and Chinese Academy of Sciences: 291–312. doi:10.1016/j.pnsc.2008.07.014.
- Djoufac Woumfo, E., and O. Vittori. 1991. "Electrochemical Behaviour of a Zinc Electrode in 8 M KOH under Pulsed Potential Loading." *Journal of Applied Electrochemistry* 21: 77–83.
- Fu, Jing, Zachary Paul Cano, Moon Gyu Park, Aiping Yu, Michael Fowler, and Zhongwei Chen. 2017. "Electrically Rechargeable Zinc-Air Batteries: Progress, Challenges, and Perspectives." *Advanced Materials* 29 (7): 1604685. doi:10.1002/adma.201604685.
- Gu, Peng, Mingbo Zheng, Qunxing Zhao, Xiao Xiao, Huaiguo Xue, and Huan Pang. 2017. "Rechargeable Zinc – Air Batteries : A Promising Way to Green Energy." *Journal of Materials Chemistry A: Materials for Energy and Sustainability* 0. Royal Society of Chemistry: 1–16. doi:10.1039/C7TA01693J.
- Jörissen, Ludwig. 2006. "Bifunctional Oxygen/air Electrodes." *Journal of Power Sources* 155 (1): 23–32. doi:10.1016/j.jpowsour.2005.07.038.
- Li, Yanguang, and Hongjie Dai. 2014. "Recent Advances in Zinc-air Batteries." *Chem. Soc. Rev.* 43 (15): 5257–75. doi:10.1039/C4CS00015C.
- Liu, Z., S. Zein El Abedin, and F. Endres. 2013. "Electrodeposition of Zinc Films from Ionic Liquids and Ionic Liquid/water Mixtures." *Electrochimica Acta* 89 (November): 635–43. doi:10.1016/j.electacta.2012.11.077.
- Pichler, Birgit, Stephan Weinberger, Lucas Rešćec, Ilena Grimmer, Florian Gebetsroither, Brigitte Bitschnau, and Viktor Hacker. 2017. "Bifunctional Electrode Performance for Zinc-Air Flow Cells with Pulse Charging." *Electrochimica Acta* 251 (August): 488–97. doi:10.1016/j.electacta.2017.08.128.
- Pletcher, Derek, Xiaohong Li, Stephen W T Price, Andrea E. Russell, Turgut Sönmez, and Stephen J. Thompson. 2016. "Comparison of the Spinel Co₃O₄ and NiCo₂O₄ as Bifunctional Oxygen Catalysts in Alkaline Media." *Electrochimica Acta* 188. Elsevier Ltd: 286–93. doi:10.1016/j.electacta.2015.10.020.
- Simons, T. J., A. A J Torriero, P. C. Howlett, D. R. MacFarlane, and M. Forsyth. 2012. "High Current Density, Efficient Cycling of Zn²⁺ in 1-Ethyl-3-Methylimidazolium Dicyanamide Ionic Liquid: The Effect of Zn²⁺ Salt and Water Concentration." *Electrochemistry Communications* 18 (1). Elsevier B.V.: 119–22. doi:10.1016/j.elecom.2012.02.034.
- Sumboja, Afriyanti, Xiaoming Ge, Guangyuan Zheng, F.W. Thomas Goh, T.S. Andy Hor, Yun Zong, and Zhaolin Liu. 2016. "Durable Rechargeable Zinc-Air Batteries with Neutral Electrolyte and Manganese Oxide Catalyst." *Journal of Power Sources* 332. Elsevier B.V.: 330–36. doi:10.1016/j.jpowsour.2016.09.142.
- Vieira, L., a. H. Whitehead, and B. Gollas. 2013. "Mechanistic Studies of Zinc Electrodeposition from Deep Eutectic Electrolytes." *Journal of the Electrochemical Society* 161 (1): D7–13. doi:10.1149/2.016401jes.
- Wadia, Cyrus, Paul Albertus, and Venkat Srinivasan. 2011. "Resource Constraints on the Battery Energy Storage Potential for Grid and Transportation Applications." *Journal of Power Sources* 196 (3). Elsevier B.V.: 1593–98. doi:10.1016/j.jpowsour.2010.08.056.
- Wang, Keliang, Pucheng Pei, Ze Ma, Huachi Xu, Pengcheng Li, and Xizhong Wang. 2014. "Morphology Control of Zinc Regeneration for Zinc-Air Fuel Cell and Battery." *Journal of Power Sources* 271: 65–75. doi:10.1016/j.jpowsour.2014.07.182.
- Zelger, Christian, Jennifer Laumen, Andreas Laskos, and Bernhard Gollas. 2016. "Rota-Hull Cell Study on Pulse Current Zinc Electrodeposition from Alkaline Electrolytes." *Electrochimica Acta* 213. Elsevier Ltd: 208–16. doi:10.1016/j.electacta.2016.07.108.
- Zhao, Haoran, Qiuwei Wu, Shuju Hu, Honghua Xu, and Claus Nygaard Rasmussen. 2015. "Review of Energy Storage System for Wind Power Integration Support." *Applied Energy* 137. Elsevier Ltd: 545–53. doi:10.1016/j.apenergy.2014.04.103.